

# **Turbulence and Viscous Mixing using Smoothed Particle Hydrodynamics**

A thesis submitted for the degree of  
Doctor of Philosophy

by

Martin Robinson

Department of Mathematical Science  
Monash University  
Australia

July 2009

# Contents

---

<b>Abstract</b>	<b>v</b>
<b>Acknowledgement</b>	<b>vii</b>
<b>Declaration</b>	<b>viii</b>
<b>Copyright Notices</b>	<b>ix</b>
<b>1 Introduction</b>	<b>1</b>
1.1 Viscous Mixing . . . . .	1
1.2 Turbulent Mixing . . . . .	4
<b>2 Smoothed Particle Hydrodynamics</b>	<b>7</b>
2.1 Interpolation . . . . .	9
2.2 Interpolation of the Derivatives . . . . .	10
2.3 Completeness . . . . .	11
2.4 Kernels . . . . .	12
2.5 Application to Incompressible Fluid Dynamics . . . . .	14
2.5.1 Quasi-compressible SPH and the Continuity Equation . . . . .	14
2.5.2 The Pressure Gradient . . . . .	15
2.5.3 Viscosity . . . . .	16
2.6 No-Slip Boundaries . . . . .	18
2.7 Time Integration . . . . .	19
2.8 Variable Smoothing Length . . . . .	22
2.9 Energy Budget . . . . .	22
2.10 Tensile Instability . . . . .	24
2.11 Finding Particle Neighbours . . . . .	25
2.12 Parallel Implementation . . . . .	25
<b>3 Viscous Mixing in a Two-Dimensional Twin Cam Mixer</b>	<b>28</b>
3.1 Measuring Mixing . . . . .	29
3.2 Chaotic Transport . . . . .	30
3.3 The Simulation Method . . . . .	33
3.4 Mixing Analysis . . . . .	33
3.4.1 Finite-Time Lyapunov Exponent . . . . .	33
3.4.2 Mixing Measure . . . . .	35
3.5 Simulation Results . . . . .	36

---

3.5.1	Timestep and Viscosity Issues . . . . .	36
3.5.2	Experimental Validation . . . . .	37
3.5.3	Increased Resolution . . . . .	40
3.6	Mixing Results . . . . .	41
3.6.1	Finite-Time Lyapunov Exponents . . . . .	41
3.6.2	Counter-rotating Simulation . . . . .	43
3.6.3	Mixing Measure and Time scales . . . . .	44
3.7	Conclusion . . . . .	48
<b>4</b>	<b>Turbulence</b> . . . . .	<b>49</b>
4.1	Two-dimensional Turbulence . . . . .	52
4.1.1	Kinetic Energy Scaling . . . . .	54
4.1.2	Dissipation Length scale . . . . .	55
4.1.3	Velocity Structure Functions . . . . .	56
4.1.4	Richardson's Particle Pair Dispersion . . . . .	57
4.2	Wall-bounded Two-Dimensional Turbulence . . . . .	58
4.3	SPH Turbulence Background . . . . .	59
4.4	Motivations for an SPH simulation of 2D Wall-Bounded Turbulence . . . . .	61
4.5	SPH Fourier Transform . . . . .	62
<b>5</b>	<b>Decaying Turbulence Simulations</b> . . . . .	<b>65</b>
5.1	SPH Simulation . . . . .	65
5.2	Initial Turbulent Velocity Field . . . . .	66
5.3	Vorticity Evolution . . . . .	67
5.4	Total Angular Momentum and Spontaneous Spin-Up . . . . .	69
5.5	Kinetic Energy Decay . . . . .	71
5.6	Average Wavenumber Decay . . . . .	72
5.7	Convergence Study . . . . .	73
5.8	Discussion . . . . .	76
<b>6</b>	<b>Forced Turbulence Simulations</b> . . . . .	<b>78</b>
6.1	Simulation Setup . . . . .	79
6.1.1	Forcing Protocol . . . . .	79
6.1.2	Resolution Requirements . . . . .	82
6.1.3	Other Parameters . . . . .	82
6.2	Initial Results . . . . .	83
6.2.1	Vorticity Evolution . . . . .	83
6.2.2	Energy Budget . . . . .	85
6.2.3	Angular Momentum . . . . .	87
6.2.4	Fourier Analysis . . . . .	88
6.2.5	Pressure Field . . . . .	91
6.2.6	Velocity Structure Functions . . . . .	93
6.2.7	Particle Pair Dispersion . . . . .	96
6.3	Sensitivity To Parameters . . . . .	99
6.3.1	Compressibility . . . . .	99
6.3.2	Resolution . . . . .	103
6.3.3	Viscous Term . . . . .	106
6.3.4	Density Smoothing . . . . .	106
6.3.5	Variable versus Constant Smoothing Length . . . . .	110

---

---

6.4	Effective Viscosity . . . . .	113
6.5	Periodic Forced Turbulence . . . . .	115
6.6	Spinning Box Turbulence . . . . .	119
6.7	Conclusion . . . . .	123
<b>7</b>	<b>Kernel Effects on Particle Clumping</b>	<b>125</b>
7.1	Radial Particle Density Function . . . . .	126
7.2	Clumping versus Spline Point position . . . . .	127
7.3	The Wendland Kernel . . . . .	127
7.4	The First Derivative of the Kernel . . . . .	131
7.5	The Fourier Transform of the Kernel . . . . .	134
7.6	Conclusion . . . . .	137
<b>8</b>	<b>Conclusion</b>	<b>138</b>
8.1	Recommendations for Future Research . . . . .	140
8.1.1	Three-dimensional Chaotic Manifolds . . . . .	140
8.1.2	Turbulent Boundary Condition and Boundary Layers . . . . .	140
8.1.3	The Velocity Structure Function . . . . .	141
8.1.4	Three-dimensional SPH Turbulence . . . . .	141
8.1.5	Particle Clumping and Kernel Fourier Transform . . . . .	141
8.1.6	Small Scale Velocity Fluctuations . . . . .	141
	<b>Bibliography</b>	<b>143</b>

# Abstract

---

This thesis describes the application of Smoothed Particle Hydrodynamics (SPH) to viscous and turbulent mixing. It is comprised of two main sections that study two important classes of mixing flows from each end of the Reynolds Number range. The first section describes an SPH study of very viscous mixing using a two-dimensional Twin Cam mixer and the development of numerical tools to study the chaotic mixing within this device. The second section studies the application of SPH to Direct Numerical Simulations (DNS) of two-dimensional turbulence in a square box with no-slip boundaries. The primary focus of this section is to evaluate how well SPH can reproduce the primary characteristics of 2D wall-bounded turbulence. These characteristics include those near the no-slip boundaries of the box (e.g. the boundary layer and vortex roll-up) as well as those in the central turbulent flow (e.g. the inverse energy and direct enstrophy cascades).

Chapter 1 provides an introduction to the two types of mixing flows that are investigated in this thesis. The chapter covers the motivations behind this research and provides a summary of the relevant literature.

Chapter 2 gives an overview of the SPH method and the particular formulation used in this thesis.

Chapter 3 describes 2D SPH simulations of a Twin Cam mixer and compares the results against experimental data and results from two published Finite Element Method (FEM) simulations. A methodology for the analysis and quantification of the chaotic mixing is presented and applied to the Twin Cam mixer. The first half of this methodology is based on the use of Finite-Time Lyapunov Exponents (FTLE) to visualise the chaotic manifolds of the flow. The topology of the manifolds describe the stretching and folding actions of the mixing, and define regions in the flow that are substantially isolated (ie. slow to mix) from neighbouring regions. A method of calculating the spatial distribution of FTLE directly from the SPH particle data is presented, which represents a considerable reduction in computational cost compared to previously published methods. The second half of the analysis methodology is based on a quantitative measure of mixing. Given a length scale of interest, this measure calculates the local amount of mixing between two or more regions. The measure is used to show the differences in both the spatial variation and total amount of mixing between the important regions in the flow previously identified by the chaotic manifolds. The chapter finishes by comparing the time scales of mixing over different length scales in the Twin Cam mixer.

Chapter 4 provides an overview of the current theoretical description of homogeneous

and isotropic 3D and 2D turbulence. It also covers recent numerical and experimental results for DNS turbulence in periodic and wall-bounded domains. A literature review of SPH turbulence is given. The chapter ends by discussing the primary motivations behind this investigation of SPH DNS of two-dimensional wall-bounded turbulence.

Chapter 5 presents the results of ensemble SPH simulations of decaying wall-bounded 2D turbulence at a Reynolds number ( $Re$ ) of 1500. These are compared against published results from a pseudospectral code. The qualitative variables of the SPH turbulence evolution (e.g. kinetic energy decay, angular momentum and average vortex wavenumber) compare well with the pseudospectral results. However, the production of long-lived coherent vortices from the boundaries is not seen in the SPH simulations. Subsequent results show that the boundary layer and vortex roll-up are modelled well by the SPH method, but excess numerical dissipation prevents the vortex from surviving once it has detached from the boundary.

Chapter 6 investigates SPH simulations of forced wall-bounded ( $Re = 1581$ ) and periodic ( $Re = 2645$ ) 2D turbulence. As for the decaying case, these results are compared against published pseudospectral simulations and physical experiments. The SPH simulations reproduce the direct enstrophy cascade well. The kinetic energy spectrum follows the expected  $k^{-3}$  scaling in the direct enstrophy range for wavelengths larger than 8 particle spacings. However, velocity fluctuations at wavelengths less than 8 particle spacings are responsible for a significant amount of numerical dissipation. This dissipation acts to weaken the inverse energy cascade and prevents the build-up of energy in the longest wavelength. Investigations into the statistics of particle pair dispersion show deviations in the expected scalings at wavelengths less than the forcing scale. These deviations are consistent with the small-scale velocity fluctuations acting as an additional forcing term and increasing the rate of mixing at small length scales.

SPH parameter studies show that the turbulence is very sensitive to the SPH sound speed, with increasing sound speed resulting in a significant increase in numerical dissipation and a subsequent reduction in the strength of the inverse energy cascade. The maximum wavelength of the small-scale velocity fluctuations decreases slowly with increasing resolution. It is estimated that a minimum particle resolution of  $3500 \times 3500$  is needed to reduce the minimum wavelength of the velocity fluctuations below the dissipation length scale of the turbulence (for  $Re = 1581$ ).

Chapter 7 compares the Cubic Spline and Wendland kernels and their effect on particle clumping in the forced 2D turbulence simulations. The Cubic Spline is found to generate significant clumping on a length scale equal to the location of the spline point (typically chosen to be the smoothing length  $h$ ). In contrast, the Wendland kernel results in a very even distribution of particles, which dramatically reduces the numerical dissipation in the forced turbulence simulations and strengthens the inverse energy cascade. Particle clumping in SPH simulations is often attributed to the Tensile Instability. However, the criteria for this instability is unchanged between the Cubic Spline and Wendland kernels leading to the conclusion that the Tensile Instability is not the cause of the clumping seen in these simulations.

# Acknowledgement

---

I would like to thank my supervisor Prof. Joseph Monaghan for his endless enthusiasm, insight and the countless cups of coffee. My co-supervisor Dr. Paul Cleary, for his suggestion of the Twin Cam mixer and for his assistance with the resultant papers. My officemates, Jules Kajtar and John Mansour, for their friendly and useful discussions. Thankyou to all the staff and students at the Mathematical Science department, especially to Gertrude Nayak and Doris Herft for helping me out even though I was terribly late with all my forms. Thankyou to my family and friends for their support, and especially to my father for always wanting to know what I was working on and for his inspirational view on life.

During my candidature I was supported financially by the Monash Graduate Scholarship and the CSIRO postgraduate scholarship, which also enabled my travel to the SPHERIC 2007 and 2008 workshops.

Thankyou to our three feline daughters, Jasmin, Holly and Audine. For always wanting to keep me company during many long hours in front of the computer.

But most of all, I'd like to thank my lovely wife, Rebecca. Thank you for keeping me sane and making me believe that anything is possible.

# Declaration

---

I hereby declare that this thesis contains no material which has been accepted for the award of any other degree or diploma in any university or equivalent institution, and that, to the best of my knowledge and belief, this thesis contains no material previously published or written by another person, except where due reference is made in the text of the thesis.

Martin Robinson

# Copyright Notices

---

Under the Copyright Act 1968, this thesis must be used only under the normal conditions of scholarly fair dealing. In particular no results or conclusions should be extracted from it, nor should it be copied or closely paraphrased in whole or in part without the written consent of the author. Proper written acknowledgement should be made for any assistance obtained from this thesis.

I certify that I have made all reasonable efforts to secure copyright permissions for third-party content included in this thesis and have not knowingly added copyright content to my work without the owner's permission.

# Preface

---

The material in Chapter 3 has been published or submitted for publication in the following papers:

- Martin Robinson, Paul Cleary, Joe Monaghan (2006), Analysis of mixing in a Twin-Cam mixer using Smoothed Particle Hydrodynamics, *Fifth Int. Conference on CFD in the Process Industries*, Melbourne.
- Martin Robinson, Paul Cleary, Joe Monaghan (2008), Analysis of mixing in a Twin-Cam mixer using Smoothed Particle Hydrodynamics, *AIChE Journal*, **54**(8):1987-1998, 2008.
- Martin Robinson, Paul Cleary (2009), "The Influence of Cam Geometry and Operating Conditions on Chaotic Mixing of Viscous Fluids in a Twin Cam Mixer", submitted to *AIChE Journal*

The material in Chapter 5 has been presented at the *SPHERIC 2007* workshop:

- Martin Robinson, Joe Monaghan, John Mansour (2007), DNS SPH simulation of 2D wall- bounded turbulence, *SPH European Research Interest Community (SPHERIC) workshop*, Madrid.

The material in Chapters 6 and 7 has been presented at the *SPHERIC 2008* workshop:

- Martin Robinson, Joe Monaghan (2008), Forced two-dimensional wall-bounded turbulence using SPH, *SPH European Research Interest Community (SPHERIC) workshop*, Lausanne.

# Chapter 1

## Introduction

---

Flows that mix together two or more types of fluids are commonplace and form the basis for many open problems across many fields of research. Some examples include supernova-driven turbulent mixing in the interstellar medium (de Avillez & Mac Low 2002), mixing in the Earth's mantle (van der Hilst 2004), the mixing of pollutants in the "street canyons" of the urban environment (Li et al. 2009) and the efficient manufacture of food and polymer products (Metcalf et al. 2006).

The wide variety of mixing flows can be roughly divided into two different categories depending on the Reynolds number of the flow. At low Reynolds numbers, the flow is laminar and the mixing is often limited by the molecular diffusivity of the fluids. Any mixing due to advection is usually inhomogeneous across the domain and depends strongly on the presence of chaotic trajectories in the flow. At higher Reynolds numbers the flow becomes turbulent, which induces mixing across a wide variety of length scales, irrespective of the particular form of the large scale mixing. Mixing in this category is very efficient, and occurs homogeneously across the entire domain of interest.

This thesis studies the application of Smoothed Particle Hydrodynamics (SPH) to two different and important classes of mixing flows that are representative of the two mixing categories defined in the preceding paragraph. The first section of this thesis involves the simulation and analysis of low Reynolds number mixing in a typical industrial mixer containing a highly viscous fluid. The second section applies SPH to the Direct Numerical Simulation (DNS) of decaying and forced turbulence in a square box with no-slip boundaries.

### 1.1 Viscous Mixing

In an industrial context, mixing flows are widespread. Nowhere is this more true than in the process industries, where mixers are used in the manufacture of products such as foods, pharmaceuticals, polymers, paints etc. Industrial mixers are often treated as black boxes, with limited understanding of the mixing processes present. Increased knowledge of how material is moved throughout a mixer, as well as tools to predict mixer geometry and movements that will reduce mixing times, is needed. Numerical simulations provide a flexible and low-cost tool to analyse the flow within an industrial mixer. New

geometries can be tested without the need to manufacture test models, and the effect of different mixing protocols can be predicted without having to manually set-up and run each experiment.

Numerical simulations of fluid flow in typical industrial mixers are often challenging due to complicated geometries involving moving parts and sharp corners. Grid-based methods such as Finite Element Methods (FEM) need to constantly regenerate the mesh to accommodate the moving objects, and these meshes often need to be further refined to correctly model fluid flow near small gaps and sharp corners. Smoothed Particle Hydrodynamics (SPH) is a Lagrangian, particle-based method that does not suffer from these disadvantages. Rather than using a fixed grid, the method interpolates the fluid variables over a disordered set of particles which move with the fluid velocity. Each particle represents a volume of fluid, so it can have its own physical properties and the advection is obtained automatically from the motion of the particles. The time history of each piece of fluid is trivial to obtain from the SPH simulation, and this reduces the computational costs of mixing analysis tools such as Finite-Time Lyapunov Exponents (FTLE) or Stretching distributions. SPH boundaries are constructed of particles which can be placed to follow the boundaries of any complex geometry, including sharp corners. Moving components such as impellers can be included in a simulation by assigning the appropriate velocity to each boundary particle. Chapter 2 provides a more detailed description of the SPH method and derives the SPH equations for a quasi-compressible fluid. It describes some of the commonly used variants for the viscous term and no-slip boundaries, and contains the details of the SPH implementation that was used to generate all the results in this thesis.

Many industrial processes require the efficient mixing of highly viscous fluids. Examples include the production of paints, polymers or food. The high viscosity of these fluids increases the power needed to operate the mixer since additional force is necessary to move the viscous fluid around the mixer, either via the motion of the impellers in a batch mixer or the pumping of fluid through a static mixer. The high viscosity also results in a laminar fluid flow due to the low Reynolds number ( $Re$ ). Without the benefits of turbulence, mixing is slow and limited by the molecular diffusivity of the fluids. It therefore becomes necessary to create many striations in the fluid via the continual application of stretching and folding operations (ie. a chaotic flow). These elongate material lines in the flow and increase the interfacial area between the different fluid components. The larger this area, the faster the diffusivity of the fluids can work to homogenise the contents of the mixer.

Chapter 3 uses SPH simulations to explore the chaotic mixing of highly viscous Newtonian fluid within a particular class of industrial mixer termed the Twin Cam mixer. This consists of a double-barrelled outer boundary containing fluid and two rotating equilateral triangular cams, one at each barrel centre. The SPH simulations are validated (favourably) against two different Finite Element simulations and a physical experiment (Avalosse & Crochet 1997, Bertrand et al. 2003).

The chapter goes on to analyse the chaotic flow in the Twin Cam mixer utilising the framework of Chaotic Advection, which describes the mixing in terms of the chaotic trajectories of mass-less particles that move with the flow. The term "Chaotic Advection" was first used in Aref (1984) and Aref (2002) gives a review of the subject. For a broader background on mixing and chaos in dynamical systems, consult books by Ottino (1989)

and Wiggins (1992).

Flows that exhibit chaotic trajectories can be divided into regions that exhibit different mixing characteristics. Regions containing regular, non-chaotic trajectories are permanently separated from the chaotic regions by Kolmogorov-Arnold-Moser (KAM) surfaces. These regular regions surround periodic elliptical points in the flow and need to be avoided to ensure a well-mixed domain over long timescales (ie. thousands of periods). Poincare sections can easily show the location of these regular regions, and are often used as a first step in mixer design due to their low computational requirements (Jana et al. 1994, Metcalfe et al. 2006). The chaotic regions of the flow can be further classified, based on the chaotic manifolds that originate from periodic hyperbolic points in the flow. These manifolds are Lagrangian structures that separate regions with very different mixing characteristics. Hyperbolic periodic points are associated with strong stretching and folding of fluid regions, and the manifolds show the topological structure of these mixing actions. Since they are material lines (or surfaces in 3D) that are advected along with the flow, these manifolds can also delineate regions that are isolated to some degree from the surrounding flow and therefore slow to mix with the rest of the domain.

Chapter 3 investigates the short term mixing behaviour in the Twin Cam mixer by examining the structure of the chaotic manifolds over time. The manifolds are ridges in the spatial map of Finite-Time Lyapunov Exponents (FTLE) (Shadden et al. 2005). This method of locating the manifolds has a number of advantages over more traditional techniques (Hobson 1993). A chaotic flow can have a very complicated manifold structure emanating from a number of periodic points. The length of each of these manifolds is infinite, so determining the periodic points and manifolds that are most important to the flow is a potential problem (Jana et al. 1994). Using the spatial map of FTLE to find the manifolds, there is no need to manually locate and classify periodic points in the flow. Furthermore, the height of the ridges indicates the amount of stretching along the manifolds, which is a good measure of the importance of the manifold to the mixing (Jana et al. 1994)

The FTLE is equivalent to the natural logarithm of length stretch measure described in Ottino (1989), the global distribution of which is often used as a quantitative measure of mixing strength (Jana et al. 1994, Metcalfe et al. 2006, Avalosse & Crochet 1997). Since the FTLE can be calculated for non-periodic flows, they have been used to study flows in the atmosphere (Pierrehumbert & Yang 1993), ocean (Shadden et al. 2005) or even biological cell evolution (Aldridge et al. 2006). The spatial distribution of FTLE is normally calculated by integrating large numbers of massless tracer particles in a known velocity field (Shadden et al. 2005, Lapeyre 2002). Chapter 3 describes a novel method of determining the spatial distribution of FTLE directly from the SPH particle data, without the need to advect tracer particles.

While the chaotic manifolds provide a qualitative view of the mixing, it is also necessary to provide a quantitative measure of the mixing. Chapter 3 defines a measure that calculates the degree to which an initial coloured region is mixed with the rest of the domain. This provides a practical measure that is directly related to the primary aim of any industrial mixer, the homogenisation of fluid areas. Unlike many existing measures with a similar aim (See Poux et al. (1991) for a review of 50 different mixing measures), this measure is local in nature and can be used determine the spatial variation in the mixing.

## 1.2 Turbulent Mixing

Mixing flows at sufficiently high Reynolds number are dominated by turbulent effects. For very viscous flows with a low Reynolds number, the mixing length scale is determined by the dimensions of the forcing term. For fully turbulent flow a forcing input at a single length scale will induce chaotic fluctuations and mixing over a wide range of scales. Naturally, this greatly improves the mixing rate, and a high Reynolds number and fully developed turbulence is therefore a desirable quality in many industrial mixers. However, the simulation of such a turbulent flow is fraught with difficulty. The resolution requirements for a Direct Numerical Simulation (DNS) are exceedingly high due to the large range of lengths scales that are involved (The ratio between the largest and smallest lengths scales is approximately  $Re^{3/4}$ ) In recent years the rapid increase in computational power due to Moore's Law has been responsible for a number of high resolution DNS experiments up to  $Re = 10^5$  (Kaneda et al. 2003). These simulations are primarily aimed at more theoretical turbulence studies that utilise Spectral Methods in order to take advantage of their excellent convergence properties. However, the convergence properties of these Spectral Methods are lost if any geometric complexity is introduced to the simulation and therefore these methods are not suitable for practical simulations of turbulent mixing.

Chapters 4 to 6 focus on the application of SPH to high resolution DNS simulations of turbulent flows. For these types of flows the primary challenge is the correct simulation of the flow. So while Chapter 3 focused mainly on the post-processing analysis of laminar mixing, these chapters aim to determine how well SPH models the wide range of length scales that are the hallmark of turbulence.

Chapter 4 provides an introduction to the current theoretical picture of three-dimensional and two-dimensional turbulence. This picture assumes a homogeneous distribution of turbulence over an infinite domain. Energy is injected into the flow at a particular length scale called the *forcing scale*. In the case of 3D turbulence, this energy is transferred to smaller and smaller length scales via the *direct energy cascade* until the effects of viscosity become dominant and the energy is dissipated at the Kolmogorov microscale (Kolmogorov 1941*a,b,c*). For 2D turbulence, the direction of the energy cascade is reversed and the *inverse energy cascade* moves the energy to larger length scales (Batchelor 1969, Kraichnan 1967). Length scales smaller than the forcing scale are instead dominated by the *direct enstrophy cascade*, which acts to decrease the length scale of structures in the vorticity field (ie. Turbulent eddies), increasingly associating the enstrophy with a fine-scale structure.

The majority of the SPH turbulence study is devoted to two-dimensional, wall-bounded decaying (Chapter 5) and forced (Chapter 6) turbulence in a square domain. The reasons behind the choice of 2D turbulence and a wall-bounded domain are detailed fully in Chapter 4. In summary, 2D turbulence provides a significant simulation challenge with relatively low resolution requirements and an expansive history of experimental, numerical and theoretical publications with which to validate the simulation. While many DNS simulations of turbulence use periodic boundary conditions in order to approximate an infinite domain, this assumption has been called into question (Tran & Bowman 2003, Davidson 2004, Lowe 2001). A wall-bounded simulation involves no such assumptions, and the no-slip boundaries result in a spontaneous spin-up of the fluid in the box (Sommeria 1986), as well as other boundary layer effects (Clercx et al. 2005) that can all be used

to evaluate how well SPH simulates turbulence in a more practical setting.

A series of papers by Clercx et al. (1999), Maassen et al. (2002), Molenaar et al. (2004), van Heijst et al. (2006) and Wells et al. (2007) describe a series of experimental and numerical investigations of decaying and forced two-dimensional turbulence in wall-bounded flows (See Clercx et al. (2005) for a review of most of the results). The numerical simulations use a highly accurate Spectral method based on Chebyshev polynomials with a semi-implicit Adams-Bashforth Crank-Nicolson time integration scheme. These results are the primary source of comparison against the SPH turbulence simulations.

Published literature on SPH turbulence has primarily focused on the development of techniques that attempt to model the smaller length scales of the turbulence rather than directly simulating them, hence reducing the resolution requirements to more practical levels. These models are typically based on existing Eulerian grid-based techniques. The majority of SPH turbulence models have focused on using the Large Eddy Simulation (LES) method combined with a Smagorinsky model for the sub-particle scale (Violeau & Issa 2007, Dalrymple & Rogers 2006, Shao et al. 2006, Issa et al. 2005, Ting et al. 2006). The LES equations are obtained by filtering the Navier-Stokes equations via the application of a Eulerian smoothing operator. The use of a smoothing operator makes this a natural method to combine with SPH, and Ting et al. (2006) and Cleary & Monaghan (1993) both state that SPH can be considered to have a form of LES already built in. These LES-based turbulence models, as well as others described in the SPH literature, are discussed in more detail in Section 4.3.

Mansour (2007) has performed the only SPH DNS prior to this thesis. Mansour ran SPH simulations of forced 2D incompressible turbulence in a periodic box. While most of Chapter 6 focuses on simulations of forced turbulence in a wall-bounded box, Section 6.5 shows results from a forced periodic box. Both these results and those by Mansour show a significantly reduced inverse energy cascade. However, in contrast to the results by Mansour, the kinetic energy spectrum in the direct enstrophy range is reproduced correctly for length scale larger than 8 particle spacings.

There are a number of differences in the SPH implementation used in Chapter 6 and that used by Mansour. Mansour added a large-scale dissipation term, which is line with the traditional periodic box simulation seen in the turbulence literature. This term is not included in order to determine if SPH can correctly reproduce the expected condensation of energy into the lowest wavenumber (this was not seen in any of the SPH simulations in this thesis). The continuity equation is used to integrate the particle densities, whereas Mansour calculated these densities directly using an SPH sum. Section 6.3.4 shows that this SPH sum smoothes out small-scale density fluctuations, acting as an additional energy sink (comparable to the viscous dissipation) for the turbulence. Finally, the Wendland kernel is used rather than the traditional Cubic Spline, which eliminates the particle clumping seen with the Cubic Spline, significantly reducing numerical dissipation and increasing the strength of the inverse energy cascade.

This thesis concludes with Chapter 7, a study of the effects of the SPH kernel on the particle clumping seen in the forced turbulence simulations. This chapter compares two different kernels, the traditional Cubic Spline and the lesser known Wendland kernel, which is based on a family of interpolation functions proposed by Wendland (1995). For each kernel, the chapter explores the statistical properties of the clumping, utilising the fact that

the turbulence, and hence the particle distribution, is homogeneous and isotropic over most of the simulation domain. The Cubic Spline is found to produce particle clumping on a length scale equal to the location of the spline point, whereas the Wendland kernel eliminates the clumping entirely. The well-known Tensile Instability (Swegle et al. 1995) is often attributed as the cause of particle clumping within SPH simulations. However, the criteria for this instability is unchanged between the Cubic Spline and Wendland kernels, indicating that it is not dominant in these simulations.

## Chapter 2

# Smoothed Particle Hydrodynamics

---

Smoothed Particle Hydrodynamics (Gingold & Monaghan 1977, Lucy 1977, Monaghan 2005) is a Lagrangian scheme, whereby the fluid is discretised into particles that move with the fluid velocity. Each particle is assigned a mass and can be thought of as the same volume of fluid over time. The fluid variables and the equations of fluid dynamics are interpolated over each particle and its nearest neighbours using a Gaussian-like kernel with compact support.

As a Lagrangian, meshless scheme, SPH has a number of advantages over mesh-based methods. Advection is taken care of automatically because the particles carry their properties with them. The movement of the fluid is simply the movement of the SPH particles. This provides an important advantage for multi-phase flows, as each particle can be assigned to a different phase. A similar advantage exists for interfacial or free-surface flows. In both cases, there is no need to explicitly track the interface or free-surface of interest, as it will be implicitly defined by the positions of the particles.

Unlike mesh-based methods, there are no prescribed connections between the SPH particles. Instead, each particle interacts with all of its neighbours according to their radial separation and the shape of the interpolating kernel. This results in a much more flexible method, without many of the issues that are involved in the generation and evolution of a complex, time-varying mesh. For example, problems involving complex, moving geometry, elastic solids or the fracture of brittle solids are all application areas where the meshless nature of SPH provides a significant advantage.

However, there are a few disadvantages with using a meshless method. Unlike grid-based codes, SPH particles are not explicitly constrained to stay in a well-ordered, stable configuration. While the shape of the kernel and the continuity equation tend to move the particles so that they are (roughly) evenly spaced, the instantaneous dynamics of the fluid or instabilities in the method can cause the particles to become disordered, reducing the simulation accuracy. Furthermore, the analysis of errors and the stability of the SPH method due to a non-regular particle distribution is difficult. Monaghan (2005) presents an analysis of the interpolation errors that occur for a 1D equi-spaced line of SPH particles. Sweigle et al. (1995) and Morris (1996) have performed a stability analysis of SPH, providing results for 1D and 2D regular grids of particles. In contrast, there is much less information available on SPH errors and instabilities for disordered particles. Monaghan

(2005) calculates an upper bound on the errors due to a randomly distributed set of particles, but notes that the random distribution is significantly more disordered than one would expect from an actual SPH simulation.

Whatever the errors inherent in the method, SPH produces satisfactory results for a wide variety of complex flows. This is often attributed to the conservation properties of SPH. It is possible to derive the non-dissipative SPH equations directly from a Lagrangian, which ensures the conservation of momentum and energy. Through a careful selection of timestepping scheme (see Section 2.7), the long-term conservation properties of the Lagrangian can be retained, with the additional advantage of ensuring that the simulation is reversible in time (in the absence of viscosity, and only up to machine precision). Gingold & Monaghan (1978) originally derived the SPH equations from a Lagrangian. More recent derivations (including a variable smoothing length) were carried out by Springel & Hernquist (2002) and Monaghan (2002).

SPH originally grew out of the astrophysical community in the late seventies, where it originally gained popularity due to its automatic adaptive resolution, which concentrated particles in areas of high density, its natural modelling of free boundaries and its conservation of angular momentum. It has been used to model such phenomena as binary stars systems (Hernquist & Katz 1989), molecular clouds (Lattanzio et al. 1985), shocks (Monaghan & Gingold 1983) and the impact of planetesimals with the earth (Cameron & Benz 1991). The SPH review article by Monaghan (1992) provides many more such examples.

More recently, SPH has been increasingly applied to more terrestrial applications involving incompressible flows. A quasi-compressible formulation of SPH (Monaghan 2005) is normally used, although there have been a number of truly incompressible formulations that have been proposed. These formulations generally rely on solving a Poisson equation to either enforce zero velocity divergence (Cummins & Rudman 1999) or zero density variation between the particles (Shao & Lo 2003). Another method has been proposed by Hu & Adams (2007) that uses an iterative predictor-correction technique to enforce both the velocity divergence and density variation conditions.

As previously mentioned, the Lagrangian nature of SPH allows the method to be easily applied to free-surface or multi-phase flows. This has made the method popular for marine or coastal hydrodynamics problems. Some examples include the modelling of breaking waves in the surf zone (Dalrymple & Rogers 2006) or over a sea-wall (Shao et al. 2006), sloshing in liquefied natural gas tankers (Delorme et al. 2005), air entrainment in fluid-structure impact (Colagrossi & Landrini 2003) or gravity currents (Monaghan et al. 1999).

SPH has been used to model the deformation or fracture of brittle or elastic solids. This can be coupled to a liquid phase for fluid-structure problems (e.g. Antoci et al. (2007)). Both Benz & Asphaug (1995) and Randles & Libersky (1996) show SPH results for a number of problems involving the fracture and fragmentation of brittle solids. Gray et al. (2001) applied SPH to both elastic and brittle solids. A commonly cited issue when applying SPH to the simulation of solids is a short-wavelength instability termed the Tensile Instability, which causes clustering in the spatial distribution of the SPH particles. This instability was first studied by Sweigle et al. (1995). Various solutions to this problem

have been proposed, including an anti-clumping force between the particles by Monaghan (2000) and the addition of dissipation terms by Randles & Libersky (1996).

SPH is also becoming used to model some industrial flows. Cleary et al. (2007) provides a summary of some applications in this area, including die casting, resin transfer moulding, pyrometallurgical processes with reactive solids and slurry flow in sag mills.

The application of SPH to special effects in film and television, as well as real-time computer games, are also popular due to the inherent flexibility of the method. For example, Next Limit Technologies (<http://www.nextlimit.com>) is a company specialising in film and television special effects using SPH. The commercial Physx library created by Nvidia ([http://www.nvidia.com/object/physx\\_new.html](http://www.nvidia.com/object/physx_new.html)), contains a real-time fluid solver based on SPH.

This chapter provides an overview of the SPH method and its application to quasi-compressible fluid dynamics. It also presents the specifics of the SPH equations and implementation details that are used to calculate all the results shown in this thesis.

## 2.1 Interpolation

SPH is based on the idea of kernel interpolation. A fluid variable  $A(\mathbf{r})$  (such as velocity or density) is interpolated using a kernel  $W$ , which depends on the smoothing length variable  $h$ .

$$A(\mathbf{r}) = \int A(\mathbf{r}')W(\mathbf{r} - \mathbf{r}', h)d\mathbf{r}'. \quad (2.1.1)$$

This is known as the *integral interpolant*. Monaghan (2005) uses a Taylor expansion of the integral interpolant to show that it estimates  $A(r)$  with at least second order accuracy, as long as the integral can be extended to the entire support region of the kernel.

To apply this to the discrete SPH particles, the integral is replaced by a sum over all particles, commonly known as the *summation interpolant*.

$$A(\mathbf{r}) = \sum_b m_b \frac{A_b}{\rho_b} W(\mathbf{r} - \mathbf{r}_b, h), \quad (2.1.2)$$

where  $m_b$ ,  $\rho_b$  and  $\mathbf{r}_b$  are the mass, density and position of particle  $b$ . The volume element  $d\mathbf{r}'$  of Equation 2.1.1 has been replaced by the volume of particle  $b$  (approximated by  $\frac{m_b}{\rho_b}$ ). This is the normal trapezoidal quadrature rule.

The SPH interpolation functions are usually calculated at the position of each particle in the domain. For particle  $a$  this becomes

$$A_a = \sum_b m_b \frac{A_b}{\rho_b} W_{ab}. \quad (2.1.3)$$

Here,  $W_{ab}$  denotes  $W(\mathbf{r}_a - \mathbf{r}_b, h)$ . The dependence of the kernel on the smoothing length

$h$  and the difference in particle positions is not explicitly stated for readability.

The errors in the summation interpolant are more difficult to determine, since by the nature of the method, these depend on the locations of the particles. Monaghan (2005) shows that a 1D equi-spaced line of particles reproduces a linear function with an error determined by the Fourier transform of the Kernel. In the case of a Gaussian kernel and where  $\Delta p$  is the particle spacing, the error is  $\mathcal{O}\left(e^{-\frac{h^2}{(\Delta p)^2}}\right)$ . The more practical and most commonly used kernel, the Cubic Spline, gives an error of  $\mathcal{O}\left(\left(\frac{\sin \pi h / \Delta p}{\pi h / \Delta p}\right)^4\right)$ . Morris (1996) investigated the dispersion relation and stability properties of SPH and found that the method was more stable using kernels whose Fourier Transforms fall off more rapidly (This particular result also assumed a 1D equi-spaced line of particles). So the interpolation errors involved in SPH seem closely related to this property of the kernel.

While the SPH summation errors can be quantified for particles on a regular grid, during a simulation the particle will not remain in this configuration and will instead become disordered (assuming a non-trivial velocity field). This disorder is bounded below a level determined by the action of the kernel and pressure equation of state. For the weakly compressible SPH formulation, these act to keep the particles evenly spaced, and density fluctuations below 1%. Using a set of  $N$  particles distributed at random over an area, the errors are similar to that of a Monte Carlo simulation,  $\mathcal{O}\left(\frac{1}{\sqrt{N}}\right)$ . But the SPH method forces the particles to be distributed in a much more orderly fashion than an entirely random arrangement, so the true error in any given simulation would fall significantly above this lower bound.

Monaghan (2005) also notes that the summation interpolant fails to even reproduce a constant exactly, or in other words, the basic method is not zeroth-order complete. Enforcing completeness in SPH is an active area of research and is described in more detail in Section 2.3.

## 2.2 Interpolation of the Derivatives

Taking the spatial derivative of Equation 2.1.1 gives

$$\nabla A(\mathbf{r}) = \int A(\mathbf{r}') \nabla W(\mathbf{r} - \mathbf{r}', h) d\mathbf{r}'. \quad (2.2.1)$$

Which, in SPH summation form for particle  $a$  is

$$\nabla A_a = \sum_b m_b \frac{A_b}{\rho_b} \nabla_a W_{ab}. \quad (2.2.2)$$

However, this form of the spatial derivative is not guaranteed to vanish when  $A(\mathbf{r})$  is constant. To ensure that it does, the derivative can be written as (Monaghan (2005))

$$\nabla A_a = \frac{1}{\Phi} (\nabla(\Phi A) - A \nabla \Phi), \quad (2.2.3)$$

where  $\Phi$  is any differentiable function. When this function is converted to SPH form, it becomes

$$\nabla A_a = \frac{1}{\Phi_a} \sum_b m_b \frac{\Phi_b}{\rho_b} (A_b - A_a) \nabla W_{ab}. \quad (2.2.4)$$

## 2.3 Completeness

It has already been mentioned that the summation interpolant (Equation 2.1.2) is not zeroth order complete. That is, it fails to reproduce a constant function

$$\sum_b m_b \frac{1}{\rho_b} W_{ab} \neq 1. \quad (2.3.1)$$

This can be fixed with a minimum of additional calculation by using a Shepard correction (Shepard (1968)), originally devised as a low cost improvement to data fitting. This correction divides the interpolant by the sum of kernel values at the particle positions, so the summation interpolant becomes

$$A_a = \frac{1}{\sum_b W_{ab}} \sum_b m_b \frac{A_b}{\rho_b} W_{ab}. \quad (2.3.2)$$

As well as enforcing zeroth order completeness, this also significantly improves the accuracy of the interpolation if the kernel for particle  $a$  is not fully supported by the other particles. For example, if  $a$  was located at a free-surface it is possible that only half of its kernel would be covered by particles. The normal summation interpolant assumes that the particles evenly cover the kernel area, and would give a result that was approximately half the true value of the variable. Using a Shepard correction, the variable is estimated to within the normal interpolation error.

Higher order completeness can be described by considering the function  $A$  as a univariate polynomial (Belytschko et al. 1998).

$$A(x) = a_0 + a_1x + a_2x^2 + \dots + a_kx^k. \quad (2.3.3)$$

The kernel  $W$  can be considered  $k$ -th order complete if it can reproduce  $A$  exactly.

Linear, or first-order, completeness is usually enforced by using the Moving Least Squares kernel  $W^{\text{MLS}}$ . This is constructed by multiplying the base kernel by a linear polynomial (Colagrossi & Landrini 2003). In two dimensions this is

$$W_b^{\text{MLS}}(\mathbf{r}_a) = [\beta_0(\mathbf{r}_a) + \beta_1(\mathbf{r}_a)(x_a - x_b) + \beta_2(\mathbf{r}_a)(y_a - y_b)] W_{ab}, \quad (2.3.4)$$

where the coefficients  $\beta$  are calculated using

$$\beta(\mathbf{r}_a) = \begin{pmatrix} \beta_0 \\ \beta_1 \\ \beta_2 \end{pmatrix} = \mathbf{A}^{-1}(\mathbf{r}_a) \begin{bmatrix} 1 \\ 0 \\ 0 \end{bmatrix}, \quad (2.3.5)$$

$$\mathbf{A}(\mathbf{r}_a) = \sum_b W_{ab} \tilde{\mathbf{A}}_{ab}, \quad (2.3.6)$$

$$\tilde{\mathbf{A}}_{ab} = \begin{bmatrix} 1 & (x_a - x_b) & (y_a - y_b) \\ (x_a - x_b) & (x_a - x_b)^2 & (x_a - x_b)(y_a - y_b) \\ (y_a - y_b) & (y_a - y_b)(x_a - x_b) & (y_a - y_b)^2 \end{bmatrix}. \quad (2.3.7)$$

Perhaps of more importance to SPH is the completeness of the derivative summation interpolant, since this is the equation that is primarily used in the method. Section 2.2 described how the derivative summation interpolant can be symmetrised in order to ensure that the derivative vanishes when given a constant function. Belytschko et al. (1998) shows how to use a process similar to the Moving Least Squares kernel to obtain a modified kernel and derivative that satisfy constant and linear completeness. This method requires the inversion of a  $(d + 1) \times (d + 1)$  matrix (for  $d$  dimensions) for every particle pair interaction. If only the kernel derivative is required, which would commonly be the case, then the method proposed by Krongauz & Belytschko (1997) can be used. This method constructs a kernel derivative from a linear combination of the derivatives of Shepard's corrected kernels. The coefficients are then calculated using the inversion of a  $d \times d$  matrix. Another popular method is described by Randles & Libersky (1996). This requires the inversion of the same  $d \times d$  matrix as Krongauz and Belytschko's, but uses symmetrisation instead of Shepard correction in order to ensure constant completeness.

## 2.4 Kernels

The properties of the SPH kernel  $W$  determine how the SPH variables are interpolated and smoothed between the particles. As a basic requirement, the kernel should be normalised to unity in order that the integral interpolant (Equation 2.1.1) reproduce a constant exactly. It should have compact support, so that SPH summations are not over all the particles in the domain. The kernel should also reduce to a delta function as  $h \rightarrow 0$ , so that the interpolant returns the exact function  $A(\mathbf{r})$  as  $h \rightarrow 0$ . These conditions can be written as

$$\int W(\mathbf{r} - \mathbf{r}', h) d\mathbf{r}' = 1, \quad (2.4.1)$$

$$W(\mathbf{r} - \mathbf{r}', h) = 0 \quad \text{for } \mathbf{r} - \mathbf{r}' > a, \quad (2.4.2)$$

$$W(\mathbf{r} - \mathbf{r}', h) \rightarrow 0 \quad \text{for } h \rightarrow 0, \quad (2.4.3)$$

where the radius of compact support  $a$  is normally equal to twice the smoothing length ( $a = 2h$ ).

Gaussian-like kernels are commonly used. While the Gaussian makes an attractive kernel due to its excellent stability properties (Morris et al. 1997, Morris 1996), its lack of compact support means that it cannot be used in practice without some modification. However, this kernel is still commonly used in theoretical investigations, as its mathematical properties simplify some analysis. In one dimension the Gaussian kernel is

$$W(r) = \frac{1}{\sqrt{\pi}} \exp(-r^2). \quad (2.4.4)$$

For practical simulations, the kernel most widely used is the Cubic Spline kernel. This is a third-order polynomial with compact support that is based on the family of spline functions by Schoenberg (1946). The Cubic Spline kernel is defined as

$$W(s) = \frac{\beta}{h^d} \begin{cases} (2-q)^3 - 4(1-q)^3 & \text{for } 0 \leq q < 1, \\ (2-q)^3 & \text{for } 1 \leq q < 2, \\ 0 & \text{for } q > 2. \end{cases} \quad (2.4.5)$$

where  $q = r/h$ ,  $d$  is the dimensionality of the kernel and  $\beta$  is a constant equal to  $1/6$ ,  $5/(14\pi)$  and  $1/(4\pi)$  for one, two and three dimensions respectively.

Higher order kernels in the same family, the Quartic or Quintic Spline (Schoenberg (1946)), can also be used, which offer improved stability (Morris (1996)) at the cost of increasing the volume of the kernel and therefore the number of particles involved in an SPH sum.

The Cubic Spline kernel is used for the viscous mixing simulations in Chapter 3 and the decaying turbulence simulations in Chapter 5. The forced turbulence simulations in Chapter 6 use the Wendland kernel, which is based on the family of interpolation functions by Wendland (1995). In Chapter 7, the use of the Wendland kernel is shown to result in significantly reduced numerical dissipation and particle clumping.

Wendland proposed an entire family of kernel functions (See Chapter 7 for more details) of which we have used a fifth-order kernel with the form

$$W(q) = \frac{\beta}{h^d} \begin{cases} (2-q)^4(1+2q) & \text{for } 0 \leq q \leq 2, \\ 0 & \text{for } q > 2. \end{cases} \quad (2.4.6)$$

where  $\beta = 7/(64\pi)$  when normalised in two dimensions.

For radially symmetric kernels, the spatial derivative of the kernel can be related to the 1D derivative of the kernel function. This allows the simplification of SPH equations found later in this chapter.

$$\nabla_a W_{ab} = \frac{\mathbf{r}_{ab}}{|\mathbf{r}_{ab}|} \frac{\partial W_{ab}}{\partial \mathbf{r}_a}. \quad (2.4.7)$$

## 2.5 Application to Incompressible Fluid Dynamics

These next few sections describe the application of the SPH method to the equations of incompressible fluid dynamics. Using the material derivative  $D/Dt$ , the relevant Navier-Stokes equations are

$$\frac{D\mathbf{v}}{Dt} = -\frac{1}{\rho}\nabla P + \frac{\mu}{\rho}\nabla^2\mathbf{v}, \quad (2.5.1)$$

$$\nabla \cdot \mathbf{v} = 0. \quad (2.5.2)$$

where  $P$  is the pressure,  $\rho$  is the density,  $\mathbf{v}$  is the velocity and  $\mu$  is the dynamic viscosity. Equation 2.5.1 is the momentum equation and Equation 2.5.2 is the continuity equation.

### 2.5.1 Quasi-compressible SPH and the Continuity Equation

SPH originated from the astrophysics community (Gingold & Monaghan 1977, Lucy 1977), where it was applied to compressible gas. In this case, the density can be computed using

$$\rho(\mathbf{r}) = \sum_b m_b W_{ab}, \quad (2.5.3)$$

which is simply the summation interpolant in Equation 2.1.2 with  $A = \rho$ . For incompressible flows, SPH algorithms usually use a quasi-compressible formulation, where the density varies by less than 1% between particles. For this case the density is typically calculated by integrating  $d\rho/dt$  for each particle over time, rather than directly calculating the density at each timestep using an SPH interpolation. This has the advantage of preserving density discontinuities at a free surface or at an interface between two fluids. In the case of the free surface, an SPH interpolation used to calculate the density at the free surface will not have enough particles to support the entire kernel, and therefore the calculated density will be significantly reduced from the true value. At the interface between two fluids with differing densities, the SPH interpolation will smooth out the density discontinuity over the length scale of the kernel. However, if the density is integrated using  $d\rho/dt$  this discontinuity will be preserved. Using  $d\rho/dt$  also provides a considerable reduction in computational effort in the case where the smoothing length  $h$  is allowed to vary (see Section 2.8).

The rate of change of density, or continuity equation, is given by

$$\frac{D\rho}{Dt} = -\rho\nabla \cdot \mathbf{v}. \quad (2.5.4)$$

Using Equation 2.2.4 to estimate  $\nabla \cdot \mathbf{v}$  with  $\Phi = \rho$ , this becomes

$$\frac{d\rho_a}{dt} = \sum_b m_b \mathbf{v}_{ab} \cdot \nabla_a W_{ab}, \quad (2.5.5)$$

where  $\mathbf{v}_{ab} = \mathbf{v}_a - \mathbf{v}_b$ . Note that  $d\rho_a/dt$  is equivalent to  $D\rho_a/Dt$  as  $\rho_a$  is the density carried by particle  $a$ .

The equation of state commonly used is (from Cole (1948))

$$P = B \left( \left( \frac{\rho}{\rho_0} \right)^\gamma - 1 \right), \quad (2.5.6)$$

where  $\gamma = 7$  is a typical value that is used throughout this thesis and  $\rho_0$  is a reference density that is usually set to the density of the fluid. Reducing  $\rho_0$  has the effect of adding a constant positive pressure, which is useful in eliminating particle voids that can occur due to the motion of the particles.

At the reference density ( $\rho = \rho_0$ ) the constant  $B$  can be related to the speed of sound  $c_s$  by

$$c_s^2 = \left. \frac{\partial P}{\partial \rho} \right|_{\rho=\rho_0} = \frac{\gamma B}{\rho_0}. \quad (2.5.7)$$

The speed of sound, and hence  $B$ , is chosen to keep the density variation between particles small (usually less than 1%). Since

$$\frac{|\delta\rho|}{\rho} = \frac{v^2}{c_s^2}, \quad (2.5.8)$$

in order to keep  $\frac{|\delta\rho|}{\rho} < 0.01$ , the constant  $B$  must be set to

$$B \geq \frac{100\rho_0 v_m^2}{\gamma}, \quad (2.5.9)$$

where  $v_m$  is an estimate of the maximum velocity of the flow.

### 2.5.2 The Pressure Gradient

Neglecting the viscous term, the momentum equation depends only on the pressure gradient

$$\frac{D\mathbf{v}}{Dt} = -\frac{1}{\rho}\nabla P. \quad (2.5.10)$$

Recall the symmetric form of the derivative introduced in Equation 2.2.3. Taking  $\Phi = \frac{1}{\rho}$  this becomes

$$\frac{1}{\rho}\nabla P = \nabla \left( \frac{P}{\rho} \right) + \frac{P}{\rho^2}\nabla\rho. \quad (2.5.11)$$

Using the SPH summation form of the spatial gradient (Equation 2.2.2) this becomes

$$\frac{d\mathbf{v}_a}{dt} = - \sum_b m_b \left( \frac{P_b}{\rho_b^2} + \frac{P_b}{\rho_b^2} \right) \nabla_a W_{ab}. \quad (2.5.12)$$

The variational study by Bonet & Lok (1999) derived a direct link between the form of the discretised continuity and pressure gradient equations. This highlights the importance of discretising these equation in the same fashion. Bonet and Lok called this *consistency*, although it is also known as *coherence* (Oger et al. 2007). Oger et al. (2007) shows that the SPH continuity and pressure gradient equations are consistent if they are derived using  $\Phi = \rho^\omega$  and  $\Phi = \frac{1}{\rho^\omega}$  respectively, where  $\omega \in \mathbb{R}$ .

The gradient of the kernel can be written as  $\nabla_a W_{ab} = \mathbf{r}_{ab} F_{ab}$ , where  $F_{ab}$  is a function of  $|\mathbf{r}_{ab}|$ . This means that the force on two particles  $a$  and  $b$  due to the pressure gradient will be equal and opposite, since  $\nabla_a W_{ab} = -\nabla_b W_{ba}$ . Note that this assumes that  $h$  is constant or a symmetric function of  $a$  and  $b$ . If this is not the case, the kernel for each particle can be redefined as  $W = 0.5(W_{ab} + W_{ba})$ .

This symmetry of the pressure gradient ensures the conservation of linear and angular momentum, an important property of most SPH implementations. Efforts to ensure linear completeness in SPH (see Section 2.3), while providing improved accuracy in estimating the pressure gradient, have a significant disadvantage in that they do not result in symmetric forces between the particles.

### 2.5.3 Viscosity

Viscosity is included by adding a viscous term  $\Pi$  to the SPH momentum equation

$$\frac{d\mathbf{v}_a}{dt} = - \sum_b m_b \left( \frac{P_b}{\rho_b^2} + \frac{P_b}{\rho_b^2} + \Pi_{ab} \right) \nabla_a W_{ab}. \quad (2.5.13)$$

There are many different forms for this term. Monaghan & Gingold (1983) first proposed a viscous term that was originally meant to allow the modelling of shocks in a gas.

$$\Pi_{ab} = -\alpha \frac{\bar{h}_{ab} \bar{c}_{ab}}{\bar{\rho}_{ab}} \left( \frac{\mathbf{v}_{ab} \cdot \mathbf{r}_{ab}}{\mathbf{r}_{ab}^2 + \beta \bar{h}_{ab}^2} \right), \quad (2.5.14)$$

where  $\bar{A}_{ab} = 0.5(A_a + A_b)$  and  $\beta$  is a small constant that ensures there is no singularity as  $|\mathbf{r}_{ab}| \rightarrow 0$ . This term conserves linear and angular momentum and vanishes for a rigid rotation.

Comparing this term to the physical viscous term for a compressible gas reveals that it has both a bulk  $\mu$  and shear  $\xi$  viscosity term that have the form (Monaghan 2005).

$$\mu = \rho \alpha h c / S, \quad (2.5.15)$$

$$\xi = 5\mu/3. \quad (2.5.16)$$

where, for the Cubic Spline kernel,  $S = 8$  for two dimensions and  $S = 10$  for three. The value of  $\alpha$  is therefore determined from the required bulk viscosity  $\mu$  using Equation 2.5.15.

However, it is often used to approximate a physical viscosity in an incompressible fluid, where it is assumed that the bulk viscosity (due to the non-zero velocity divergence of the particles) is negligible. Cleary (1998) proposed an alternate form for the viscous term, based on a derivation of the SPH thermal equation. This term includes an explicit dynamic viscosity term for each particle.

$$\Pi_{ab} = -\frac{C\mu_a\mu_b}{\rho_a\rho_b(\mu_a + \mu_b)} \left( \frac{\mathbf{v}_{ab} \cdot \mathbf{r}_{ab}}{\mathbf{r}_{ab}^2 + \beta\bar{h}_{ab}^2} \right), \quad (2.5.17)$$

where the constant  $C = 19.8$  was calculated by numerical experimentation against known transient flows.

Monaghan has since proposed a new version of his viscous term which is based on the dissipative term in shock solutions based on Riemann solvers (Monaghan 1997). This viscosity was initially derived to prevent the unphysical penetration of colliding gas clouds but is also successful when modelling the viscosity for incompressible fluids. For this viscosity

$$\Pi_{ab} = -\alpha \frac{v_{sig}(\mathbf{v}_{ab} \cdot \mathbf{r}_{ab})}{\bar{\rho}_{ab}|\mathbf{r}_{ab}|}, \quad (2.5.18)$$

where  $v_{sig} = 2(c_s + |\mathbf{v}_{ab} \cdot \mathbf{r}_{ab}|/|\mathbf{r}_{ab}|)$  is a signal velocity that represents the speed at which information propagates between the particles. This form of  $\Pi_{ab}$  will be used throughout most of this thesis.

It is also possible to derive an SPH viscous term directly from the physical viscosity term  $\frac{\mu}{\rho} \nabla^2 \mathbf{v}$ , using a method similar to that used to derive Equation 2.2.4. However, this results in an interpolation equation using the second derivative of the kernel, which is more sensitive to errors at low resolutions (Morris et al. 1997). In addition, the second derivative of the Cubic Spline kernel is non-smooth and therefore not suitable for use as an interpolation function.

Morris et al. (1997) derived a viscous term by combining a SPH first derivative with a Taylor series expansion. In this way, only the first derivative of the kernel is used.

$$\Pi_{ab} = \frac{m_b(\mu_a + \mu_b)\mathbf{r}_{ab} \cdot \nabla_a W_{ab}}{\rho_a\rho_b\mathbf{r}_{ab}^2} \mathbf{v}_{ab}, \quad (2.5.19)$$

$$\Pi_{ab} = \frac{m_b(\mu_a + \mu_b)\mathbf{v}_{ab}}{\rho_a\rho_b} \left( \frac{1}{\mathbf{r}_{ab}} \frac{\partial W_{ab}}{\partial \mathbf{r}_a} \right), \quad (2.5.20)$$

where the second line assumes that the kernel is radially symmetric (see Equation 2.4.7).

The main disadvantage of this approach over that of Monaghan and Cleary is that this

term no longer conserves angular momentum.

## 2.6 No-Slip Boundaries

There are three primary methods of modelling no-slip boundaries in an SPH simulation. The first approximates the boundary as a collection of SPH particles that move with a prescribed velocity equal to that of the boundary. Figure 2.1(a) shows an example of this. The black particles are the SPH boundary particles. They interact with the fluid particles (coloured blue/grey in colour/grayscale) in much the same way as regular SPH particles, except that their velocity is always equal to that of the boundary.

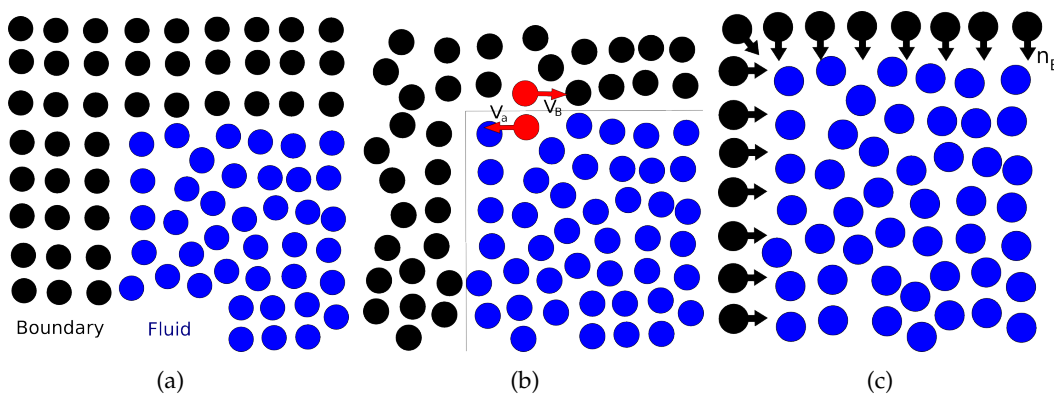


**Figure 2.1:** Three different SPH boundary methods. The boundary particles are drawn as black circles, whereas the fluid particles are blue or grey depending on whether you are viewing this picture in colour or grayscale. The three methods shown are: (a) Layers of fixed SPH fluid particles. The boundary particles are exactly the same as regular SPH particles, however they move with a set velocity. (b) Ghost Particles. The boundary particles mirror the fluid particles on the other side of the boundary. (c) Lennards-Jones repulsive force particles. The arrows indicate the direction of the boundary force that each boundary particle exerts on the fluid particles.

For this method, The interaction of a fluid particle  $a$  and boundary particle  $\beta$  occurs through the normal momentum (2.5.13) and continuity equations (2.5.5). In order for the particle densities to be calculated correctly, the velocity of the boundary particles that is used in the continuity equation  $\mathbf{v}_\beta$  is always equal to the velocity of the boundary  $\mathbf{v}_B$ . However, the boundary particle velocity  $\mathbf{v}_\beta$  used in the momentum equation can be calculated differently depending on the order of the boundary condition required. For a zeroth-order boundary condition this velocity is simply set to the velocity of the boundary  $\mathbf{v}_\beta = \mathbf{v}_B$ . For a first-order condition the velocity of the boundary particles will be anti-symmetric with a gradient equal to the velocity gradient at the boundary. In order to approximate this, Morris et al. (1997) extrapolated  $\mathbf{v}_a$  across the boundary in order to set  $\mathbf{v}_\beta = \frac{T_{\beta B}}{T_{aB}} \mathbf{v}_{aB} + \mathbf{v}_B$ , where  $T_{aB}$  is the tangential distance between particle  $a$  and the boundary plane.

The second boundary method does not use fixed SPH particles but instead mirrors the fluid particles across the boundary to create so-called *ghost* particles. In this method, the velocity of each ghost particle is set to the negative of its corresponding fluid particle

$\mathbf{v}_\beta = -\mathbf{v}_a$ . This provides a first-order no-slip boundary condition that is easily implemented for plane boundaries. However difficulties arise near curved boundaries (each fluid particle must mirror the surrounding fluid particles through a different boundary tangent) and sharp corners (care must be taken to avoid an increase in the mass of ghost particles due to separate fluid volumes mirroring to overlapping volumes).

The third boundary method uses a single layer of particles that repel the fluid particles using a radial force similar to a Lennards-Jones repulsive force (Monaghan 1994). This provides a very flexible and low computational cost boundary that can be used for more complicated geometries, while sacrificing some of the accuracy of the previous methods.

The repulsive particles are fixed to the boundary and also exert viscous forces on the fluid particles through the normal viscosity term. The boundary force per unit mass on particle  $a$  from a boundary particle  $\beta$ , where  $T_{a\beta}$  is the tangential distance between  $a$  and  $\beta$ , and  $N_{a\beta}$  is the normal distance, is given by (Monaghan 2005)

$$\mathbf{f}_{a\beta} = -\frac{m_a}{m_a + m_\beta} B(T_{a\beta}, N_{a\beta}) \mathbf{n}_\beta, \quad (2.6.1)$$

where  $\mathbf{n}_\beta$  is the unit normal vector to the boundary. The function  $B$  is chosen so that it increases rapidly for small  $N$ , so as to prevent the particle from penetrating the wall. Its variation with  $T$  ensures that the particle feels no change in force as it moves tangentially along the boundary. Monaghan et al. (2003) gives the definition of  $B$  as

$$B(x, y) = F(y)G(x), \quad (2.6.2)$$

$$G(x) = \begin{cases} \left(1 - \frac{x}{\Delta p}\right) & \text{if } 0 < x < \Delta p, \\ 0 & \text{otherwise.} \end{cases} \quad (2.6.3)$$

$$F(y) = \begin{cases} \frac{2}{3}\beta & \text{if } 0 < q < 2/3, \\ \beta \left(2q - \frac{3}{2}q^2\right) & \text{if } 2/3 < q < 1, \\ \frac{1}{2}\beta(2 - q)^2 & \text{if } 1 < q < 2, \\ 0 & \text{otherwise,} \end{cases} \quad (2.6.4)$$

where  $q = y/h$ . Finding the correct normal vector  $\mathbf{n}_\beta$  can be difficult near sharp corners in the boundary. Large changes in the direction of neighbouring boundary normals can lead to a very small value of  $N$  (since  $N_{a\beta} = |\mathbf{n}_\beta \cdot \mathbf{r}_{a\beta}|$ ), which results in an unnaturally large boundary force. To fix this problem, each sharp point is represented with a particle that has two normals equal to those of its neighbouring boundary particles. A more stable value for  $\mathbf{n}_\beta$  is calculated from these normals and the position of the interacting fluid particle (see Figure 2.2 and Monaghan et al. (2003))

## 2.7 Time Integration

An important property of SPH is its firm basis in the conservation of momentum and energy. Monaghan (2002) shows how the equations of SPH can be directly derived from

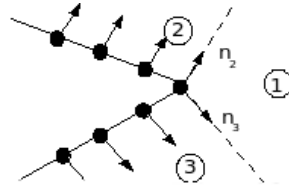


**Figure 2.2:** Multiple boundary normals for sharp corners. For a fluid particle in region 2, use  $\mathbf{n}_2$ . In region 3 use  $\mathbf{n}_3$ . In region 1 use the unit radial vector in the direction from the corner particle to the fluid particle

the Lagrangian of a non-dissipative fluid in a potential (See also Springel & Hernquist (2002) for a different derivation). In order to preserve this Lagrangian over time and ensure the best long-term conservation of energy, it is best to use a geometric integrator for the timestepping.

Geometric, or symplectic, integrators (Hairer et al. 2003) are commonly used for molecular and celestial mechanics simulations. While they lack the absolute accuracy of methods like the Runge-Kutta, they are designed to preserve (exactly) the Lagrangian of a system and so have much improved long-term behaviour. They are also reversible in time for non-dissipative systems, which is useful as a simple check on the accuracy of a simulation (e.g. reverse the velocities of every particle and see if they retrace their motion).

In all the simulations presented in this thesis, the second-order leapfrog timestepping scheme is used. Ignoring density and viscosity, this is

$$\mathbf{r}^{\frac{1}{2}} = \mathbf{r}^0 + \frac{\delta t}{2} \mathbf{v}^0, \quad (2.7.1)$$

$$\mathbf{v}^1 = \mathbf{v}^0 + \delta t F(\mathbf{r}^{\frac{1}{2}}), \quad (2.7.2)$$

$$\mathbf{r}^1 = \mathbf{r}^{\frac{1}{2}} + \frac{\delta t}{2} \mathbf{v}^1, \quad (2.7.3)$$

where  $F = \frac{d\mathbf{v}}{dt}$  is calculated using the SPH momentum equation.

$F$  is also dependent on the density and this can be found by integrating the continuity equation. This is commonly done by calculating the continuity equation at the mid-point, since information on the particle neighbours is already known. However, this causes the timestepping to be no longer reversible. To ensure reversibility, the rate of change in density must be calculated at the end of the timestep like so

$$\rho^{\frac{1}{2}} = \rho^0 + \frac{\delta t}{2} D(\mathbf{r}^0, \mathbf{v}^0), \quad (2.7.4)$$

$$\rho^1 = \rho^{\frac{1}{2}} + \frac{\delta t}{2} D(\mathbf{r}^1, \mathbf{v}^1), \quad (2.7.5)$$

where  $D = \frac{d\rho}{dt}$ . Adding viscosity, of course, must remove the reversibility of the algorithm. The calculation of the viscous term requires an estimate of the velocity at the mid-point. This can be obtained by stepping the velocity a half-step using the  $F$  from the previous timestep. The final timestepping scheme then becomes

$$\mathbf{r}^{\frac{1}{2}} = \mathbf{r}^0 + \frac{\delta t}{2} \mathbf{v}^0, \quad (2.7.6)$$

$$\mathbf{v}^{\frac{1}{2}} = \mathbf{v}^0 + \frac{\delta t}{2} F(\mathbf{r}^{-\frac{1}{2}}, \mathbf{v}^{-\frac{1}{2}}, \rho^{-\frac{1}{2}}), \quad (2.7.7)$$

$$\rho^{\frac{1}{2}} = \rho^0 + \frac{\delta t}{2} D(\mathbf{r}^0, \mathbf{v}^0), \quad (2.7.8)$$

$$\mathbf{v}^1 = \mathbf{v}^0 + \delta t F(\mathbf{r}^{\frac{1}{2}}, \mathbf{v}^{\frac{1}{2}}, \rho^{\frac{1}{2}}), \quad (2.7.9)$$

$$\mathbf{r}^1 = \mathbf{r}^{\frac{1}{2}} + \frac{\delta t}{2} \mathbf{v}^1, \quad (2.7.10)$$

$$\rho^1 = \rho^{\frac{1}{2}} + \frac{\delta t}{2} D(\mathbf{r}^1, \mathbf{v}^1). \quad (2.7.11)$$

The timestep  $\delta t$  is bounded by the standard Courant condition

$$\delta t_1 = \min_a \left( 0.8 \frac{h_a}{v_{sig}} \right), \quad (2.7.12)$$

where the minimum is taken over all the particles and  $v_{sig} = c_a + c_b$  is the signal velocity between particles  $a$  and  $b$ .

Morris et al. (1997) gives the timestep condition for viscous diffusion as

$$\delta t_2 = \min_a \left( 0.125 \frac{h_a^2}{\nu} \right), \quad (2.7.13)$$

which is based on the typical viscous diffusion timestep used in finite difference methods.

If radial force boundary particles are used, then the timestep condition is given by Monaghan et al. (2003) as

$$\delta t_3 = \min_a \left( \frac{N_{a\beta}}{0.1 c_s} \right). \quad (2.7.14)$$

The final timestep is generated by taking the minimum of these three conditions.

$$\delta t = \min(\delta t_1, \delta t_2, \delta t_3). \quad (2.7.15)$$

## 2.8 Variable Smoothing Length

While the smoothing length  $h$  can be constant in time and space, it is sometimes useful to vary  $h$  with the density of the particle so that

$$h_a = \sigma \left( \frac{m_a}{\rho_a} \right)^{1/d}. \quad (2.8.1)$$

where  $d$  is the dimensionality of the simulation and  $\sigma$  is a constant that determines the average number of neighbours for a particle. A typical value is  $\sigma = 1.3$ . Equation 2.8.1 is in line with the concept of the SPH particle as being a constant mass of fluid, so it is natural for the volume of a constant mass particle to vary consistently with the density.

A variable smoothing length implementation of SPH is necessary in fully compressible simulations so that the number of neighbours for each SPH particle is roughly constant. However, in quasi-compressible SPH simulations, where the density variations are expected to be minor, a variable  $h$  implementation is not expected to produce significantly different results.

If an SPH sum is used to calculate the particle densities and  $h_a$  is used in the sum for  $\rho_a$  (Equation 2.5.3), then the density equation and Equation 2.8.1 form an implicit pair that can be easily solved with point iteration (or even more quickly with a Newton-Raphson scheme). In order to speed the convergence further, the particles that have a converged  $h$  and  $\rho$  pair can be removed from subsequent iterations as long as  $W_{ab} = W(\mathbf{r}_a - \mathbf{r}_b, h_a)$  in the density sum. If the density is found by integrating the continuity equation, as is done for all the simulations in this thesis, then the smoothing length for every particle can be updated after the new density is calculated.

When using a variable  $h$  it is important to ensure that the SPH equations are symmetric between particle pairs. This is done by combining the kernels between particle pairs like so

$$W_{ab} = 0.5 (W(\mathbf{r}_a, h_a) + W(\mathbf{r}_b, h_b)), \quad (2.8.2)$$

or

$$W_{ab} = W(\mathbf{r}_a - \mathbf{r}_b, 0.5(h_a + h_b)). \quad (2.8.3)$$

The latter form is used throughout this thesis.

## 2.9 Energy Budget

The acceleration that an SPH particle experiences is calculated from the addition of a pressure, viscous and optional external force (e.g. gravity)

$$\frac{d\mathbf{v}_a}{dt} = F_a^{\text{press}} + F_a^{\text{visc}} + F_a^{\text{extern}}. \quad (2.9.1)$$

Note that these forces are per unit mass. Taking the dot product of this momentum equation with the particle velocity  $\mathbf{v}_a$ , multiplying by  $m_a$  and summing over all particles (2.9.1) becomes

$$\sum_a m_a \mathbf{v}_a \cdot \frac{d\mathbf{v}_a}{dt} = \sum_a m_a \mathbf{v}_a \cdot F_{\text{press}} + \sum_a m_a \mathbf{v}_a \cdot F_{\text{visc}} + \sum_a m_a \mathbf{v}_a \cdot F_a^{\text{extern}}, \quad (2.9.2)$$

$$\frac{d}{dt} \sum_a m_a \mathbf{v}_a \cdot \mathbf{v}_a = \frac{dE_{\text{elast}}}{dt} + \frac{dE_{\text{visc}}}{dt} + \frac{dE_{\text{extern}}}{dt}. \quad (2.9.3)$$

The term on the left hand side is a rate of change in total kinetic energy with time, while the terms on the right are a rate of change in total elastic, viscous and external energies. This can be used to track the transfer of energy. The non-dissipative SPH momentum equation (see Equation 2.5.12) can be derived from a Lagrangian (see Monaghan (2005) for details) and therefore conserves the total kinetic and elastic energy of the system. Adding in the contribution from the viscous energy loss, the total energy of the system should be close to constant throughout the simulation. This provides a useful check of simulation accuracy. If the total energy were not close to constant, this would point to a problem in the timestepping scheme (e.g. size of the timestep).

Using the momentum equation detailed in Equation 2.5.12, the change in elastic energy term on the right hand side becomes

$$\frac{dE_{\text{elast}}}{dt} = \sum_a \sum_b m_a m_b \left( \frac{P_a}{\rho_a^2} + \frac{P_b}{\rho_b^2} \right) \mathbf{v}_a \cdot \nabla_a W_{ab}, \quad (2.9.4)$$

$$= \sum_a m_a \left( \frac{P_a}{\rho_a^2} \sum_b \mathbf{v}_{ab} \cdot \nabla_a W_{ab} \right). \quad (2.9.5)$$

Using the continuity equation (2.5.5) this becomes

$$\frac{dE_{\text{elast}}}{dt} = \sum_a m_a \left( \frac{P_a}{\rho_a^2} \frac{d\rho_a}{dt} \right), \quad (2.9.6)$$

$$= \sum_a m_a \frac{du_a}{dt}, \quad (2.9.7)$$

where  $du_a/dt$  is the non-dissipative rate of change of elastic energy per unit mass for particle  $a$  (Monaghan (2005)).

The rate of change of viscous energy can be calculated directly from its definition in the momentum equation (2.5.13). The rate of change of external energy is calculated using the force  $F_a^{\text{extern}}$  defined in Equation 2.9.1

$$\frac{dE_{\text{visc}}}{dt} = \sum_a m_a \sum_b m_b \Pi_{ab} \mathbf{v}_a \cdot \nabla_a W_{ab}, \quad (2.9.8)$$

$$\frac{dE_{\text{extern}}}{dt} = \sum_a m_a \mathbf{v}_a \cdot F_a^{\text{extern}}. \quad (2.9.9)$$

## 2.10 Tensile Instability

One persistent SPH problem has been the tendency of particles to clump together in small groups, effectively reducing the resolution and increasing errors in the interpolant due to the non-regular particle distribution. The cause of this clumping is normally regarded to be the SPH tensile instability. Swegle et al. (1995) performed a one dimensional stability analysis and concluded that this instability occurred between particles when  $W''T > 0$ , where  $W''$  is the second derivative of the kernel and  $T$  is a pressure stress that is negative under compression and positive in tension. So, for an initial inter-particle distance  $\Delta p$  greater than the minima of  $W'$  (i.e.  $\Delta p > 0.76h$  for the Cubic Spline kernel), the motion of the particles will be unstable if they experience a negative pressure. Morris (1996) has performed a more detailed analysis of SPH stability properties.

The tensile instability is generally a problem for SPH simulations of solids under tension. However, there is still a tendency for liquid simulations to exhibit this particle clumping effect, although it is unclear if the tensile instability is the cause of this. Chapter 7 shows a significant level of clumping present in simulations of forced 2D turbulence, which is entirely eliminated through the use of the Wendland kernel. Since the shape of this kernel (and the sign of its second derivative) is very similar to the Cubic Spline, the effects of the tensile instability according to the analysis of Swegle et al. (1995) should be unchanged when moving between these kernels. Since this is not the case, it is likely that the particle clumping experienced in our simulations is due to some other effect.

Monaghan (2000) has proposed introducing an additional force between the particles to reduce particle clumping. This force  $f_{ab}$  is added to the momentum equation

$$\frac{d\mathbf{v}_a}{dt} = - \sum_b m_b \left( \frac{P_b}{\rho_b^2} + \frac{P_a}{\rho_a^2} + f_{ab} + \Pi_{ab} \right) \nabla_a W_{ab}, \quad (2.10.1)$$

and is based on the kernel function  $W$

$$f_{ab} = 0.01 \left( \frac{P_a}{\rho_a^2} + \frac{P_b}{\rho_b^2} \right) \left( \frac{W(\mathbf{r}_{ab})}{W(\Delta p)} \right)^n. \quad (2.10.2)$$

This anti-clumping force is used in all the SPH simulations in this thesis that employ the Cubic Spline kernel. For the forced turbulence simulations in Chapter 6 the Wendland kernel is used and no anti-clumping term is added.

## 2.11 Finding Particle Neighbours

Given the incompressibility of the simulations in this thesis, and hence the (relatively) constant particle distribution, finding the neighbours of each particle is straightforward and can be done using a simple and efficient link list data structure. The domain is divided into square cells of side  $2h_{max}$ , where  $h_{max}$  is the maximum smoothing length taken over all the particles (see Figure 2.3). A single pass over the particles is used to assign each particle to its own cell. To find the neighbours of a particle, it is a simple matter of searching through all the particles within that particle's cell and the surrounding cells and accepting those particles for which  $|\mathbf{r}_{ab}| < 2 \max(h_a, h_b)$ .

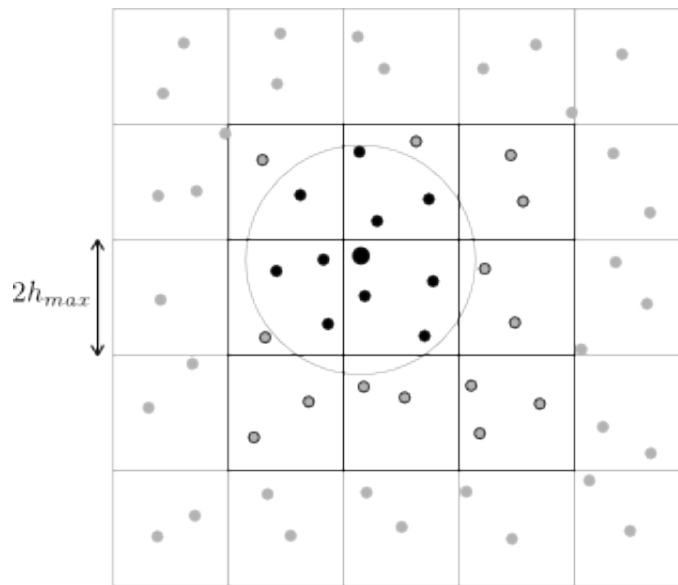


**Figure 2.3:** The domain is divided into cells with sides of length  $2h_{max}$ . A particle can find its neighbours by looking in its own and neighbouring cells. The large black particle is the particle of interest  $a$ . Its interaction radius ( $2h$ ) is shown by the surrounding circle. Given that the cells have side length greater than or equal to this radius, particle  $a$  only has to search its own cell and the surrounding cells for its neighbours. It then tests each particle  $b$  in these cells to see if  $|\mathbf{r}_{ab}| < 2 \max(h_a, h_b)$ . If this is true then particle  $b$  is a neighbour (the neighbours are coloured black in the figure, while particles that fail this test are grey with a black outline. Particles that are not considered at all are coloured solid grey)

## 2.12 Parallel Implementation

The DNS turbulence simulations in this thesis required the implementation of a parallel SPH code, due to their large resolution requirements. Since these simulations had a simple, square geometry and no free surface, the domain decomposition technique used is relatively simple.

The entire domain is divided into square regions, one for each CPU (See Figure 2.4). Each CPU operates on its own set of particles, and knows which CPUs are its neighbours. For all particles that are closer than  $2h_{max}$  to the boundary of a neighbour, the CPU sends information about these particles to that neighbour. In this case,  $h_{max}$  is the maximum

smoothing length for all of particles in that CPU's domain. In this way, as well as having its own particles, each CPU has sufficient information about all particles within  $2h_{max}$  of its borders. Once a particle moves out of the domain of a CPU, it sends that particle to the relevant neighbour.

A useful result of this technique is that periodic boundary conditions are simple to implement. Adding a periodic boundary is a simply matter of setting the correct neighbours for each CPU domain.

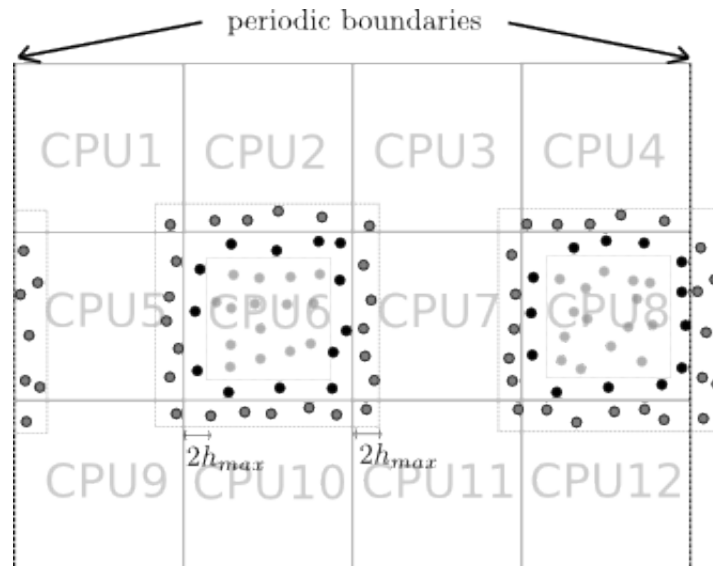


**Figure 2.4:** Each CPU swaps the information of particles within  $2h_{max}$  of its neighbour with that neighbour. This figure shows this for CPU6 and CPU8. Particles that do not interact with neighbouring CPUs are coloured solid grey. Particles within the current CPU that might interact with neighbouring CPUs are coloured black. Information about these particles (e.g. position, velocity, density etc.) is passed to the relevant neighbour. This is a two way process. The neighbouring CPUs also send information back about particles that might interact with the current CPU (these particles are coloured grey with a black outline). Periodic boundaries are implemented by setting the proper neighbourhood relationships. For example, CPU8 considers CPU5 to be its neighbour to the right, and *visa versa*.

Information about the particles is passed between each CPU using the OpenMPI library, an open source implementation of the official Message Passing Interface (MPI) standards (<http://www.mpi-forum.org/>). This implementation can therefore be used on a parallel computer cluster where the CPU's do not have access to shared memory.

Figure 2.5 shows how this parallel implementation scales as a function of the number of CPUs used. The y-axis shows the speed-up factor, which is normalised by the time taken per timestep using just one CPU. A reference line has been added that shows a perfect linear speed-up. The simulation used to generate these results was two-dimensional and used  $700 \times 700$  particles that are evenly distributed within a square domain with periodic boundaries. These results show that the parallel SPH simulation is quite efficient, with a speed-up that is close to linear right up to 36 CPUs. This corresponds to approximately 13,600 particles per CPU. This is expected since SPH is primarily a local, rather than global, method. Each CPU needs to know only about its own particles and the particles

from its neighbours within  $2h_{max}$ . It is therefore much more straightforward to efficiently divide the workload and minimise communication between the CPUs. This SPH code does calculate some global measures (e.g. average density, total kinetic energy etc.) but these are not required for the basic SPH method.

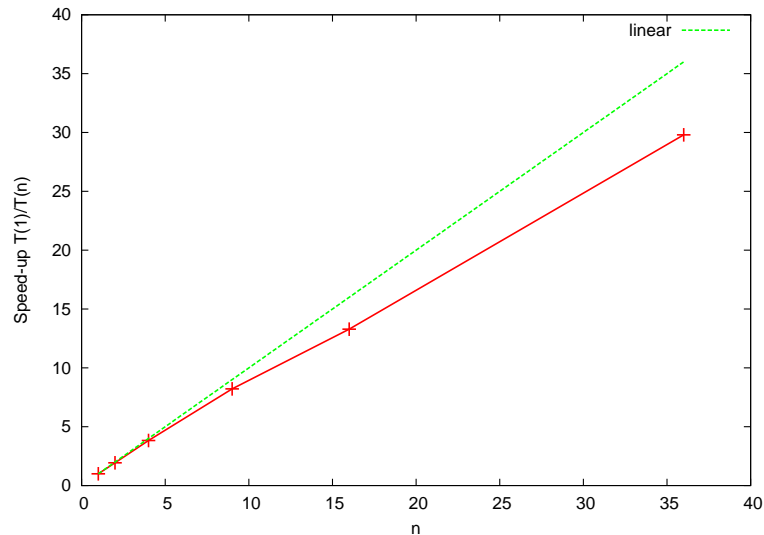


**Figure 2.5:** Plot of Speed-up versus number of CPUs. Speed-up is measured by  $T(1)/T(n)$ , where  $T(n)$  is the time taken for one timestep using  $n$  CPUs.

More complicated simulations would require a more flexible domain decomposition technique. Warren & Salmon (1993, 1995) have implemented an excellent parallel SPH algorithm for compressible gas simulation in an astrophysical context. Due to the uneven distribution of particles for their simulations, a simple division of the domain into squares would be inadequate, as each CPU would have very different numbers of particles and the entire simulation would be limited by the most heavily loaded CPU. Warren and Salmon uses Morton ordering to construct equal length lists of particles that are close together in space, then gives a list to each CPU. They also mention that Peano-Hilbert ordering would give an even better decomposition. Of course, this complicates the communication between CPUs, since the domains are no longer based on a simple spatial structure. Warren and Salmon use a parallel Oct-Tree to find neighbours, calculate self-gravity particle interactions and communicate between CPUs, however this level of complexity might not be necessary for an incompressible simulation.

## Chapter 3

# Viscous Mixing in a Two-Dimensional Twin Cam Mixer

---

This chapter describes a 2D SPH study of a Twin Cam mixer and compares the results against experimental data and results from two published Finite Element Method (FEM) simulations. In order to analyse the mixing processes in the Twin Cam mixer, this chapter presents a method for calculating the Finite-Time Lyapunov Exponent (FTLE) using SPH particle data. The FTLEs can be used to locate the unstable and stable manifolds in the flow and indicate where mixing is either promoted or inhibited. Also presented is a local measure of how mixed two or more fluids are at any given point in the domain. This is used to find the time scales of mixing over different regions in the domain and at different length scales. The results in this chapter have been previously published by the author in Robinson et al. (2008).

The purpose of this work is to evaluate the effectiveness of SPH, FTLEs and our mixing measure in simulating and analysing the mixing in a typical industrial mixer at low Reynolds numbers. Applications in this regime include food and polymer processing. At such low Reynolds numbers the flow is laminar and the power needed to operate a mixer is increased due to the extra force required to move the fluid around the mixer. Without the benefits of turbulence, mixing is slow and often limited by the diffusivity of the fluids. Therefore, a knowledge of the mixer design and its effect on the mixing processes is important in providing uniform and efficient mixing.

The experimental validation uses data from the work of Avalosse & Crochet (1997). They constructed an experimental Twin Cam mixer and used it to track the mixing of a coloured volume of fluid for a low Reynolds number ( $Re = 0.001$ ). Avalosse and Crochet compared their experimental results of the Twin Cam mixer with a 2D Finite-Element Method (FEM) simulation. The base mesh was a regular grid in circular coordinates, with a constant angular resolution, and with the radial resolution higher near the circle defined by the rotating tips of the triangular cams. The elements that intersected the straight edges of the cams were re-meshed at every timestep using an automatic algorithm based on Delaunay triangulation. Bertrand et al. (2003) also simulated a 2D Twin Cam mixer using FEM. To model the moving cams, they used the Lagrange multiplier based fictitious domain method. This was combined with an adaptive mesh refinement at each timestep,

which was applied near the cam tips.

An SPH simulation of a Twin Cam mixer has been implemented that matches the experimental and FEM configuration of Avalosse & Crochet (1997) and Bertrand et al. (2003). Section 3.5.2 shows that over a period of one cam revolution the results of the SPH simulation compare well against both the FEM simulations and the experiment. After this time the chaotic motion of the fluid causes the results to diverge from the experiment. However, due to unavoidable differences between the simulation and the experiment, most notably any three-dimensional effects, this is to be expected. In fact, similar differences are seen in the FEM simulation by Avalosse & Crochet (1997).

The proposed method for calculating Finite Time Lyapunov Exponents from SPH data is given in Section 3.4.1. Section 3.6.1 describes the FTLE maps for the Twin Cam simulation, which clearly show the unstable and stable manifolds of the flow. A given material volume in the flow will be elongated and folded along an unstable manifold, and stretched apart by a stable manifold. So these manifolds give a geometrical description of the mixing processes present in the flow. Since the manifolds also act as separatrices, they show how the inner regions of the Twin Cam mixer, between the cams and the manifolds, are isolated from the rest of the domain, thus inhibiting the mixing of these two regions.

Section 3.4.2 presents the proposed mixing measure, which provides a quantitative measure of how "mixed" two or more fluids are over a given length scale. Section 3.6.3 applies this measure to the Twin Cam mixer. This Section focuses on the evolution of the mixing between the two cam barrels of the mixer and also the mixing between the inner and outer regions (ie. across the manifolds). The results confirm the qualitative results obtained from the FTLE maps, that the mixing is inhibited between the inner and outer regions in each cam barrel. Furthermore, the evolution of the mixing measure at different length scales shows that the mixing between these two regions is mostly dissipative in nature, whereas the mixing between the two cam barrels is mainly due to the large scale chaotic motions of the fluid.

## 3.1 Measuring Mixing

Ottino (1989) has developed a popular mixing theory, which is based on the calculation of several variables along the paths of material points in the flow. He has proposed a commonly used measure of mixing strength: length stretch. Avalosse and Crochet applied this measure to their simulation of the Twin Cam mixer. If  $dx$  is a material length that deforms into  $dX$  after time  $T$ , then Ottinos length stretch is defined as

$$\chi(dX, t) = \lim_{|dx| \rightarrow 0} \frac{|dX|}{|dx|} \quad (3.1.1)$$

Ottino's length stretch is directly related to the chaos theory notion of Lyapunov Exponents  $\sigma$ , which are a measure of how quickly material trajectories diverge from their initial conditions and an indication of chaos if  $\sigma > 0$ . The Lyapunov Exponent  $\sigma$  is calculated from Ottinos length stretch by taking its limit over an infinite time period

$$\sigma = \lim_{T \rightarrow \infty} \frac{1}{T} \ln \chi \quad (3.1.2)$$

Usually the Lyapunov Exponent of interest is the maximum over all possible orientations of the initial material length. All further references in this chapter refer to the maximum Lyapunov Exponent. As with length stretch, higher values of  $\sigma$  can indicate a higher strength of mixing locally at that point, since a patch of material in an area of high  $\sigma$  will be stretched out, exposing more surface area to the surrounding material. The Lyapunov Exponent has the advantage over Ottino's length stretch in that it does not depend on the initial orientation of the material length and only depends on the maximum stretching, which is the quantity of interest for incompressible mixing. Lyapunov Exponents can also be used to find the stable and unstable manifolds of the flow, which provide information about the global mixing processes. These manifolds are explained in more detail in the next section. While Lyapunov Exponents are only useful for periodic flows, as the flow must be fully defined over infinite time, the concept has been extended to finite times (Finite Time Lyapunov Exponents, FTLE) and finite sizes (FSLE) (Artale et al. 1997, Pierrehumbert & Yang 1993, Lapeyre 2002, Joseph & Legras 2002).

As well as a measure of the quality of mixing at a point, there is also a need to calculate how mixed two or more materials are. There are many different methods to calculate this, many depending on the particular application. Poux et al. (1991) describes nearly 50 different mixing measures proposed in the literature. However, all of these measures are global. They can be used to calculate the amount of mixing locally by dividing up the region of interest. However, as most of the methods are based on statistical analysis, there must be sufficient sample points in each region to reduce the error to a reasonable level. Section 3.4.2 presents a local mixing measure that easily calculates the amount of mixing with fewer sample points.

## 3.2 Chaotic Transport

One of the important features of a chaotic system are its stable and unstable invariant manifolds and their associated hyperbolic or stagnation points. Knowledge of the location and movement of these features gives important insight into the mixing and transport of the system (Ottino 1989, Holmes 1990, Rom-Kedar et al. 1990).

The process of mixing can be described in terms of the stretching and folding of the flow. The fluid is stretched apart along the stable manifolds and folded along the length of the unstable manifolds. Figure 3.1 shows this process diagrammatically.

Consider the motion of a passive, massless point that moves with the flow velocity (hereafter termed a material point). A stable manifold has the defining property that a material point, initialised on the stable manifold, will approach its hyperbolic point as  $t \rightarrow \infty$ . The labelling of these manifolds as stable is often confusing, as the definition of stability for these manifolds differs from the traditional engineering view. Using the traditional view of stability, one might expect that a material point initialised on or near a stable manifold would approach that manifold over time and be resistant to small perturbations. However, the opposite is true. Any perturbation to a material point on a stable manifold will cause the particle to move further away from that manifold. The labelling of this type

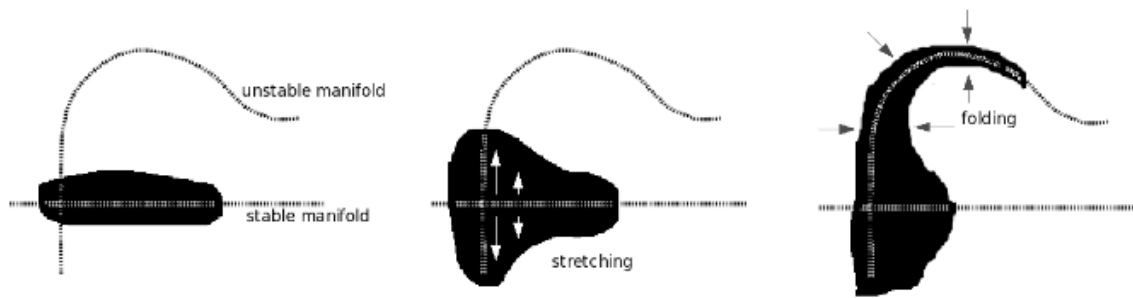


**Figure 3.1:** Diagram showing how an initial blob of fluid (the black region) is first stretched out away from the stable manifold and then folded along the length of the unstable manifold.

of manifold as stable actually refers to the stable nature of the hyperbolic point within the 1D domain of the manifold itself. Material points initialised within this domain approach the hyperbolic point over time, and are resistant to tangential perturbations along the manifold.

The property of stable manifolds most related to the mixing is that a pair of particles straddling the manifold will separate faster than any other nearby pairs (except of course for another pair straddling the same manifold). It is this last property that can be exploited to find the manifolds. FTLEs are a (finite-time) measure of the exponential divergence of two closely spaced points, so the maxima in the spatial distribution of FTLE indicate the presence of a stable manifold. However, it must be noted that this is not always the case. Regions of maximum shear will also show up as FTLE maxima, so care must be taken when interpreting the results.

A similar description, but reversed in time, can be used for unstable manifolds. A material point initialised on an unstable manifold will approach its hyperbolic point in reverse time ( $t \rightarrow -\infty$ ). Additionally, a pair of particles straddling the unstable manifold will separate faster than any other nearby pairs in reverse time (i.e. they will approach the manifold faster than any other nearby pairs). Hence, calculating the FTLE spatial distribution using a negative time step will show the unstable manifolds as maxima in the FTLE distribution. Note again that the labelling of these manifolds as unstable is quite different from the traditional view of stability and refers only to the nature of the hyperbolic point within the 1D domain of the manifold. A material point initialised near an unstable manifold will approach the manifold over time and be resistant to small perturbations.

Consider the phase space of a simple unforced pendulum as an example (Figure 3.2). The stable and unstable manifolds are drawn as solid black lines and intersect at the hyperbolic point at  $(2\pi, 0)$ . Material points on the stable manifold approach this point over time, whereas points on the unstable manifold move away. Perturbations to points on the stable manifold will cause the point to diverge exponentially away from the manifold, whereas points on the unstable manifold will be resistant to such perturbations.

The phase space of the pendulum example also shows the importance of the manifolds in understanding the dynamics of the flow. The manifolds act as separatrices, dividing the region into areas of very different dynamics. The trajectories shown as dashed red

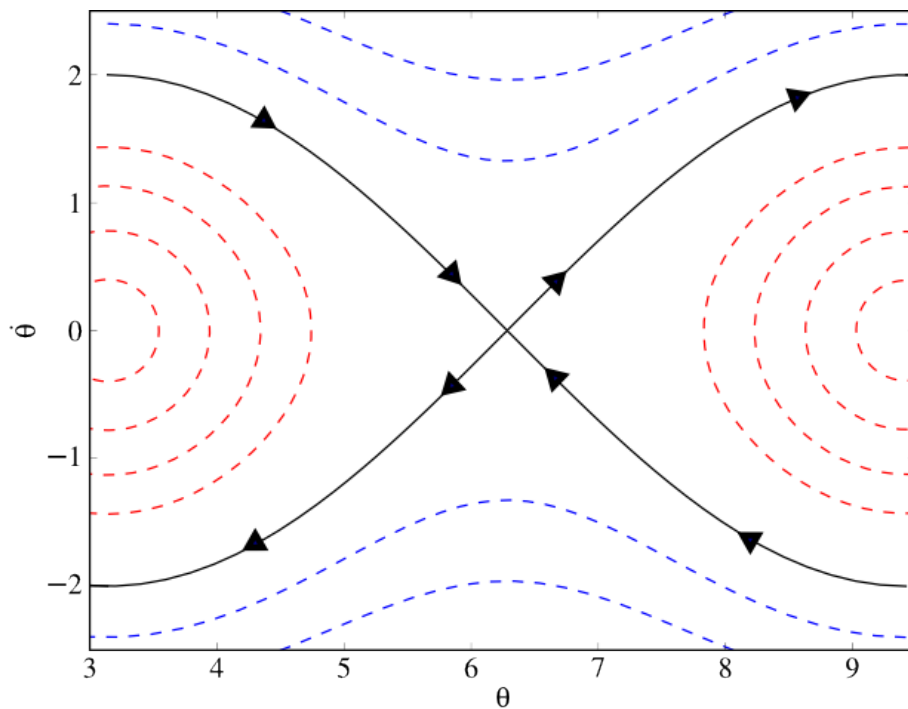


**Figure 3.2:** Phase space of a simple unforced pendulum. The stable and unstable manifolds are shown as a solid black line. These manifolds divide the space into regions of contrasting dynamics of the pendulum. Material particles on the stable manifold approach the central hyperbolic point over time, whereas particles on the unstable manifold move away from the hyperbolic point over time.

lines correspond with the pendulum oscillating between positive and negative angular velocity, while the trajectories outside the manifolds (blue dashed lines) correspond to the pendulum continually rotating in a single direction.

### 3.3 The Simulation Method

The SPH simulation described in this chapter uses the standard quasi-compressible formulation described in Chapter 2. The continuity equation was integrated over time (Equation 2.5.5) to obtain the particle densities and a variable smoothing length  $h$  was used. The viscous term was calculated using the Monaghan form (Equation 2.5.18) and Monaghan's anti-clumping term (Equation 2.10.2) was added to the momentum equation. The Cubic Spline was used for the kernel and the ratio of smoothing length to particle spacing was set to 1.3. The no-slip boundaries are modelled using a single layer of boundary force particles and the sharp corners of the cams are modelled with single particles with multiple normals, as described in Section 2.6.

### 3.4 Mixing Analysis

#### 3.4.1 Finite-Time Lyapunov Exponent

The FTLE is calculated from the trajectories of particles over a finite-time period  $T$ . What follows is a brief derivation of the FTLE, see the excellent description by Shadden et al. (2005) for a more in depth discussion. Consider two material points in the flow at  $t = t_0$ , separated by  $\delta\mathbf{x}$ . Gradients in the velocity field between the two points will cause their separation to change over time. Using a first order approximation of the velocity gradient, the separation after time  $T$ ,  $\delta\mathbf{X}$ , will be (using tensor component notation)

$$\delta X^i = \left( \frac{\partial v^i}{\partial x^j} \delta x^j \right) T. \quad (3.4.1)$$

The magnitude of this separation is given by

$$\|\delta\mathbf{X}\| = T \sqrt{\delta x^i \frac{\partial v^j}{\partial x^i} \frac{\partial v^k}{\partial x^j} \delta x^k}. \quad (3.4.2)$$

The maximum separation of the two particles will occur when they are aligned along the eigenvector associated with the largest eigenvalue of  $\partial\mathbf{v}/\partial\mathbf{x}$ . Thus, if  $\lambda_{max}$  is the absolute value of the maximum eigenvalue of  $\partial\mathbf{v}/\partial\mathbf{x}$  (i.e. the square root of the maximum eigenvalue of  $(\partial\mathbf{v}/\partial\mathbf{x})^T(\partial\mathbf{v}/\partial\mathbf{x})$ ), then

$$max\|\delta\mathbf{X}\| = \lambda_{max}\|\overline{\delta\mathbf{x}}\|T, \quad (3.4.3)$$

where the bar over  $\delta\mathbf{x}$  indicates that it is aligned with the eigenvector corresponding to  $\lambda_{max}$ . This can be written

$$\max\|\delta\mathbf{X}\| = e^{\sigma T}\|\overline{\delta\mathbf{x}}\|, \quad (3.4.4)$$

where  $\sigma$  is the FTLE. That is, the magnitude of the exponential separation velocity between two neighbouring particles. Re-arranging (3.4.4) to obtain the following expression for  $\sigma$

$$\sigma = \frac{1}{T} \ln(\lambda_{\max} T). \quad (3.4.5)$$

Grid-based numerical methods use tracer particles to calculate the FTLE (e.g. Shadden et al. (2005) or Lapeyre (2002)). Since the tracers can be initialised on a regular grid, finite-differencing can be used to estimate the spatial velocity gradient  $\partial\mathbf{v}/\partial\mathbf{x}$ . For a Lagrangian method like SPH, it is much more efficient to directly use the trajectories of the SPH particles. Unlike the tracer particles, the SPH particles will not be regularly spaced. However, the gradient can be found at a particular SPH particle  $a$  by using a linear least-squares method on the irregularly spaced particles surrounding the base particle.

Assume a linear velocity gradient around particle  $a$  given by

$$v^i(x^j) = A^{ij}(x^j - x_a^j) + v_a^i, \quad (3.4.6)$$

$$A^{ij} = \frac{\partial v_i}{\partial x_j}. \quad (3.4.7)$$

Consider a particle  $b$  with an initial separation from  $a$  of  $\delta\mathbf{x}_{ab}$ . After time  $T$  the SPH simulation will have calculated the final separation  $\delta\mathbf{X}_{ab}$  of these particles. Using the linear velocity gradient, the final separation  $\delta\mathbf{X}_{ab}$  is given by

$$\delta X_{ab}^i = A^{ij} \delta x_{ab}^j T. \quad (3.4.8)$$

In principle, only two such particles (in a 2D simulation) would be needed to solve Equation 3.4.8 for the velocity gradient components  $A^{ij}$ . However, since the velocity gradient is very sensitive to errors in the particle separations, we have chosen to use all of the particles within the smoothing length ( $2h$ ) of the base particle  $a$  (i.e. the base particle's neighbours) in order to give a robust estimation. It is reasonable to assume that the velocity gradient will be constant over this area.  $A^{ij}$  is found by minimising the following sum over all the neighbouring particles

$$\sum_b \left( \delta X_b^i - A^{ij} \delta x_b^j T \right)^2. \quad (3.4.9)$$

Once the velocity gradient is found, its maximum eigenvalue can be found and substituted into Equation 3.4.5 to find the FTLE of particle  $a$ . This entire process can then be repeated for all the SPH particles within the domain.

### 3.4.2 Mixing Measure

While the spatial distribution of FTLE and the chaotic manifolds of the flow provides insight into the topological nature of the mixing process, it is also useful to quantify the mixing in order to compare the mixing between different regions of the mixing or to evaluate the mixing timescales. This section defines a mixing measure that quantifies how well an initial dyed region of fluid is mixed into the rest of the domain.

This mixing measure is defined as follows. Given a set of particles each having one of a possible  $C$  colours, the amount of mixing  $M(\mathbf{r})$  measures how mixed the colours are using a particular length scale  $L$ .  $M_a = M(\mathbf{r}_a)$  is calculated at each SPH particle  $a$  in the domain, and the length scale defines a circular (or spherical in 3D) region around each particle with a radius equal to  $L$ . All the SPH particles within this sub-region contribute to the amount of mixing  $M_a$ .

The mixing measure  $M(\mathbf{r})$  is defined as:

$$M(\mathbf{r}) = \frac{\mathbf{s}_L(\mathbf{r}) \cdot \mathbf{s}_g - M_{min}}{1 - M_{min}}, \quad (3.4.10)$$

where  $\mathbf{s}_L(\mathbf{r})$  is a vector of the ratios of different coloured particles in the local sub-region. This sub-region is defined as all the particles within a radius  $L$  from the point  $\mathbf{r}$ . The global ratio  $\mathbf{s}_g$  is simply  $\mathbf{s}_L(\mathbf{r})$  evaluated over the entire flow region ( $\mathbf{s}_g$  is therefore independent of  $\mathbf{r}$ ) and  $M_{min}$  is the minimum possible value of  $\mathbf{s}_L(\mathbf{r}) \cdot \mathbf{s}_g$ .

$$\mathbf{s}_L(\mathbf{r}) = \frac{1}{\sqrt{\sum_{i=1}^C \left(\frac{n_i(\mathbf{r})}{N_i}\right)^2}} \left( \frac{n_1(\mathbf{r})}{N_1}, \frac{n_2(\mathbf{r})}{N_2}, \dots, \frac{n_C(\mathbf{r})}{N_C} \right), \quad (3.4.11)$$

$$\mathbf{s}_g = \frac{1}{\sqrt{C}} (1, 1, \dots, 1), \quad (3.4.12)$$

$$M_{min} = \frac{1}{\sqrt{C}}. \quad (3.4.13)$$

where  $n_i(\mathbf{r})$  is the number of particle within radius  $L$  of  $\mathbf{r}$  with colour  $i$ , and  $N_i$  is the total number of particles in the simulation with colour  $i$ .

This measure is invariant to translation and rotation of the spatial coordinate system. It changes linearly with the colour ratios in the sub-region and does not depend on the initial global colour ratios, since  $\mathbf{s}_g$  is invariant. At large length scales equal to the entire domain, all the particles by definition are completely mixed ( $M(\mathbf{r}) = 1$ ). At length scales equal to the distance between the particles, the particles are completely segregated ( $M(\mathbf{r}) = 0$ ).

The mixing measure  $M(\mathbf{r})$  thus defined is a measure of how similar the colour ratios within the local sub-region are to the colour ratios present in the entire domain. For example, consider an experiment in which an area equal to one quarter of the total domain area was assigned colour 1 and the remaining particles were assigned colour 2. Points

further than  $L$  away from the interface between the two areas will have  $M(\mathbf{r}) = 0$  and the remainder will have  $0 \leq M(\mathbf{r}) \leq 1$  depending on their distance from the interface. As the experiment continues the particles are mixed according to a chaotic flow that induces homogeneous mixing of the particles. After a suitable time period the particles will be fully mixed and all the points in the domain will have close to  $N/4$  particles of colour 1 and  $3N/4$  particles of colour 2 in their local subregion. This gives a mixing measure over the entire domain of  $M(\mathbf{r}) \approx 1$ .

### 3.5 Simulation Results

A diagram of the Twin Cam geometry is shown in Figure 3.3. The boundary of each cam is an equilateral triangle and the outer boundary is formed from the union of two circular perimeters centred around each cam. The fluid used for the experimental results (Avalosse & Crochet 1997) was a Newtonian aqueous solution of glucose, with a viscosity of 50 Pa s and a density of 1500 kg/m<sup>3</sup>. The counter-clockwise rotating cams are moving at 0.5 rpm, which gives a Reynolds number in the order of 0.001.

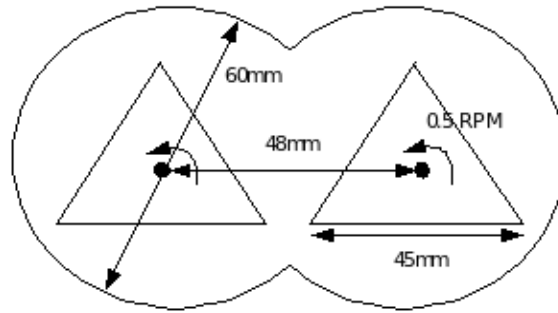


Figure 3.3: Geometry of a Twin Cam mixer.

#### 3.5.1 Timestep and Viscosity Issues

The viscous time scale can be estimated from that of a flow between two concentric cylinders (Batchelor (1970), page 203). Taking the distance between the cylinders as  $d = 10$  mm and assuming the inner cylinder is rotating with the same period as the cams while the outer is at rest, we find:

$$\frac{t_{visc}}{t_{cam}} = \frac{\rho d^2 / \pi^2 \mu}{120} \approx 2.5 \times 10^{-6}. \quad (3.5.1)$$

Since SPH is an explicit method, with a viscous timestep:

$$\delta t_{visc} = \frac{\rho h^2}{\mu} = 3 \times 10^{-5}, \quad (3.5.2)$$

the SPH simulation would need  $4 \times 10^6$  steps to allow the cams to move through one revolution. This is impractical for what should be a small-scale 2D simulation.

However, since the time-scale of the viscous forces is so small compared with the rotating cams, the viscosity can be significantly reduced without affecting the transport of the fluid. The ratio  $t_{visc}/t_{cam}$  will increase but remain much less than 1. This increases the time needed for the viscous forces to equilibrate to a state that balances the pressure and boundary forces, but as long as this time scale remains very small compared to the rotational time scale this will not affect the flow dynamics or the transport of the fluid.

The viscosity in these simulations was therefore reduced to 0.005 Pa s in order to speed up the explicit integration. This is a factor of  $10^{-4}$  smaller than the experimental viscosity and  $t_{visc}/t_{cam} \approx 2.5 \times 10^{-2}$ . The simulation has been run with higher viscosities up to 0.05 Pa s, demonstrating no distinguishable effect on the results, which confirms that the reduced viscosity has negligible impact on the solution.

#### 3.5.2 Experimental Validation

The results of the SPH simulation can be validated against the experiment performed by Avalosse & Crochet (1997). Figure 3.4 shows the initial conditions for both the SPH simulation and experiment (top row). This figure also shows the simulation and experiment after the cams have rotated through 1 revolution (middle row) and 1 1/3 revolutions (bottom row), taken at times 120 s and 160 s respectively.

The motion of the cams divides the coloured blob into two segments along a line that is roughly diagonal from the lower right tip of the left cam to the top of the right cam (This line is actually a stable manifold of the flow. See Figure 3.7, top, for an image of this line). There is a stationary point at the centre of the domain, so particles near this point have a lower velocity. This causes a trail of particles behind the bulk of the coloured particles as they leave the centre of the domain, which shortens to form a kink or hook in the blob (seen most clearly in the lower region of the leftmost chamber at  $t = 120$  s). The blob is stretched out as it is moved around the chamber, due to lower velocities near the walls of the chamber. Once the leading edges of the divided blobs have completed a revolution and are once again between the cams, both are further divided along the same line as the initial division, and the mixing process continues.

The transport of the coloured blob of fluid follows the experiment well. Over a period of one cam revolution (middle row), most of the features of the coloured blob are captured by the simulation. The main deviations from the experiment occur at the leading edge of the two coloured segments formed when the initial blob is torn apart. Once these two segments return to the centre of the mixer, the highly chaotic central region amplifies any transport errors accumulated during the simulation. At 4/3 cam revolutions (bottom row), the general features of the coloured blob can be seen in the simulation, but some are reasonably different from the experiment (for example, the upper T feature in the experiment near the centre of the domain is not reproduced in the simulation).

Adding more particles can reduce the numerical errors present in the SPH simulation. However, it was found that increasing the number of particles did not correctly capture either the upper T feature (shown at 4/3 cam revolutions) or the leading wedge in the left cam (shown at 1 cam revolution just above the lower right corner of the left cam). These two features were also not modelled correctly in the Finite Element simulations of Avalosse and Crochet and Bertrand et al., indicating that there is a physical process that

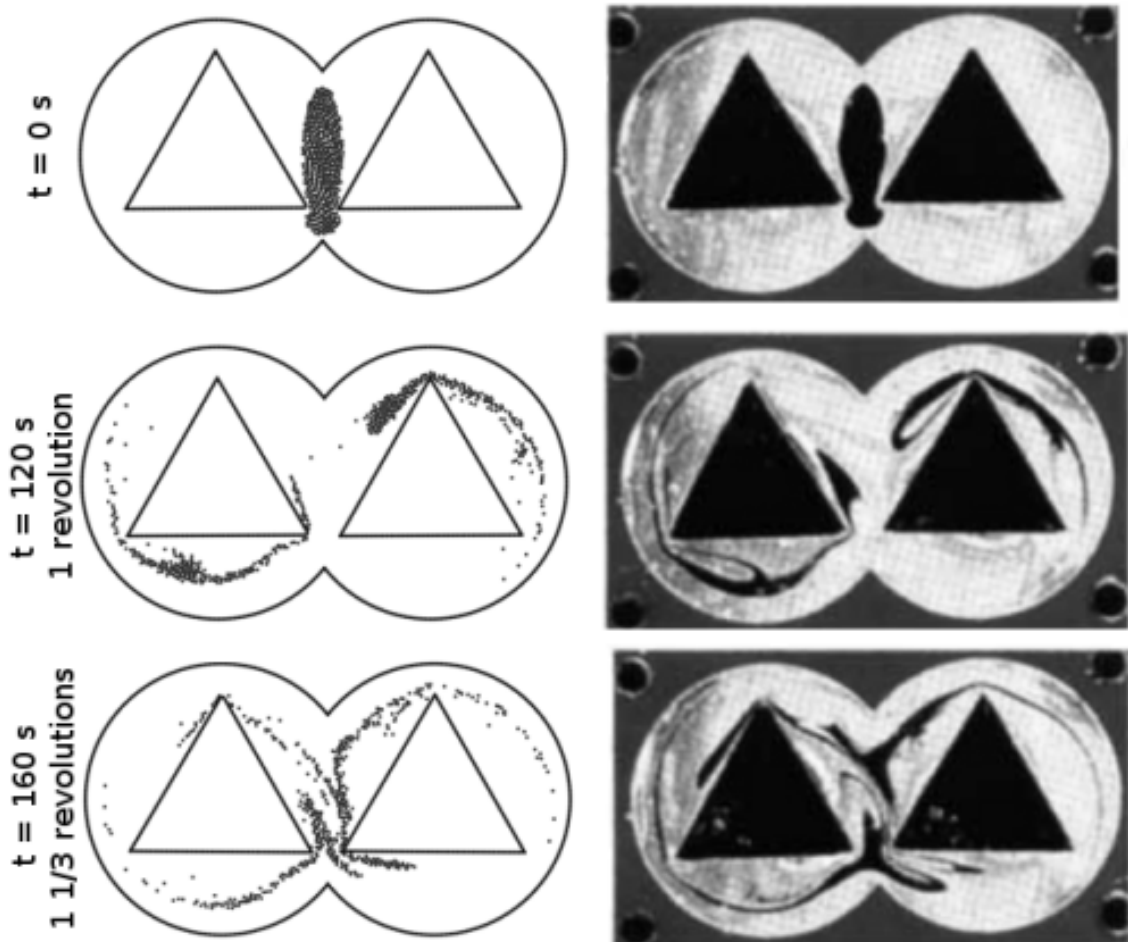


**Figure 3.4:** Comparison between the experiment performed by Avalosse and Crochet (right), and the SPH simulation results (left)

is not being modelled in any of the simulations (e.g. 3D effects).

Figure 3.5 compares the SPH simulation against the two Finite-Element simulations by Avalosse & Crochet (1997) and Bertrand et al. (2003). The initial conditions of both FEM simulations are only a rectangular approximation to the experimental blob, so we have initialised the SPH simulation using a similar rectangular blob. All the simulations have problems capturing the leading edge of the two separated segments. Avalosse and Crochet's simulation and the SPH simulations both underestimate the size of these two features, while Bertrand's overestimates them. The features of the blob in the SPH simulation are remarkably similar to Avalosse and Crochet's, except that the SPH simulation does not have the erroneous striations passing through the centre of the domain. Overall, the SPH simulation, with no adaptive resolution or remeshing requirements, compares very well to both the FEM simulations.

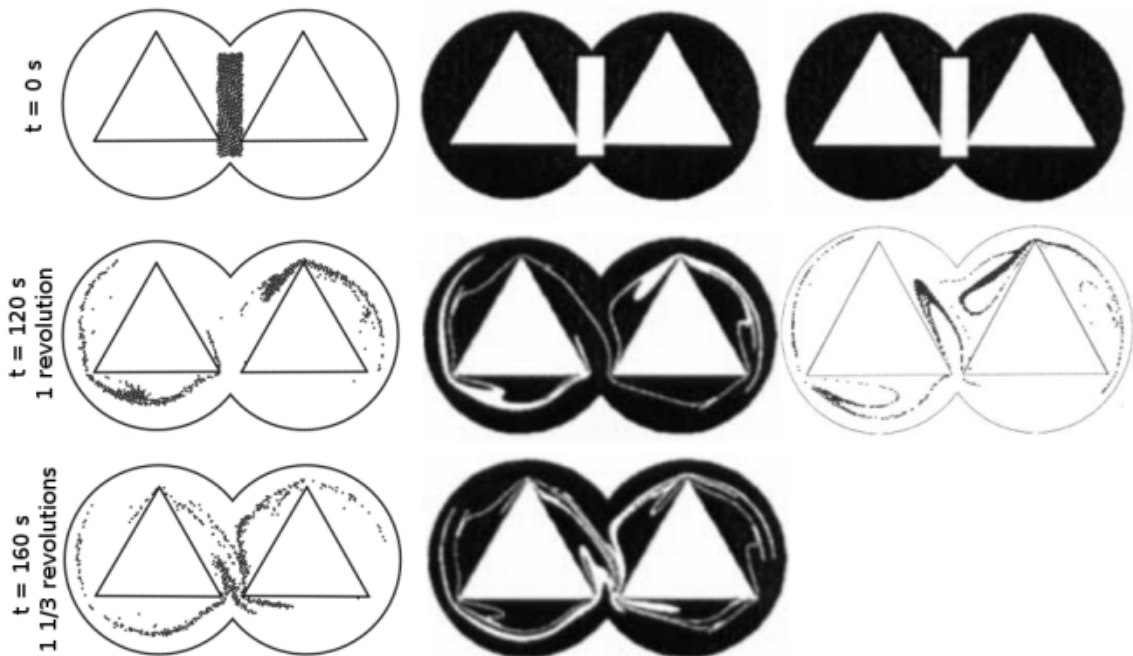


**Figure 3.5:** Comparison of SPH simulation (left column), the simulation by Avalosse and Crochet (middle column) and the simulation by Bertand et al. (right column) at three different times.

The SPH simulations shown in Figures 3.4 and 3.5 use 7995 particles (160 particles along the horizontal). Avalosse and Crochet use 7724 grid points in their simulation. Bertrand et al. initially uses 2388 finite elements to represent the domain, but this is before the mesh refinement around the cam edges. Using a rough visual estimate, the total number of elements after the mesh refinement was approximately 6000. So all three simulations have roughly comparable resolution. At this resolution, running the SPH simulations takes about 22 minutes per cam revolution on a single 3.2GHz Pentium 4 processor.

### 3.5.3 Increased Resolution

To establish that the results had converged and no more improvement could be gained from additional resolution, the SPH simulation was run again with an increased resolution of 18500 particles (240 particles across the horizontal) and 52000 particles (400 across the horizontal). The results are presented in Figure 3.6. There is no change in the general shape of the coloured blob over the first cam revolution, indicating that the results have converged over this time scale. However, after the first 120 s the chaotic flow tends to amplify small changes. In particular, the slight sharpening of the hook just below the left cam at  $t = 120$  s leads to a change in the blob shape near the lower right corner of the left cam at  $t = 160$  s.

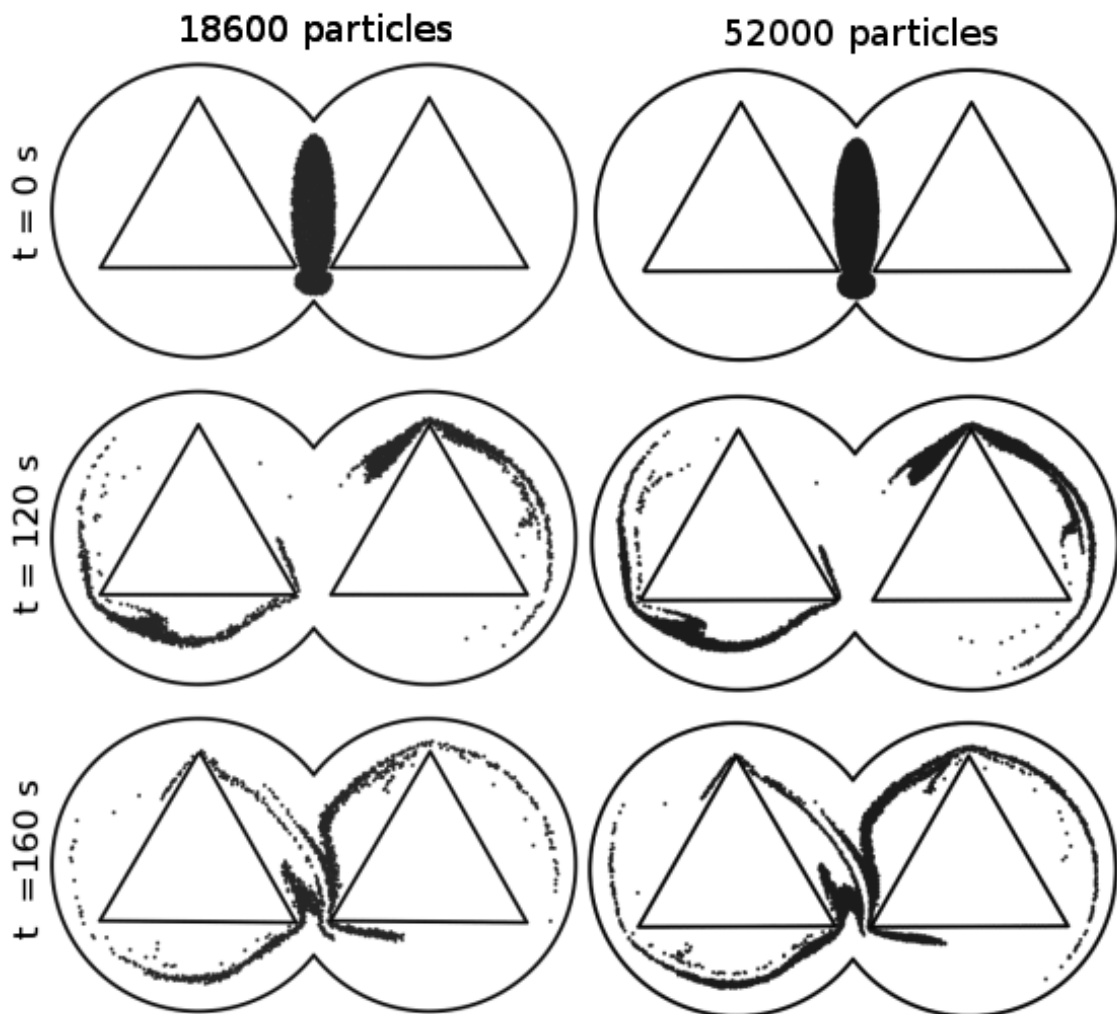


**Figure 3.6:** SPH simulation using an increased resolution of 18,600 and 52,000 particles.

A significant advantage of the higher resolution is that the particles more smoothly represent the blobs shape and pick up finer detail. To achieve this result without increasing the resolution, massless tracer particles could be added to the simulation. These would not change the movement of the SPH particles, but would cheaply fill in the details of the blob of interest.

## 3.6 Mixing Results

### 3.6.1 Finite-Time Lyapunov Exponents

Figure 3.7 shows the results of calculating both the forward and backward time FTLE over a time interval of one cam rotation. The maxima ridges in these plots clearly show the location of the main stable and unstable manifolds.

These manifolds are redrawn together in Figure 3.8, along with the results at two subsequent times. This figure shows both the location of the manifold's fixed hyperbolic point (the intersection of the stable and unstable manifolds at the centre of the domain) as well as the many homoclinic points formed as the two manifolds criss-cross each other around the cams. A homoclinic point is the intersection of a stable and an unstable manifold originating from the same hyperbolic point. As  $t \rightarrow \infty$ , these points will approach that hyperbolic point. The presence of transverse homoclinic points (which these points are) indicates the presence of chaotic orbits, which are essential for good mixing.

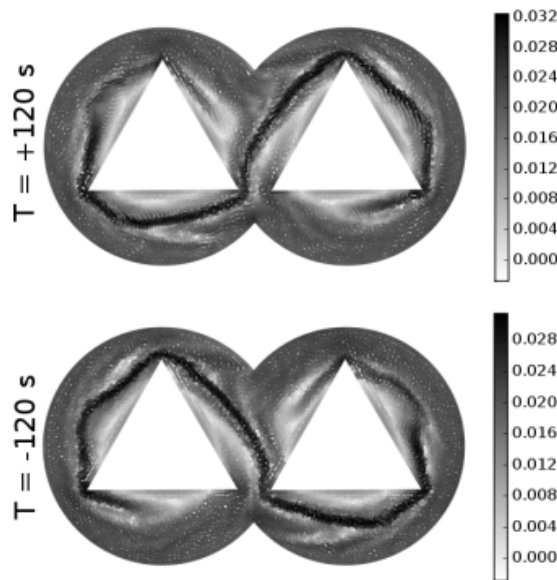


**Figure 3.7:** Top: Forward-time FTLE with  $T = +1$  cam revolution and  $t_0 = 0$  s. Bottom: Reverse-time FTLE with  $T = -1$  cam revolution and  $t_0 = 120$  s

The location of the manifolds in Figure 3.8 shows the geometry of the stretching and folding actions of the mixer. The blob of fluid surrounding the cams is stretched out along the stable manifold and folded around the cams along the unstable manifold. However, the particular geometry of these manifolds means that not all of their effects on the mixing are positive. Both stable and unstable manifolds act as separatrices for the flow, i.e. there is very little flux of material across these lines. For the Twin Cam mixer, this means that fluid is trapped between the tangle of manifolds and the cams and does not mix with the rest of the domain. With respect to the mixing measure  $M$  introduced earlier, this means that the slowest increase of  $M$  over time would be obtained by initially colouring the particles between the manifold and the cams a different colour from the rest of the domain. This is explored in more detail further on in this chapter (see Figure 3.12)

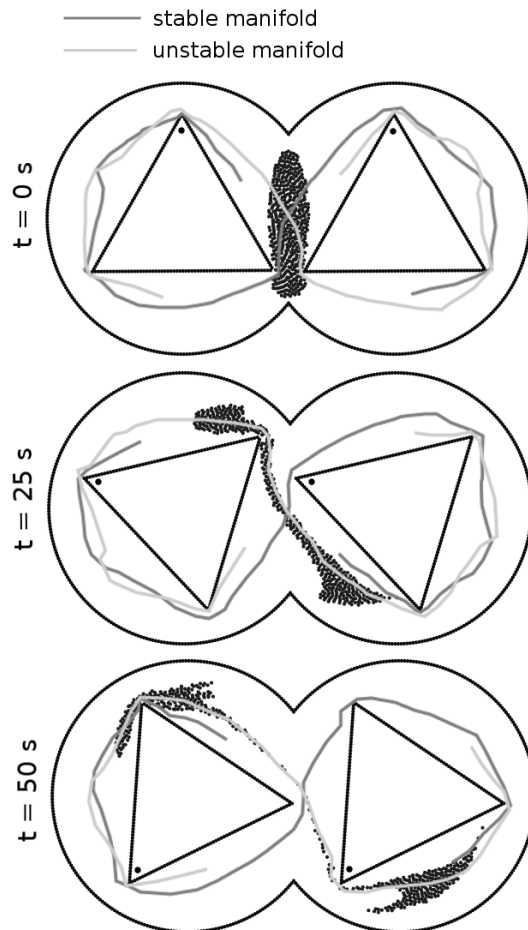


**Figure 3.8:** Top: The unstable and stable manifolds extracted from the FTLE maps shown in Figure 3.7, redrawn together along with the coloured blob of fluid. Middle and Bottom: Similar plots of the manifolds at subsequent times.

### 3.6.2 Counter-rotating Simulation

The previous simulations had the two cams rotating in the same direction at a constant speed of 0.5 rpm. This configuration is expected to produce good mixing. For the case where the cams are rotating at the same speed but opposite directions, the experiment performed by Avalosse and Crochet indicates that there should be little or no mixing between the two chambers of the mixer. This provides an interesting case to explore what happens to the manifolds in a poor mixing flow, as well as a simple test of the simulation accuracy. Figure 3.9 shows the results for the counter-rotating simulation.

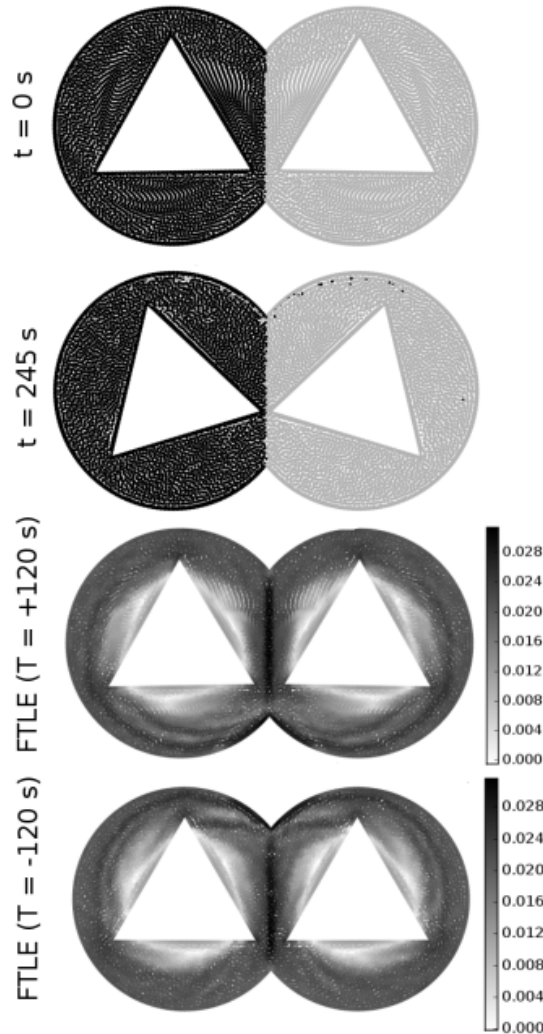


**Figure 3.9:** Counter-rotating Twin Cam simulation. Top: coloured particles at  $t = 0$  s; Middle top: coloured particles at  $t = 245$  s; Middle bottom: FTLE with  $T = +120$  s; Bottom: FTLE with  $T = -120$  s.

The top plot in Figure 3.9 shows the particles initialised at  $t = 0$  s. The particles in the left chamber are given a different colour to those in the right chamber. The plot below this shows the particles at  $t = 245$  s. The interface between the two colours is preserved almost exactly, even though the fluid particles have been rotated though just over two periods. The small flux of particles from one chamber to the other near the top corner

of the outside chamber  $(x, y) = (60, 55)$  (in mm) is a physical effect. The experiment by Avalosse and Crochet showed a similar flux.

The bottom two plots of Figure 3.9 shows the SPH particles coloured according to their forwards and backwards-time FTLE (calculated using  $T = \pm 120$  s). This shows a linear vertically orientated, strong unstable and stable manifold at  $x = 60$  mm. Since both manifolds are coincident, every point along their length is a homoclinic point. However, these are degenerate homoclinic points, which, unlike the transverse kind, do not indicate chaotic mixing. Furthermore, these manifolds act as separatrices, and this prevents any fluid in the left chamber from entering the right and visa versa.

### 3.6.3 Mixing Measure and Time scales

This section explores the time scales of the mixing, and in particular the effect that the tangle of manifolds has on these time scales. Figure 3.10 shows the same Twin Cam mixer simulation with particles once again coloured so that the domain is split evenly between two colours. Once again the two cams are rotating in the same direction (counter-clockwise) at a constant speed of 0.5 rpm. The location of the particles is shown after 500 s (just over four cam rotations), as is a plot of the particles coloured by the amount of mixing using the mixing measure  $M(\mathbf{r})$  defined previously and a length scale of  $L = 3.25$  mm.

Mixing between the two chambers proceeds rapidly. After 500 s the light and dark particles are significantly mixed in the outer regions of the mixer. However, the inner regions are largely unmixed and are still primarily composed of their original particles. This is expected, since we have already determined from the FTLE maps that the tangle of manifolds wrapped around the cams prevents fluid in this inner region from mixing with the rest of the domain, due to the manifolds acting as separatrices.

Compare this with the simulation depicted in Figure 3.11, where the particles are coloured so that the inner regions between the manifolds and the cam walls are coloured grey (this region is approximated as a circular area). For these initial conditions the only mixing possible is between the inner and outer regions, and as can be seen, over the 500 s the only mixing that occurs is a slow diffusion of the colours near the boundary. This confirms the analysis based on the separatrices from the FTLE calculations.

To get a clearer idea of the time scales of mixing for these two different initial particle colourings, Figure 3.12 plots the average mixing measure  $M$  (average taken over all the particles) versus time for both cases. Changing the radius of the subregions used to calculate the amount of mixing shows how the fluid is mixed over different length scales. The smallest subregion radius used is  $L = 0.8125$  mm, which is 1/150th of the width of the domain or just over the average distance between each particle. The largest radius used is  $L = 15$  mm, which is 1/8th of the domain width.

The left column in Figure 3.12 shows the first case, where the particles in each chamber of the mixer are given different colours. Since the fluid transport in this case is dominated by mixing outside the tangle of manifolds, this gives an indication of the mixing time-scales in the outer region. As can be seen, all of the length scales plotted reach a plateau close to their maximums by around 1000 s (8.3 revolutions). Before this time, it can be seen that the slope of  $M$  increases for larger length scales. This means that larger length

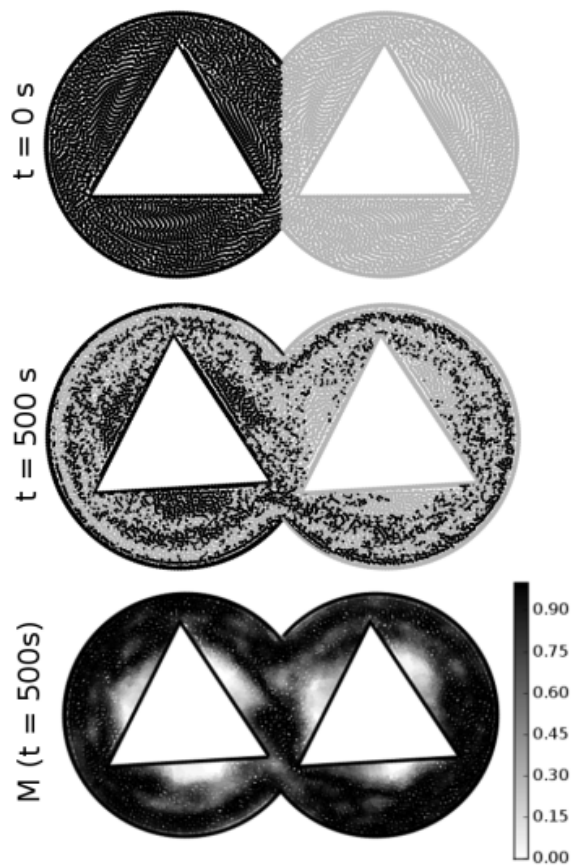


**Figure 3.10:** Particles in each mixing chamber coloured separately. The two cams are both rotating counter-clockwise at 0.5 rpm (the original configuration). Top: coloured particles at  $t = 0 \text{ s}$ ; Middle: coloured particles at  $t = 500 \text{ s}$ .

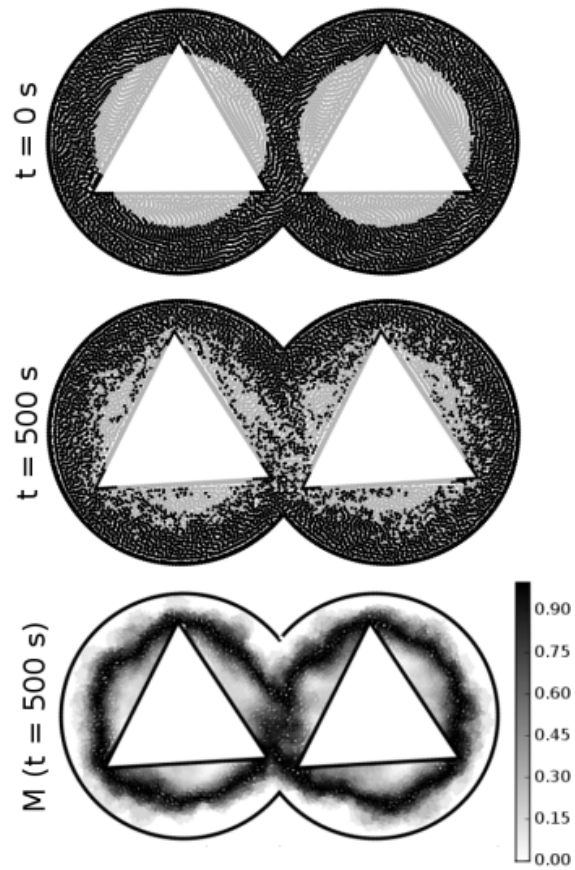


**Figure 3.11:** Particles coloured grey between the tangle of manifolds and the cam walls. The two cams are both rotating counter-clockwise at 0.5 rpm. Top: coloured particles at  $t = 0 \text{ s}$ ; Middle: coloured particles at  $t = 500 \text{ s}$ ; Bottom: mixing measure  $M$  at  $t = 500 \text{ s}$  and using  $r_m = 3.25 \text{ mm}$ .

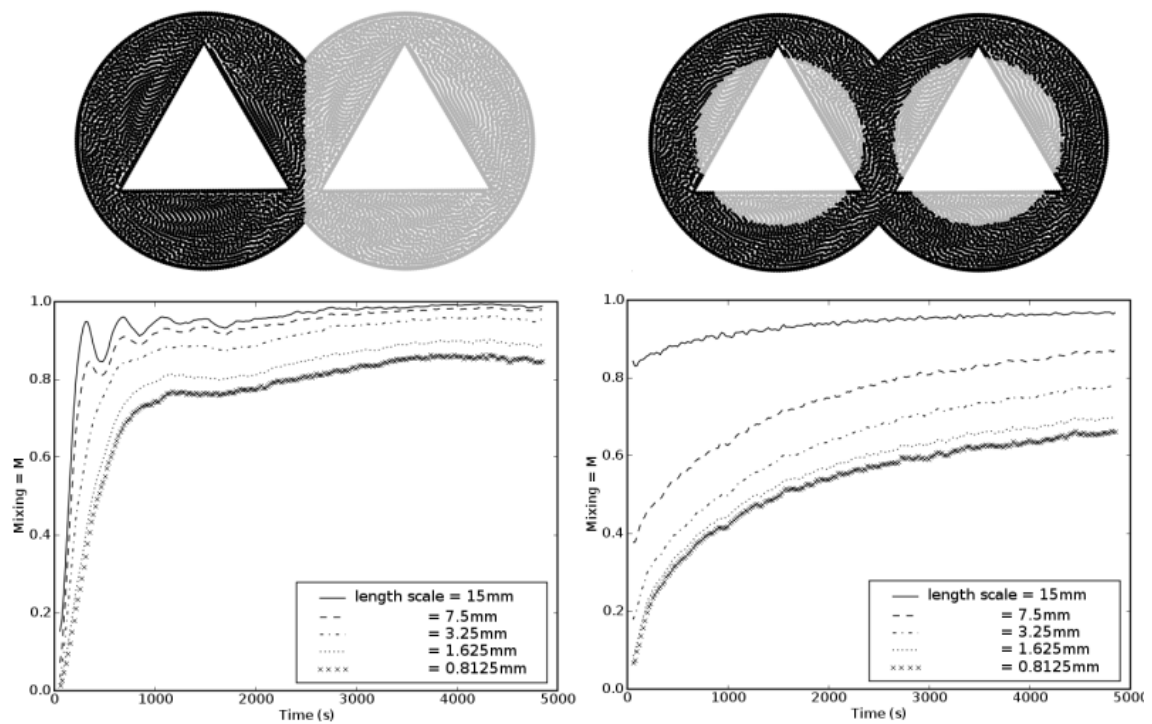


**Figure 3.12:** Average  $M$  (taken over the all the particles) vs. time for the initial conditions depicted in the top row of figures. The left side shows the mixing between the two chambers over time, whereas the right shows the mixing between the inner region trapped by the tangle of manifolds and the rest of the domain. Each line plot represents a different length scale used to calculate the mixing.  $M = 0$  indicates no mixing whereas  $M = 1$  indicates that the fluids are fully mixed. A full revolution of the cams takes 120 s, so the mixing plots show about 41 revolutions. Both cams are rotating counter-clockwise.

scales are mixing more quickly than the smaller, which is an indication of the greater effect of the chaotic mixing process compared to the smaller scale diffusion processes.

The right plot in Figure 3.12 shows the second case, where particles inside the tangle of manifolds are given a different colour to the rest of the domain. These particles start out more mixed than the first case, due to the larger interface between the two colours, especially at larger length scales. However, the rate of mixing is significantly reduced in this case. Even after 5000 s the average mixing measure still has not reached a maximum. The rate of mixing for different length scales is also very different than the previous case. The slope of  $M$  now increases for smaller length scales, indicating that diffusion processes, rather than chaotic mixing, play a larger role in the mixing between these two regions.

### 3.7 Conclusion

SPH is very well suited to modelling mixing processes for a fluid with high viscosity. There is no need to numerically solve any extra equations in order to track material points or determine concentrations, as each particle represents a volume of fluid for the duration of the simulation. Moving objects with sharp corners, essential to any practical mixer, are also simply modelled via moving boundary particles. Most importantly, the fluid transport is accurately modelled. The SPH simulation of a Twin Cam mixer compares well against experiment and two other finite-element simulations.

FTLE spatial maps are useful tools for analysing chaotic mixing. They can be used to locate stable and unstable manifolds in the flow, which provides valuable information on the barriers to mixing for a given piece of mixing equipment and where mixing is best promoted. We have presented a method of obtaining FTLE spatial maps directly from SPH particle data, and analysed the mixing processes in the Twin Cam mixer. When co-rotating, this mixer generates chaotic orbits in the outer portion of the domain, which promote mixing in this region. However, the tangle of stable and unstable manifolds surrounding the cams act as separatrices in the flow and prevent fluid transport out of a region close in to the flat edges of the cams, so this area does not mix well with the fluid in the rest of the domain. When the mixer is counter-rotating, the stable and unstable manifolds are coincident in a single, linear line down the centre of the domain, preventing fluid transport from one chamber to the other. Since the manifolds have no transverse intersection points, no chaotic orbits are generated and there is no significant mixing of the fluid.

## Chapter 4

# Turbulence

---

Turbulence is a common occurrence in fluid flow and examples surround us everyday. From smoke rising from a candle, breaking up into loops and whirls until it disperses, to the chaotic vortices of water as it flows past a bridge pylon. Leonardo da Vinci drew one of the oldest and most well-known images of turbulent flow (Figure 4.1), showing a stream of water falling into a pool. It shows how the turbulence is made up of similar eddies at many different scales. In the central region of the turbulence, Leonardo explicitly shows how the larger eddies are made up of many smaller eddies. All homogeneous turbulence is characterised by a wide range of self-similar scales. This is shown again in Figure 4.2, which shows a pyroclastic volcanic eruption from Mt St. Helens (Taken from Ecke (2005)) at three different length scales.

For such a common characteristic of fluid flow, turbulence has continually frustrated all attempts to fully explain and predict its motion. In 1883 Reynolds set up a famous experiment showing fluid flow along a straight pipe and the transition of the initially laminar flow to turbulence. He argued that the transition to turbulence was controlled by a dimensionless parameter known now as the Reynolds number  $Re = Ul/\nu$ , where  $U$  and  $l$  are characteristic velocity and length scales (e.g. In the case of Reynold's experiment  $l$  was the pipe diameter and  $U$  the mean flow velocity) and  $\nu$  is the kinematic viscosity. Almost half a century later, Richardson (1926) proposed the notion of an energy cascade, where the motion of the turbulence transforms the energy of large scale vortices (also known as eddies, whorls or circulations) into smaller and smaller eddies until viscosity takes over and the energy is dissipated. As Richardson (circa. 1922) describes it: "Big whorls have little whorls that feed on their velocity, and little whorls have lesser whorls and so on to viscosity".

Kolmogorov (1941 $a,b,c$ ) took this description further by defining an *inertial* range of length scales. Imagine an experiment where energy is injected into the flow at a large length scale  $l$ . This energy moves down to smaller scales as per Richardson's cascade until it is mopped up by the viscosity at a much smaller length scale  $\eta$ . The range of scales much smaller than  $l$  and much larger than  $\eta$  is known as the inertial range. It is assumed that the flow dynamics in the inertial range are unaffected by the particular form of the large-scale forcing or the effects of viscosity. The forcing simply enables energy to be injected into the flow, and once that energy has moved down to smaller scales and has reached



**Figure 4.1:** *Leonardo da Vinci's illustration of turbulence* (The Royal Collection ©2004, Her Majesty Queen Elizabeth II)

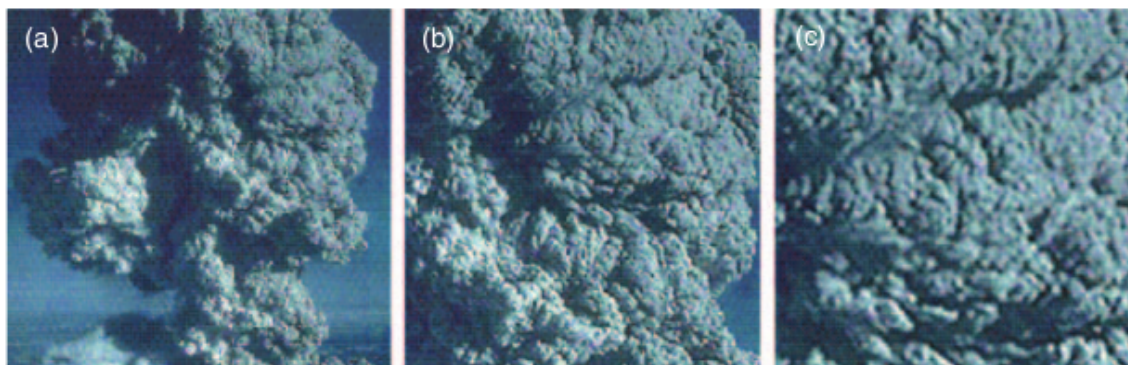


**Figure 4.2:** *Pyroclastic eruption of Mt. St. Helens shown in (a) is expanded by a factor of 2 in (b) and another factor of 2 in (c). Taken from Ecke (2005)*

---

the inertial range, it has "forgotten" the specific form of the forcing term and is instead entirely determined by the properties of the turbulent cascade. Experiments show that turbulence is only fully developed when the inertial range is sufficiently large. That is, when the forcing scale  $l$  is sufficiently larger than the viscous dissipation scale  $\eta$ .

Kolmogorov theorised that the statistical properties of the second velocity structure function  $[\delta v]^2 = [(\mathbf{v}(\mathbf{x} + r\hat{\mathbf{e}}) - \mathbf{v}(\mathbf{x})) \cdot \hat{\mathbf{e}}]^2$  (where  $\hat{\mathbf{e}}$  is a direction that has no effect on the velocity structure function for isotropic turbulence) have a universal form that only depends on the scale  $r$  and the dissipation rate  $\epsilon$

$$\langle [\delta v]^2 \rangle = \beta \epsilon^{2/3} r^{2/3}. \quad (4.0.1)$$

where the spatial average of any variable  $A$  is denoted as  $\langle A \rangle$ . This is known as Kolmogorov's *two-thirds law*, and when applied to the kinetic energy spectrum  $E(k)$  it can be shown that (Davidson (2004))

$$E(k) = \alpha \epsilon^{2/3} k^{-5/3}. \quad (4.0.2)$$

Kolmogorov's two-thirds law has been repeatedly validated through both numerical and experimental results. However, once this theory is extended to  $n$ -th order structure functions problems start to develop. Performing a similar derivation for the  $n$ -th order velocity structure gives

$$\langle [\delta v]^n \rangle = \beta_n (\epsilon r)^{n/3}. \quad (4.0.3)$$

When  $n$  rises above 3, experiments have shown that the exponent  $n/3$  starts to drop. When  $n = 12$ , this exponent has a value of  $\approx 2.8$  (Davidson (2004)). This effect has been blamed on *intermittency*, which states that the scales in the inertial range are not self-similar as Kolmogorov suggests. As the length scale decreases, the dissipation rate  $\epsilon = 2\mu S_{ij}S_{ij}$  (where  $S_{ij}$  is the strain-rate tensor  $S_{ij} = \frac{1}{2} \left[ \frac{\partial v_i}{\partial x_j} + \frac{\partial v_j}{\partial x_i} \right]$ ) becomes increasingly intermittent in space. In a particular region, the dissipation might no longer be equal to the globally averaged dissipation  $\langle \epsilon \rangle$  but could be much higher or lower depending on the local dynamics of the flow. Taking this into account means that Kolmogorov's theory is no longer universal between boundary layers, jets, wakes etc. as the spatial form of the dissipation will change between different turbulent flows.

Obtaining a universal theory of turbulence is clearly one of the more difficult and important problems of physics today. Direct Numerical Simulation (DNS) holds some promise that new data from these numerical experiments will lead to new insight. However, a DNS simulation is hampered by the prodigious resolution requirements that are required to achieve the Reynolds numbers that lead to fully developed turbulence. The ratio between the forcing length scale  $l$  and the dissipation length scale  $\eta$  (also known as the *Kolmogorov microscale*) is (Davidson (2004))

$$\eta \sim l Re^{-3/4}. \quad (4.0.4)$$

As an example, fully developed turbulence in a pipe can occur over a range of Reynolds numbers  $1000 < Re < 50,000$  (Ecke (2005)). This gives a resolution requirement ranging from  $178^3$  to  $3344^3$ .

Nevertheless, modern advances in high performance computing have led to a number of high Reynolds number DNS experiments. For example, the Japanese Earth Simulator achieved a Reynolds number of  $Re \approx 10^5$  using a grid of  $4096^3$  nodes (Kaneda et al. (2003)).

## 4.1 Two-dimensional Turbulence

Two-dimensional turbulence retains the same properties of randomness and chaotic advection that are the hallmarks of its three-dimensional equivalent. However, the reduction in dimensionality has profound effects on the main turbulent processes. The direct energy cascade is replaced by a *direct enstrophy cascade*. Enstrophy is defined as  $\omega^2/2$ , where  $\omega = \nabla \times \mathbf{v}$  is the vorticity. As the name suggests, the direct enstrophy cascade continually transfers enstrophy to smaller and smaller scales. But perhaps the most obvious change from three dimensions, and the primary characteristic of two-dimensional turbulence, is that the energy cascade has been reversed in direction and the kinetic energy now moves to larger length scales. This is known as the *inverse energy cascade*.

The origin of many of these effects lies in the lack of vortex stretching in two dimensions. In three dimensions the vorticity equation is

$$\frac{D\omega}{Dt} = (\omega \cdot \nabla)\mathbf{v} + \nu \nabla^2 \omega. \quad (4.1.1)$$

The second term on the right-hand side governs the change in vorticity for a fluid element due to viscous stresses. The first term controls the change in vorticity as the fluid element is stretched. Since material lines are continually being extended by a turbulent flow, this is a dominant effect in three-dimensional turbulence.

In two dimensions, the vortex stretching term disappears and the only change in vorticity is due to viscous forces. In a high  $Re$  flow these will be minimal and hence the vorticity in 2D turbulence is materially conserved as  $Re \rightarrow \infty$ . The primary action of the turbulence on a volume of fluid is to stretch it out into a filamentary structure. Since the vorticity of a material point is relatively constant in comparison to the turbulent time scale, an initial vorticity element will also be stretched out over time into a filament. This will continue until the vorticity gradients become too great and the vorticity filament is dissipated due to the viscous forces arising from the second term in Equation 4.1.1.

This process is given the term *direct enstrophy cascade*. It refers to the movement of enstrophy from the large to small length scales until it is mopped up at the dissipation scale. The word cascade implies that this action is local in wavenumber space and that the enstrophy moves through all scales on the way to the bottom. However, vortices of quite different length scales can interact in the flow (Davidson (2004)), indicating that this is not the case. Nevertheless, the term cascade is well established in the literature, presumably due to the so-called direct energy cascade in three-dimensional turbulence.

This leads to the hallmark of two-dimensional turbulence, the *inverse energy cascade*. Rather than the kinetic energy held in large scale vortices moving to smaller and smaller scales, as occurs in three dimensions, the opposite is true for two-dimensional turbulence. The process by which this occurs is not quite as clear as the enstrophy cascade. Proposals include the merger of like-signed vortices (Ayrton (1919), Fujiwhara (1921)) and that the growth in kinetic energy length scales is related to the increasing length of the vorticity filaments (Davidson (2004)). However, Davidson (2004) provides an explanation as to why the inverse energy cascade must exist. Consider the usual momentum and vorticity equations

$$\frac{D\mathbf{v}}{Dt} = -\nabla\frac{P}{\rho} - \nu\nabla \times \omega, \quad (4.1.2)$$

$$\frac{D\omega}{Dt} = \nu\nabla^2\omega. \quad (4.1.3)$$

Taking the dot product of both sides with the velocity  $\mathbf{v}$  and then averaging the result over all space (recall that all divergences average to zero due to the assumed spatial homogeneity of the turbulence) gives

$$\frac{d}{dt} \left[ \frac{1}{2} \langle \mathbf{v}^2 \rangle \right] = -\nu \langle \omega^2 \rangle, \quad (4.1.4)$$

$$\frac{d}{dt} \left[ \frac{1}{2} \langle \omega^2 \rangle \right] = -\nu \langle (\nabla\omega)^2 \rangle, \quad (4.1.5)$$

The first equation means that as  $\nu \rightarrow 0$  the total kinetic energy will be conserved, since  $\langle \omega^2 \rangle$  will always be finite. However, as  $Re \rightarrow \infty$ , the increasing filamentation of vortex elements means that the vorticity gradients  $\nabla\omega$  will always be great enough that the average vorticity  $\langle \omega^2 \rangle$  will always decline monotonically.

In terms of the kinetic energy spectrum  $E(k)$ , the average kinetic energy and vorticity are given by

$$\frac{1}{2} \langle \mathbf{v}^2 \rangle = \int_0^\infty E(k) dk, \quad (4.1.6)$$

$$\frac{1}{2} \langle \omega^2 \rangle = \int_0^\infty k^2 E(k) dk. \quad (4.1.7)$$

Since the integral for  $\langle \omega^2 \rangle$  is weighted towards larger wavenumbers, the conservation of the average kinetic energy and the decline of the average enstrophy implies that any initial kinetic energy spectrum must decrease (over time) at large  $k$  and increase at small  $k$ . This provides a reasonable explanation for the existence of an inverse energy cascade.

### 4.1.1 Kinetic Energy Scaling

In the late sixties Batchelor (1969) and Kraichnan (1967) published their seminal papers on two-dimensional turbulence. They both proposed the existence of the both the inverse energy cascade and the direct enstrophy cascade and made the key assumption that the interactions of the turbulent eddies were local in wavenumber. That is, if an eddy was in the inertial range  $\eta \ll k^{-1} \ll l$  then it does not feel the large-scale structures at  $l$  or the dissipation at  $\eta$  and the only interactions that occur are between eddies of similar scale. For example, Kraichnan visualised the transfer of energy and vorticity from wavenumber  $k = n$  as the result of *triad interactions* between wavenumbers  $n - 1$ ,  $n$  and  $n + 1$ .

Using this assumption, Batchelor proposed that the kinetic energy spectrum is self-similar over time and space and that the enstrophy cascade gives rise to the scaling law

$$E(k) \sim \beta^{2/3} k^{-3}. \quad (4.1.8)$$

Kraichnan derived a similar equation and went on to give the scaling law that results from the inverse energy cascade. This is identical in derivation and form to the energy cascade scaling that occurs in three dimensions.

$$E(k) \sim \epsilon^{2/3} k^{-5/3}. \quad (4.1.9)$$

Consider an infinite domain of incompressible fluid that has energy injected at wavenumber  $k_f$  due to some forcing action. At length scales larger than the forcing scale the flow will be dominated by the inverse energy cascade and so  $E(k) \sim k^{-5/3}$  for  $k \ll k_f$ . For length scales smaller than the forcing scale the turbulence is driven by the direct enstrophy cascade and  $E(k) \sim k^{-3}$  for  $k \gg k_f$ .

Numerical and experimental results have confirmed this energy spectrum for the  $k^{-5/3}$  range. However, the  $k^{-3}$  scaling is not as well accepted and there is significant evidence that the true scaling is slightly steeper than  $k^{-3}$ . Recent numerical and experimental results suggest that  $E(k) \sim k^{-n}$ , where  $n$  is usually close to 3 but can range between  $3 \leq n < 4$  (see Davidson (2004), Lindborg & Alvelius (2000), Mansour (2007) and references within).

A key underlying problem for the  $k^{-3}$  scaling proposed by Kraichnan and Batchelor seems to be the assumption that the enstrophy transfer is a true cascade. That is, that interactions between vortices are strictly local in wavenumber. However, this assumption has been shown to be false. In fact, Davidson (2004) shows that a kinetic energy spectrum of  $E(k) \sim k^{-3}$  directly implies that the interactions between wavenumbers cannot be local.

As well as these non-local interactions, another open problem that does not fit the theories by Kraichnan and Batchelor is the existence of *coherent vortices*. These are long-lived energetic vortex structures that survive the filamentation process and which interact with each other in a similar manner to a group of point-vortices. Over time they can merge with each other to create larger vortices, hence moving energy to larger scales and becoming part of the inverse energy cascade. Numerical simulations of decaying turbulence have tracked these coherent vortices (McWilliams (1990)) over time and show that their

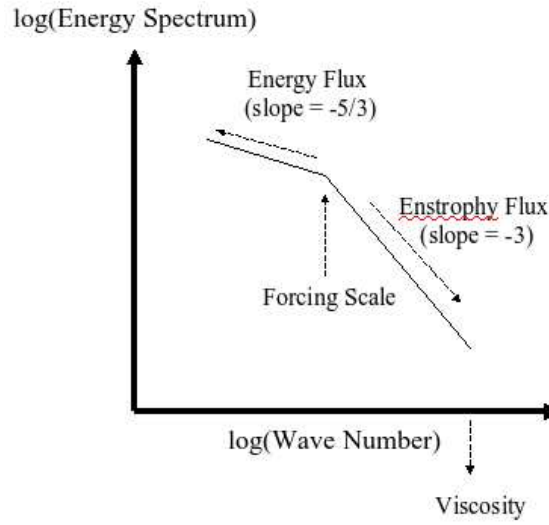


**Figure 4.3:** Diagram showing the expected scaling of the kinetic energy spectrum for fully turbulent flow in an infinite domain. Energy is injected at wavenumber  $k = k_f$  and is mostly transferred to larger and larger length scales (the remaining amount lost to viscosity is vanishingly small as  $Re \rightarrow \infty$ ). The enstrophy injected at  $k = k_f$  is transferred to smaller scales by the direct enstrophy cascade until it is mopped up at the dissipation length scale  $k = k_\eta$ .

origins lie in the initial vorticity field rather than emerging from the cascade process.

#### 4.1.2 Dissipation Length scale

Let  $l$  be the size of the large, energy containing vortices in the turbulence. As detailed above, enstrophy is transferred down to smaller scales until the vorticity gradients are large enough that the filament is destroyed through the action of viscosity. This occurs at the dissipation length  $\eta$ . The corresponding characteristic velocity at these large and small length scales are  $v_l$  and  $v_\eta$  respectively.

We can assume that the Reynolds number at the dissipation length will be in the order of unity (i.e.  $v_\eta \eta / \nu \sim 1$ ). In two-dimensions the vorticity is materially conserved, except at scales near or below the dissipation length. Therefore we can say that  $v_l / l \sim v_\eta / \eta$ . Rearranging these equations shows that the ratio between large and small scales is

$$\frac{\eta}{l} \sim \frac{1}{\sqrt{Re}}, \quad (4.1.10)$$

where  $Re = lv_l / \nu$ . In a similar fashion, the ratio between velocities at these two length scales is

$$\frac{v_\eta}{v_l} \sim \frac{1}{\sqrt{Re}}. \quad (4.1.11)$$

### 4.1.3 Velocity Structure Functions

The kinetic energy spectrum provides a useful description of a turbulent flow because it describes the relative contributions of the different length scales to the motion of the fluid. The velocity structure functions provide similar information. However, since it does not involve the calculation of a fourier transform, it is significantly easier to calculate from a disordered set of SPH particles.

The  $n$ -th order velocity structure function is defined as

$$\langle [\delta v]^n \rangle = \langle [(\mathbf{v}(\mathbf{x} + r\hat{\mathbf{e}}) - v_x(\mathbf{x})) \cdot \hat{\mathbf{e}}]^n \rangle. \quad (4.1.12)$$

For a general turbulent flow this will be dependent on the time  $t$ , location  $\mathbf{x}$ , direction  $\hat{\mathbf{e}}$  and the separation distance  $r$ . For statistically steady turbulence the time dependence disappears. The location dependence is removed assuming homogeneous turbulence and the assumption of isotropic turbulence eliminates the dependence on direction. Thus we are left with a function depending only on the separation distance  $r$ .

Given the predominance of the kinetic energy spectrum  $E(k)$  in turbulence theory and the natural relation that exists between this spectrum and the second order velocity structure function  $\langle [\delta v]^2 \rangle$ , it is useful to formally relate the two. Davidson (2004) derives the following relationship

$$\langle [\delta v]^2 \rangle \approx \int_{\pi/r}^{\infty} E(k) dk + (r/\pi)^2 \int_0^{\pi/r} k^2 E(k) dk. \quad (4.1.13)$$

The first term is the kinetic energy contained in all scales below  $r$  whereas the second is proportional to  $r^2$  times the vorticity in all scales larger than  $r$ . In three dimensions the vorticity in the large scales tends to be very small, hence it is a common assumption that  $\langle [\delta v]^2 \rangle$  only has a contribution from all the energy in the scales smaller than  $r$ . This is a very intuitive idea, since it is natural to think that only scales below  $r$  will affect the velocity structure function. However, in two dimensions (as is often the case) the opposite is true.

Assuming that the kinetic energy spectrum is proportional to  $E(k) \sim k^{-n}$ , this means that the enstrophy spectrum is  $\Omega(k) \sim k^2 E(k) \sim k^{-(n-2)}$ . For  $n < 3$ , which is always the case in three-dimensional turbulence, the first term will dominate in Equation 4.1.13 and the velocity structure function becomes

$$\langle [\delta v]^2 \rangle \sim r^{n-1}, \quad \text{for } n < 3. \quad (4.1.14)$$

For  $n \geq 3$ , the vorticity spectrum takes over and the velocity structure function starts to be dominated by the integral scale  $l$

$$\langle [\delta v]^2 \rangle \sim r^2 l^{n-3}, \quad \text{for } n > 3, \quad (4.1.15)$$

$$\langle [\delta v]^2 \rangle \sim r^2 \ln(l/r), \quad \text{for } n = 3. \quad (4.1.16)$$

We know from Section 4.1.1 that the direct enstrophy cascade in two-dimensional turbulence results in at least  $n = 3$  for  $\eta < r < l$ . Furthermore, this exponent is often found to be greater in numerical and experimental results. So, for two-dimensional turbulence the velocity structure function no longer has a close relationship to the kinetic energy spectrum and instead becomes dominated by the vorticity at large scales.

Given that the velocity structure function is not as successful at separating the different length scales in 2D turbulence, more attention in this thesis is given to calculating the kinetic energy spectrum rather than the velocity structure functions. However, in order to provide a complete description of the flow, Section 6.2.6 does give results for the velocity structure function of an SPH simulation of forced 2D turbulence.

#### 4.1.4 Richardson's Particle Pair Dispersion

The work by Richardson (1926) on single particle and pair dispersion was one of the earliest successful predictions of turbulence theory. It remains one of the most practical, since it is often useful in modelling small-scale diffusion and mixing processes in a wide range of turbulent flows. Pair dispersion in particular is a useful quantity, since unlike single particle dispersion it is mainly dependent on the small-scale velocity fluctuations of the flow (Boffetta & Sokolov (2002)).

Consider a pair of particles that are initially separated by some distance  $\delta\mathbf{r}$ . If this distance is much greater than the dissipation scale  $|\delta\mathbf{r}| \gg \eta$  then it is expected that the growth of  $|\delta\mathbf{r}|$  only depends on the initial separation and the velocity difference between the particles (i.e. we are assuming that viscous effects are negligible). Dimensional arguments give the form of  $\langle[\delta\mathbf{r}]^2\rangle$  as (Davidson (2004), although this was originally proposed by Lin (1972))

$$\frac{d}{dt}\langle[\delta\mathbf{r}]^2\rangle \sim \langle[\Delta v]^2\rangle^{1/2}\langle[\delta\mathbf{r}]^2\rangle^{1/2}. \quad (4.1.17)$$

Using the values of  $\langle[\Delta v]^2\rangle$  from Section 4.1.3 this becomes (for an infinite domain)

$$\frac{d}{dt}\langle[\delta\mathbf{r}]^2\rangle \sim \langle[\delta\mathbf{r}]^2\rangle, \quad \text{for } \eta < |\delta\mathbf{r}| < l, \quad (4.1.18)$$

$$\frac{d}{dt}\langle[\delta\mathbf{r}]^2\rangle \sim \langle[\delta\mathbf{r}]^4\rangle^{3/4}, \quad \text{for } l < |\delta\mathbf{r}|. \quad (4.1.19)$$

Finally, integrating these gives the expected growth rate of  $\langle[\delta\mathbf{r}]^2\rangle$

$$\langle[\delta\mathbf{r}]^2\rangle \sim e^t, \quad \text{for } \eta < |\delta\mathbf{r}| < l, \quad (4.1.20)$$

$$\langle[\delta\mathbf{r}]^2\rangle \sim t^3, \quad \text{for } l < |\delta\mathbf{r}|. \quad (4.1.21)$$

The key assumption of this argument is that sufficient time has elapsed that the particle pair has forgotten its initial conditions. This so-called *memory time* is of order  $|\delta\mathbf{r}|_0/|\Delta v|_0$ ,

where the subscript  $|\cdot|_0$  indicates an initial condition.

## 4.2 Wall-bounded Two-Dimensional Turbulence

The key property of bounded 2D turbulent flows is that the inverse energy cascade causes a build-up of energy in the wavenumber  $k = 1$  corresponding to the size of the domain. Kraichnan (1967) predicted this and compared the process to Einstein-Bose condensation. For decaying turbulence in a periodic box the end steady-state condition will be a pair of vortices of opposite sign. For an example, see the numerical results by Smith & Yakhot (1993). However, most simulations of periodic turbulence aim to mimic an infinite domain, and thus include some sort of large-scale viscous term to eliminate any kinetic energy condensation.

The assumption that a periodic box can approximate an infinite domain has been called into question. Tran & Bowman (2003) contest this assumption by arguing that a large-scale dissipation term would also remove a significant proportion of the enstrophy and that any energy not removed would be reflected down to the direct enstrophy range (ie.  $\eta \ll k^{-1} \ll l$ ), altering the results from the unbounded case. Davidson (2004) notes that the periodic boundaries cause artificial anisotropy and long-range correlations in the flow at scales near the size of the box. Lowe (2001) investigated the effects of periodic boundary conditions in two-dimensional turbulence and found that they were felt at length scales 100 times smaller than the size of the box.

Perhaps the most practical problem with turbulence in a periodic box is that it ignores the effects that non-slip and stress-free boundary conditions can have on the turbulence. This is a natural concern for any real-world turbulent flow. A series of papers by Clercx et al. (1999), Maassen et al. (2002), Molenaar et al. (2004), van Heijst et al. (2006), Wells et al. (2007) describe a series of experimental and numerical investigations of decaying and forced two-dimensional turbulence in wall-bounded flows. See Clercx et al. (2005) for a review of most of the results. Clercx et al. found that the boundaries were a significant source of vorticity and vorticity gradients in the flow. Whenever a vortex came near a boundary it would create a boundary layer response. This boundary layer could separate from the wall and move into the interior of the flow as a high intensity vorticity filament. The primary effect of these filaments was to disrupt the condensation vortex structure. In the case of a circular no-slip boundary the inverse energy cascade would build up into a pair of vortices with opposite sign. The vorticity filaments from the boundary would gradually grow another dipole vortex pair until it replaced the old pair. This process would then repeat itself for the duration of the experiment. For a square boundary, pressure forces normal to the wall impart a net torque to the flow and spin-up the flow into a single large monopole vortex that fills the entire domain. In this case the vorticity filaments from the boundary randomly destroy this structure. After a brief period of random turbulent motion the vortex reforms, often rotating in the opposite direction.

In an interesting experiment, Wells et al. (2007) constructed a square box filled with fluid on a rotating table. The table was given a constant angular rotation, which induced Ekman pumping and restricted the flow to be quasi-two-dimensional. The constant angular velocity was then given a sinusoidal perturbation. This caused the boundary layer to be rolled up into a coherent vortex and injected into the centre of the domain in the same

manner as the vorticity filaments discussed above. Each perturbation caused more vortices to be injected into the flow, which all interacted with each other to form a fully developed turbulent flow.

Li & Montgomery (1996), Li et al. (1997) have also performed decaying turbulence simulations in a circular wall-bounded domain. They too note the importance of the boundaries in injecting vorticity into the flow, as well as the significant increase in kinetic energy decay this causes as compared with the periodic case.

An early experiment of two-dimensional bounded turbulence in a square box was performed by Sommeria (1986). The turbulence was driven by a constant in time array of alternating vortices, rather than the usual random-in-time forcing. The results show that once the Reynolds number is high enough, the kinetic energy of the flow condenses into the same large monopole vortex as reported by Clercx et al. The structure persists for long periods of time with random short periods of destruction and reformation.

### 4.3 SPH Turbulence Background

Recently, there have been a few different turbulence models proposed for SPH. Monaghan (2002, 2004) based a model on the Lagrangian Averaged Navier-Stokes Alpha (LANS- $\alpha$ ) model (see Geurts & Holm (2006) for more details). The LANS- $\alpha$  model is a Lagrangian version of Large Eddy Simulation (LES). In LES a smoothing operator is applied to the Navier-Stokes equations in order to obtain an equation in terms of a smoothed velocity  $\bar{v}$  and pressure  $\bar{P}$ . On the other hand, LANS- $\alpha$  only smoothes the transport velocity term rather than the full Eulerian velocity field. In terms of the SPH method, this means that the particles are moved with the smoothed velocity  $\bar{v}$ . However, Monaghan and Mansour (2007) found that calculating the extra terms in the momentum equation required very expensive iterations over the particles and currently this method is not suitable for practical use.

Violeau & Issa (2007) derive four different turbulence models for SPH. The first two are based on the standard one and two-equation turbulent transport equations. These equations assume that the turbulence acts as a viscous term, called the *eddy viscosity*. Violeau and Issa use a Prandtl's one-equation for the first model and the standard  $k - \epsilon$  equations for the second. Violeau and Issa compare these two models with another based on the Reynolds Stress Model (RSM), which discards the eddy viscosity assumption and aims to calculate the Reynolds stresses directly. All three models are applied to a 2D open-channel turbulent flow and a 2D collapsing water column. The results show significant improvement between the models when moving from the Prandtl model to the  $k - \epsilon$  and then to the RSM model. However, there are still significant differences between the SPH results and the benchmark experiments. In the case of the open-channel flow the velocity profile from the SPH results were compared to experiment and a FEM  $k - \epsilon$  simulation. Both the FEM and experimental results were significantly closer to each other than the SPH results.

There have been two attempts to derive an SPH turbulence model based on a stochastic pdf model. Violeau et al. (2002) uses the Generalised Langevin Model, while Welton (1998) uses a Monte Carlo approach. What makes Welton's method remarkable is that, in order to reduce the statistical error introduced by the Monte Carlo method the number of

particles involved in each kernel estimation  $\tilde{N}$  needs to be in the order of thousands. In order to reduce the computational demand this involves, Welton uses an algorithm based on the Fourier series expansion of the kernel in order to calculate the kernel estimates for all particles in  $O(N)$  time, rather than the usual  $O(N\tilde{N})$  (where  $N$  is the total number of particles).

However, the majority of SPH turbulence models have focused on using the LES method combined with a Smagorinsky model for the sub-grid (or sub-particle in this case) scale. Violeau & Issa (2007) applied this model to an open-channel flow and a collapsing water column and Dalrymple & Rogers (2006) used it to simulate breaking waves. Shao et al. (2006) used an LES SPH model in conjunction with a fully incompressible SPH code in order to simulate breaking waves over a horizontal deck and a sea-wall. Other SPH LES results can be found in Issa et al. (2005) and Shao & Gotah (2004).

Ting et al. (2006) used an SPH LES model to simulate the turbulent flow over a backwards facing step. Standard wall functions were used to estimate the velocity close to the no-slip boundaries. Unlike most of the papers mentioned above, results were included comparing standard SPH and the LES SPH. Ting et al. found that standard SPH produced reasonable results and that the addition of the turbulence models did not improve these significantly. They echoed the conclusions by Cleary & Monaghan (1993) that SPH can be considered to have a form of LES already built in and that SPH involves some sort of dissipative term that prevents the accumulation of energy at the sub-grid scales.

All of these papers involve the addition of a turbulence model to standard SPH. However, there has been few attempts to study how well standard SPH can model the full range of turbulent scales in a Direct Numerical Simulation (DNS). Mansour (2007) has performed the only SPH DNS prior to this thesis. Mansour used standard SPH as well as the LANS- $\alpha$  based model by Monaghan (2002) (termed  $\alpha$ -SPH) in order to simulate forced 2D incompressible turbulence in a periodic box. Mansour found that while SPH reproduces an inverse energy cascade, its strength is much weaker than expected. This was attributed to the weakness of the SPH viscosity term at small scales and the resultant action of this term over a much broader range of scales than expected by theory. The  $\alpha$ -SPH model failed to improve on these results. In fact, the model caused an increase in numerical kinetic energy at short scales, although Mansour notes that a further increase in the length scale of the smoothing should reverse this trend. This was only attempted in 1D simulations due to the computational requirements of the model.

The results in this thesis apply SPH to both decaying and forced turbulence in a two-dimensional no-slip wall-bounded domain. The purpose of this study is to provide more insight on how well SPH models turbulent flow and hopefully answer some of the open questions left by Mansour, namely the source of the excess kinetic energy at small length scales and how this affects the inverse energy cascade. We have chosen to simulate turbulence in a wall-bounded domain, which will give a clearer picture of how SPH turbulence behaves in a more practical setting and without the complications introduced by the periodic boundary condition. While Mansour explicitly prevented the energy from condensing at the domain scale through a large-scale dissipation term, we have not included this in order to determine if SPH can reproduce the domain-filling vortices that are the expected end-state of bounded 2D turbulence. We have also used the SPH continuity equation to integrate the densities rather than directly calculating the densities

through an SPH sum. Section 6.3.4 describes how calculating the densities through an SPH sum smoothes out small-scale density fluctuations which results in an additional energy sink for the flow, in some cases strong enough to be the same order as the viscous dissipation. We have also used the Wendland kernel (for the forced turbulence simulations only) rather than the traditional Cubic Spline. The results in Chapter 7 show that the Wendland kernel entirely removes particle clumping and decreases numerical dissipation, significantly increasing the strength of the inverse energy cascade.

## 4.4 Motivations for an SPH simulation of 2D Wall-Bounded Turbulence

Besides fundamental turbulence research, the primary reason for simulating two-dimensional turbulence for any numerical code is that it makes an ideal benchmark test. Turbulence has a well-deserved reputation of being difficult to simulate, due to the complex, chaotic nature of the flow as well as the high resolution requirements. Two-dimensional turbulence reduces the resolution requirements significantly. In addition to the reduction in dimensionality, the smallest length scale in the flow  $\eta$  scales much slower with the Reynolds number ( $\eta = Re^{-1/2}l$  rather than  $\eta = Re^{-3/4}l$ ). At the same time, the move from three-dimensions to two makes the flow more difficult to simulate correctly due to the increased importance of the small-scale motions of the fluid. The inverse energy cascade produces a much closer link between the small and large length scales in two-dimensions. If the small scales are not simulated correctly, it could disrupt the cascade of energy to lower wavenumbers and hence change the large-scale properties of the flow. Conversely, if the small scales are incorrectly modelled in three-dimensions, the results will only affect these and smaller scales.

The field of turbulence is expansive, and any new simulation has the advantage that there are many numerical, experimental and theoretical results to compare against, especially if the simulation is of the traditional turbulent periodic box. One of the first numerical simulations of turbulence was performed by Lilly (1969). Going back even further, the first major experiment on turbulence is usually attributed to Reynolds (1883). Since this time there has been no shortage of subsequent experimental and numerical results. There is also a large body of theoretical predications thanks to the pioneering work of Richardson (1926), Kolmogorov (1941*a*), Batchelor (1969), Kraichnan (1967) and many others since.

Turbulence is general characteristic of high Reynolds number flow. Given a region with a homogeneous and isotropic forcing protocol and far away from any boundaries, the resultant turbulent flow will also be homogeneous and isotropic. This is advantageous since it allows the use of many different analysis tools, most notably, the Fourier transform. Most theories of turbulence revolve around the division of the flow into different length scale ranges and the scaling laws of various spectra (e.g. kinetic energy, enstrophy) within these ranges. Another useful tool that can be used to analyse the flow in homogeneous turbulence is the use of spatial and/or temporal statistics. For example, Chapter 7 describes how the distribution of SPH particles in a forced turbulence simulation is reduced to a function describing the probability of finding a pair of particles at a given separation. The distribution of SPH particles has a large impact on the accuracy of the method, and a turbulent box is an ideal domain to study this property. A turbulent flow will naturally produce the significant amount of disorder in the particles, and

since this disorder will be homogeneous and isotropic across the domain this allows the construction of such a simple statistical view of the data.

## 4.5 SPH Fourier Transform

Most published simulations and experiments use the kinetic energy spectrum as a benchmark against turbulence theory and other published work. In order to perform a similar comparison with the SPH data, a method is needed to perform a Fourier transform over the SPH particles. Since they will be unevenly distributed, traditional Fast Fourier Transform methods are of no use unless the particle variables are first interpolated to a grid, which would artificially reduce the spectrum at large wavenumbers.

Mansour (2007) proposed a SPH Fourier transform by taking the usual form of the Fourier transform and simply replacing the integral with an SPH sum over all the particles. For example, a 2D Fourier transform over a periodic square of side  $2L$  is

$$F(\mathbf{k}) = \frac{1}{L^2} \int_{-L}^L \int_{-L}^L f(\mathbf{r}) e^{-i\frac{\pi}{L}\mathbf{k}\cdot\mathbf{r}} dx dy, \quad (4.5.1)$$

where  $\mathbf{k}$  is an integer wavevector and  $f(\mathbf{r})$  is the function being transformed. Converting this equation into an SPH summation, this becomes

$$F(\mathbf{k}) = \frac{1}{L^2} \sum_{b=1}^N f_b e^{-i\frac{\pi}{L}\mathbf{k}\cdot\mathbf{r}_b} \frac{m_b}{\rho_b}, \quad (4.5.2)$$

where  $\mathbf{r}_b$ ,  $m_b$  and  $\rho_b$  are the position, mass and density of particle  $b$  and  $f_b$  is the variable that is being transformed to the Fourier domain.

Mansour (2007) tested the accuracy of this SPH Fourier transform in 1D using a number of test spectra and density profiles and found that accurate results were obtained up to wavenumber  $k_c = 0.42N$ , where  $N$  is the number of particles along that dimension.

It is useful to test this transform using conditions that are likely to be encountered in the 2D turbulence simulations performed during this thesis. Particle positions are obtained from the forced 2D periodic turbulence simulation described in Chapter 6. This simulation contains 300x300 particles arranged in a periodic square box with sides  $L = 1$ . The particle positions are taken at a time point during the simulations after the turbulence has become fully developed ( $t \approx 31$ ), so the particles are arranged in a disordered pattern typical of the turbulence simulations described in this thesis. A new particle variable  $f_a$  was assigned to these particles according to the test spectrum given by

$$f_a = \sum_{\mathbf{k}=(-150,-150)}^{(150,150)} \begin{cases} |\mathbf{k}|^{-5/3} \cos\left(\frac{\pi}{L}\mathbf{k}\cdot\mathbf{r}_a\right), & \text{for } 0 \leq |\mathbf{k}| < 8, \\ |\mathbf{k}|^{-3} \cos\left(\frac{\pi}{L}\mathbf{k}\cdot\mathbf{r}_a\right), & \text{for } 8 \leq |\mathbf{k}|. \end{cases} \quad (4.5.3)$$

The SPH Fourier transform in Equation 4.5.2 was calculated, then the 2D spectrum  $F(\mathbf{k})$  was collapsed to a 1D spectrum by averaging over the angles in wavenumber space. That is

$$F(k) = \frac{1}{\sum_{k-1 < |\mathbf{k}| \leq k} 1} \sum_{k-1 < |\mathbf{k}| \leq k} |F(\mathbf{k})|, \quad (4.5.4)$$

where  $k = |\mathbf{k}|$ . Figure 4.4 shows  $F(k)$  versus wavenumber  $k$ . Also drawn are two reference lines indicating the shape of the test spectrum in Equation 4.5.3. Very good agreement to the test spectrum is obtained up to a wavenumber of  $k \approx 80 = 0.26N$ , which corresponds to a wavelength of 3.75 particle spacings. Figure 4.5 shows the percentage error between  $F(k)$  and  $k^{-3}$  for  $k \geq 8$  as well as two references lines showing  $\pm 10\%$ .

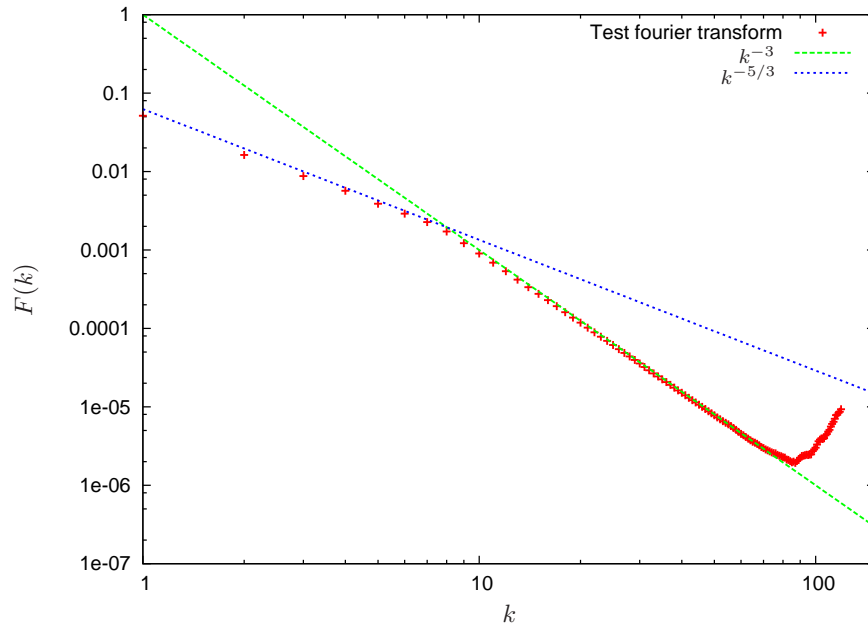


**Figure 4.4:** SPH Fourier transform of the test spectrum defined in Equation 4.5.3. The particle positions are taken from  $t \approx 31$  from a typical forced 2D periodic turbulence simulation described in Chapter 6. The wavenumber  $k$  has a wavelength of  $\lambda = \frac{2L}{k}$ , where  $2L$  is the width of the periodic box.

Most of the turbulence simulations in Chapter 6 use square boxes surrounded by no-slip boundaries, so these results will no longer satisfy the periodic assumption. Following the example of Wells et al. (2007), the variable to be transformed is first reduced by its mean and then a Hann window is applied. So, if  $f_b$  is the variable of interest then it is pre-processed using

$$f_b = \begin{cases} 0.5(1 - \cos(\pi(|\mathbf{r}_b| + 1))) \left( f_b - \frac{\sum_a x_a}{N} \right), & \text{for } |\mathbf{r}_b| \leq 1, \\ 0, & \text{otherwise.} \end{cases} \quad (4.5.5)$$

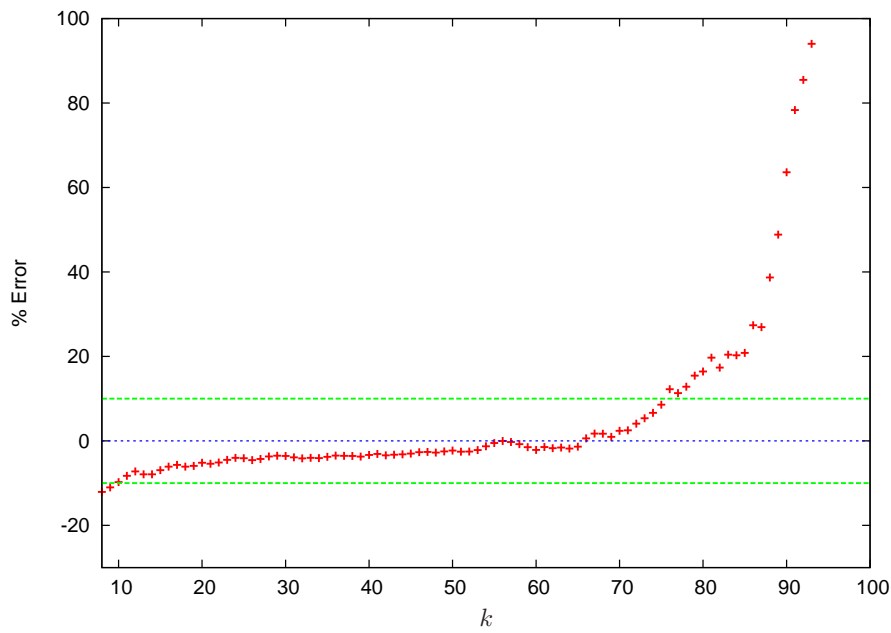


**Figure 4.5:** Percentage difference between the calculated test spectrum shown in Figure 4.4 and  $k^{-3}$ . The deviation from 0% at small  $k$  is due to length scales at  $k < 8$  mixing with those where  $k > 8$  (see the definition of the test spectrum in Equation 4.5.3).

As well as enforcing the periodic assumption, this also reduces the effect of the boundaries on the resulting spectrum. This is beneficial, since we are generally concerned with the kinetic energy spectrum of the homogeneous turbulence in the centre of the domain.

## Chapter 5

# Decaying Turbulence Simulations

---

The simulation of decaying turbulence involves creating an initial turbulent velocity (or vorticity) field and following the evolution of this field over time. In this case we are interested in the simulation of two-dimensional wall-bounded turbulence. Since the turbulence is 2D, we expect that it will be relatively long-lived, due to the approximate conservation of kinetic energy at high Reynolds numbers. We also expect the formation of an inverse energy cascade, where the kinetic energy contained in the initial eddies moves into larger and larger vortex structures until it cannot grow further due to the size of the domain. The geometry used for these SPH simulations was a square box with no-slip boundaries. Following the results of Clercx et al. (1999), we know that this particular geometry will most likely cause a spontaneous spin-up of the total angular momentum, along with the formation of a single large vortex filling the majority of the domain. The spin-up of the fluid within the box is due to the torque exerted on the fluid via the pressure forces perpendicular to the boundaries. The formation of the large vortex is due to the energy carried by the inverse energy cascade condensing at the lowest possible wavenumber.

The purpose of these investigations is to evaluate how successful SPH is in the simulation of decaying turbulence. In order to perform a comparison with another method, we have used the decaying turbulence simulations by Clercx et al. (1999). Clercx has utilised a Chebyshev polynomial pseudo-spectral method, along with an explicit Adams-Bashforth scheme for the advection term and an implicit Crank-Nicolson scheme for the diffusion term. Spectral methods are commonly used for DNS simulations of turbulence due to their high accuracy and exponential convergence rates. Their main disadvantage is the difficulty in incorporating boundary conditions more complicated than a periodic box.

### 5.1 SPH Simulation

These simulations used the standard quasi-compressible SPH method described in Chapter 2. The viscosity term was calculated using the Monaghan form (Equation 2.5.18) and the density for each particle was found by integrating the continuity equation (Equation 2.5.5).

The particle's position and velocity were integrated using the Leapfrog second order

method described in Section 2.7. In order to preserve the reversibility of the simulation (in the absence of viscosity),  $d\rho/dt$  was calculated using the particle's position and velocity at the end, rather than the middle, of the timestep.

The no-slip boundaries were modelled using four layers of immovable SPH particles. These boundary particles were identical to the other fluid particles in every way except that their positions were constant.

The Reynolds number was set to  $Re = LU/\nu = 1500$  based on the half-width of the box  $L$  and the initial RMS velocity  $U$  of the particles. The particle densities were set to  $\rho = 1000$ . Most of the results shown in this chapter use 300x300 particles.

The Cubic Spline kernel was used for all the simulations in this chapter.

## 5.2 Initial Turbulent Velocity Field

The initial velocity field was chosen to match that used by Clercx et al. (1999). The SPH particles were positioned on a grid at  $t = 0$  and their velocity was calculated from a 2D 65x65 Chebyshev series.

$$v_a = \sum_{n=0}^{65} \sum_{m=0}^{65} C_{nm} \cos(n \cos^{-1}(x_a)) \cos(m \cos^{-1}(y_a)) \quad (5.2.1)$$

where  $x_a$  and  $y_a$  are the x and y coordinates of particle  $a$ 's position. The coefficients  $C_{nm}$  were randomly generated from a zero-mean Gaussian distribution with variance  $\sigma_{nm}$  given by

$$\sigma_{nm} = \frac{n}{\left[1 + \left(\frac{1}{8}n\right)^4\right]} \frac{m}{\left[1 + \left(\frac{1}{8}m\right)^4\right]} \quad (5.2.2)$$

In order to ensure a quiet start at the no-slip boundaries, the initial velocity field was gradually reduced down to zero near the boundaries using a smoothing function  $f(x)f(y)$  where

$$f(x) = 1 - \exp(-100(1 - x^2)^2) \quad (5.2.3)$$

The resultant velocity field is not necessarily divergence-free. However, Clercx's pseudospectral code ensures that it is by projecting the velocity onto a divergence-free subspace. Following this example, we have performed a similar operation on the velocity field defined by (5.2.1) - (5.2.3).

Any velocity field can be separated into its divergence-free component  $\mathbf{v}_d$  and the gradient of a scalar  $\phi$

$$\mathbf{v} = \mathbf{v}_d + \nabla\phi \quad (5.2.4)$$

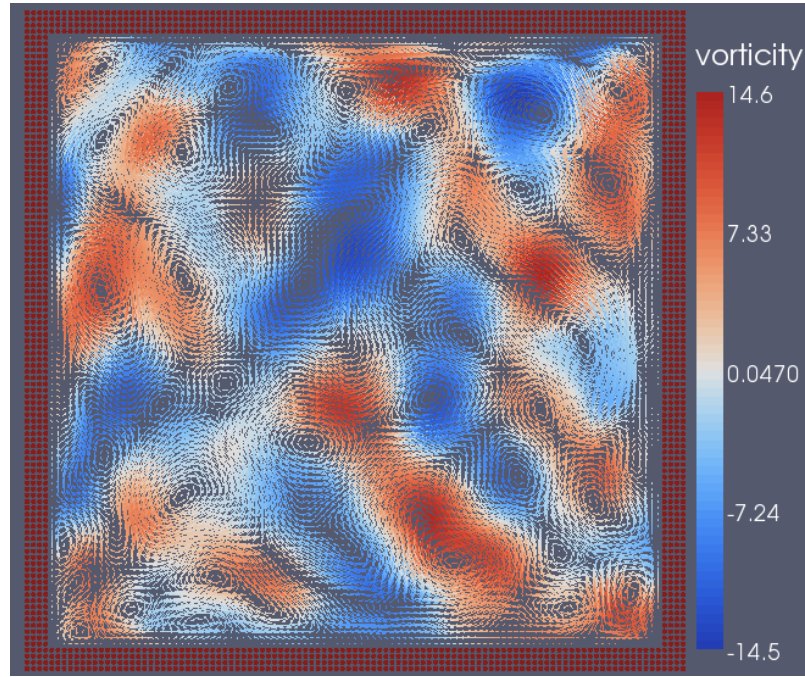


**Figure 5.1:** Example initial velocity field for decaying turbulence simulation. Arrows depict the velocity field and are coloured by the vorticity. The four layers of red dots around the edges of the box denote boundary SPH particles

Taking the divergence of both sides gives

$$\nabla \cdot \mathbf{v} = \nabla^2 \phi \quad (5.2.5)$$

Since the SPH particles are initially positioned on a grid, this equation can be solved for  $\phi$  using a second order finite difference method. The divergence free velocity field  $\mathbf{v}_d = \mathbf{v} - \nabla \phi$  is then normalised so that the total kinetic energy  $E(0) = 1$  per unit mass. Figure 5.1 shows an example of an initial velocity field generated using this method.

In order to be absolutely consistent, the pressure of the particles should be set to match the given velocity field. However, this was not expected to alter the results significantly as the SPH pressures quickly evolve to match the velocity field over a time scale set by the sound speed, which is 10 times greater than the maximum velocity of the flow.

### 5.3 Vorticity Evolution

The vorticity for each particle  $a$  is determined as follows. Let  $X_a = [\mathbf{r}_{1a}, \mathbf{r}_{2a}, \dots, \mathbf{r}_{Na}]$  be a vector containing the relative positions of the  $N$  neighbour particles surrounding  $a$ . Let  $V_a = [\mathbf{v}_{1a}, \mathbf{v}_{2a}, \dots, \mathbf{v}_{Na}]$  be a vector of the relative velocities of the neighbouring particles. Assuming a linear velocity field around particle  $a$ , these two vectors are related by

$$V_a = \nabla_a \mathbf{v} X_a. \quad (5.3.1)$$

The velocity gradient  $\nabla_a \mathbf{v}$  is solved from this over-determined set of linear equations by a least squares method. The vorticity  $\omega_a = \nabla_a \times \mathbf{v}$  can be calculated directly from  $\nabla_a \mathbf{v}$ .

Figure 5.2 shows a number of snapshots from the simulation with the particles coloured by the vorticity. The vorticity range has been clipped between  $\pm 5$  in order to show the vortex structure at later times. Figure 5.2 shows the evolution of the vorticity field from the initial turbulent field to the final state, a single large vortex taking up most of the domain. Note that this is an example of the most likely evolution of the turbulence field, corresponding to a strong spin-up (i.e. increase in total angular momentum) of the fluid into a single large vortex. Clercx et al. (1999) reported three main categories of evolution, the other two being a weak or delayed spin-up and no spin-up at all. This last case is characterised by having a final state consisting of a pair of vortices with opposite spin. See Section 5.4 for more details.

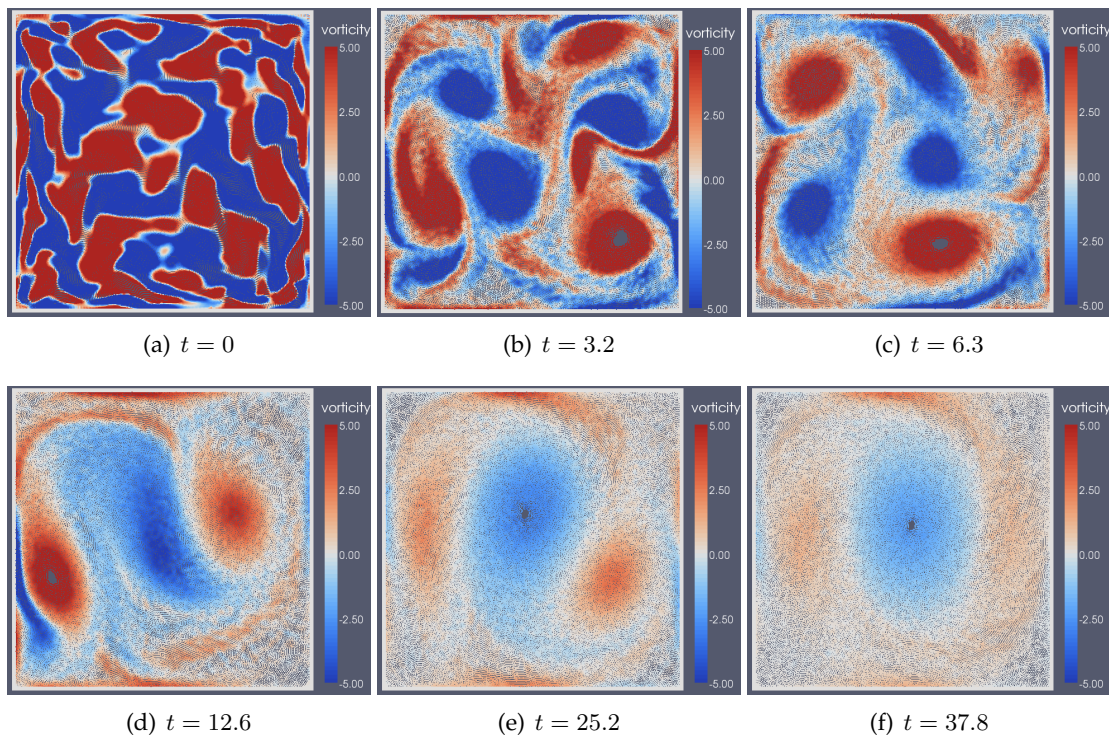


**Figure 5.2:** Evolution of a typical decaying turbulence simulation, which shows the decay of the initial turbulent vorticity field to a single large vortex. The particles are coloured by vorticity, which has been clipped to  $\pm 5$  in order to show the field at later times.

The initial evolution of the vorticity field occurs quite rapidly. Vortices usually either merge with neighbours with a similar rotation direction or are stretched out into thin vortex filaments (and ultimately erased through the action of viscosity) by vortices with an opposite spin. More rarely, a large vortex can be split by a counter-rotating vortex into two smaller but still coherent vortices. After  $t \approx 20$  the flow has settled down enough so that there are only a few vortices left, and typically one main vortex that is comparable to the size of the domain. This main vortex is also the indicator of the spontaneous increase in total angular momentum for the flow, also known as the spontaneous spin-up. Subsequent to this, the other, smaller vortices gradually fade away until only the single,

large vortex remains, along with the boundary layers that it excites along the surrounding walls.

Most of these snapshots show strong boundary layers being generated by vortex interactions with the walls. These are lifted away from the boundary to form vortex filaments. However, these are generally short-lived and do not persist as coherent vortices. In the spectral simulations by Clercx et al. (1999), the vortex filaments contributed significantly to the turbulence during the stages from  $t \approx 1$  to  $t \approx 20$ . The filaments are generated at the boundary and move into the flow to become either elongated vorticity filaments or rolled up to form a coherent vortex. This vortex would often pair up with an existing vortex to form a dipole structure. In the SPH results, the vorticity filaments are produced at the boundary and lifted away to briefly form elongated filaments before they are erased by viscosity. Very occasionally the filament would roll up to become a roughly round vortex, however these structures were always much weaker than the surrounding structures and were always quickly dissipated. Our results are therefore more similar to the periodic case, where coherent vortices are always embedded into the initial velocity field (McWilliams (1990)) and do not evolve out of the inverse energy cascade or interactions with the walls.

## 5.4 Total Angular Momentum and Spontaneous Spin-Up

Figure 5.3 shows the normalised total angular momentum  $\tilde{L}(t) = L(t)/L_n(t)$  for 12 randomly initialised simulations. The total angular momentum  $L(t)$  is normalised by  $L_n(t)$ , the angular momentum of an equivalent mass of fluid with identical kinetic energy  $E(t)$  moving in rigid body rotation (i.e.  $\tilde{L}(t) = L(t)/\sqrt{4\rho E(t)}$ ). Of the 12 simulations, 10 of them show the rapid, spontaneous spin-up that was mentioned in the previous section. The other 2 simulations show little or no spin-up (thicker purple lines). This is close to the ratio reported by Clercx et al. for their pseudospectral results. Out of 12 simulations by Clercx et al., 8 showed a strong spin-up, 2 a weak spin-up and the final 2 showed no spin-up.

This strong spin-up is the primary characteristic of turbulence in a square wall-bounded domain. Due to the square geometry of the boundary, the pressure force normal to the wall exert a net torque on the flow. The particular direction of this torque is highly dependant on the initial velocity field. We have used an initial field with an angular momentum close to zero and hence different random fields produce a spin-up in either direction. van Heijst et al. (2006) showed with experiments of decaying turbulence that simulations with a net initial angular momentum could still spin-up in either direction, although if the spin-up was in the opposite direction to the initial value then the strength of the final spin-up was reduced accordingly.

For the SPH simulations that show a strong spin-up, they generally reach an angular momentum of  $\tilde{L} = 0.6$  by  $t = 60$ . This is a slightly faster evolution than the plots given by Clercx et al. (1999), who reported that  $\tilde{L}$  typically reached 0.6 after about  $t = 100$ . If the SPH results are evolving more quickly than the pseudospectral results, this could be due to excess dissipation in the flow, or the lack of long-lived vorticity injection from the boundaries. However, the angular momentum is a very chaotic variable and Clercx only provides plots from two simulations that show a strong spin-up. So this observation could very well be biased according to the particular simulations chosen by Clercx.

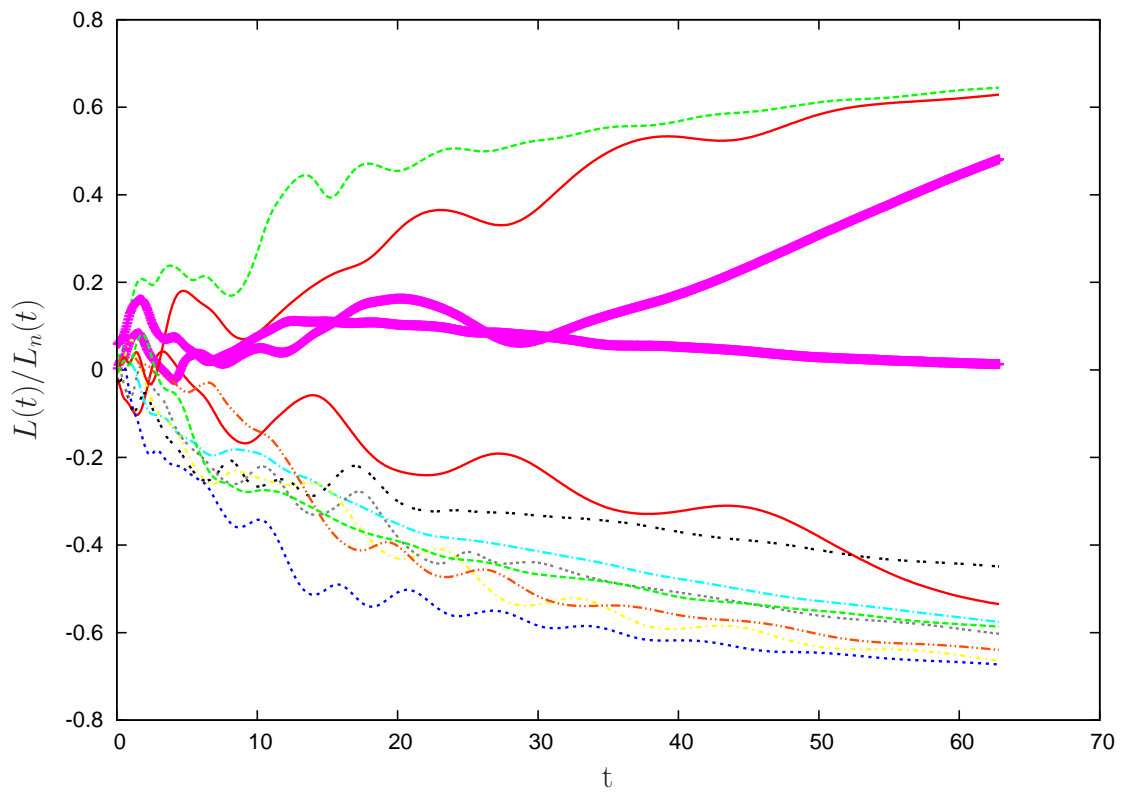


**Figure 5.3:** Each line gives the time evolution of the total normalised angular momentum for each ensemble run. The normalised angular momentum is given by  $L(t)/L_n(t)$ , where  $L_n(t)$  is the angular momentum of an equivalent mass of fluid with the same kinetic energy  $E(t)$  moving in rigid body rotation. That is,  $L_n(t) = \sqrt{4\rho E(t)}$

Figure 5.4 shows the vorticity evolution for one of the SPH simulations that showed little or no spin-up. As is characteristic of these cases, instead of evolving into a single monopole vortex the initial turbulence instead decays to a dipole vortex structure. This is seen most clearly in the snapshot at  $t = 25.2$ . There is still obviously a stronger vortex of the two, but the dipole structure persists long enough to only cause a weak spin-up. Looking back at the angular momentum plots in Figure 5.3, this vorticity evolution corresponds to the thick purple  $\tilde{L}(t)$  plot that shows no spin-up until  $t = 30$  when  $\tilde{L}(t)$  suddenly starts to increase. At this time the weaker vortex of the dipole dissipates, allowing the remaining vortex to induce the spontaneous spin-up.

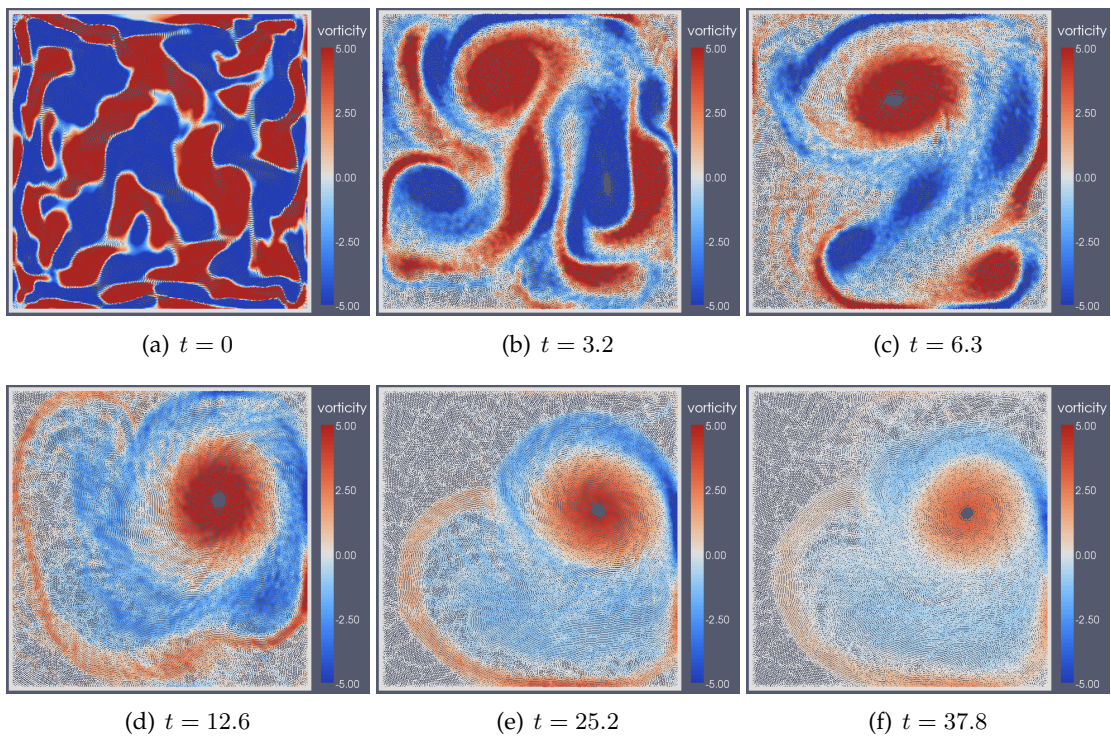


**Figure 5.4:** Evolution of a decaying turbulence simulation that shows the rarer case where there is no spontaneous spin-up of the fluid.

## 5.5 Kinetic Energy Decay

Figure 5.5 shows the variation of total kinetic energy with time. This ensemble statistic is calculated by averaging over the 12 different simulation runs. The total kinetic energy  $E(t)$  is then normalised by the initial kinetic energy  $\tilde{E}(t) = E(t)/E(0)$ . For reference, the initial kinetic energy is  $E(0) = 2000$ .

After an initial rapid decrease in kinetic energy from  $t = 0$  to  $t \approx 20$ , the kinetic energy decay levels off into an approximately exponential decay over time. This exponential decay in the kinetic energy occurs with the formation of the large monopole or dipole vortex and allows this vortex structure to persist over a much greater period of time than the initial turbulent flow. The evolution of  $E$  for the SPH simulations is similar to that reported by Clercx et al. (1999). For  $Re = 1500$ , their pseudospectral results showed a

decay from  $\tilde{E} = 1$  to  $\tilde{E} = 0.001$  over approximately 60 time units. This is consistent with the SPH results.

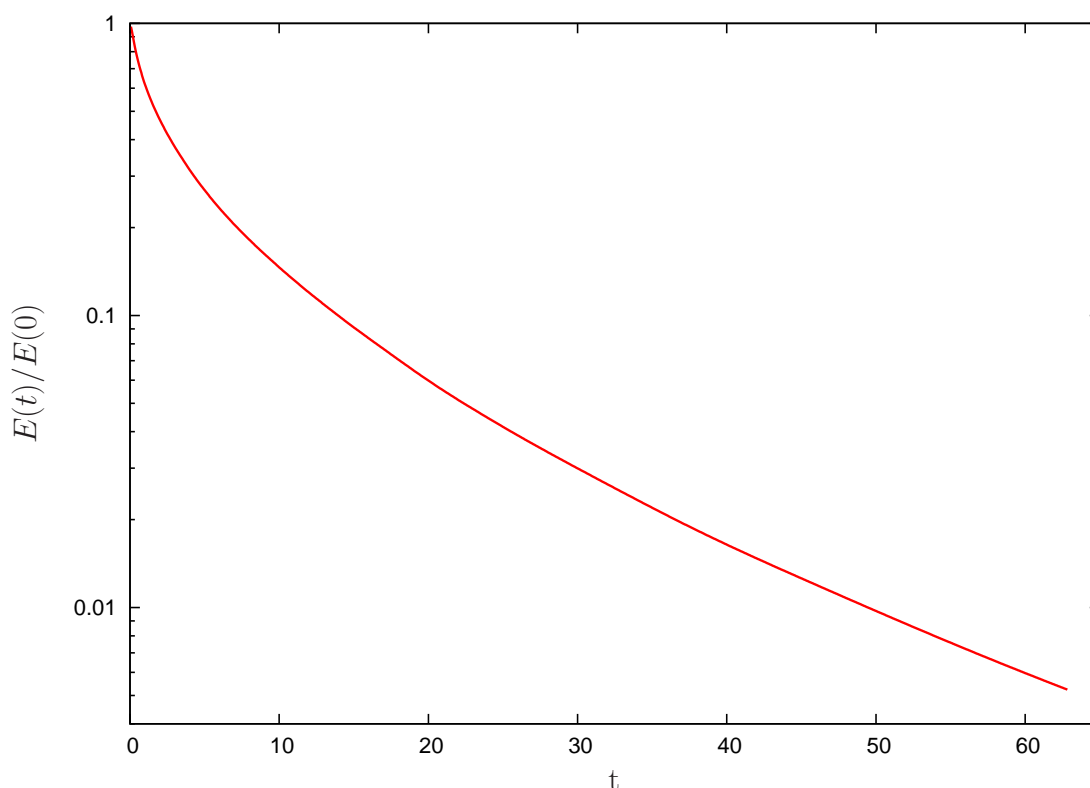


**Figure 5.5:** Ensemble average of total normalised kinetic energy for all 12 decaying turbulence simulations.

## 5.6 Average Wavenumber Decay

In Fourier or wavenumber space the total enstrophy  $\Omega(t)$  is related to the kinetic energy spectrum by

$$\Omega(t) = \frac{\pi^2}{L^2 M} \int_0^\infty k^2 E(k) dk. \quad (5.6.1)$$

where  $E(k)$  is the kinetic energy at the wavenumber  $k$  (defined such that the wavelength of each mode is  $\lambda = \frac{2L}{k}$ ) and  $M$  is the total mass. It is reasonable to define an "average" squared wavenumber  $\langle k^2 \rangle$  as (Clercx et al. (1999))

$$\langle k^2 \rangle = \frac{\Omega(t)}{E(t)} \sim \frac{\int_0^\infty k^2 E(k) dk}{\int_0^\infty E(k) dk} \quad (5.6.2)$$

This variable is an indication of the average squared size of the eddies present in the turbulence. Taking an ensemble average of the average wavenumber over all 12 SPH simulations gives the plot shown in Figure 5.6. Also shown in this plot are two reference

lines. Clercx et al. (1999) found that the decay in  $\langle k^2 \rangle$  was approximately  $t^{-0.63}$  from  $t \approx 0.7$  to  $t \approx 10$ . This scaling is depicted by the lower, violet reference line. The decay in  $\langle k^2 \rangle$  for the SPH simulation is slightly less than this over the same time period, indicating that the evolution of the kinetic energy into larger and larger vortex structures is slower for the SPH simulations. In other words, the strength of the inverse energy cascade is weaker.

After  $t \approx 20$  the turbulence in the SPH simulation clearly enters a different evolutionary stage. Leading up to this time, over  $10 < t < 20$  the decay in the average wavenumber begins to level off. At  $t \approx 20$  this trend is suddenly reversed and  $\langle k^2 \rangle$  resumes decaying. After this time a significant amount of fluctuation is introduced to the plot of  $\langle k^2 \rangle$ . The rate of decay for  $t > 20$  is approximately  $t^{-0.5}$ , as shown by the higher, green reference line.

This sudden change in  $\langle k^2 \rangle$  signals the formation of the large monopole vortex that is the typical end-state of these simulations. The interesting point to make about the dominant "kink" in  $\langle k^2 \rangle$  is that it is not smoothed out due to the ensemble averaging over the 12 simulations. All these simulations have different initial velocity fields that lead to quite different evolutions for the turbulent flow. As we have already noted, the coherent vortices and hence the germination of the large monopole vortex is always embedded in this initial velocity field. It is therefore interesting that this vortex (or the dipole vortex in the case of no spin-up) is formed at approximately the same time in each simulation, and its effect on the average wavenumber of the flow is so consistent across the ensemble simulations.

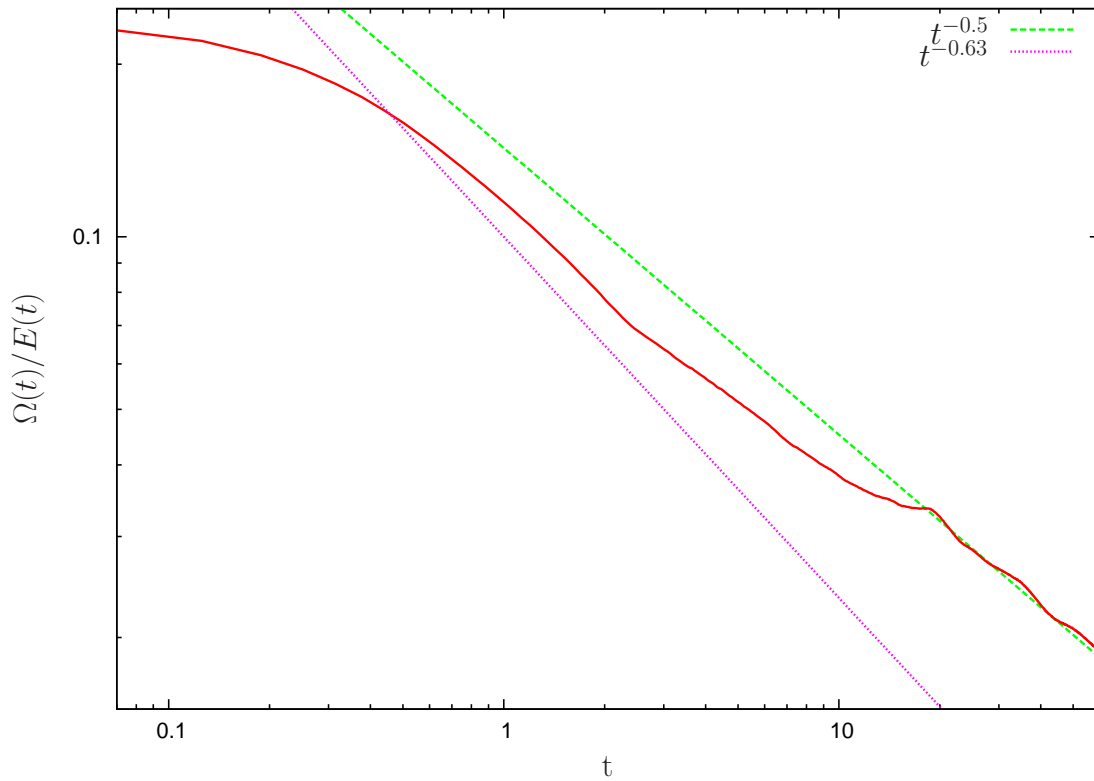
Returning to the comparison with the pseudospectral results, the plot of  $\langle k^2 \rangle$  from Clercx et al. (1999) shows very similar behaviour at  $t \approx 20$ . It is difficult to determine from the plot in this paper, but the rate of decay of  $\langle k^2 \rangle$  for  $t > 20$  seems very similar to the SPH results.

## 5.7 Convergence Study

The numerical method SPH is based on both the integral interpolant (Equation 2.1.1) and the summation interpolant (Equation 2.1.2). The integral interpolant has a second order accuracy with the smoothing length  $\mathcal{O}(h^2)$ . The accuracy of the summation interpolant is more complicated and depends on the distribution of the particles and hence the dynamics of the flow.

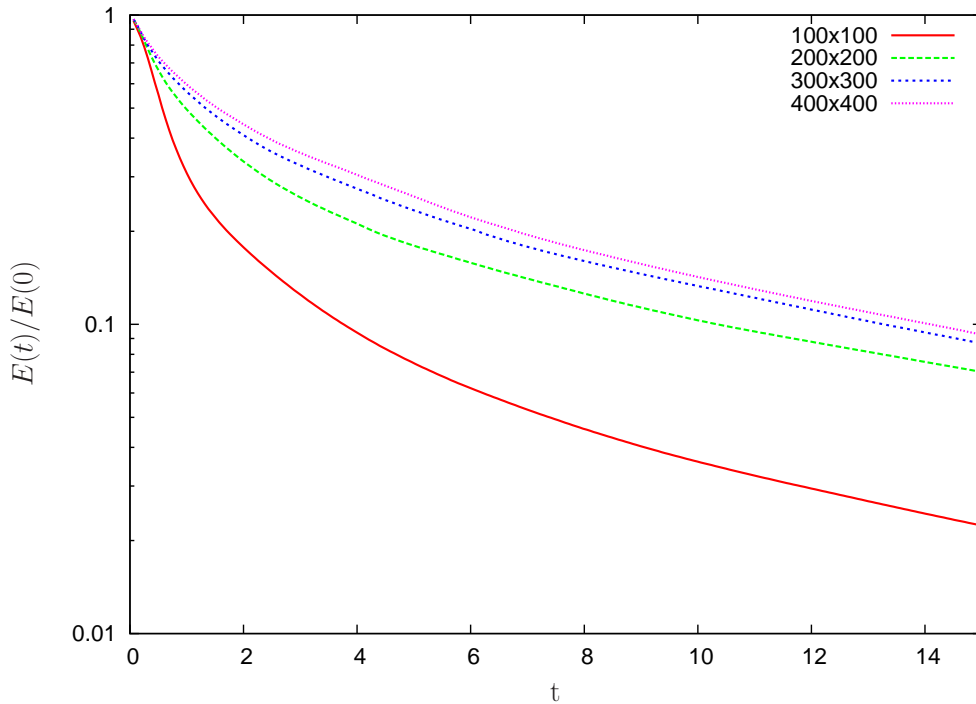
When performing a convergence study using SPH, it is important to vary both the number of particles used in the simulation, as well as the ratio of smoothing length to particle spacing  $h/\Delta p$ . Increasing the number of particles while keeping  $h/\Delta p$  constant decreases the smoothing length  $h$ , which increases the accuracy of the integral interpolant while keeping the error due to the summation interpolant constant. Of course, if it is this latter error that is dominating the solution, increasing the number of particles while keeping  $h/\Delta p$  fixed will have little effect on the solution.

Figure 5.7 shows the kinetic energy decay for a few different resolutions. The ratio of smoothing length to particle spacing  $h/\Delta p$  is kept constant at 1.95 (all other SPH parameters, including the Reynolds number, are also kept constant). At the lowest resolution



**Figure 5.6:** Ensemble average of  $\Omega(t)/E(t)$  (solid red line), where  $E(t)$  is the total kinetic energy and  $\Omega(t)$  is the total enstrophy. This gives an estimate of the mean squared wavenumber  $\langle k^2 \rangle$ . The higher dashed green reference line shows the average slope of the SPH results for  $t > 20$ , the lower dashed violet reference line shows the scaling reported by Clercx et al. (1999) over the time period  $0.7 < t < 10$ .

the accuracy of the simulation is poor and there is a substantial amount of numerical dissipation. As the resolution is increased, this dissipation is reduced and once the number of particles has increased beyond 300x300 there is no longer a significant change in the results, indicating that the solution (or at least this particular variable of the solution) has converged.



**Figure 5.7:** Decay of total normalised kinetic energy  $\tilde{E}(t)$  from the same initial velocity field for different resolutions.  $h/\Delta p$  is kept constant.

Figure 5.8 shows the long-term kinetic energy decay for increasing values of  $h/\Delta p$ . In each simulation the number of particles is also altered in order to keep  $h$  constant at 0.013. This keeps the accuracy of the integral interpolant constant while varying the error for the summation interpolant. Using a value of  $h/\Delta p = 1.3$  (a commonly used value in the SPH literature), the long term decay of kinetic energy is significantly enhanced due to the excess dissipation caused by a noisy velocity field. However, setting  $h/\Delta p \geq 1.4$  dramatically reduced this error and brought the results more into line with the pseudospectral kinetic energy decay rate.

For  $h/\Delta p \geq 1.4$ , the long term evolution of the total kinetic energy does not converge to a single decay rate. This is due to the chaotic nature of the decaying turbulence. While all the simulations have an identical initial velocity field, the variations in particle number and  $h/\Delta p$  causes each simulation to evolve into a different flow. In a similar manner to the angular momentum results shown in Section 5.4, some simulations experience a strong spin-up while others only have a weak spin-up.

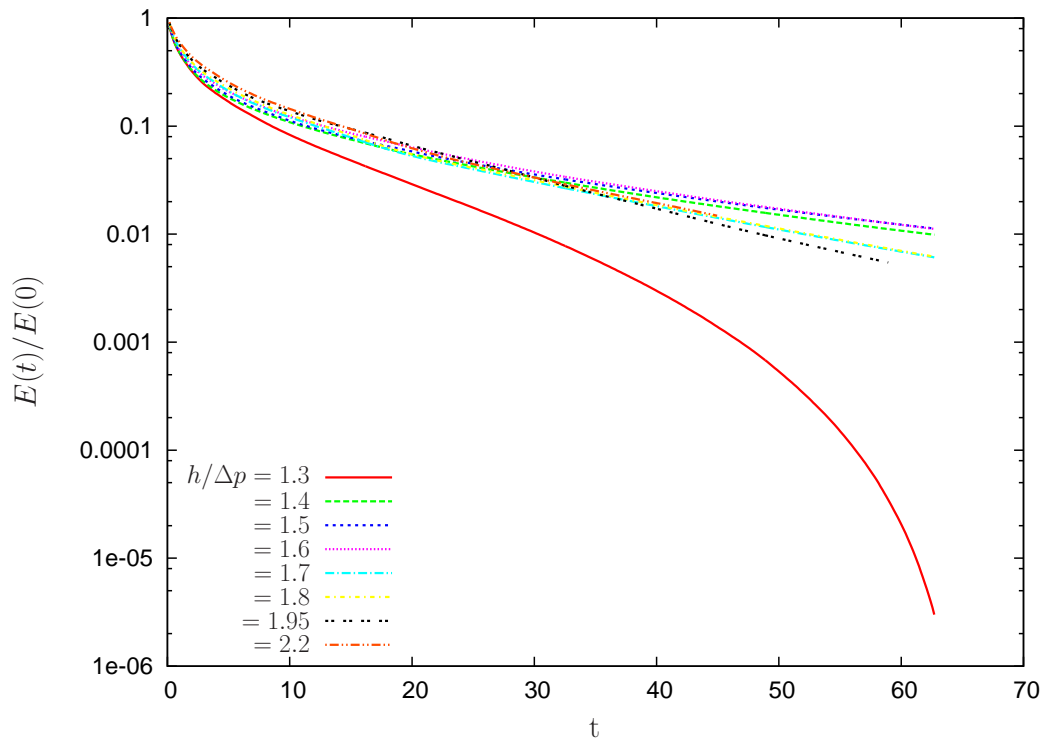


**Figure 5.8:** Decay of total normalised kinetic energy  $\bar{E}(t)$  from the same initial velocity field for different values of  $h/\Delta p$ . The smoothing length  $h$  is kept constant.

## 5.8 Discussion

The SPH results for decaying turbulence show a good agreement with all of the quantitative results from Clercx et al. (1999). The decay of kinetic energy and the likelihood of a spontaneous spin-up match well. The evolution of the angular momentum shows that this spin-up seems to occur more rapidly for the SPH results. However, this is countered by the decay of the average squared wavenumber  $\langle k^2 \rangle$  which shows a clear phase change at  $t \approx 15$  which signals the formation of the final state for the turbulent decay. Clercx et al. (1999) shows an identical phase change at the same time.

The most significant difference between the two simulations are qualitative in nature. Clercx et al. (1999) emphasises the importance that the boundaries play in injecting high intensity vorticity gradients into the flow. Clercx shows that these vorticity filaments can roll up and persist for long times, travelling far into the interior of the flow as coherent vortices. This has been confirmed in both numerical experiment and experimental results. In the SPH simulations strong boundary layers were generated at the boundaries in a similar manner to that described by Clercx. However, once these were lifted away from the wall they quickly dissipated without forming coherent vortices. This problem is investigated in more detail in Section 6.6, which shows the results of an SPH simulation of forced turbulence driven by the generation of vorticity filaments from the boundary. The results are compared against a experiment performed by Wells et al. (2007)

However, the lack of the correct long-term evolution of the vorticity filaments generated from the boundaries seems to have little impact on the ensemble statistics of the decaying

turbulence. This is counter to the arguments by Clercx et al., but may only apply for the particular case of decaying turbulence. The next chapter details SPH simulations of continually forced turbulence in a square box, the results of which do not agree either qualitative or quantitatively with Clercx's pseudospectral simulations.

## Chapter 6

# Forced Turbulence Simulations

---

This chapter describes SPH simulations of forced two-dimensional turbulence in a wall-bounded domain. The geometry is identical to the simulations of decaying turbulence shown in the previous chapter, a square box of fluid surrounded by no-slip boundaries. However, for these simulations the velocity field is set to zero at  $t = 0$  and energy is continually injected into the fluid via the addition of a forcing term to each particles' momentum equation.

The setup of these SPH simulations and the form of the forcing term were chosen to match the pseudo-spectral simulations by Molenaar et al. (2004) (these results also appear in Molenaar (2004), Clercx et al. (2005) and van Heijst et al. (2006)). These simulations use a spectral method based on Chebyshev polynomials with a semi-implicit Adams-Bashforth Crank-Nicolson time integration scheme. This method is used to obtain a solution for the two-dimensional vorticity equation with the addition of an external stochastic forcing term  $Q$

$$\frac{\partial \omega}{\partial t} + (\mathbf{v} \cdot \nabla) \omega = \frac{1}{Re} \nabla^2 \omega + Q. \quad (6.0.1)$$

Molenaar et al. (2004) found that the combination of a strong inverse energy cascade and the torque exerted on the fluid by the square boundaries quickly evolved the turbulent flow into a single large monopole vortex with the same length scale as the domain. This vortex persisted for long periods of time (in the order of 100's of time units) before suddenly breaking up due to the injection of high amplitude vorticity filaments produced from the boundary layers. However, the turbulence quickly organised itself into a single vortex again, spinning in the same or opposite direction as the original. This breakup and reformation would typically last about 5-15 time units. Figure 6.1 shows a sample of the vorticity plots obtained by Molenaar et al. (2004) at  $Re = 3000$ . They show the single large vortex at one time instant, the breakup of this vortex and then the subsequent reformed vortex spinning in the opposite direction.

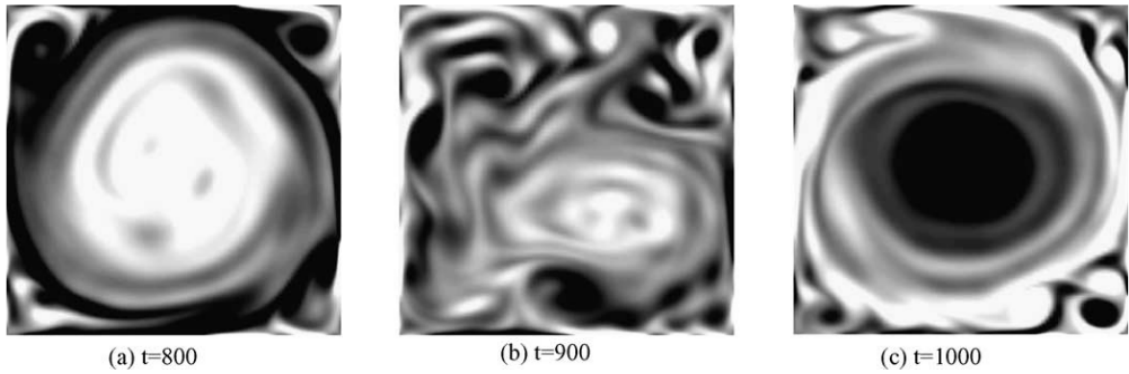


**Figure 6.1:** Vorticity distribution showing an example of the single large vortex structure that was found by Molenaar et al. (2004) in their pseudo-spectral simulations of forced 2D bounded turbulence. (a) the vortex (b) sudden breakdown of the vortex (c) newly reformed vortex spinning in the opposite direction.

## 6.1 Simulation Setup

We have reproduced the parameters of the simulation described in Molenaar et al. (2004). There is a slight inconsistency between the timestep reported in Molenaar’s PhD thesis ( $\Delta t = 3.4 \times 10^{-4}$ ) and this paper ( $\Delta t = 4 \times 10^{-4}$ ). We have used the value reported in the PhD thesis, however this is not expected to change the results.

### 6.1.1 Forcing Protocol

The forcing term used by Molenaar et al. (2004) acts on a very narrow range of vorticity modes ( $|\mathbf{k}| \in [7, 9]$ , where the wavenumber  $k$  has a wavelength of  $\lambda = \frac{2L}{k}$ ). This term has a complex amplitude  $a_{\mathbf{k}}$  which is evolved in time using a random walk first proposed by Lilly (1969).

$$a_{\mathbf{k}} = A\sqrt{1 - \sigma^2}e^{i\pi g_{\mathbf{k}}} + \sigma a_{\mathbf{k}-1}, \quad (6.1.1)$$

where  $A$  is a constant that determines the strength of the forcing and  $g_{\mathbf{k}}$  is a random variable sampled at each timestep from a Gaussian distribution with zero mean and a standard deviation of one. For all the forced simulations described in this chapter, the input forcing amplitude is set to  $A = 6$  to match the simulation by Molenaar et al. (2004).

Lilly describes this random walk as an approximation to the following stochastic differential equation

$$\frac{\partial a_{\mathbf{k}}}{\partial t} = -\frac{a_{\mathbf{k}}}{\tau} + \lim_{\Delta t \rightarrow 0} \frac{\hat{a}_{\mathbf{k}}}{\sqrt{\tau \Delta t/2}}, \quad (6.1.2)$$

where  $\hat{a}_{\mathbf{k}} = Ae^{i\pi g}$  and  $\sigma$  is assumed to be close to but less than 1. The constant  $\tau$  is related to the timestep  $\Delta t$  by

$$\frac{\tau}{\Delta t} = \frac{1}{2} \left( \frac{1 + \sigma}{1 - \sigma} \right). \quad (6.1.3)$$

While  $\partial a_{\mathbf{k}}/\partial t$  becomes singular as  $\Delta t \rightarrow 0$ ,  $a_{\mathbf{k}}(t)$  itself is well behaved and is given by integrating Equation 6.1.2

$$a_{\mathbf{k}}(t) = e^{-t/\tau} \left[ a_{\mathbf{k}}(0) + \int_0^t \lim_{\Delta t \rightarrow 0} \frac{\hat{a}_{\mathbf{k}}(t')}{\sqrt{\tau \Delta t/2}} e^{t'/\tau} dt' \right], \quad (6.1.4)$$

Thus,  $\tau$  is the decay time of  $a_{\mathbf{k}}$ . In order to ensure that the decay time is independent of the timestep  $\Delta t$ ,  $\sigma$  is calculated using

$$\sigma = \frac{1 - \Delta t/2\tau}{1 + \Delta t/2\tau}, \quad (6.1.5)$$

which is simply a rearrangement of Equation 6.1.3.

In his forced simulations, Molenaar et al. (2004) set the forcing correlation term  $\sigma$  to  $\sigma = 0.98$  and had a timestep equal to  $\Delta t = 3.4 \times 10^{-4}$ . This corresponds to  $\tau = 0.01683$ , which is the value used in all the simulations in this chapter.

The applied forcing term to SPH particle  $a$  is denoted by  $\mathbf{F}_a$ , and is added to the momentum equation for each particle

$$\frac{D\mathbf{v}_a}{Dt} = - \sum_b m_b \left( \frac{P_b}{\rho_b^2} + \frac{P_b}{\rho_b^2} + \Pi_{ab} \right) \nabla_a W_{ab} + \mathbf{F}_a. \quad (6.1.6)$$

$\mathbf{F}_a$  is found by sampling from a forcing field  $\mathbf{F}(\mathbf{r})$  (ie.  $\mathbf{F}_a = \mathbf{F}(\mathbf{r}_a)$ ). This forcing field is calculated by summing the contributions from each of the forcing modes  $|\mathbf{k}| \in [7, 9]$ . Each forcing mode has a complex mode amplitude with amplitude  $\mathbf{C}_{\mathbf{k}}$  and phase  $\phi_{\mathbf{k}}$ .  $\mathbf{F}(\mathbf{r})$  is therefore given by

$$\mathbf{F}(\mathbf{r}) = \sum_{|\mathbf{k}| \in [7,9]} \mathbf{C}_{\mathbf{k}} \sin \left( \frac{\pi}{L} \mathbf{k} \cdot \mathbf{r} + \phi_{\mathbf{k}} \right), \quad (6.1.7)$$

where  $L$  is the half width of the box. Since  $\mathbf{F}(\mathbf{r})$  is required to be divergence-free, the form of  $\mathbf{C}_{\mathbf{k}}$  is chosen to be

$$\mathbf{C}_{\mathbf{k}} = B_{\mathbf{k}} \begin{pmatrix} k_y \\ -k_x \end{pmatrix}, \quad (6.1.8)$$

where  $k_x$  and  $k_y$  are the two components of the wavenumber vector  $\mathbf{k}$ .

Molenaar et al. (2004) applied the forcing field  $Q(\mathbf{r})$  to the scalar vorticity field. Using the complex mode amplitudes  $a_{\mathbf{k}}$  calculated from the random walk given previously in

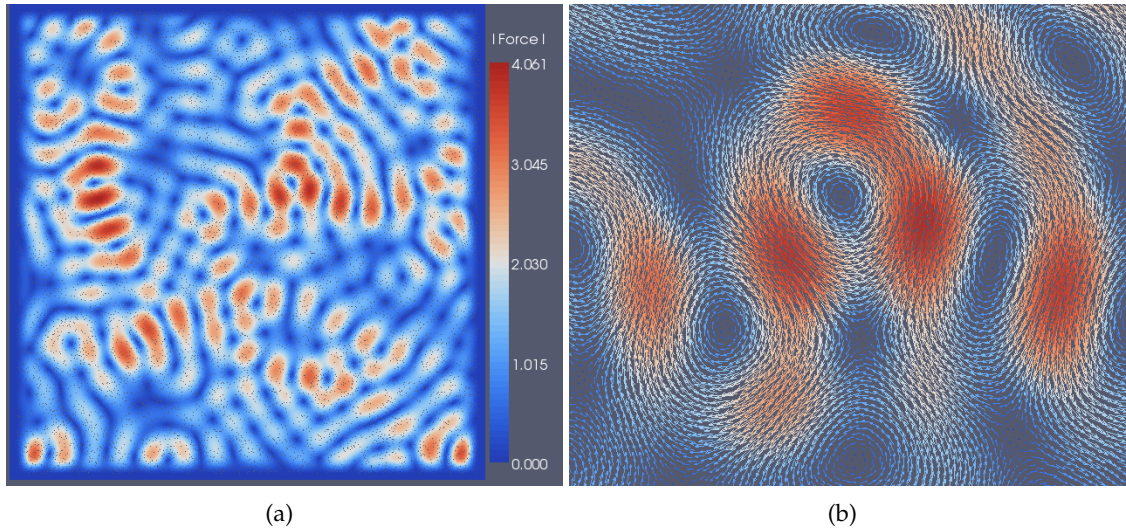
Equation 6.1.1,  $Q(\mathbf{r})$  is defined as

$$Q(\mathbf{r}) = \sum_{|\mathbf{k}| \in [7,9]} a_{\mathbf{k}} \cos\left(\frac{\pi}{L} \mathbf{k} \cdot \mathbf{r}\right). \quad (6.1.9)$$

The relationship between this vorticity forcing field and the SPH velocity forcing field  $F(\mathbf{r})$  is given by  $Q(\mathbf{r}) = \nabla \times F(\mathbf{r})$ . Combining this with Equations 6.1.7, 6.1.8 and 6.1.9 allows the calculation of the SPH mode amplitudes  $B_{\mathbf{k}}$  from the vorticity amplitudes  $a_{\mathbf{k}}$

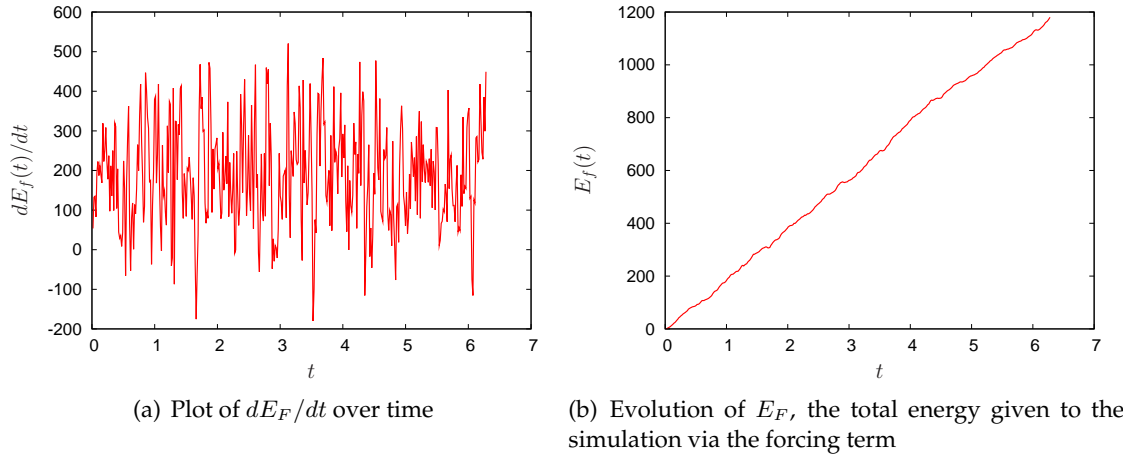
$$B_{\mathbf{k}} = \frac{a_{\mathbf{k}} L}{\pi |\mathbf{k}|^2}. \quad (6.1.10)$$

Figure 6.2 shows an example of the generated forcing field  $\mathbf{F}(\mathbf{r})$ . Figure 6.2(a) shows the entire domain with the particles coloured by the magnitude of the forcing term, while Figure 6.2(b) shows a zoomed in picture with the particles represented by vectors that are scaled and orientated using  $\mathbf{F}_a$ .



**Figure 6.2:** Example of the instantaneous forcing term  $\mathbf{F}_a$ . (a) Entire domain. Particles are coloured by the magnitude of the forcing term. (b) Close up. Forcing term vectors are scaled and coloured by the magnitude of the forcing term.

One disadvantage of this particular forcing term is that it does not ensure a constant power input over time. For example, Mansour (2007) uses a forcing term that enforces a constant power input. Figure 6.3(a) shows a plot of  $dE_F/dt = \sum_a \mathbf{F}_a \cdot \mathbf{v}_a$ , which is the total power input to the simulation by the forcing term  $\mathbf{F}$ . As can be seen, the variance of this term is quite significant. However,  $dE_F/dt$  is a stationary process with a constant mean and hence  $E_F$  has a relatively constant time derivative over large enough time scales. The primary time scale of the turbulence is the vortex turn over time  $T = l/U = 1.27$ . Figure 6.3(b) shows that the slope of  $E_F$  is constant over this time scale.



**Figure 6.3:** This particular forcing term does not provide for a constant power input. However over a time scale equal to the vortex turn over time  $T = l/U = 1.27$  the variation of the total power input with time has an approximately constant slope

### 6.1.2 Resolution Requirements

The Reynolds number of the forced turbulence simulations cannot be set in advance because we do not have a characteristic velocity for the flow, only the strength and decay time of the forcing term. However, once the simulation has been performed and the turbulence has reached a statistically steady state, the average RMS velocity of the flow can be used to estimate a Reynolds number.

For all the results presented in this chapter, the input viscosity was set to  $\nu = 5 \times 10^{-4}$ , which matches the viscosity used by Molenaar et al. (2004). Once the simulation has reached a statistically steady state, the final RMS velocity was found to be  $U = 0.79$ . Using this characteristic velocity and the half-width of the box  $L = W/2$  as the characteristic length scale  $l$  gives a Reynolds number of  $Re = 1581$ .

The dissipation length scale for this case is

$$\eta = \frac{l}{\sqrt{Re}} = \frac{W}{79}. \quad (6.1.11)$$

Using a resolution of 300x300 particles and  $h/\Delta p = 1.95$  means that the smoothing length is equal to  $h = W/154$ , which is double the required resolution. For comparison, Molenaar et al. (2004) uses 161 Chebychev modes in the pseudospectral forced turbulence simulations, which is roughly comparable to the SPH resolution. Using 300x300 particles, we are able to resolve mode 150 without aliasing.

### 6.1.3 Other Parameters

The geometry and SPH code used for this simulation are identical to those used in the decaying turbulence simulations, except that the Wendland kernel was used instead of the Cubic Spline. The benefits of this choice will be explored in Chapter 7.

The reference density was set to  $\rho_0 = (995/1000)\rho$  (where  $\rho = 1000$ ), in order to induce a constant positive pressure and reduce some of the particle voids that occurred at the centre of high amplitude vortices. Some voids still remain, but are not expected to contribute significantly to the simulation, as strong vortex centres tend to be isolated from the rest of the flow.

The characteristic maximum velocity (used to set the SPH pressure scale) was set to  $v_m = 2.0$ , which corresponds to a sound speed of  $c_s = 20.0$ .

## 6.2 Initial Results

This section describes the results of the forced turbulence simulation, comparing them to the pseudo-spectral simulations of Molenaar et al. (2004) as well as the theoretical predications for homogeneous 2D turbulence that were explained in Chapter 4.

### 6.2.1 Vorticity Evolution

Figure 6.4 shows a number of snapshots from the simulation with the particles coloured by vorticity. Initially all the eddies have sizes comparable to half the forcing term length scale and the vorticity field looks similar to a regular array of vortices. The movement of the fluid starts slowly at first and it is clear that the particles are moving under an artificial force. From  $0 < t < 3$  vorticity filaments grow out from each vortex and start linking up neighbours with similar signs. At this point, some of the vortices have tripled in size and many have become very elongated. From  $3 < t < 15$  the vortices continue to grow in size and long filaments of vorticity become more common. The length of these filaments also continue to grow, at times reaching half of the box width. During this time the movement of the particles has become more natural and "fluid-like" and the effects of the forcing term become less clear as time goes on.

Over  $15 < t < 30$  the average scale of the vortices and filaments continue to grow, but at a slower pace. The turbulent vortices continually create strong boundary layers at the walls, which are subsequently lifted and advected away from the wall. The fate of these vorticity structures are difficult to distinguish, as the flow is not made up of stable and long-lived coherent vortices as in the case of the decaying turbulence. Rather, most of the vortices are constantly being stretched, folded, merged or ripped apart by other vortices or the forcing term. It is perhaps more accurate to call them turbulent eddies rather than vortices. But it is clear to see that the boundary layers formed at the walls interact with and directly evolve the turbulent flow in the interior. Once the boundary layer is lifted away from the wall it is either merged into an existing eddy (causing it to become more energetic) or the boundary layer is rolled up to form a new eddy, which can persist for many turn-over times.

After  $t \approx 30$  the apparent growth in the average length scale of the eddies and filaments seems to level off. This simulation has been run until  $t \approx 375$ , and there is no substantial change to the nature of the vorticity field up to this point. There is certainly no further self-organisation of the flow into the single large monopole vortex reported by Molenaar et al. (2004). Using their pseudospectral simulations, Molenaar et al. reported that the

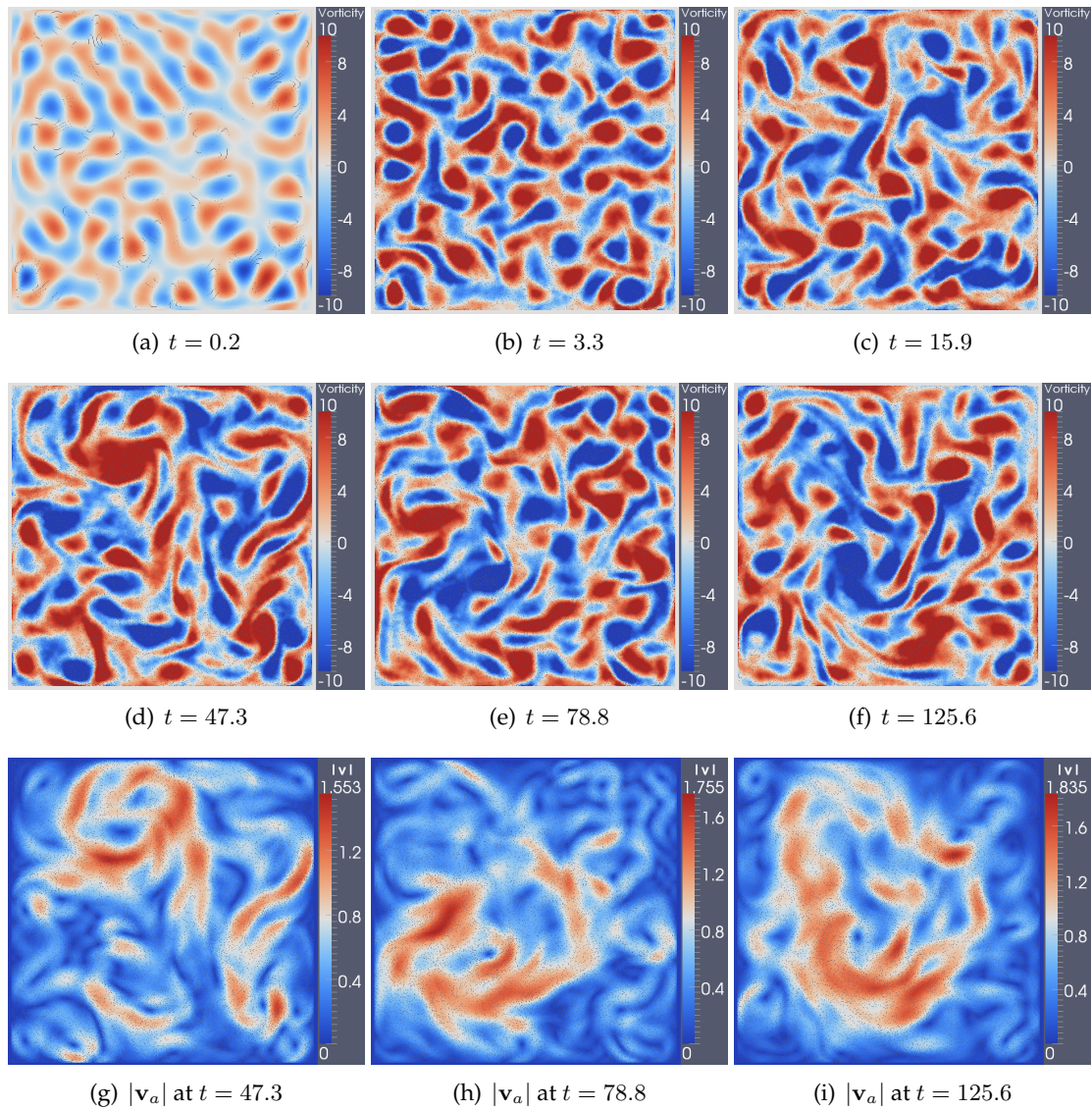


**Figure 6.4:** Evolution of a typical forced turbulence simulation. Plots (a)-(f) show particles coloured by vorticity, which has been clipped to  $-10 \leq \omega \leq 10$  in order to clearly show the vortex structures of the flow. Plots (g)-(i) show the magnitude of the particle's velocity

flow had organised itself into a single domain-filling vortex by  $t = 10$  (Figure 6.1 contains two typical examples of this vortex) and that this structure persisted for long times (ranging from 50-500 time units).

However, the flow in the SPH simulation does continue to evolve after  $t \approx 30$ . Around this time the velocity magnitude field is usually comprised of three or four separately rotating sections. This is difficult to see in the vorticity field as each rotating section is comprised of a number of eddies, but is more apparent in the velocity magnitude plots shown in 6.4(g), (h) and (i). From  $30 < t < 70$  the velocity field continues to evolve in a chaotic fashion. The sections dissipate, reform and interact with each other, but at any one instant there are usually three or four dominant structures. The flow suddenly changes at around  $65 < t < 70$ , when suddenly a single large velocity structure appears. This structure evolves in size and shape but continues as a coherent structure for the remainder of the simulation. Its size dominates the flow domain, initially taking up  $\frac{1}{2} \times \frac{1}{2}$  of the box, but growing over time until it levels out at about  $\frac{2}{3} \times \frac{2}{3}$  of the domain (this occurs at about  $t \approx 100$ )

The scale of the vorticity field associated with this large velocity structure is quite different. While it is clear that there is a dominate vorticity eddy located near the centre of the structure, its size is typically only  $\frac{1}{5} \times \frac{1}{5}$  of the domain size. The other vorticity eddies located within the velocity structure orbit this primary eddy in a manner similar to a rigid body rotation. This does not mean that these eddies are fixed or coherent in nature, they continue to evolve and interact with each other over time.

### 6.2.2 Energy Budget

Figure 6.5 shows the energy budget (See Section 2.9) for the forced turbulence SPH simulation. Plot (a) shows the energy evolution during  $0 < t < 3$ . At this time the turbulent flow has yet to develop and the motion of the particles is heavily correlated to the action of the forcing term. At first all the energy from the forcing term is transferred to the kinetic energy of the particles. Once the particles start moving and generating viscous stresses, the increase in kinetic energy slows and most of the forcing term power is dissipated through the viscous term. Plot (b) shows the contributions of the forcing and viscous term to the total energy over the entire simulation. The vast proportion of energy input to the system by the forcing term is being dissipated by the viscous term. The gradients of both of these energy plots are almost opposite each other.

Plot 6.5(c) shows the evolution of the total kinetic energy. Almost all the energy that is not mopped up by the viscosity is transferred to the motion of the particles. The kinetic energy evolution shows three distinct phases in the simulation. From the previous section and Figure 6.4 we know that from  $t = 0$  to  $t \approx 30$  is a time of rapid growth in the average vortex size. This corresponds to the initial rapid growth in the total kinetic energy of the fluid. From  $t \approx 30$  to 180, there is not much apparent change in the vorticity field but there is a gradual but steady increase in the kinetic energy. This corresponds to the formation and growth of the large-scale velocity structure described in Section 6.2.1. However, while the size of this structure levels out at about  $t \approx 100$ , the increase in the total kinetic energy continues long after this time. After  $t \approx 180$  the kinetic energy levels off and fluctuates slowly around an average value of 1300, corresponding to an RMS velocity of  $v_{rms} = 0.8$ .

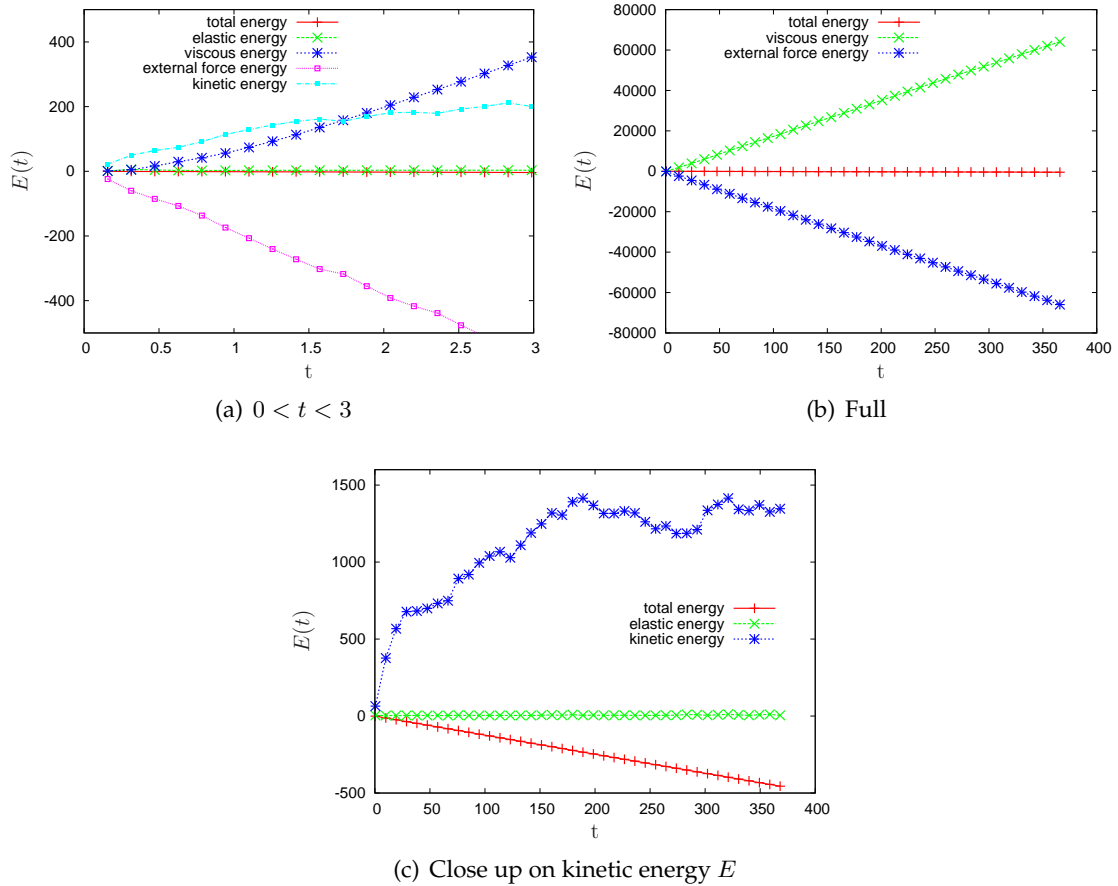


**Figure 6.5:** Energy Budget for the forced turbulence simulation. (a) shows the energies at an early time  $0 < t < 3$ . (b) shows the contributions of the forcing term and viscous term to the total energy. (c) shows the evolution of the total kinetic energy, elastic energy and the total energy. This total energy plot is the same as for (b), but the scale of this plot shows the small energy loss from the simulation over time (under 0.1% of the energy input from the forcing term). The elastic energy is approximately constant at 3.5 for the duration of the simulation.

The pseudo-spectral simulations by Molenaar et al. (2004) show a dramatically different result. Their time evolution of the total kinetic energy shows rapid fluctuations over the entire simulation ( $0 < t < 1000$ ), with rises and falls between  $E = 2250$  and  $E = 13500$  in 20 time units not being uncommon. In contrast, the SPH total kinetic energy gradually asymptotes to  $E \approx 1300$  and stays within  $\pm 200$  of this value. The average RMS velocity reported in Molenaar et al. (2004) was  $v_{rms} = 1.5$ , which corresponds to a kinetic energy of  $E = 4500$  and is significantly greater than the peak SPH kinetic energy.

Given that our forcing term and simulation setup is identical to that used by Molenaar et al. (2004), these results are disappointing but not unexpected given the absence of the large monopole vortex in the SPH simulation. The viscous dissipation in these results is significantly greater than for the pseudo-spectral simulations, which weakens the action of the inverse energy cascade. Kraichnan (1967) predicted that as long as the forcing scale was sufficiently greater than the dissipation scale, then nearly all (or exactly all in the limit of  $Re \rightarrow \infty$ ) the energy will be transferred to larger length scales, sidestepping the viscous dissipation entirely. Equation 4.1.4 states that the kinetic energy is conserved as  $\mu \rightarrow 0$ , so any input energy will only add to the total kinetic energy. Of course, this only applies to an infinite domain, and the dissipation due to the no-slip boundaries will always be a substantial contribution to the overall energy budget. In the case of the simulations by Molenaar et al., the contributions from the no-slip boundaries lead to large positive and negative fluctuations in  $E$ . In contrast, the SPH results show a much slower evolution of  $E$ . The vast majority of the energy input from the forcing term is immediately removed by the viscous term instead of being transferred to larger length scales via the inverse energy cascade.

### 6.2.3 Angular Momentum

Figure 6.6 shows the time evolution of the normalised angular momentum  $\tilde{L}(t) = L(t)/L_n(t)$ , which is normalised by the equivalent mass of fluid rigidly rotating with kinetic energy equal to  $E(t)$  (i.e.  $L_n(t) = \sqrt{E(t)4\rho}$ ). For this SPH simulation the angular momentum initially rises to a value of 0.1 at  $t \approx 40$  before falling to -0.5 by  $t \approx 100$ . Thereafter it fluctuates around this value for the remainder of the simulation.

The normalised angular momentum reported by Molenaar et al. (2004) for their pseudo-spectral simulations asymptotes to a similar magnitude. For the vast majority of their simulation  $\tilde{L}(t)$  remains near  $\pm 0.6$ . This is entirely due to the self-organisation of the turbulence into a large monopole vortex. While the SPH results do not show this single large vortex, the asymptotic behaviour of the SPH angular momentum is similar to the pseudo-spectral results.

However, the transient behaviour of the SPH angular momentum is quite different. For the pseudo-spectral simulations, random transitions between  $\tilde{L}(t) = 0.6$  and  $-0.6$  often occur (on average, once every 150 time units). The time it takes for  $\tilde{L}(t)$  to transition between 0.6 and  $-0.6$  is typically 5-15 time units. These random transitions occur during the break-up and subsequent reformation of the large monopole vortex. The initial spin-up of the fluid and the formation of the large monopole vortex occurs at  $t \approx 10$ . Comparing this with the SPH results, the initial spin-up for the SPH simulation takes 100 time units, which is significantly longer. There are no random transitions similar to that seen in the pseudo-spectral results.

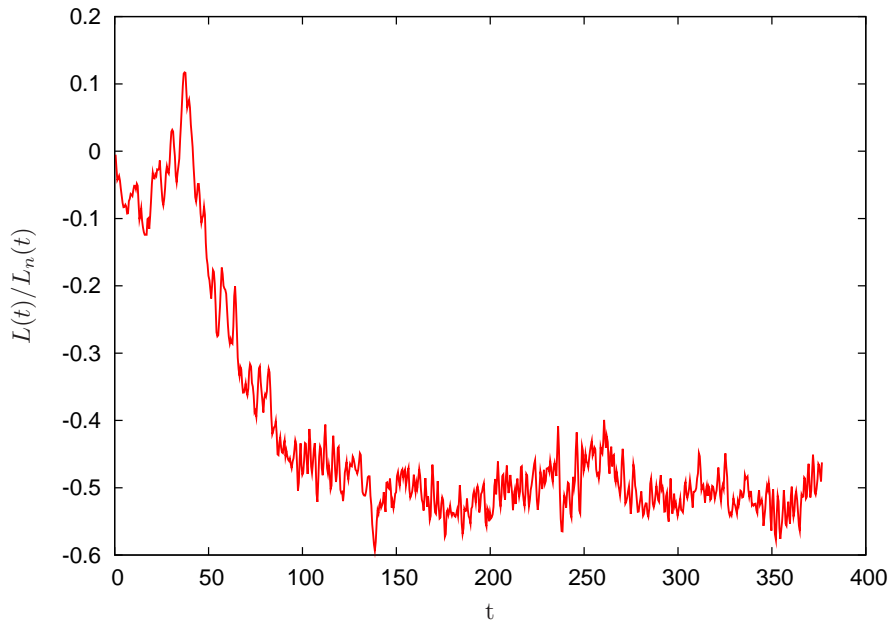


**Figure 6.6:** Normalised angular momentum for the SPH forced turbulence simulation.

#### 6.2.4 Fourier Analysis

Fourier analysis is a common method of describing a turbulent flow. Turbulence simulations are often carried out in a square box with periodic boundaries, and a significant proportion of the theoretical predictions are concerned with the scaling of various variables (e.g. kinetic energy, vorticity etc.) at different length scales. The ubiquitous Fourier transform, very efficient when using a regular grid, is more difficult to calculate when using unstructured particle positions. We are using the SPH Fourier transform proposed by Mansour (2007) and described in Section 4.5.

Figure 6.7 shows the result of applying this transform to the kinetic energy of the particles  $\frac{1}{2}m_a\mathbf{v}_a \cdot \mathbf{v}_a$  at four different times during the simulation. Since the boundary conditions for this simulation are not periodic, the kinetic energy of the particles are first normalised to a zero mean and filtered by a Hann window (described in Section 4.5). Also plotted in Figure 6.7 are two reference lines showing the expected kinetic energy scaling for length scales larger than the forcing scale (the blue dotted line plots  $k^{-5/3}$ , which is the expected scaling for length scales dominated by the inverse energy cascade) and those smaller (the green dashed line plots  $k^{-3}$ , which shows the expected scaling for the direct enstrophy cascade). The wavenumber axis on the plots is normalised by the average forcing wavenumber (i.e.  $\tilde{k} = k/8$ ). The spectra in (c) and (d) are averaged over 6.3 turn over times in order to smooth out the fluctuations that occur at smaller wavenumbers. Plots (a) and (b) are not time-averaged because the spectrum is evolving rapidly at these times.

The first spectrum is taken at  $t = 0.2$  and is dominated by a peak at  $\tilde{k} = 2$  due to the fact that the velocity field is a direct result of the forcing term rather than any turbulent dynamics. In other words, the energy injected at the forcing scale has not had enough time to distribute to the other modes. Note that this plot is the only one of the four that

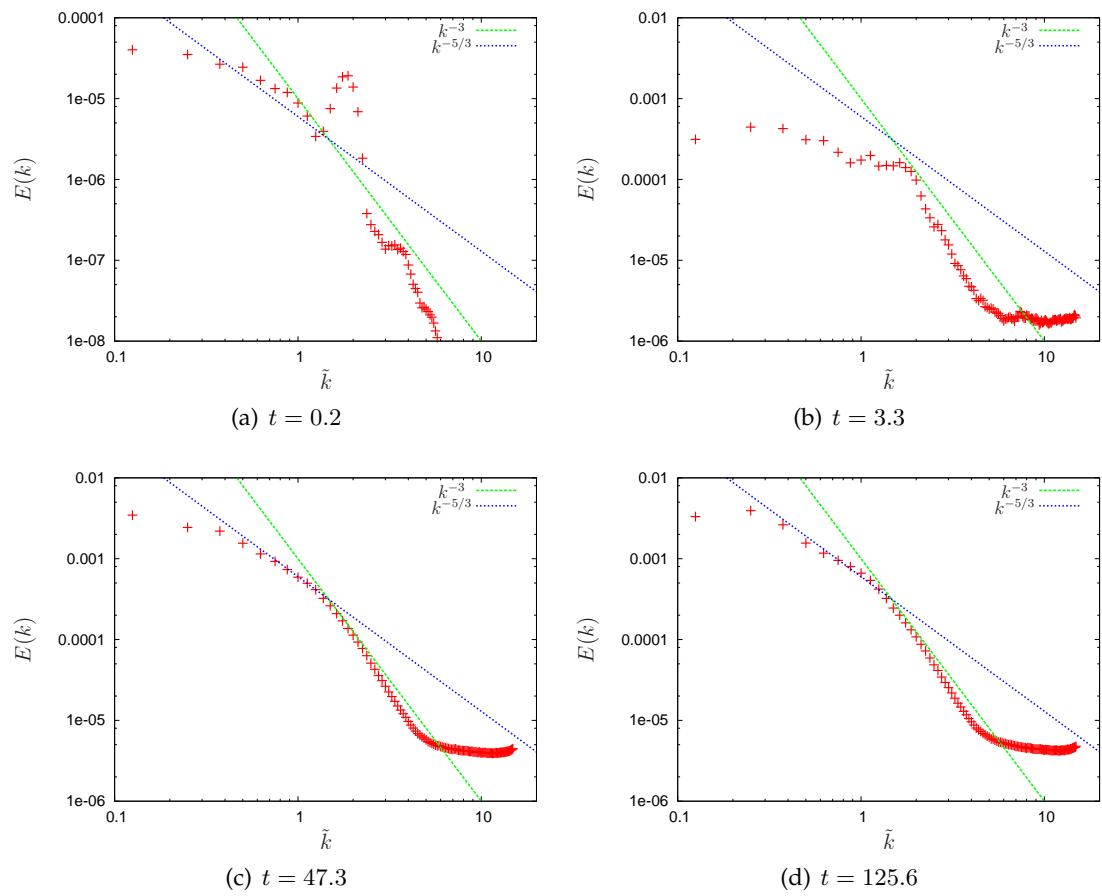


**Figure 6.7:** Evolution of the kinetic energy spectrum

uses a lower range for the y-axis as the total kinetic energy is still very small at this time.

The peak at  $\tilde{k} = 2$  quickly disappears and at  $t = 3.3$  cannot be seen at all. At this time the spectrum has shifted significantly higher due to the increased kinetic energy and the gradients above and below the forcing scale have become flatter, although the slope of the spectrum is still quite far from the expected values.

By  $t = 47.3$  the turbulence is fully developed and the spectrum is much closer to the theoretically expected scaling laws (ie. the dashed reference lines). From the forcing scale down to about  $\tilde{k} = 4.5$  the kinetic energy spectrum scales as expected, indicating that the direct enstrophy cascade is reproduced well over this range. The slope of the spectrum is slightly steeper than  $k^{-3}$ , however numerous numerical and experimental results (See Section 4.1.1) have shown the existence of such a steeper direct enstrophy range. Above  $\tilde{k} = 4.5$  (this corresponds to a length scale of  $8.3\Delta p$ , where  $\Delta p$  is the average particle spacing) the spectrum starts to flatten to approximately  $k^{-0.3}$  due to higher than expected velocity fluctuations at these length scales. Since the viscous dissipation is proportional to  $k^2\mathbf{E}(\mathbf{k})$ , these fluctuations could cause a significant excess of small scale viscous dissipation, a possibility we will return to later.

At this point it is useful to remind the reader of the results of Section 4.5, which showed that the SPH Fourier transform was accurate for  $\tilde{k} < 10$ . Therefore, it can be concluded that the velocity fluctuations seen in the kinetic energy spectrum for  $\tilde{k} > 4.5$  is a real effect and not due to the errors in the calculation of the Fourier transform.

For length scales larger than the forcing scale  $\tilde{k} < k_f$  the spectrum follows the  $k^{-5/3}$  line well until  $\tilde{k} = 0.5$ , when the gradient starts to flatten. Since we are simulating turbulence in a wall-bounded box, and not an infinite domain, it is expected that energy will build up (or condense) in the largest length scales so that the kinetic energy spectrum will diverge from the  $k^{-5/3}$  scaling for very small  $\tilde{k}$ , becoming significantly larger. However, in the case of our SPH simulation the opposite is true and the gradient of the spectrum is not even large enough to satisfy  $k^{-5/3}$ .

Over the large time period between  $t = 47.3$  and  $t = 125.6$  this situation is improved slightly, with a small amount of extra energy appearing in the larger length scales. This, coupled with the gradual increase in the total kinetic energy shown in Figure 6.5(b), indicates the presence of a weak inverse energy cascade. However, the strength of this energy flux is much weaker than expected, and the build-up of kinetic energy eventually stops due to viscous dissipation without producing the large monopole vortex that is expected for 2D bounded turbulence.

Figure 6.8 shows the spectra for kinetic energy  $\frac{1}{2}\mathbf{v} \cdot \mathbf{v}$  and viscous power  $\mathbf{f}_v \cdot \mathbf{v}$  at  $t = 47.3$  (where  $\mathbf{f}_v$  is the viscous force on each particle due to the viscous term in the momentum equation). Both these spectra have been averaged over 6.3 turn over times.

From the viscous dissipation spectrum it can be seen that the excess velocity fluctuations in scales smaller than  $k = 4.5$  causes a sudden and significant increase in viscous dissipation at these length scales. For  $\tilde{k} > 4.5$  the spectrum approximately scales as  $k^{1.0}$ . Given its magnitude, it is probable that this excess dissipation is causing the retardation of the inverse energy cascade. The majority of the particle's kinetic energy is being lost at these smaller scales before it can be transferred to the larger length scales.

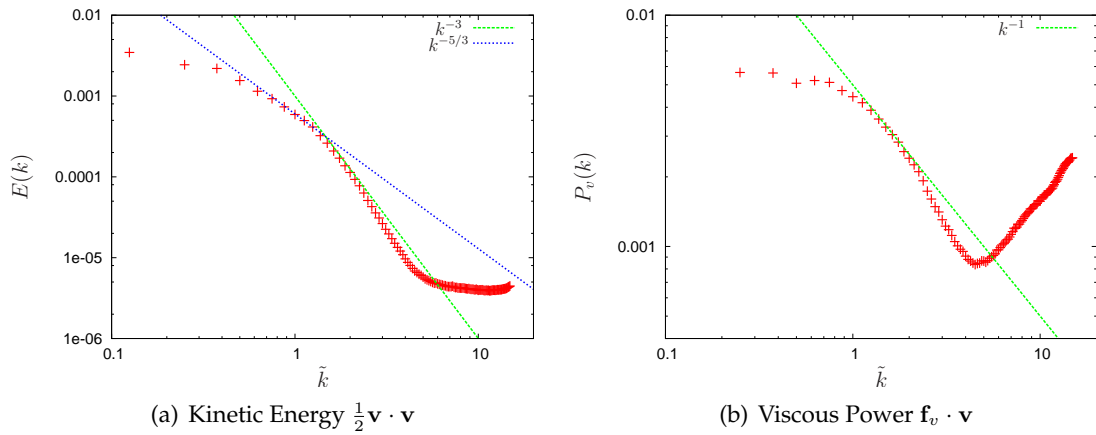


**Figure 6.8:** Comparison between selected spectra at  $t = 47.32$ .

For  $\tilde{k} < 4.5$ , the viscous power spectrum is consistent with both the expected scalings and the kinetic energy spectrum. Also shown with the viscous power spectrum is a reference line indicating the expected scaling (i.e.  $k^{-1}$ ) in the direct enstrophy range (assuming a kinetic energy spectrum of the form  $E \sim k^{-3}$ ). The spectrum follows this scaling well. It is slightly steeper, but this is entirely consistent with the kinetic energy spectra shown in Figure 6.7.

Molenaar et al. (2004) did not calculate any spectra from his pseudospectral simulations. Given that the majority of the energy was condensed at the largest length scale, the kinetic energy spectrum would have been dominated by this effect. However, Wells et al. (2007) has published kinetic energy spectra from their forced 2D turbulence experiment in a oscillating box. The box is given a constant global rotation (in addition to the oscillating rotation that induces the turbulence) which prevents the energy condensation at  $k = 1$ . They show a  $k^{-5/3}$  kinetic energy slope for the inverse energy range ( $\tilde{k} < 1$ ) and  $k^{-3-\alpha}$  for the direct enstrophy range ( $\tilde{k} > 1$ ), where  $\alpha$  grows from 0 for  $Re = 50,000$  to 0.4 for  $Re = 5000$ . The kinetic energy slope in our SPH results is approximately  $k^{-3.4}$  for  $1 < \tilde{k} < 4.5$ , which corresponds well to these results.

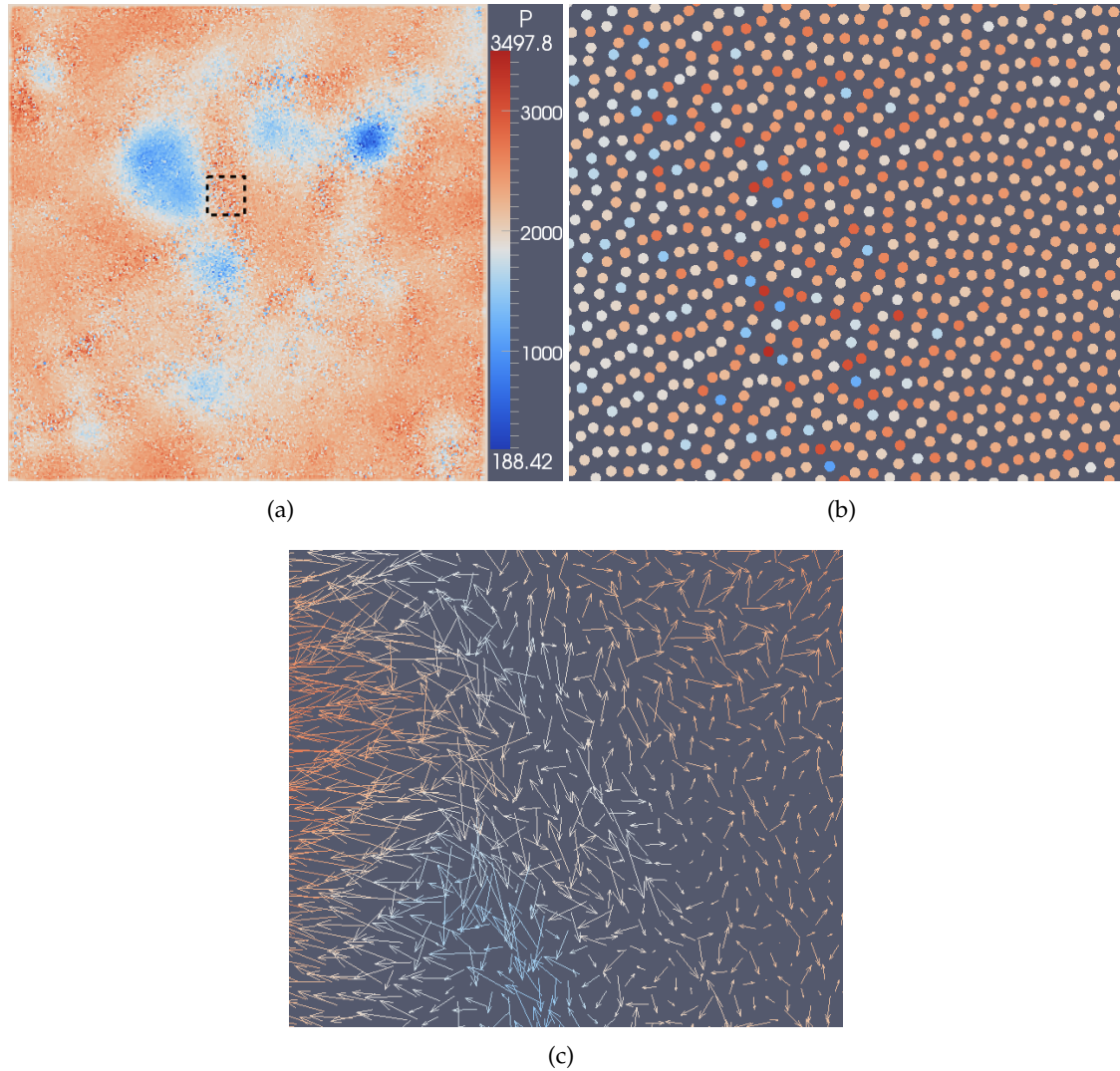
### 6.2.5 Pressure Field

This section explores the spatial distribution and the Fourier transform of the SPH pressure field in the simulation of forced 2D turbulence.

Figure 6.9(a) shows the spatial pressure field at  $t = 37.7$ . The most obvious features in this figure are the circular regions of low pressure, which correspond (as would be expected) with the centre of strong vortices in the flow. However, as well as these large scale features, Figure 6.9(a) shows a significant amount of small scale pressure fluctuations. While only a single timestep is shown here, these fluctuations in the pressure field are typical of the entire simulation.

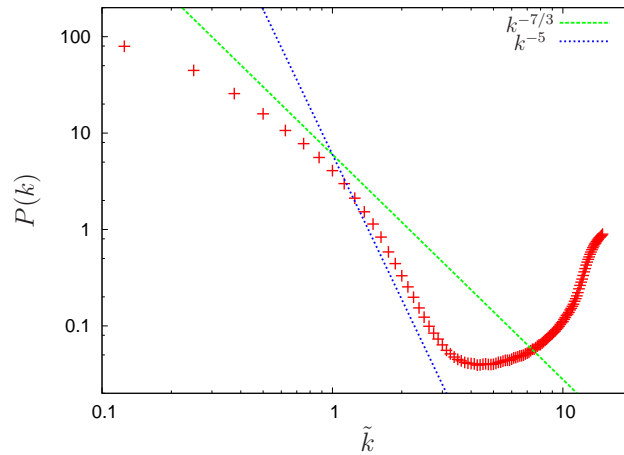
Figure 6.9(b) shows a close up of a small region in the flow. This shows that the pressure is quite variable between closely spaced particles, with pressure changes of over 1000 not uncommon between neighbouring particles.

Figure 6.9(c) shows an arrow plot of the SPH pressure gradient  $-\nabla P/\rho$ . This is calculated using the normal pressure gradient equation introduced in Section 2.5.2. The noisy pressure field results in a large variation in the direction and strength of the pressure gradient between neighbouring particles. It is reasonable to expect that these variations would induce velocity fluctuations in the SPH particles on a similar length scale, which are likely to be related to the velocity fluctuations already seen in the kinetic energy spectra.



**Figure 6.9:** Spatial distribution of the SPH pressure field at  $t = 37.7$ . (a) Full pressure field. Dashed square indicates location of close up region. (b) Close up of SPH pressure field. (c) SPH Pressure gradient  $-\nabla P/\rho$  over the same region.

Figure 6.10 shows the SPH Fourier transform of the pressure field averaged over  $31.4 < t < 47.1$  (6.3 turn over times). Jun (2006) performed an experimental study of electro-magnetically forced 2D turbulence in a freely-suspended soap film and found that the pressure spectrum  $P(k)$  scaled as  $k^{-7/3}$  for  $k < 1$  and  $k^{-5}$  for  $k > 1$ . These results confirm the theoretically predicted scalings given by Batchelor (1953). However, it must be noted that there is no firm consensus on these pressure scaling laws (Jun (2006)). Reference lines showing these expected scalings are drawn as dashed lines in Figure 6.10.



**Figure 6.10:** *SPH pressure spectrum averaged over  $31.4 < t < 47.1$*

At medium wavenumbers around the forcing scale  $\tilde{k} = 1$  the SPH pressure spectrum follows the expected scalings reasonably well, although the spectrum gradient both above and below the forcing scale is slightly lower than the reference lines. However, given that the expected scaling laws are still debated in the turbulence literature, these variations are acceptable.

At low wavenumbers the SPH spectrum deviates significantly below the reference line. This is consistent with the kinetic energy spectra discussed in the previous section, and is due to the lack of large scale structure formation in the SPH simulation.

However, the most significant deviation occurs at high wavenumbers. For  $\tilde{k} > 3.5$  (wavelengths less than 10.7 particle spacings), the small scale pressure fluctuations cause the SPH spectrum to increase significantly. This is due to the pressure fluctuations seen previously in Figure 6.9.

Given the strength of the pressure fluctuations and their effect over a wide range of length scales, it is possible that the noise seen in the SPH pressure field has a significant impact on the evolution of the turbulence. Section 6.3.1 explores this impact by varying the sound speed of the simulation, in effect altering the scale of the pressure field.

The tendency of the quasi-compressible SPH method to produce fluctuations in the pressure field has been previously noted in the SPH literature (e.g. Lee et al. (2008) or Colagrossi & Landrini (2003)). Colagrossi & Landrini (2003) present a method to remove these fluctuations by periodically smoothing the density field. Section 6.3.4 investigates the effects of smoothing the density field on the turbulence and the energy conservation of the simulation.

### 6.2.6 Velocity Structure Functions

Another method to investigate the velocity field at different length scales is to calculate the velocity structure functions

$$\langle [\delta \mathbf{v}(r)]^n \rangle = \langle [\mathbf{v}(x+r) - \mathbf{v}(x)]^n \rangle. \quad (6.2.1)$$

In order to calculate this function using the SPH data, all  $N^2$  particle pairs  $(a, b)$  are ordered according to their separation  $r = |\mathbf{r}_a - \mathbf{r}_b|$ . They are binned into discrete values of  $r$  equal to  $r_d = r_1, r_2, r_3, \dots$ . At the end of this operation, there are  $N(r_d)$  particle pairs in each bin.

The velocity structure function  $\langle [\delta \mathbf{v}(r)]^n \rangle$  is then calculated for each bin

$$\langle [\delta \mathbf{v}(r_d)]^n \rangle = \langle [\mathbf{v}_a - \mathbf{v}_b]^n \rangle_{(a,b)}, \quad (6.2.2)$$

$$= \frac{1}{N(r_d)} \sum_{(a,b)} [\mathbf{v}_a - \mathbf{v}_b]^n, \quad (6.2.3)$$

where the average  $\langle \cdot \rangle_{(a,b)}$  is over all the  $N(r_d)$  particle pairs in each bin.  $N(r_d)$  will be different for each  $r_d$ , but as long as it is sufficiently large to provide an accurate statistical mean the velocity structure function will be accurate.

Figure 6.11 shows the result of this calculation with  $n = 2$  at  $t = 47.3$ . The x-axis is the particle separation normalised by the average particle spacing, i.e.  $\tilde{r} = r/\Delta p$ . So the forcing length scale  $k_f$  corresponds to  $\tilde{r}_f = 37.5$ . Also shown are the expected scalings for  $\langle [\delta \mathbf{v}(r_d)]^2 \rangle$  according to the derivation in Davidson (2004). As with all the expected scalings quoted in this chapter, this derivation assumes that the forced turbulence is generated in an infinite domain. For  $\nu < \tilde{r} < \tilde{r}_f$ , where  $\nu$  is the dissipation length scale,  $\langle [\delta \mathbf{v}(r_d)]^2 \rangle$  should scale as  $\tilde{r}^2$ . For large length scales that are sufficiently smaller than the size of the domain,  $\langle [\delta \mathbf{v}(r_d)]^2 \rangle \sim \tilde{r}^{2/3}$ .

The SPH results for the velocity structure scaling are not quite what is expected from the theory. For scales smaller than the forcing scale  $\tilde{r} < \tilde{r}_f$ , the scaling is  $\langle [\delta \mathbf{v}(r_d)]^2 \rangle \sim \tilde{r}^s$ , where  $s \approx 1.7$ . For larger scales  $\tilde{r}_f < \tilde{r} \ll W$ , where  $W$  is the width of the box,  $s \approx 1.0$ .

Another notable feature of  $\langle [\delta \mathbf{v}(r_d)]^2 \rangle$  is the smooth nature of the scaling across  $\tilde{r} = 8.3$ , which is the scale where the kinetic energy spectrum levels out. It is reasonable to expect that since the kinetic energy spectrum indicated excess velocity fluctuations at length scales smaller than this, this would show up in the velocity structure plot as an increase in the value of  $\langle [\delta \mathbf{v}(r_d)]^2 \rangle$  for these values of  $\tilde{r}$ . However, a closer analysis of the relationship between the kinetic energy spectrum  $E(k)$  and  $\langle [\delta \mathbf{v}(r_d)]^2 \rangle$  shows that this is not the case for 2D turbulence.

From Davidson (2004), the relationship between these two functions (assuming homogeneous, isotropic turbulence in an infinite domain) is approximately

$$\langle [\delta \mathbf{v}(r)]^2 \rangle \approx \int_{\pi/r}^{\infty} E(k) dk + (r/\pi)^2 \int_0^{\pi/r} k^2 E(k) dk. \quad (6.2.4)$$

The first term on the right hand side of this equation is the kinetic energy held in the length scales smaller than  $r$  and the second is equal to  $(r/\pi)^2$  times the enstrophy held

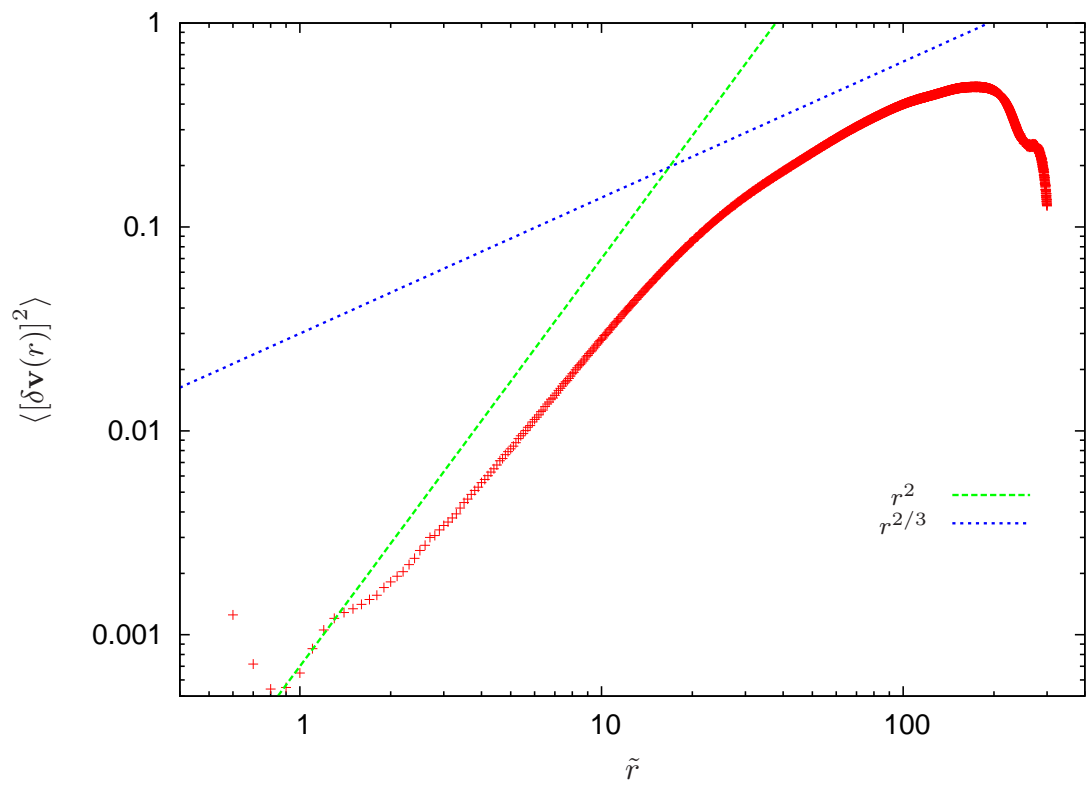


**Figure 6.11:** Velocity Structure Function  $\langle [\delta \mathbf{v}(r)]^n \rangle$  with  $n = 2$ . Taken at  $t = 47.3$  with the forcing scale corresponding to  $\tilde{r}_f = 37.5$ .

in scales larger than  $r$ . For three-dimensional turbulence the second term is generally assumed to be insignificant since the vorticity spectrum at larger scales is very small. Hence the velocity structure function is easily related to the kinetic energy spectrum. In two-dimensional turbulence this is no longer the case and for  $\tilde{r} < \tilde{r}_f$  this function is now dominated by the second term (Davidson 2004). Since  $\langle [\delta \mathbf{v}(r)]^2 \rangle$  for  $\tilde{r} < \tilde{r}_f$  is now governed largely by the vorticity at the larger scales, the excess kinetic energy at scales below 8.3 particle spacing would not be expected to alter the velocity structure function.

The influence of the large scale vorticity on  $\langle [\delta \mathbf{v}(r)]^2 \rangle$  also provides an explanation as to why the scalings do not match up with those predicted for turbulence on an infinite domain. The large-scale vorticity for wall-bounded turbulence is expected to be significantly different from the infinite case and will naturally be dominated by the effects of the bounded domain. This in turn will significantly alter the velocity structure function.

### 6.2.7 Particle Pair Dispersion

As a large part of this thesis is devoted to mixing, it makes sense to check how well this SPH simulation follows the expected particle pair dispersion statistics described in Section 4.1.4. This will give a reasonable prediction of how well SPH is suited to the simulation of any form of turbulent mixing. Since pair dispersion is a process that is dominated by small-scale fluctuations in particle velocities, it is expected that the results for bounded turbulence will be similar to the infinite domain case (at least for values of particle separation much smaller than the domain width).

Earlier methods of calculating the average particle pair dispersion  $\langle |\delta \mathbf{r}| \rangle$  simply involved following a large number of particle pairs with an initial separation of  $|\delta \mathbf{r}|_0$  over time. However, both Boffetta & Sokolov (2002) and Rivera & Ecke (2005) point out a number of problems with this technique. The scaling of  $\langle |\delta \mathbf{r}| \rangle$  calculated this way is dependant on the initial separation of the particle pair. Also, at any given time in a pair's evolution their separation will be affected by a wide range of scales, potentially covering both the direct enstrophy and the inverse energy ranges. This leads to an unnecessary contamination between the length scales.

The solution to this problem lies in the use of *exit time* (also known as *doubling time*) statistics. For a given constant  $p$ , let  $r_n = p^n r_0$ ,  $n = 1, 2, 3, \dots$  be a set of separations in the inertial range. For a random set of particle pairs that have an initial separation of  $r_n$ , calculate the time taken  $T(r_n)$  for each pair to separate to the subsequent separation length  $r_{n+1}$ . Assuming that  $p$  is large enough to satisfy the necessary condition that each pair "forgets" its exact initial conditions by the time it reaches  $r_{n+1}$ , this will give an accurate representation of the particle pair dispersion statistics while minimising any contamination between the length scales. Following the example set by Rivera & Ecke (2005), we have used  $p = 1.2$ .

Starting from Equation 4.1.20, it is a simple matter to find that in the direct enstrophy range  $\tilde{\eta} < \tilde{r} < \tilde{r}_f$  (where  $\tilde{r}$  is a normalised separation distance so that  $\tilde{r} = 1$  is the average SPH particle separation and  $\tilde{r}_f = 37.5$  is the forcing length scale) the average exit time  $\langle T(r) \rangle$  is expected to be constant with  $r$  (Rivera & Ecke 2005). Similarly, Equation 4.1.21 implies that for scales larger than  $r_f$  (the inverse energy cascade region) this value is expected to scale by  $\langle T(r) \rangle \sim t^{2/3}$ .

Applying the exit time method to SPH data is made difficult since it is not possible to specify the initial separation of a random particle pair. Additionally, it was desired that this be a post-processing technique, so the particle positions were only known every 100 time steps (due to space storage limitations), rather than every timestep. In light of these restrictions, the normal exit time technique has been slightly modified. Instead, a large number of random particle pairs were followed over time until their separations became greater than  $p|\delta\mathbf{r}|_0$ , where  $|\delta\mathbf{r}|_0$  is their initial separation. Then, the relevant finite-time Lyapunov exponent  $\lambda$  was calculated for each pair using the time taken ( $\Delta t$ ) for them to separate.

$$\lambda = \frac{1}{2\Delta t} \ln \left( \frac{|\Delta\mathbf{r}|^2}{|\Delta\mathbf{r}|_0^2} \right). \quad (6.2.5)$$

The exit time  $T$  can be found from Equation 6.2.5 using  $\Delta t = T$  and  $|\Delta\mathbf{r}|/|\Delta\mathbf{r}|_0 = p$ .

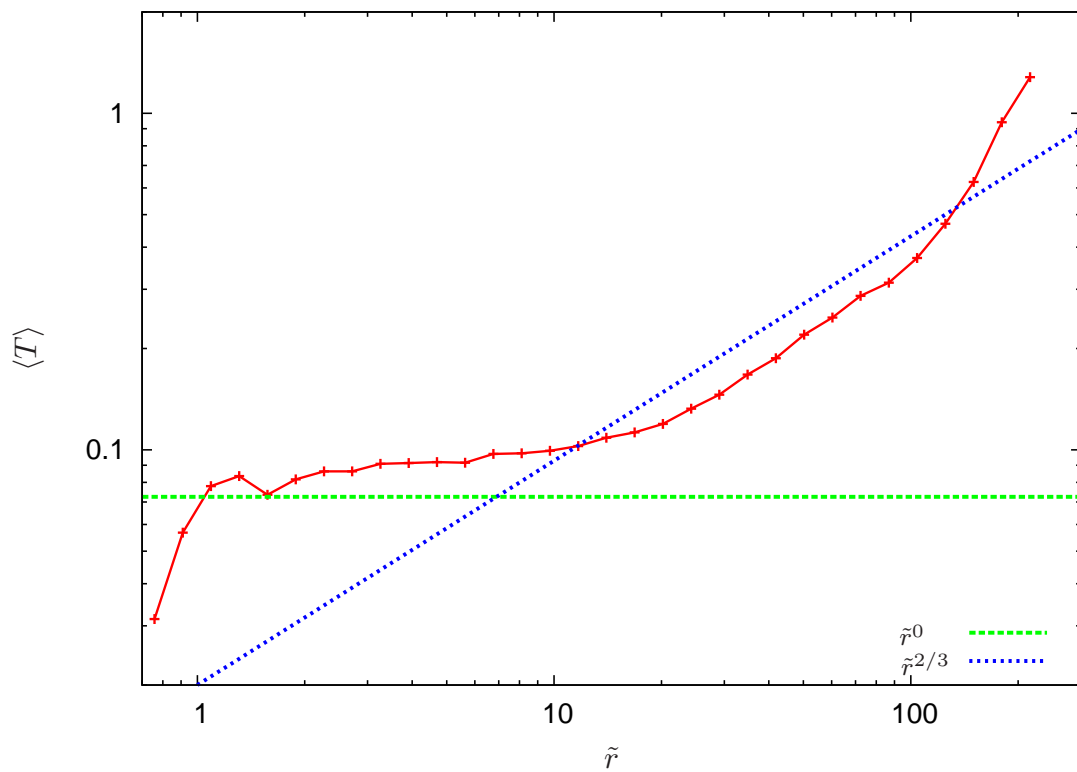
$$T = \frac{\ln p}{2\lambda}. \quad (6.2.6)$$

Figure 6.12 shows the result of this computation for the forced turbulence simulation. This plot of  $\langle T \rangle$  was obtained by averaging 100,000 particle pairs that were randomly selected from the centre of the domain  $-0.75 \leq r_x, r_y \leq 0.75$  over the time period  $22.1 \leq t \leq 24.3$ . The two reference lines show the expected scaling for both sides of the forcing length scale.

The forcing scale for the normalised particle separation is at  $\tilde{r}_f = 37.5$ . In this case this does not correspond with the slight bend in  $\langle T \rangle$ , which occurs at  $\tilde{r} \approx 20$ . Below this the mean exit time scale as  $\langle T \rangle \sim \tilde{r}^{0.1}$ , which is slightly different from the constant scaling that is expected in this region. For larger length scales  $\langle T \rangle$  follows the expected  $\tilde{r}^{2/3}$  scaling quite well until  $\tilde{r} \approx 100$ , when the effects of the bounded domain become apparent. Once the initial particle separation becomes close to the size of the box, the boundaries act to prevent the particles from separating further and hence the mean exit time is increased at these length scales. For very small scales below the average particle separation  $\tilde{r} < 1$  the value of  $\langle T \rangle$  drops sharply, which is consistent with the strong pressure force that would result if a particle pair became closer than  $\tilde{r} = 1$ .

Rivera & Ecke (2005) performed a quasi-two-dimensional turbulence experiment using a stratified flow that was electromagnetically forced. They presented mean exit times for the pair dispersion and found that there existed a clear difference between the direct enstrophy and the inverse energy ranges, the boundary of which occurred at the forcing scale. In the direct enstrophy range they found that  $\langle T \rangle$  was constant with  $\tilde{r}$  and in the inverse energy scale they found that  $\langle T \rangle \sim \tilde{r}^{0.83}$ . There was some mixing of the length scale for  $\tilde{r} = p^{-1}\tilde{r}_f, p^0\tilde{r}_f$  and  $p^1\tilde{r}_f$ , but all other results are consistent with these scalings.

The results from the SPH simulations do not show such a clear agreement with the theoretically predicted values. The separation of particles at length scales above the forcing scales seems accurately represented, however for scales below  $\tilde{r} = \tilde{r}_f$  the results are quite different. This is unlikely to be caused by calculating the exit times from Lyapunov exponents. Any extra mixing of the length scales would only affect the values of  $\tilde{r}$  close to the forcing scale  $\tilde{r}_f$ . However, the gradient of  $\langle T \rangle$  is greater than expected over a wide range



**Figure 6.12:** Particle pair exit time  $\langle T \rangle$  is the average time taken for a particle pair to separate from  $\tilde{r}$  to  $p\tilde{r}$ , where  $p = 1.2$ . The average is taken using 100,000 particle pairs from  $t = 22.1$  to  $t = 24.3$ .

of scales where  $1 < \tilde{r} < r_f$ . A potential cause for this behaviour is the fact that the motion of the SPH particles, unlike physical material points, are constrained to constantly maintain a relatively even spatial distribution. However, even if this constraint did affect the particle pair separations, it seems unlikely that this would have an effect at length scales up to  $\tilde{r} = \tilde{r}_f$ . Rather, this should be localised near  $\tilde{r} = 1$ . Additionally, this effect should be weaker at longer scales, which would result in a negative gradient for  $\langle T \rangle$ .

A more consistent explanation is the existence of a secondary forcing scale within  $1 < \tilde{r} < 8.3$ . The kinetic energy spectrum plot shown earlier showed a significant amount of excess velocity fluctuation within this region. Assuming that there exists a source of energy at these small length scale, this would set up a secondary inverse energy cascade, which would steepen the slope of  $\langle T \rangle$ . This would also increase the gradient of the kinetic energy spectrum, which is consistent with the measured spectra of  $E \sim \tilde{k}^{-3.4}$  for  $4.5 < \tilde{k} < k_f$ .

## 6.3 Sensitivity To Parameters

This section describes the results of varying some of the SPH simulation parameters. Section 6.3.1 explores the effects of varying the sound speed, which alters the compressibility of the fluid. Section 6.3.2 varies the two resolution parameters, the number of particles and the ratio of smoothing length to average particle separation  $h/\Delta p$ . Section 6.3.3 considers several different forms of the SPH viscous term.

### 6.3.1 Compressibility

The SPH simulations used in this thesis are only approximately incompressible. The equation of state is given by

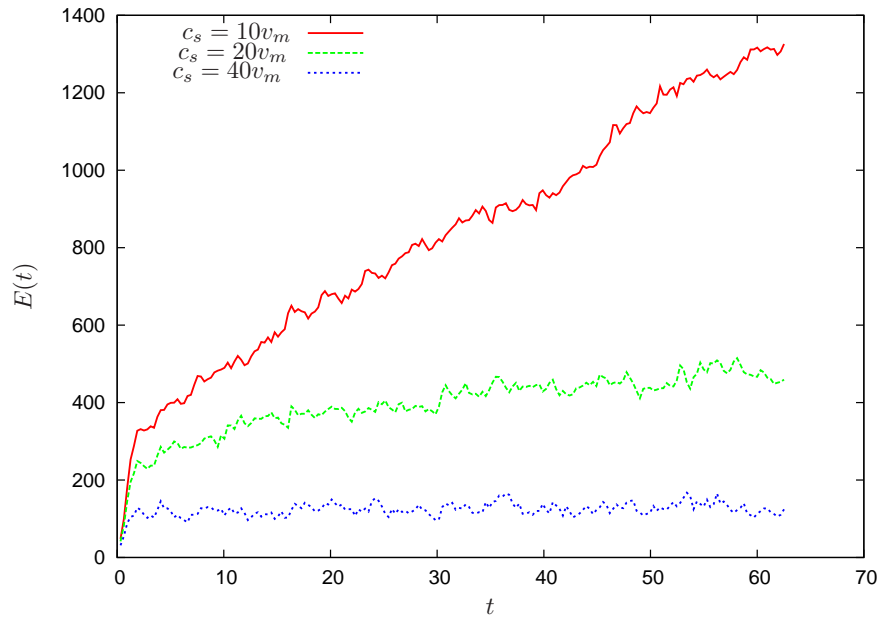
$$P = B \left( \left( \frac{\rho}{\rho_0} \right)^\gamma - 1 \right), \quad (6.3.1)$$

where  $B = \rho_0 c_s^2 / \gamma$ . The sound speed  $c_s$  governs how incompressible the fluid is. It is typically set to 10 times the maximum velocity in order to keep density variations within 1%.

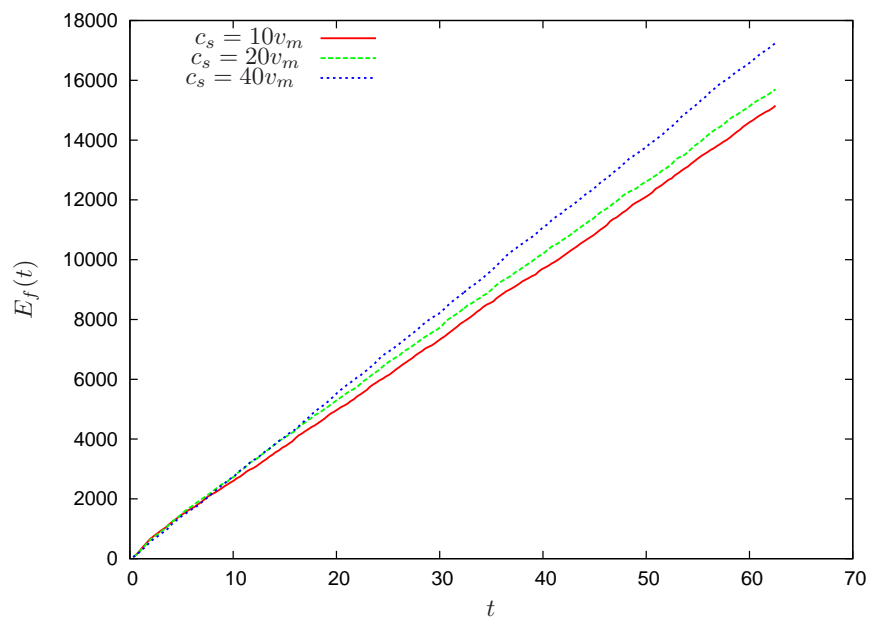
Another parameter dependent on the sound speed is the timestep. In order to keep the time integration stable and satisfy the Courant condition, the timestep  $\Delta t$  must satisfy

$$\Delta t \leq 0.4 \frac{h}{c_s}. \quad (6.3.2)$$

Three different SPH simulations of the forced turbulence were setup with varying sound speeds. In order to keep everything else constant, the timestep condition was altered so that the timestep was the same across all simulations (each simulation still satisfied the original Courant Condition).



(a) Total Kinetic Energy



(b) Total energy input due to the forcing term

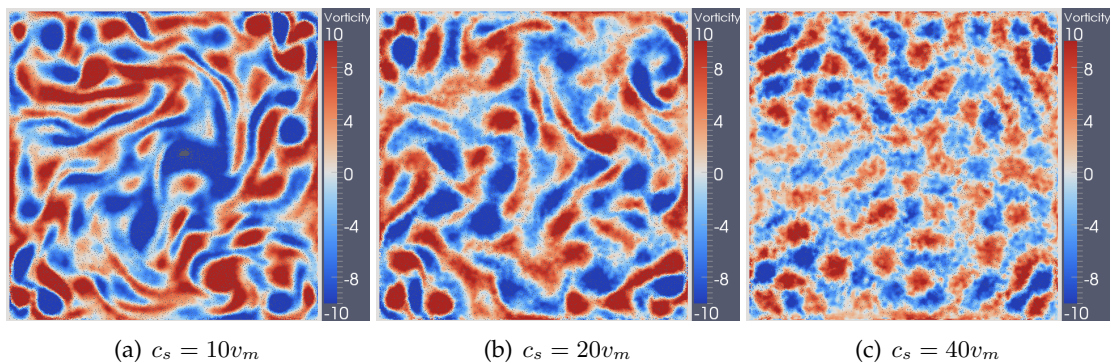
**Figure 6.13:** Variation of kinetic energy and energy input (due to the forcing term) with sound speed. While the sound speed is altered, the timestep size is unchanged between these simulations.

Figure 6.13(a) shows plots of total kinetic energy versus time for each of these simulations. The sound speed was varied between  $10v_m$  to  $40v_m$ , where  $v_m$  is the characteristic maximum velocity for the simulations (this is set to  $v_m = 2.0$ ). The timestep for the simulations was set to  $\Delta t = h/100v_m$  so that all of the simulations would satisfy the Courant Condition. This timestep is four times smaller than the timestep used to generate all the results shown previously in this chapter (these simulations used  $c_s = 10v_m$  and  $\Delta t = h/25v_m$ ).

The total kinetic energy plots indicate dramatically different flows for each simulation. After the initial sharp rise in kinetic energy for each case, the gradient of the subsequent steady but more gradual growth of kinetic energy is a good indication of the strength of the inverse energy cascade and the accuracy of the simulation. It is clear that these factors are significantly different between the simulations. Increasing the sound speed has the effect of severely reducing the strength of the inverse energy cascade. So much so that for  $c_s = 40v_m$  the cascade has disappeared entirely.

It should also be noted that the increase in kinetic energy for  $c_s = 10v_m$  is also significantly stronger than for the original simulation, which has a much longer timestep. In the original simulation (shown in Figure 6.5),  $E(t) \approx 700$  at  $t = 60$ , whereas Figure 6.13(a) gives  $E(t) \approx 1300$  at  $t = 60$ . It seems unlikely that the decrease in timestep size has changed the characteristics of the forcing term, as it has been constructed to be independent of  $\Delta t$ . Additionally, the ratio of the forcing decay time to the timestep is  $\tau/\Delta t = 66.55$ , so the evolution of the forcing term should be more than adequately sampled in time. So it seems more likely that the change in timestep size is improving the accuracy of the simulation and hence the strength of the inverse energy cascade.

Returning to the  $c_s = 40v_m$  simulation, it is interesting to see that even though the total kinetic energy is significantly lower, the power input due to the forcing term (shown in Figure 6.13(b)) is actually greater for this case. This is due to the fact that the flow in this simulation is closely coupled to the structure of the forcing term, and does not evolve into a more independent, turbulent flow. Hence, the velocity field will be more correlated to the force field, which results in a greater power input.



**Figure 6.14:** Vorticity fields at  $t = 59.7$  using different sound speeds. Each image is labelled by the sound speed  $c_s$  of the corresponding simulation.

Figure 6.14 shows the vorticity field at  $t = 59.7$  for each sound speed. The vortex structures for  $c_s = 10v_m$  are much larger than the other simulations, an indication of the

increased strength of the inverse energy cascade. For  $c_s = 40v_m$ , the flow is not even fully turbulent, and the vorticity field looks very similar to the form of the forcing term. This continues for the duration of the simulation. Another difference between the three simulations is the greater levels of noise in the vorticity fields (and therefore increased noise in the velocity field) with increasing sound speed.

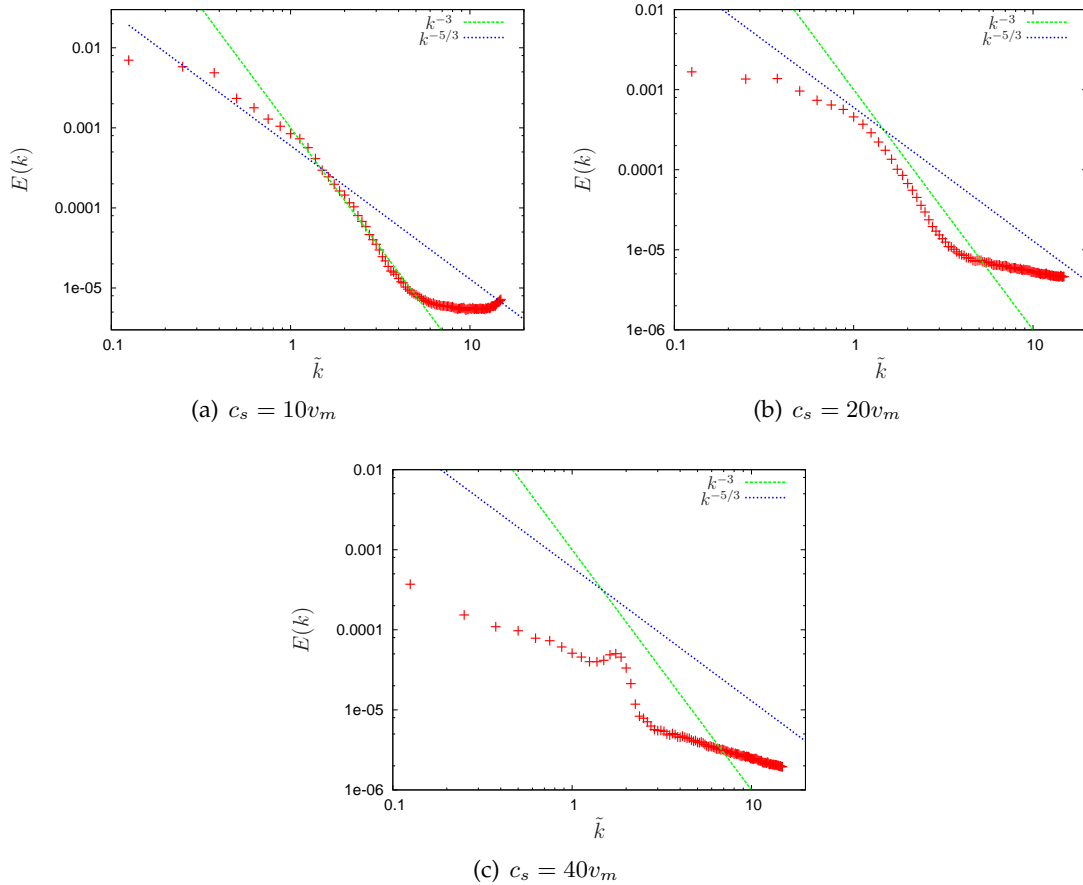


**Figure 6.15:** Kinetic energy spectrum at  $t = 59.7$  using different sound speeds. Each image is labelled by the sound speed  $c_s$  of the corresponding simulation.

Figure 6.15 shows the corresponding kinetic energy spectra at the same time  $t = 59.7$ . As the sound speed of the simulations increase, there is a clear decrease in the proportion of energy at the larger length scales, which is consistent with the total kinetic energy evolution. Figure 6.15 also shows that the range of the excess kinetic energy, which we have previously noted occurred for wavenumbers  $\tilde{k} > 4.5$ , moves to larger length scales as the sound speed increases. In other words, the problematic velocity fluctuations seem to grow in scale as the incompressibility of the simulation is increased.

Section 6.2.5 showed that there is a significant amount of small scale fluctuations in the pressure field that occur over a similar range of length scales as the velocity fluctuations. The scale of the SPH pressure field is proportional to  $c_s^2$ , so these results provide evidence that the pressure fluctuations contribute strongly to the velocity fluctuations and therefore the total numerical dissipation of the simulation. If so, this is unlikely to be a one-way effect, since strong small scale variations in the velocity field could also lead to

an increase in the particle disorder, which would feed back into the density and pressure fields. While the results in this thesis do not prove the existence of such an instability, this remains a promising avenue for future research.

### 6.3.2 Resolution

As detailed in Section 6.1.2, 300x300 particles is double the theoretical resolution needed to resolved a simulation at  $Re = 1581$ . It is also comparable to the resolution used by Molenaar et al. (2004) in their pseudospectral results. However, the kinetic energy and viscous power spectra shown in Figure 6.8(a) and 6.8(b) indicate that there are significant velocity fluctuations and viscous dissipation occurring at length scales less than 8.3 particle spacings. Assuming that the length scale that this occurs is related to the resolution of the simulation, it might be possible to reduce this to down to below the required resolution of the turbulence (i.e. the dissipation length).

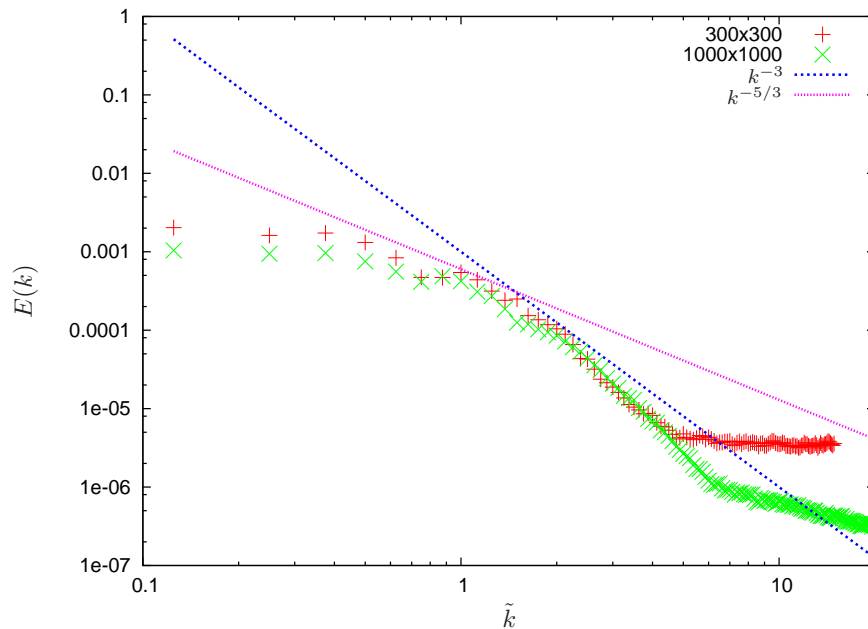


**Figure 6.16:** Kinetic energy spectrum for two different particle resolutions, 300x300 and 1000x1000. Also shown are two reference lines showing the expected kinetic energy spectrum scalings for  $\tilde{k} > 1$  (i.e.  $k^{-3}$ ) and  $\tilde{k} < 1$  (i.e.  $k^{-5/3}$ ).

Figure 6.16 shows the kinetic energy spectrum of two simulations, one using 300x300 particles and the other using 1000x1000. These spectra are taken at  $t = 19.2$  and have been scaled so that they lie on top of each other. While the spectrum from the 300x300 simulation deviates from  $k^{-3}$  at about  $\tilde{k} = 4.5$  ( $k = 36$ ), the 1000x1000 simulation deviates at about  $\tilde{k} = 6.5$  ( $k = 52$ ). The dissipation length for 2D turbulence at  $Re = 1581$  is at mode  $k_\nu = 79$ . Assuming that the movement of the deviation length scale is linear with resolution, the required resolution in order to fully resolve the turbulence and keep the velocity fluctuations below the dissipation length is approximately 3500x3500 particles. This resolution requirement is clearly excessive for a 2D turbulence simulation at  $Re \approx 1500$ .

While it is straightforward that the accuracy of the simulation should improve with increasing resolution, it is surprising how sensitive it is to the other resolution parameter, the ratio of smoothing length to particle spacing  $h/\Delta p$ . The previous chapter on the decaying turbulence showed a significant improvement in the accuracy of the simulation when  $h/\Delta p$  was increased from 1.3 to 1.95. However, once it reached 1.95 the results converged and any subsequent increases had little effect on the evolution of the turbulence. For the forced turbulence there is clearly a large and fundamental difference in the flow produced using either  $h/\Delta p = 1.3$  or  $h/\Delta p = 1.95$ . However, increasing this value past 1.95 still results in a significant increase in the strength of the inverse energy cascade.

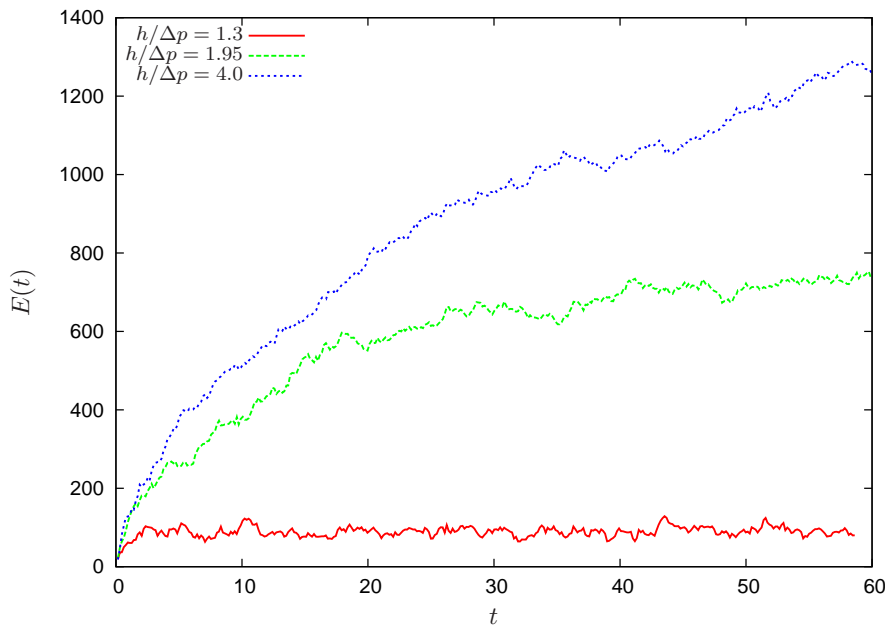


**Figure 6.17:** Total kinetic energy for three different values of  $h/\Delta p$ . Particle resolution kept constant at  $300 \times 300$ .

Figure 6.17 shows plots of total kinetic energy from three different simulations with  $h/\Delta p = 1.3$ , 1.95 and 4.0. The number of particles is held constant at  $300 \times 300$ . The previous results show that the rate of increase in total kinetic energy is a good indicator of the strength of the inverse energy cascade. It is the larger modes that contain most of the kinetic energy of the turbulence and they will therefore contribute most strongly to the total kinetic energy  $E$ . In Figure 6.17, the rate of increase in  $E$  is significantly higher for  $h/\Delta p = 4.0$  than the usual value of  $h/\Delta p = 1.95$ . By  $t = 60$  there is an almost 100% increase in  $E$  between the two simulations. In contrast, the simulation using  $h/\Delta p = 1.3$  shows a very weak or non-existent inverse energy cascade, with  $E$  not rising above 175. Figure 6.18(a) shows a typical vorticity plot for this simulation. Compared with Figures 6.18(b) and 6.18(c), the flow for  $h/\Delta p = 1.3$  is clearly not turbulent and is instead highly correlated with the forcing term.

The kinetic energy and viscous power spectra for the  $h/\Delta p = 1.95$  and  $h/\Delta p = 4.0$  simulations are shown in Figure 6.19. The kinetic energy spectrum for  $h/\Delta p = 4.0$  shows a greater proportion of energy in the larger length scales, which is expected from the total kinetic energy plots. At the smaller length scales there is a much greater increase

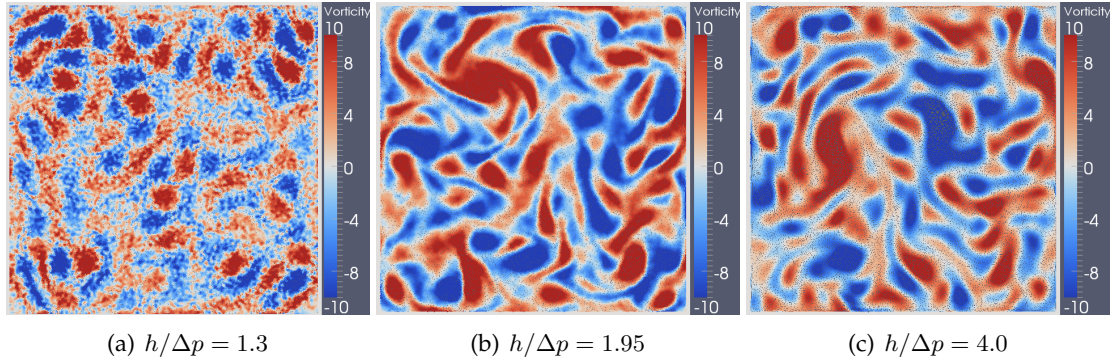


**Figure 6.18:** Simulation snapshots comparing three different values of  $h/\Delta p$ . Particles are coloured by vorticity and  $t = 47.2$  for all three frames.

in the kinetic energy at modes  $\tilde{k} > 5$ . Given that the viscous power and kinetic energy spectra are related by  $P_v(k) = k^2 \mathbf{E}(k)$ , this extra small scale kinetic energy should result in an increase in the small scale dissipation. However, this is not the case. In fact, for  $\tilde{k} > 7$  the gradient of the viscous power spectrum for  $h/\Delta p = 4.0$  becomes negative. This decrease in viscous dissipation is due to the effect of the smoothing kernel on the viscous term. Mansour (2007) showed that the smoothing action of the kernel weakens the viscous dissipation at small scales.

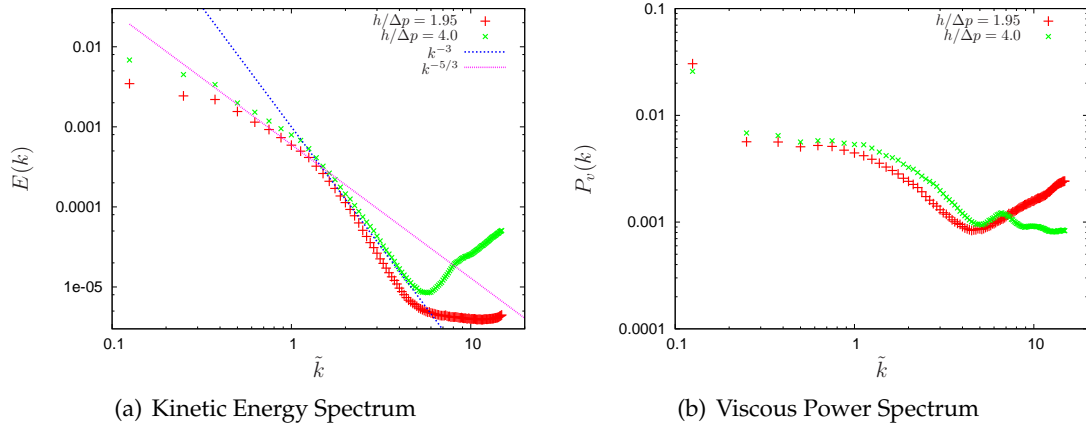


**Figure 6.19:** Spectra comparing two different simulations using  $h/\Delta p = 1.95$  and  $h/\Delta p = 4.0$ . All the spectra are taken at  $t = 47.2$ .

The decrease in small scale viscous dissipation results in the increase of total kinetic energy seen in Figure 6.17. Since less energy is dissipated, the inverse energy cascade moves more energy to the larger length scales, slightly increasing the kinetic energy spectrum at these scales. Another positive effect of the increase size of the kernel is that the kinetic energy scaling for  $1 < \tilde{k} < 5$  is much improved and exactly follows the expected scaling ( $k^{-3}$ ).

However, while the increase of  $h/\Delta p$  from 1.95 to 4.0 does reduce the excess dissipation seen in the SPH simulation, the fundamental problems of the simulation still remain. The increase in the strength of the inverse energy cascade does not result in the formation of

the expected large monopole vortex. Furthermore, the small scale velocity fluctuations are increased along with the increased kernel size, most likely due to the weakening of the viscous dissipation at these scales.

### 6.3.3 Viscous Term

There have been numerous SPH viscosity terms produced in the literature. Given that it is an excessive viscous dissipation that is preventing the formation of the expected monopole vortex, it is worthwhile to investigate the effects of using different SPH viscous terms.

We have used three different viscosity terms. The first is the Monaghan form (Equation 2.5.18) that is used in most of the results presented in this thesis. The other two are the forms by Cleary (Equation 2.5.17, found in Cleary (1998)) and Morris (Equation 2.5.19, found in Morris et al. (1997)).

Figure 6.20 shows the evolution of total kinetic energy for the three viscous terms. The Monaghan and Morris viscous terms give very similar results, with the total kinetic energy for both terms rising asymptotically to  $E = 750$ . The Cleary term results in a slightly higher amount of energy removed due to the viscosity, resulting in a final total kinetic energy of  $E = 500$ . However, given that the pseudo-spectral forced turbulence simulations (using the same forcing term and fluid parameters as the SPH simulation) in Molenaar et al. (2004) report an average total kinetic energy of  $E = 4500$ , the difference between the three SPH viscous terms is seen as not significant when compared with these results. A similar comparison between these viscous terms was also carried out for the periodic forced turbulence simulation described in Section 6.5. Once again, no significant difference was found between the different viscosities. So while the SPH viscosity does seem to be causing an excess dissipation that is preventing energy from moving into the larger scales, this dissipation is not sensitive to the particular form of the viscous term and is merely a symptom of an underlying problem (e.g. small and medium-scale velocity fluctuations).

### 6.3.4 Density Smoothing

This section shows the results of periodically smoothing the density field in order to remove the small scale pressure fluctuations that were discussed in Section 6.2.5. The effects of this smoothing on the turbulence as well as the energy budget for the SPH simulation are shown.

SPH was originally developed for compressible astrophysical flows with large density changes. For these cases it was natural to calculate the density at each particle using an SPH summation interpolant

$$\rho_a = \sum_b m_b W_{ab}. \quad (6.3.3)$$

However, for quasi-compressible flows the density variation is kept within 1% and it is

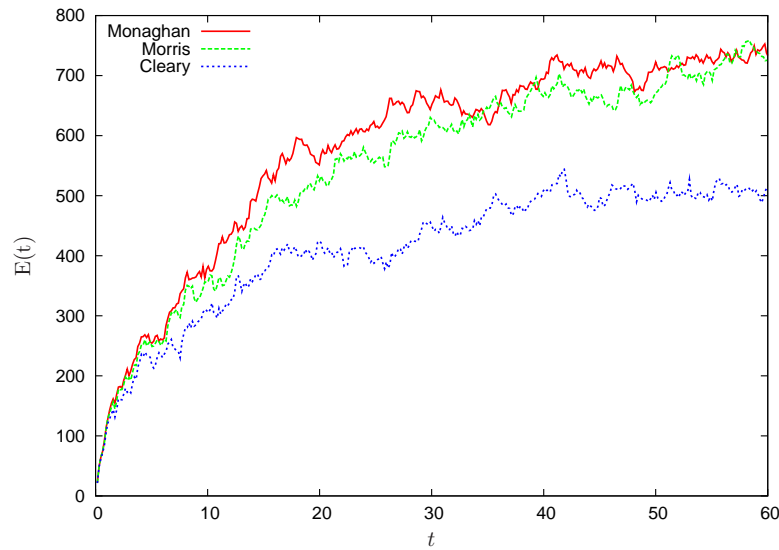


**Figure 6.20:** Normalised total kinetic energy for three different forms of the SPH viscous term.

much more computationally efficient to calculate the density by integrating the continuity equation (2.5.5). However, the quasi-compressible SPH formulation has previously been shown to produce large fluctuations in the density field (Lee et al. 2008, Colagrossi & Landrini 2003). The forced turbulence results in this chapter also show a significant level of pressure fluctuations, up to a length scale of approximately 10 particle spacings. In addition, the scale of the pressure force between the particles has a large effect on the numerical dissipation and the strength of the inverse energy cascade.

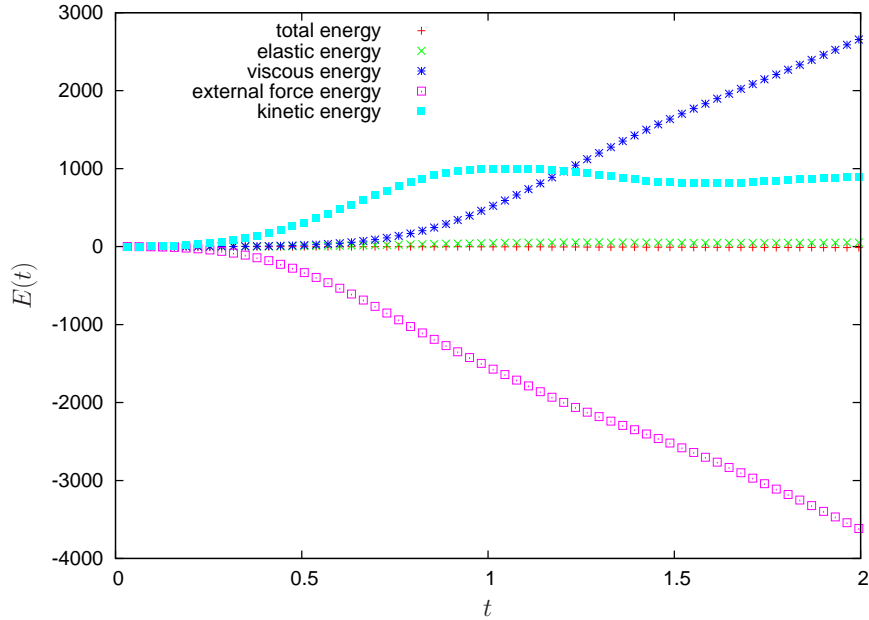
Colagrossi & Landrini (2003) found that periodic use (once every 20 time steps) of a density sum similar to Equation 6.3.3 almost entirely eliminated the pressure fluctuations in a dam break simulation. Instead of the normal SPH kernel  $W_{ab}$ , they used the Moving Least Squares kernel shown in Section 2.3. While it might be argued that much of the improvement to the pressure field is cosmetic, as the method cannot “see” anything below the length scale of the kernel anyway, Colagrossi and Landrini showed that the smoothed pressure field also resulted in an improvement in the shape of the free-surface once the dam break wave had rebounded from the side of the tank.

While the improvements to the pressure field are significant, the effects of the density smoothing on the energy conservation are less clear. As detailed in Chapter 2, the SPH implementation used in this thesis was designed to preserve the Lagrangian of the system and to exactly conserve the total energy in the simulation. The use of density smoothing operator will smooth out the pressure gradients of the flow, removing the potential energy contained in these gradients.

In order to investigate the effect of a density smoothing operator on the energy budget, a forced turbulence simulation was set up using 150x150 particles. The forcing term parameters were  $A = 6$  and  $\tau = 1$ . The ratio of smoothing length to particle spacing was  $h/\Delta p = 1.95$  and  $\rho = \rho_0 = 1000$ . The sound speed was  $c_s = 20$  and the box dimensions were  $2 \times 2$ . The viscosity was  $\nu = 0.0003$ .

Figure 6.21 shows the first few seconds of the energy budget for the simulation with the

standard SPH configuration with no density smoothing. The energy transfer proceeds as expected. Initially all the energy from the forcing term is transferred to the kinetic energy of the particles. Once the total kinetic energy reaches saturation, the viscous term takes over and all the forcing term energy is then transferred to viscous energy.



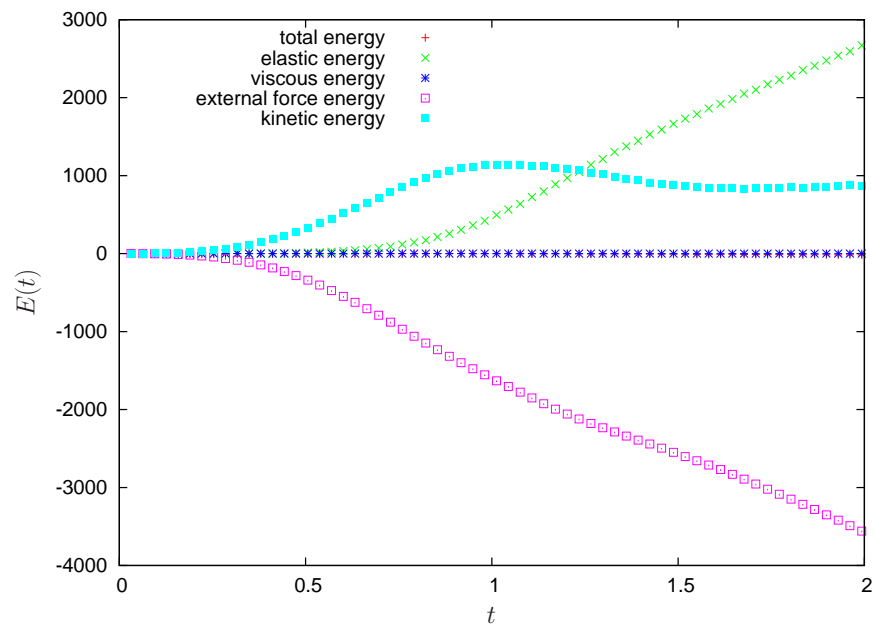
**Figure 6.21:** Energy budget for forced turbulence with no density smoothing. Viscosity included.

Figure 6.22 shows the energy budget for the case when density smoothing is included and the viscosity is turned off ( $\nu = 0$ ). The density is reinitialised every 50 time steps using a SPH sum with a Shepard corrected kernel.

$$\rho_a = \frac{1}{\sum_b W_{ab}} \sum_b m_b W_{ab}. \quad (6.3.4)$$

In this case the density smoothing takes the place of the viscous term. Once the total kinetic energy of the particles grows beyond a certain point, the energy from the forcing term starts moving into the elastic energy of the particles. Note that this isn't an accumulation of stored energy within the system. The pressure forces between the particles do not increase along with the rise in total elastic energy. Rather, this increase represents energy that is going into the system as an elastic potential and is then removed due to the density smoothing acting to smooth the pressure gradient.

Figure 6.23 shows the case with density smoothing and the viscous term included. Here, once the kinetic energy is saturated, the energy from the forcing term is divided equally between the elastic and viscous energy terms. The energy lost due to viscosity is dramatically reduced in this simulation. Interestingly, this reduction is balanced perfectly by the energy loss due to the density smoothing itself. The point at which the kinetic energy saturates is the same for all simulations ( $\approx 1000$ ), indicating that the significant changes in viscous and elastic energy do not have much effect on the overall motion of the particles.



**Figure 6.22:** Energy budget for forced turbulence. Density smoothing every 50 time steps using a Shepard corrected kernel. No viscosity.

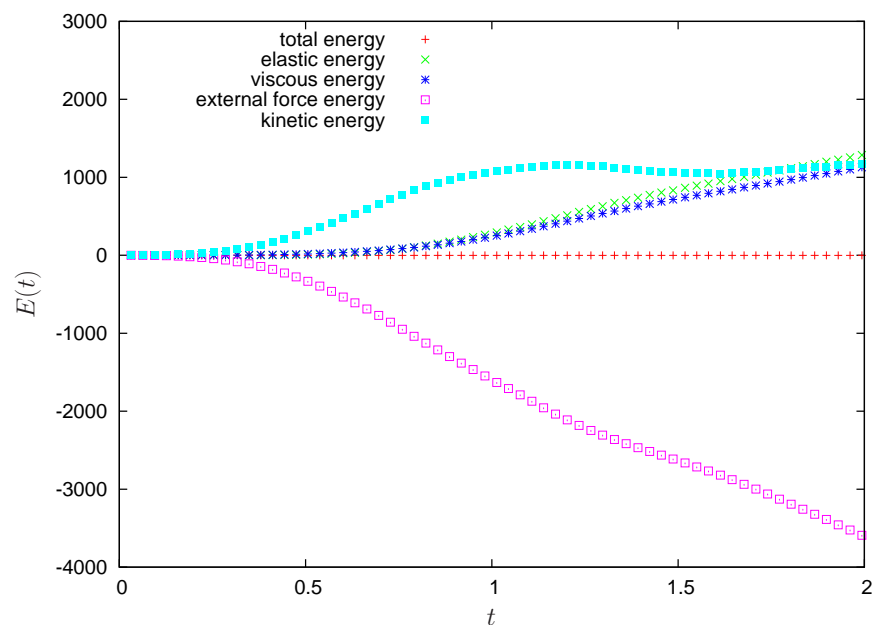


**Figure 6.23:** Energy budget for forced turbulence. Density smoothing every 50 time steps using a Shepard corrected kernel. Viscosity included.

Increasing the resolutions from 150x150 to 300x300 gives a similar picture. For these next results the forcing term correlation was changed to  $\tau = 0.01683$ . This results in a forcing term identical to that used for the 300x300 forced turbulence simulations described earlier in this chapter. Figure 6.24 shows the energy budget for the new simulation. The growth in elastic energy is significantly reduced from the 150x150 simulation and never rises above the total kinetic energy. Still, a substantial amount of energy is still lost due to the density smoothing, approximately 50% of the total kinetic energy by  $t = 60$ .

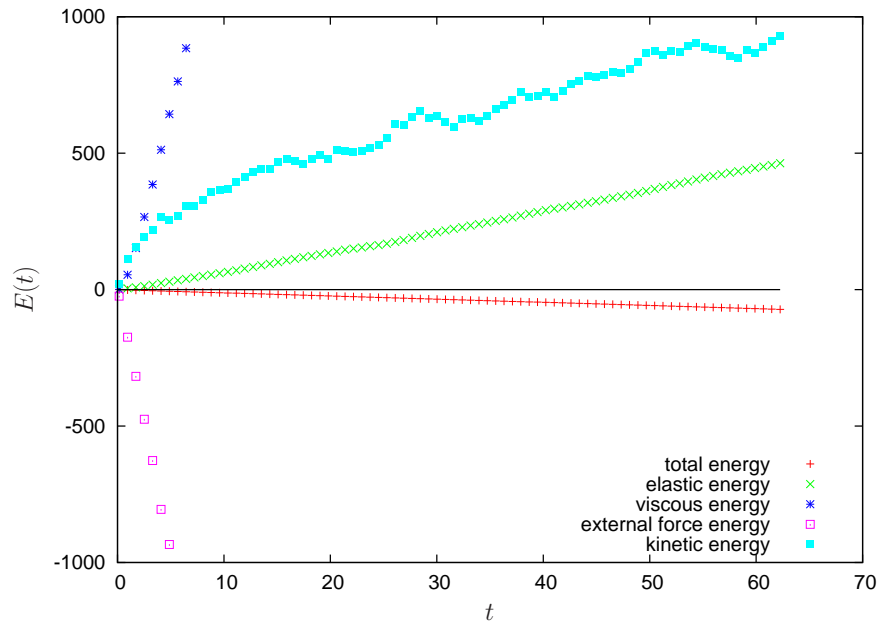


**Figure 6.24:** Energy budget for the forced turbulence simulation using 300x300 and a forcing term correlation of  $\tau = 0.01683$  (these are the same parameters used throughout Section 6.2). Density smoothing included every 50 time steps.

This loss of energy, while concerning from an energy conservation point of view, does not seem to effect the simulated turbulence. Figure 6.25 shows a comparison of the total kinetic energy between the case with no density smoothing, and smoothing every 50 time steps. While there are differences between the two plots, they are minor. Similarly, the kinetic energy and viscous dissipation spectra of the two simulations have no significant differences.

In conclusion, the density smoothing significantly changes the energy distribution for the simulation but results in a similar flow evolution. The use of the smoothing operator certainly reduces the energy lost from the simulation due to viscous dissipation. However, this reduction is exactly balanced by the potential energy loss due to the smoothing of the pressure gradients. In either case, the effect on the turbulent flow and the strength of the inverse energy cascade is identical.

### 6.3.5 Variable versus Constant Smoothing Length

SPH can be formulated either with a constant smoothing length  $h$  or one that varies between particles according to their densities (See Section 2.8). The latter uses the following

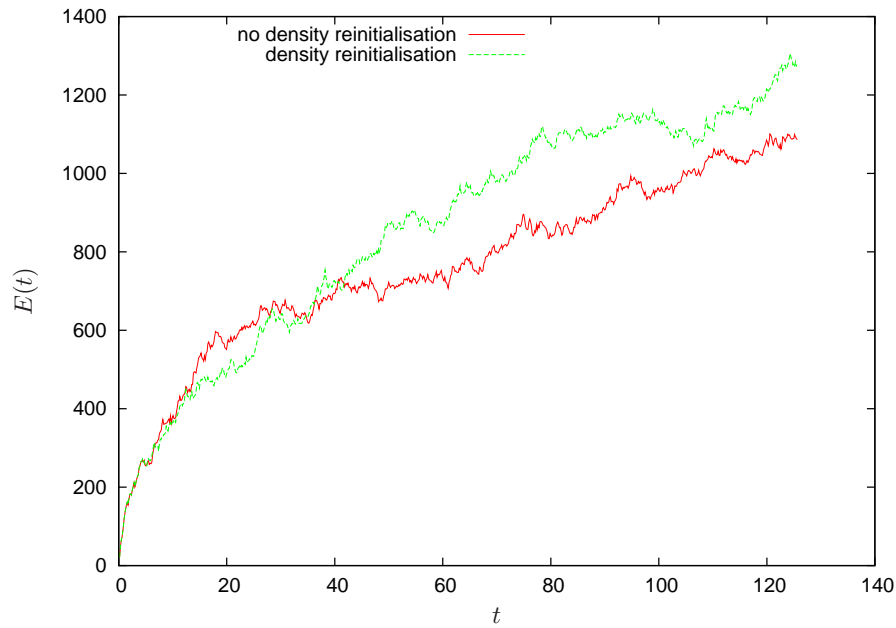


**Figure 6.25:** Comparing the total kinetic energy, the addition of density smoothing does not change the simulation significantly

equation to determine a particle's smoothing length

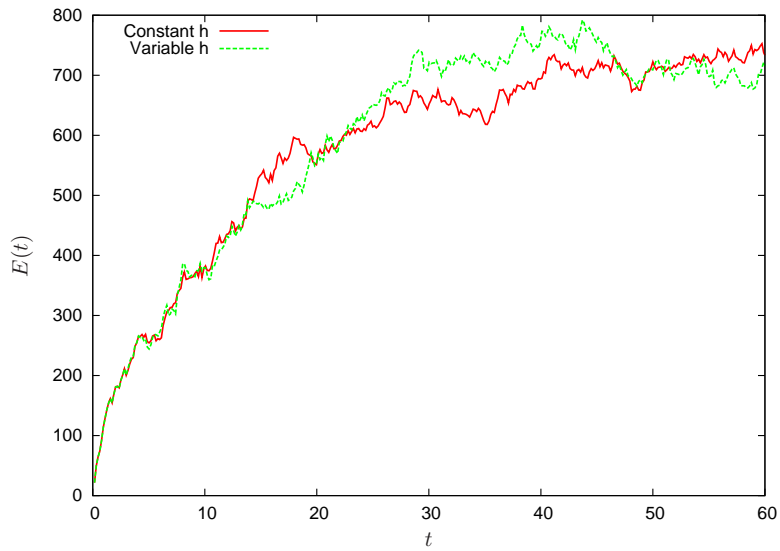
$$h_a = \sigma \left( \frac{m_a}{\rho_a} \right)^{1/d}. \quad (6.3.5)$$

Either formulation resulted in largely similar results for the forced turbulence, except that the variable  $h$  simulation experienced a gradual loss of mass over time.

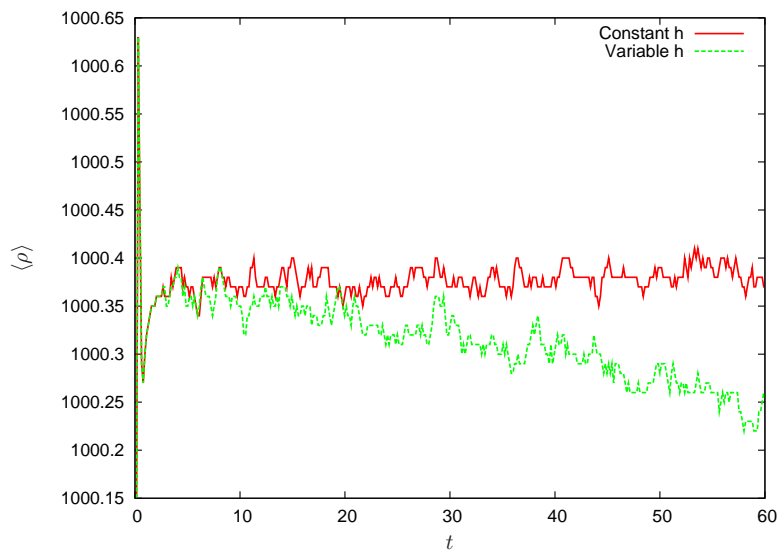
Figure 6.26(a) shows the evolution of kinetic energy for both simulations. It indicates that the strength of the inverse energy cascade is not dependant on what formulation is used. Similar results were obtained from the kinetic energy and viscous spectra, as well as the evolution of the vorticity field.

However, the one difference between a constant or variable  $h$  is the slow but persistent loss of mass over time, as calculated from the density of the particles. Figure 6.26(b) shows a plot of average density versus time for both simulations. Over a time period  $0 < t < 60$  the average density reduces from  $\langle \rho \rangle = 1000.34$  to  $\langle \rho \rangle = 1000.23$ . This is a very small change and does not have any effect on the accuracy of the simulation over this time period. Due to the fact that there is no advantage to be gained through the use of a variable  $h$ , all other forced turbulence simulations in this thesis use a constant smoothing length.

The gradual loss in mass is due to an inconsistency in the rate of change of density equation. The equation used for the results in Figure 6.26 is



(a) Normalised total kinetic energy



(b) Average density

**Figure 6.26:** Comparison of spatially varying and constant smoothing length  $h$ .

$$\frac{d\rho}{dt} = \sum_b m_b \mathbf{v}_{ab} \cdot \nabla_a W_{ab}. \quad (6.3.6)$$

However, given that the particle densities are defined as

$$\rho_a = \sum_b m_b W(\mathbf{r}_a - \mathbf{r}_b, h_a), \quad (6.3.7)$$

and assuming a  $h_a(t)$  that is time-dependant, the rate of change of density then becomes

$$\frac{d\rho_a}{dt} = \sum_b m_b \left[ (\mathbf{v}_a - \mathbf{v}_b) \cdot \nabla_a W_{ab} + \frac{\partial W_{ab}}{\partial h_a} \frac{\partial h_a}{\partial \rho_a} \frac{d\rho_a}{dt} \right], \quad (6.3.8)$$

$$= \frac{1}{\Omega_a} \sum_b m_b \mathbf{v}_{ab} \cdot \nabla_a W_{ab}. \quad (6.3.9)$$

where  $\Omega_a$  is defined as

$$\Omega_a = 1 - \frac{\partial h_a}{\partial \rho_a} \sum_b m_b \frac{\partial W_{ab}}{\partial h_a}. \quad (6.3.10)$$

This equation represents a correction to  $d\rho/dt$  due to the time-varying nature of the smoothing length. A similar correction also applies to the SPH momentum equation. Monaghan (2002) gives the corrected momentum equation as

$$\frac{d\mathbf{v}_a}{dt} = - \sum_b m_b \left( \frac{P_b}{\Omega_a \rho_b^2} + \frac{P_b}{\Omega_b \rho_b^2} + \Pi_{ab} \right) \nabla_a W_{ab}. \quad (6.3.11)$$

## 6.4 Effective Viscosity

The homogeneous nature of the turbulence in these simulations allows the definition of a measure of simulation accuracy that is spatially and time independent. This provides a single quantitative measure of the accuracy that can be used to compare different 2D turbulence simulations. It also provides a measure of the excess numerical dissipation seen in the forced turbulence simulations.

We start with the usual Navier-Stokes momentum equation with an additive forcing term  $\mathbf{F}$

$$\frac{D\mathbf{v}}{Dt} = -\nabla \frac{P}{\rho} - \nu \nabla \times \omega + \mathbf{F}. \quad (6.4.1)$$

Taking the dot product of both sides with the velocity  $\mathbf{v}$  gives a rate of change of kinetic energy on the left hand side and terms corresponding to the pressure, viscous and forcing

term power on the right. The flow is assumed to be incompressible, so  $\nabla \cdot \mathbf{v} = 0$ .

$$\frac{D}{Dt} \left[ \frac{1}{2} \mathbf{v}^2 \right] = -\nabla \cdot \left[ \frac{P\mathbf{v}}{\rho} \right] - \nu [\omega^2 + \nabla \cdot (\omega \times \mathbf{v})] + \mathbf{F} \cdot \mathbf{v}. \quad (6.4.2)$$

We then take the spatial average  $\langle \cdot \rangle$  of this equation. Assuming that the turbulence in the box is statistically homogeneous, the average gradient of  $P\mathbf{v}/\rho$  and  $\omega \times \mathbf{v}$  in any direction will be approximately zero and therefore all the divergences will integrate to zero. Of course, this will not be true near the non-slip boundaries, but should be valid over the majority of the domain.

$$\frac{d}{dt} \left[ \frac{1}{2} \langle \mathbf{v}^2 \rangle \right] = -\nu \langle \omega^2 \rangle + \langle \mathbf{F} \cdot \mathbf{v} \rangle. \quad (6.4.3)$$

For the SPH simulation, if the force on each particle  $\mathbf{f}$  is divided into viscous  $\mathbf{f}_v$ , pressure  $\mathbf{f}_p$  and forcing terms  $\mathbf{f}_F$  (where  $\mathbf{f}_F$  is  $\mathbf{F}$  evaluated at the particle's position), then the SPH equivalent to (6.4.2) for any particle will be

$$\mathbf{f} \cdot \mathbf{v} = \mathbf{f}_p \cdot \mathbf{v} + \mathbf{f}_v \cdot \mathbf{v} + \mathbf{f}_F \cdot \mathbf{v}. \quad (6.4.4)$$

We will assume that the SPH pressure and viscous terms are accurate approximations to their continuum equivalents. Making the same assumptions and spatial averages as the continuum case we end up with the SPH equivalent to (6.4.3).

$$\langle \mathbf{f} \cdot \mathbf{v} \rangle = -\nu_{eff} \langle \omega^2 \rangle + \langle \mathbf{f}_F \cdot \mathbf{v} \rangle. \quad (6.4.5)$$

The spatial averages in this equation are easily calculated and the Effective Viscosity  $\nu_{eff}$  for the simulation can be found. Table 6.1 shows values for the spatial averages and  $\nu_{eff}/\nu$  (where  $\nu$  is the actual viscosity given to the SPH simulation) for the forced turbulence simulation using the classic Cubic Spline kernel, the Modified Cubic Spline (See Chapter 7), the Wendland kernel with no-slip walls (for the square box) and the Wendland kernel using periodic boundary conditions (i.e. no walls). The results are taken from the simulation while it is statistically steady ( $t > 20$ ) and they are given as *mean*  $\pm$  *standard deviation* over the time period  $20 < t < 50$ .

The Effective Viscosity calculated in this way is simply a comparison between the SPH simulation and the expected continuum case. Given the velocity, vorticity and forcing terms reported by the SPH simulation, the Effective Viscosity is the viscosity expected in the continuum. It does not say anything about the source of the difference between the viscosity given to the SPH simulation  $\nu$  and the Effective Viscosity  $\nu_{eff}$ .

The no-slip walls, even though they violate the assumption of homogeneity, do not seem to alter the results significantly from the periodic boundary conditions. The Effective Viscosity calculated using the Wendland kernel and no-slip boundaries ( $1.6 \pm 0.042$ ) is very close to the Effective Viscosity calculated using this kernel and the periodic boundary conditions ( $1.5 \pm 0.194$ ).

**Table 6.1:** *Effective Viscosity and accompanying spatial averages using the Cubic Spline, Modified Cubic Spline, Wendland kernel with no-slip boundary conditions and the Wendland kernel with periodic boundary conditions*

Simulation	$\nu_{eff}/\nu$
Cubic Spline	$3.4 \pm 0.105$
Modified Cubic Spline	$2.57 \pm 0.088$
Wendland (no-slip boundaries)	$1.6 \pm 0.042$
Wendland (periodic boundaries)	$1.5 \pm 0.194$

Simulation	$\langle \mathbf{f} \cdot \mathbf{v} \rangle$	$\langle \mathbf{f}_p \cdot \mathbf{v} \rangle$
Cubic Spline	$0.0074 \pm 0.1088$	$0.1802 \pm 0.1085$
Modified Cubic Spline	$0.0172 \pm 0.0988$	$0.1717 \pm 0.09899$
Wendland (no-slip boundaries)	$0.0155 \pm 0.1052$	$0.1849 \pm 0.1067$
Wendland (periodic boundaries)	$0.03399 \pm 0.1028$	$0.1918 \pm 0.1015$

Simulation	$\langle \omega^2 \rangle$	$\langle \mathbf{f}_p \cdot \mathbf{v} \rangle$
Cubic Spline	$169.6 \pm 15.58$	$-7.467 \times 10^{-5} \pm 0.00345$
Modified Cubic Spline	$200.34 \pm 12.89$	$5.88 \times 10^{-6} \pm 0.0043$
Wendland (no-slip boundaries)	$211.9 \pm 14.49$	$-1.35 \times 10^{-4} \pm 0.0033$
Wendland (periodic boundaries)	$209.7 \pm 11.08$	$1.16 \times 10^{-4} \pm 0.01997$

Also, (6.4.3) makes the assumption that  $\langle \nabla \cdot \left[ \frac{P\mathbf{v}}{\rho} \right] \rangle = 0$ . The SPH equivalent to this term,  $\langle \mathbf{f}_p \cdot \mathbf{v} \rangle$ , is also recorded in Table 6.1. Given that the mean is very close to zero and the standard deviation is at least an order of magnitude less than then next smallest term ( $\langle \mathbf{f} \cdot \mathbf{v} \rangle$ ) for all simulations, this assumption is valid for the SPH simulation.

The Effective Viscosity therefore provides a meaningful measure of the actual viscous dissipation occurring in the SPH simulation of forced turbulence. The results discussed thus far all use the Wendland kernel (with no-slip boundaries). The Effective Viscosity calculated for this kernel is 60% greater than the actual viscosity given as a parameter to the simulation.

## 6.5 Periodic Forced Turbulence

The flow in the wall-bounded simulations already shown in this chapter contain a number of important processes that all must be simulated correctly. The no-slip boundaries act as a source of high amplitude vorticity filaments and the square geometry of the box exerts a net torque to the fluid, which results in a rapid increase in total angular momentum. At the same time, the turbulent flow in the centre of the box results in the formation of the inverse energy and direct enstrophy cascades. The purpose of this section is to investigate how well our SPH implementation reproduces the effects of the turbulent cascades in isolation, without the contributions from the no-slip boundaries. Similarly, Section 6.6 explores the boundary layer effects without the complication of the central

turbulent flow.

This section presents the results of an SPH simulation of forced turbulence in a periodic box. Without the no-slip boundaries there are no longer any sources of torque on the fluid and hence no spin-up. There are also no sources of strong vorticity filaments to disrupt any self-organised structures. However the basic processes of 2D turbulence remain, most importantly the inverse energy cascade. For both the decaying and forced 2D turbulence in a double-periodic box, the end state is expected to be a double dipole vortex, caused by the condensation of kinetic energy in the longest possible wavelength, which is the width of the box. For the case of continually forced turbulence this should be a steady-state, since there are no longer any vorticity filaments from the boundaries to disrupt the double vortex.

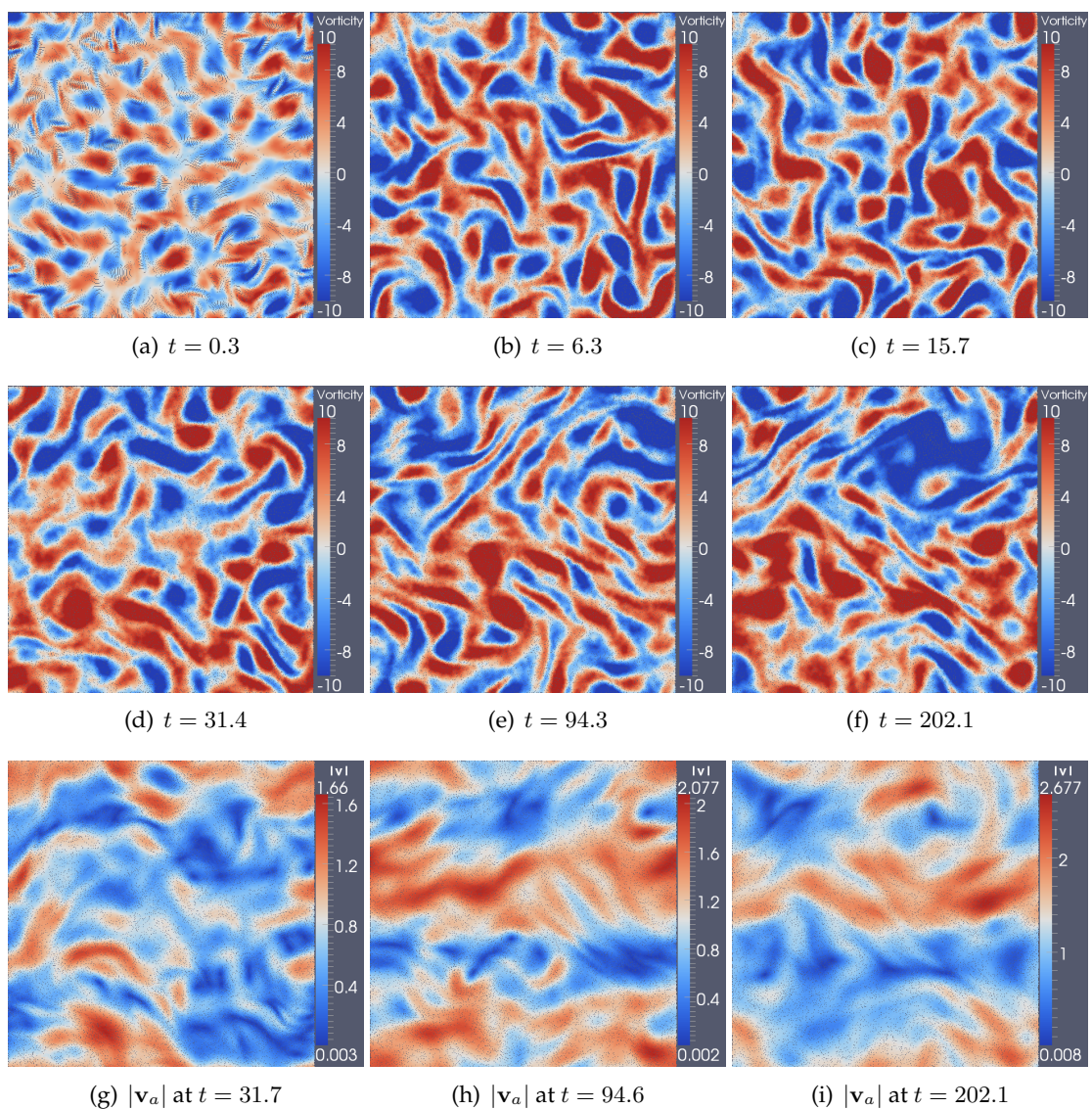


**Figure 6.27:** Evolution of the periodic forced turbulence simulation. Plots (a)-(f) show particles coloured by vorticity, which has been clipped to  $-10 \leq \omega \leq 10$  in order to clearly show the vortex structures of the flow. Plots (g)-(i) show the magnitude of the particle's velocity

All the input parameters for this simulation, for the forcing term as well as the SPH method, were identical to the previous wall-bounded simulations.

The evolution of the vorticity field for the periodic simulation is shown in Figure 6.27. In a similar fashion as the wall-bounded case, there is a rapid increase in the scale of the eddies from  $t = 0$  to  $t \approx 15$ . From  $15 < t < 30$ , the growth in eddy scale gradually increases until it levels out at about  $t \approx 30$ .

The general shape of the vortices in the periodic simulation is quite different to the wall-bounded case. Whereas in the previous simulations the vortices tended to be rounder, the vortices shown in these snapshots are more elongated and filamentary. Often these filaments will line up in a local region in space, effectively giving the turbulence in that region a “grain”.

The vorticity and velocity fields continue relatively unchanged until a large dipole structure starts to emerge at  $t \approx 70$ . These structures are characterised by a greater density of like-signed eddies in a particular region of the flow, as well as large roughly circular structures in the velocity field. They can be seen in Figure 6.27(f) at the upper left quadrant and the rightmost edge of the bottom right quadrant. The dipole structure becomes more prominent from  $70 < t < 100$ . This growth levels off at  $t \approx 100$  and the features of the vorticity and velocity field are unchanged for the remainder of the simulation.

Figure 6.28 shows the evolution of total kinetic energy for the periodic simulation. Without the extra dissipation due to the no-slip boundaries, the total kinetic energy increases at a much faster rate. The turbulence is followed until the dissipation halts the energy build-up and the simulation reaches a steady state at  $t \approx 200$ . Apart from this levelling out, the strongest feature in the evolution of  $E$  is the kink that can be seen at  $t \approx 100$ . This corresponds to the halt in the evolution of the velocity and vorticity fields, once the dipole structure has fully formed. Subsequent to this, the build-up of energy in the flow is reduced, but it takes until  $t \approx 200$  for it to halt entirely.

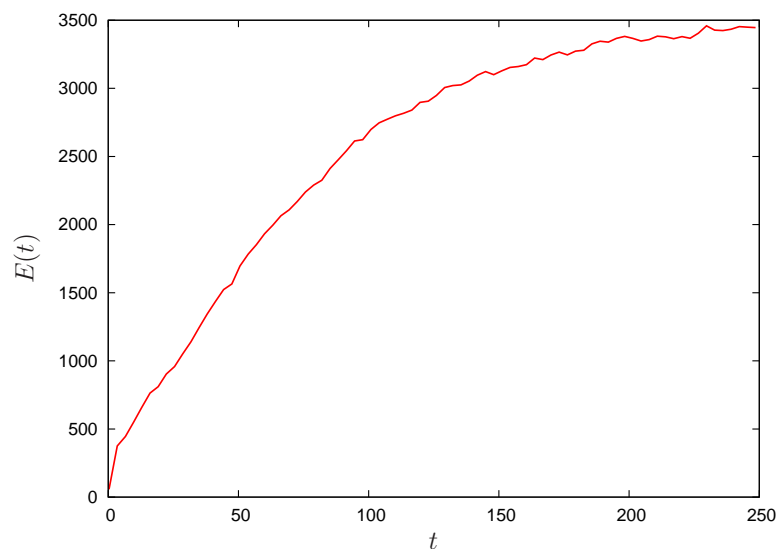


**Figure 6.28:** Normalised total kinetic energy for periodic forced turbulence simulation.

The kinetic energy spectra corresponding to a subsample of the vorticity plots are shown

in Figure 6.29. The evolution of the spectra is similar to the wall-bounded case. A direct enstrophy cascade range is quickly established by  $t = 6.6$  which follows the expected scaling of  $k^{-3}$  very well. Energy slowly builds up in the smaller wavenumbers over time until by  $t = 202.1$  the spectra for  $\tilde{k} > 1$  scales as  $E \sim k^{-5/3}$ . While this indicates the presence of an inverse energy cascade, the condensation of energy into  $k = 1$  and the associated steepening of the spectra at this wavenumber is not seen.

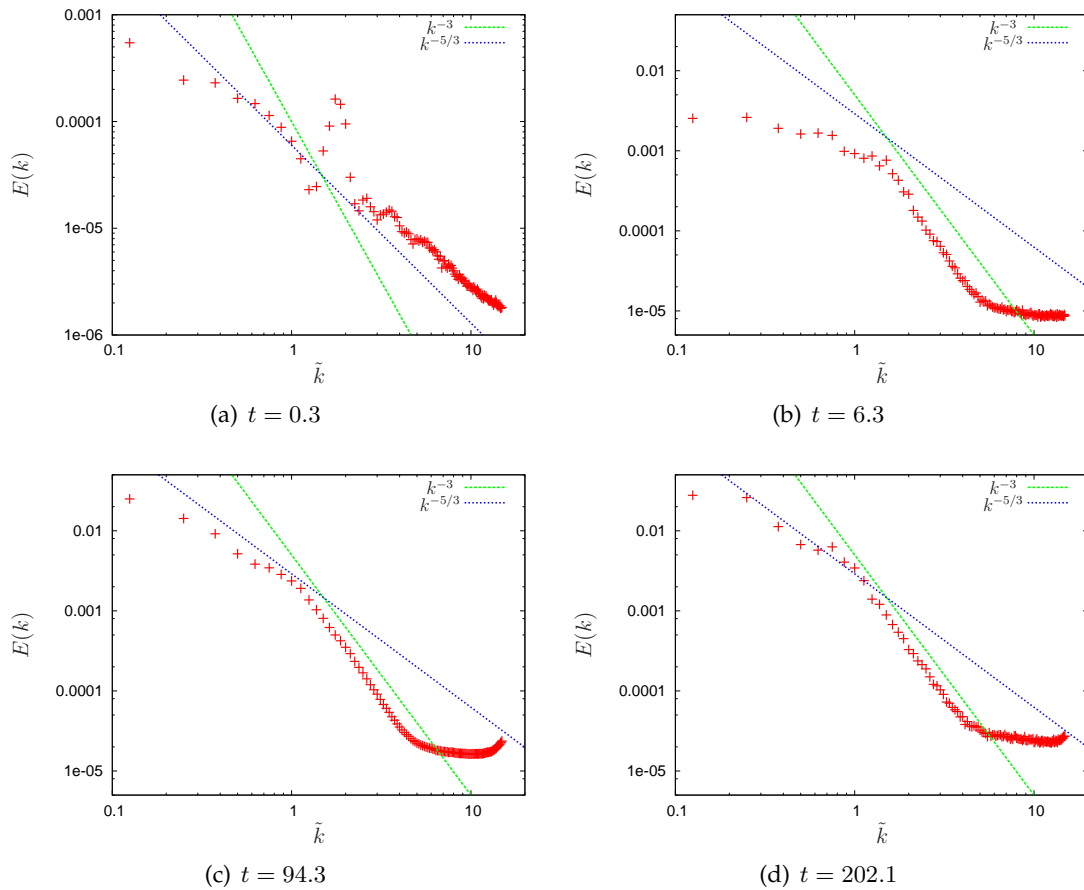


**Figure 6.29:** Evolution of the kinetic energy spectrum for the periodic forced turbulence simulation.

The results from SPH simulation of forced periodic turbulence produce a similar picture to the wall-bounded case. The direct enstrophy cascade is reproduced well down to  $\tilde{k} = 4.5$ , and there is clear evidence of an inverse energy cascade. However, the strength of this cascade is much weaker than expected, and does not result in the condensation of energy into the longest mode.

Tran & Bowman (2004) introduced a notation to describe the strength of the inverse energy cascade for periodic 2D turbulence. They stated that the strength of the cascade is characterised by the fraction  $r$  of the input energy that escapes viscosity and is transferred to the larger scales. A *strong* cascade occurs when  $1 - r \ll 1$ . Tran & Bowman (2004) used a pseudospectral code to simulate forced turbulence in the case where the forcing scale is not sufficiently removed from the dissipation scale. They found that the inverse energy cascade is remarkably robust, and that even in the absence of the direct

enstrophy range the strength of the inverse energy cascade for  $Re = 2000$  was  $r = 0.3$ . For our SPH simulations, where the forcing scale is well removed from the dissipation scale and the energy spectra shows a clear direct enstrophy cascade of  $k^{-3}$ , this value should be close to  $r = 1$ . However, the calculation of  $r$  over the time period  $10 < t < 30$  gives a value of  $r = 0.145$ , which is significantly lower than expected.

The periodic forced turbulence SPH simulations by Mansour (2007) also found the presence of a weak inverse energy cascade. However, Mansour reported quite a different energy spectra in the direct enstrophy range ( $\tilde{k} > 1$ ), with a scaling of approximately  $k^{-5}$ . This was attributed to the SPH viscosity acting over a range of scales that is unphysically broad, enough to affect the forcing scale and remove the existence of an inertial range. This  $k^{-5}$  scaling was reported for an SPH simulation at  $Re = 1064$  that was forced at  $k = 10$ , which is comparable to the forcing scale used in our simulations. Our results indicate that for  $Re = 2645$  (periodic turbulence) and  $Re = 1581$  (wall-bounded turbulence) this forcing scale is sufficiently removed from the dissipation range to allow the creation of an inertial range and a direct enstrophy cascade.

In conclusion, the removal of the no-slip boundaries does not substantially alter the performance of the inverse energy and direct enstrophy cascades. This is physically correct, as strength of both of these cascades is independent of the boundaries and depends only on the homogeneous turbulent flow in the centre of the box. This result indicates that the weak inverse energy cascade and the lack of energy condensation in the longest mode is not a consequence of the incorrect simulation of the no-slip boundaries or the boundary layer.

## 6.6 Spinning Box Turbulence

One of the primary roles that the no-slip boundaries play in wall-bounded turbulence is the generation of high intensity vorticity filaments that are created via the boundary layer and then advected into the centre of the domain. These filaments and the coherent vortices that they evolve into have a strong impact on the evolution of the turbulence. In the case of decaying turbulence presented in Chapter 5, it was found that the boundaries produced these vorticity filaments, but they quickly dissipated once they had separated from the wall and did not seem to have a significant impact on the evolution of the turbulence. In particular, none of the filaments were rolled up into long-term coherent vortices. This did not match the pseudospectral simulations by Clercx et al. (1999) nor the experimental results by Maassen et al. (2002). In the forced turbulence simulations presented earlier in this chapter the situation was improved. It was found that the filaments did form coherent vortices that persisted for many turn over times within the flow. Furthermore, the boundary layers were clearly a strong source of vorticity. If an eddy approached a boundary layer of a similar sign, the boundary layer (once detached from the wall) would merge with the eddy to form a stronger and larger structure.

In order to resolve how well SPH models the production and evolution of the vorticity filaments at the wall, the oscillating box used by Wells et al. (2007) was setup as an SPH simulation. Wells et al. present results from an experiment and matched pseudospectral simulations of forced turbulence that use the high intensity vorticity structures that are generated at the walls as a forcing protocol. The geometry of these experiments is the traditional square box that is made two-dimensional or quasi-two-dimensional. The box

is then given a sinusoidally varying angular velocity. The variation in the angular velocity of the box promotes strong boundary layers, which roll up in the corners to form vortices. Once the rotation of the box changes direction these move away from the corner and along the wall of the box. The vortices then roll up the boundary layer along the wall (this will have an opposite sign, since the direction of the spin has been reversed) and form a dipole vortex. These dipoles are advected into the interior of the domain and persist for many oscillation periods. They interact with each other and so rapidly build up a fully turbulent flow. The input vortices from the walls will always have a similar width that is based on the Reynolds number of the flow and the oscillating frequency. Therefore, this provides a practical method to inject energy into the flow at a particular forcing scale.

The SPH geometry for this simulation is the same square box with four layers of SPH boundary particles to model the no-slip boundaries. In order to simulate the oscillation of the box, the boundary particles are given a sinusoidally varying angular velocity  $\Omega(t)$

$$\Omega(t) = A \sin(ft). \quad (6.6.1)$$

An SPH simulation was implemented with parameters that matched one of the pseudo-spectral simulations described in Wells et al. (2007). The oscillation amplitude is  $A = 0.75$  and the frequency is  $f = 1$ . This gives a dimensionless frequency of  $\mathcal{F} = f/A = 1.25$  and a Reynolds number of  $Re = UL/\nu = AL^2/\nu = 5000$ , where  $L$  is the half-width of the box.

The evolution of the SPH vorticity field is shown in Figure 6.30. The velocity of the particles at  $t = 0$  was initialised in a similar fashion as the decaying turbulence simulations in Chapter 5. This was done to break any initial four-fold symmetries and to provide an initial turbulent flow to encourage dipole formation at the boundaries (Wells et al. (2007) uses a similar initial velocity field).

After one oscillation  $\tilde{t} = 1$  the vorticity of the particles shows a strong negative boundary layer forming on all four sides of the box. This is being rolled up in the corners and in the centre of the walls due to vortices already present in the flow.

Wells et al. (2007) estimates the size of the boundary layer thickness  $\delta$  following the example by Kundu (1990)

$$\frac{\delta}{l} \approx \pi \sqrt{\frac{2}{Re\mathcal{F}}}. \quad (6.6.2)$$

For these simulation parameters, this gives an estimated thickness of  $\delta \approx 0.0561$ . This is a reasonable approximation to the size of the boundary layers seen in the SPH simulations. Taking their width once they have separated from the walls, the thickness in the SPH simulation ranges from  $\delta = 0.05$  to  $\delta = 0.1$ .

More easily measured, and perhaps more relevant to the evolution of the flow is the size and strength of the vortices formed by the roll up of the boundary layer. Wells et al. (2007) estimates these from assuming that the area of the vortex is given by  $A_v = \pi r^2 = l\delta$ . Thus, the radius  $r$  is given by

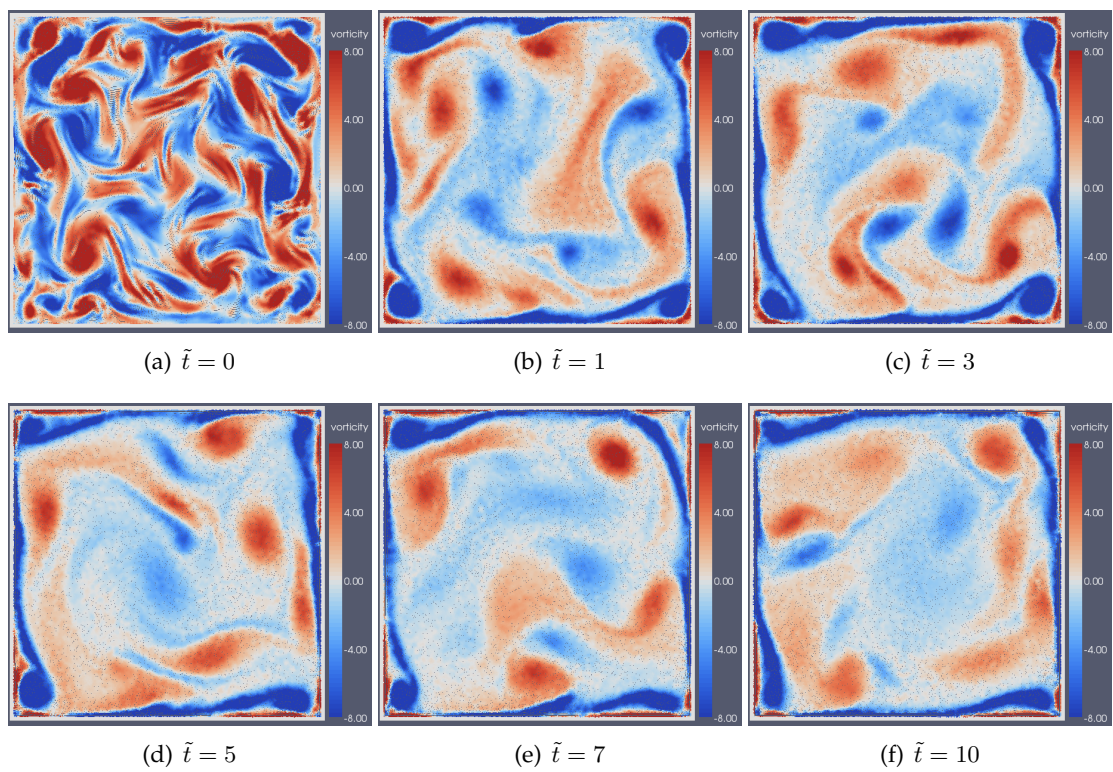


**Figure 6.30:** Evolution of the vorticity field in the oscillating box. The time  $\tilde{t}$  has been scaled by the oscillation period.

$$\frac{r}{l} \approx \left( \frac{2}{Re\mathcal{F}} \right)^{1/4}. \quad (6.6.3)$$

From this equation the expected radius of the input vortices is  $r = 0.134$ . This matches well with both the SPH and the pseudospectral results by Wells et al. (2007). The vortices formed at the corners during the SPH simulation have a radius that ranges within  $0.10 < r < 0.15$ .

Assuming a parabolic vorticity distribution in the vortices of the form  $\omega(x) = \omega_{max}(1 - (x/r)^2)$ , Wells et al. (2007) estimates that the maximum vorticity  $\omega_{max}$  is given by

$$\frac{|\omega_{max}|}{A} \approx 0.29\sqrt{Re\mathcal{F}}. \quad (6.6.4)$$

This results in  $\omega_{max} \approx 22.9$  for this simulation. Wells et al. (2007) reports a maximum vorticity of  $\omega_{max} = 25$  whereas the value recorded by the SPH simulation ranges between  $18 < \omega_{max} < 21$ .

These results indicate that the boundary layer at the wall and the vortices created by the roll-up of this layer are being modelled accurately by the SPH simulation. Their size and strength correspond well to both theoretical predictions and an independent pseudospectral simulation.

Unfortunately, while the forcing term provided by the no-slip boundaries is accurately simulated, the interior of the flow does not match up to either the experimental results or the simulations by Wells et al. (2007). The vorticity plot at  $\tilde{t} = 1$  in Figure 6.30 gives a good picture of the expected steady state for the oscillating box at  $Re = 5000$  and  $\mathcal{F} = 1.25$ . The turbulent eddies in the interior roll up the boundary layers to form dipole structures which are advected into the middle of the box. These dipole structure interact with other dipoles, forming a turbulent cascade.

However, in the SPH simulation the initial turbulent velocity field dies away over the duration of the simulation. For  $0 < \tilde{t} < 6$  the remaining turbulence in the interior helps to advect the dipole structures away from the walls and often into (and across) the centre of the domain. However, after  $\tilde{t} \approx 7$  the strength of the interior vortices has died away to the point where the newly formed dipoles do not move further than  $2r$  away from the wall. The instances of dipole-dipole interaction are rare and very weak, and the motion of the fluid starts to obtain a four-fold symmetry that contains little of the random and chaotic hallmarks of turbulence flow. The strength of the dipole structures is significantly lower than expected. While the average vortex amplitude in the SPH simulation was found to be  $\omega_{mean} = 5.6$  over the time period  $9 < \tilde{t} < 10$ , Wells et al. (2007) reports a value of  $\omega_{mean} = 17.5$ .

The results in this section indicate that the boundary layer near the no-slip boundaries is modelled accurately by the SPH implementation. This is in-line with the results given by Violeau & Issa (2007), which showed that SPH can produce accurate log-laws for the velocity of turbulent channel flow near a no-slip boundary. This section also examines the subsequent detachment of the boundary layer and its roll-up into a coherent vortex. This process is modelled well in the SPH results and matches existing experimental results by

Wells et al. (2007). However, once the vortices move away from the boundary and into the central flow, they are dissipated on a much shorter timescale than expected.

## 6.7 Conclusion

While the SPH simulations of decaying turbulence in the previous chapter compared well with other published pseudo-spectral simulations, the results for forced turbulence are not as promising. Two-dimensional forced wall-bounded turbulence is characterised by the formation of a large monopole vortex and the injection of high amplitude vorticity filaments from the boundaries. While SPH accurately models the boundary layers and the initial formation of the high amplitude vorticity filaments from the walls, the evolution of the turbulence in the interior of the flow suffers from excessive dissipation, which prevents the formation of the monopole vortex and dissipates the injected filaments before they can significantly contribute to the flow.

The excess dissipation seen in the SPH turbulence simulations is due to velocity fluctuations at small and medium length scales. These show up in kinetic energy spectra as a deviation from the expected direct enstrophy scaling of  $k^{-3}$  for length scales less than 8 particle spacings. Since the viscous dissipation  $P_v(k)$  is related to the kinetic energy  $E(k)$  via  $P_v(k) \sim k^2 E(k)$ , these velocity fluctuations result in a significant energy sink, which dissipates a large proportion ( $\approx 85\%$ ) of the kinetic energy before it can be transferred to longer wavelengths through the action of the inverse energy cascade. The velocity fluctuations also act as an additional forcing scale for the flow, which seems to be affecting the mixing properties of the simulation. Particle pair dispersion results indicate that these fluctuations increase the rate of mixing at smaller length scales.

On a more promising note, the SPH results indicate that the direct enstrophy cascade is modelled correctly and produces the  $k^{-3}$  scalings for wavelength greater than 8 particle spacings. This is in contrast to existing SPH results by Mansour (2007), which did not find the existence of a direct enstrophy cascade. Even though the inverse energy cascade is significantly weakened by the excess dissipation, this cascade was still present in the SPH results, and the kinetic energy spectra followed the expected  $k^{-5/3}$  scaling for medium wavelengths.

The excess dissipation seen in these results does not arise from a lack of resolution, and care is taken to ensure that the smoothing length  $h$  is smaller than the expected dissipation scale of the turbulence. The excess dissipation can be moderated somewhat by using extreme resolutions. However, resolution studies indicate that in order to prevent the velocity fluctuations from affecting the turbulence (i.e. moving the fluctuations below the inertial range) the resolution would need to be in excess of 3500x3500 particles. Even a relatively simple 2D turbulence simulation would not be feasible at these resolutions, much less a three dimensional simulation.

The SPH results also show a significant amount of pressure fluctuations at length scales less than 10 particle spacings. Studies varying the numerical sound speed (and therefore the scale of the pressure field) indicate that the viscous dissipation and the strength of the inverse energy cascade are both very sensitive to this parameter. Attempts to smooth the pressure field via the periodic smoothing of the density field did not result in any substantial improvements. While the density smoothing removes some of the excess viscous

dissipation, this is exactly balanced by the potential energy lost due to the smoothing of the pressure gradients.

In conclusion, the SPH method used in this thesis is unsuitable for modelling continually forced 2D turbulence. While some aspects of the turbulent flow are reproduced well, the fundamental problem lies in the excess dissipation produced by the method. This results in a much lower than expected flux of kinetic energy to longer wavelengths. The cause of this problem cannot currently be identified.

These problems are perhaps more significant for 2D turbulence rather than 3D. Due to the inverse energy cascade, the small scales must be correctly modelled in order to obtain the (more obvious) large scale flow. For three-dimensional turbulence, the flux of energy is reversed and any excess dissipation would only be expected to affect smaller length scales.

However, for SPH to be considered a useful numerical method for turbulent simulations it is important that the energy dissipation is modelled accurately. Furthermore, it is likely that the velocity fluctuations and excess dissipation will complicate the development of any SPH turbulence model. Existing SPH turbulence models have not shown any significant improvement in performance over standard SPH. Many such models involve the addition of an extra dissipative term in order to remove any energy below the resolution limit of the simulation. However, the SPH method is overly dissipative to begin with, so this would not be expected to improve the situation. In addition, many turbulence models rely on the accurate calculation of local velocity gradients, which is not currently possible due to the small and medium scale noise in the velocity field.

## Chapter 7

# Kernel Effects on Particle Clumping

---

One artifact often observed in SPH simulations is the tendency of the particles to cluster together, leading to large variations in the particle spacing. This artifact is usually attributed to the SPH Tensile Instability. The Tensile Instability was first studied by Swegle et al. (1995) who found that the SPH method was unstable for negative pressures. This instability is mostly seen in simulations of solids under tension. However, it has also been reported in simulations of gas (Schussler & Schmitt 1981) and liquid (Meleán et al. 2004) dynamics.

Initial SPH simulations of forced turbulence using the Cubic Spline kernel resulted in a significant level of particle clumping, even when a constant positive pressure was applied by reducing the reference density in the equation of state. This chapter presents the results from a statistical study of the particle clumping and its relationship to the properties of the Cubic Spline kernel and the lesser known Wendland kernel.

Figure 7.1 shows a typical distribution of SPH particles during the forced turbulence simulation, using a Cubic Spline kernel with  $h/\Delta p = 1.95$  (where  $\Delta p$  is the average particle spacing). The particles are unevenly spaced, and the distribution of the particles is characterised by clumps of two or more particles separated by large voids.

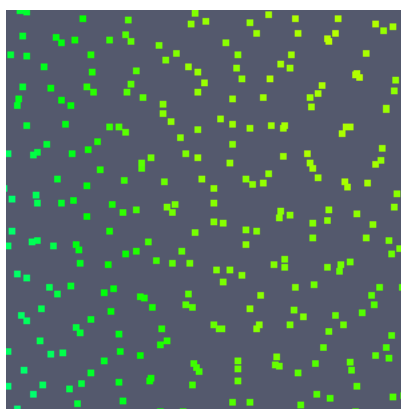


**Figure 7.1:** Typical particle distribution for forced turbulence simulation. The Cubic Spline kernel is used with  $h/\Delta p = 1.95$

One advantage of the forced turbulence simulations is that the turbulent flow (sufficiently far away from the boundaries) is homogeneous both in time and space. We would therefore expect that the statistical properties of the particle distribution would be constant over the entire domain (except close to the boundaries, if there are any). This allows the calculation of a Radial Particle Density Function  $R_\rho$ , which we can use to investigate the nature of the particle clumping.

## 7.1 Radial Particle Density Function

The Radial Particle Density Function  $R_\rho$  is calculated by taking a random sample of  $N$  particle pairs that are separated by a distance of less than  $2h$  and at least  $0.25$  away from the boundaries. A histogram of their separations  $H(r) = \text{hist}(|\mathbf{r}_{ab}|)$  is calculated (Figure 7.2(a)). This histogram is then divided by the area of each bin and the total number of particle pairs. It is normalised by multiplying by the average area of each particle, which ensures that  $R_\rho = 1$  when the particle number density is equal to the average particle number density of the simulation. If each bin has its lower and upper limits as  $r = r_l$  and  $r = r_u$ , then  $R_\rho$  is defined as

$$R_\rho(r) = \frac{H(r)4h^2}{N(r_u^2 - r_l^2)}. \quad (7.1.1)$$

Figure 7.2(b) shows  $R_\rho$  for the forced turbulence simulation using the Cubic Spline kernel (the same simulation that produced the particle distribution in Figure 7.1). The radial distance has been scaled by the smoothing length  $q = r/h$ . A clear peak can be seen at  $q \approx 1$ . There is also a minimum at  $q \approx 0.5$ , which roughly corresponds to the average particle spacing. In contrast, a particle distribution that was regularly spaced would have a clear peak at the average particle spacing. Instead, the peak that can be seen at  $r = h$  means that the particles tend to form groups of particles a distance of  $h$  apart. Subsequent simulations varying the value of  $h$  (but keeping the particle spacing constant) show that the peak in  $R_\rho$  follows the value of  $h$ .

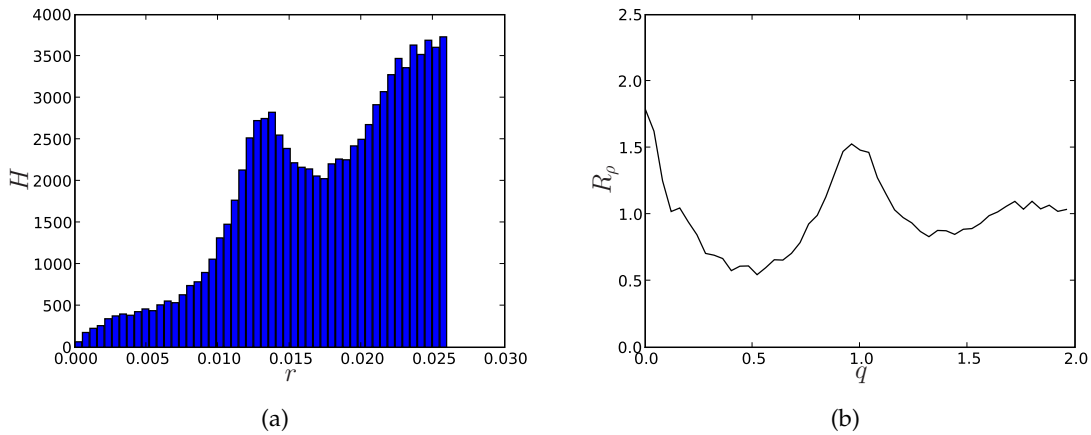


**Figure 7.2:** (a) Histogram of particle separations for 90000 random particle pairs. (b) Radial particle density function  $R_\rho$  for the same set of particle pairs.

## 7.2 Clumping versus Spline Point position

The equation of a Cubic Spline kernel is

$$W(s) = \frac{\beta}{h^d} \begin{cases} (2-q)^3 - 4(1-q)^3 & \text{for } 0 \leq q < 1, \\ (2-q)^3 & \text{for } 1 \leq q < 2, \\ 0 & \text{for } q > 2. \end{cases} \quad (7.2.1)$$

For this kernel,  $q = 1$  or  $r = h$  is also the location of the join between the first two subintervals of the kernel, hereafter termed the *spline point*. To see if the maxima in  $R_\rho$  follows  $h$  or the location of the spline point, a new kernel generalising the Cubic Spline has been defined. This kernel locates the spline point at  $q = q_0$ , while keeping the radius of the kernel at  $q = 2$ .

$$W_g(q) = \frac{\beta}{h^d} \begin{cases} (2-q)^3 - \frac{4}{q_0^3}(q_0-q)^3 & \text{for } 0 \leq q < q_0, \\ (2-q)^3 & \text{for } q_0 \leq q < 2, \\ 0 & \text{for } q > 2. \end{cases} \quad (7.2.2)$$

where  $\beta = 10/(h^2\pi(32 + 4q_0^3))$  in 2D. This kernel was inspired by Price (2004), who derived a similar kernel with an arbitrary order and two spline points.

Further tests using this kernel with varying  $q_0$  revealed that the peak in  $R_\rho$  follows the placement of the spine point. Figure 7.3 shows four plots of  $R_\rho$ , each using a different value of  $q_0$ . The location of the spline point is highlighted by a dashed vertical line. In each plot the peak in  $R_\rho$  clearly corresponds with the location of the spline point (i.e.  $q = q_0$ ).

This indicates that the tendency of particles to clump together is directly related to a property of the kernel. In the case of the Cubic Spline kernel, this is the location of the spline point. Using this information, it is straightforward to see that  $q_0$  must be set to the initial particle spacing in order to minimise particle clumping. The result is shown in Figure 7.3(a) and 7.4, which show the Radial Particle Density Function and a typical distribution of particles with  $q_0 = \Delta p/h = 0.5$  (where  $\Delta p$  is the average particle spacing). This particular kernel (i.e. the Generalised Cubic Spline with  $q_0 = 0.5$ ) is referred to as the Tuned Cubic Spline for the remainder of this Chapter, although it should be noted that it is only tuned for a particular value of  $\Delta p/h$ .

At this point, it should be stated that these simulations do not use the anti-clumping term described by Monaghan (2000). While the addition of this term decreases  $R_\rho$  over the range  $0 < r < 0.25$ , it does not affect the location or size of the peak in  $R_\rho$ .

## 7.3 The Wendland Kernel

Wendland (1995) has proposed a radial interpolation function  $\psi$  that has compact support

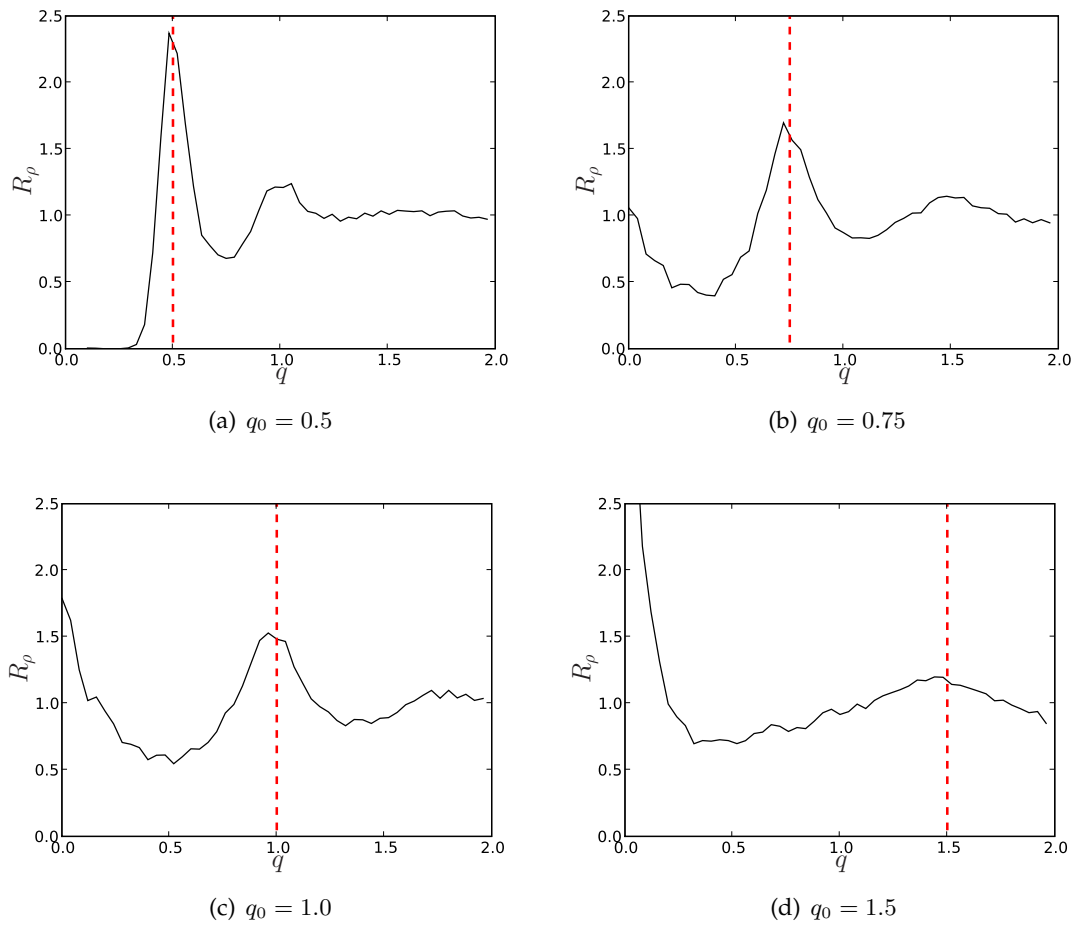


**Figure 7.3:** Radial Particle Density  $R_\rho$  for the Generalised Cubic Spline with a variety of different values of  $q_0$ .

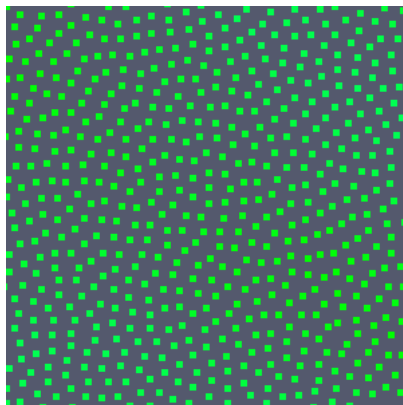


**Figure 7.4:** Typical particle distribution for forced turbulence simulation using a Generalised Cubic Spline kernel with  $q_0 = \Delta p/h = 0.5$

and is positive definite. In other words,  $\psi(q)$  is zero for  $q > 2$  and the interpolation matrix formed from

$$A = (\psi(|\mathbf{r}_a - \mathbf{r}_b|))_{1 \leq a, b \leq N} \quad (7.3.1)$$

is positive definite for all sets of particles  $\mathbf{r}_1, \dots, \mathbf{r}_N$ . Wendland derived a family of such functions  $\psi_{l,k}$  where  $l = \lfloor d/2 \rfloor + k + 1$  and  $d$  is the dimensionality. Each function is a polynomial of degree  $\partial\psi_{l,k} = l + 2k$  and has  $2k$  continuous derivatives around  $q = 0$  and  $2k + \lfloor d/2 \rfloor$  continuous derivatives around  $q = 2$ . For the purposes of this thesis we have chosen to define the Wendland kernel as  $W(q) = \psi_{3,1}$ , which is (in two dimensions)

$$W(q) = \frac{\beta}{h^d} \begin{cases} (2-q)^4(1+2q) & \text{for } 0 \leq q \leq 2, \\ 0 & \text{for } q > 2. \end{cases} \quad (7.3.2)$$

where  $\beta = 7/(64\pi)$ .

Compared with the Cubic Spline kernel, this is a fifth degree polynomial, instead of three. It has the same number of continuous derivatives at  $q = 0$  and one extra continuous derivative at  $q = 2$ . In these terms, it is the closest function in the Wendland family to the Cubic Spline. It would be interesting to explore the Wendland functions of higher degree, as higher order Cubic Spline kernels have been shown to provide additional stability benefits (Morris (1996)). Since all the Wendland functions have the same compact support, no extra particles would be involved in the interpolants and the increase in computational effort would be minor.

Figure 7.5 shows the Wendland kernel  $W(q) = \psi_{3,1}$  for  $d = 2$  (the Wendland kernels in two dimensions are the same as for three), compared with three other relevant kernels: the Gaussian, Cubic Spline and the Tuned Cubic Spline (the Generalised Cubic Spline with  $q_0 = 0.5$ ). In terms of its general shape, the Wendland kernel falls somewhere between the Cubic Spline and the Tuned Cubic Spline. It is slightly more concentrated around  $q = 0$  than the Cubic Spline and therefore the inner particles contribute more to the summation interpolant.

One clear advantage of the Wendland kernel is its effect on particle clumping. It has been reported by Capone et al. (2007) that the Wendland removes the need to correct for the Tensile Instability, presumably because it eliminates particle clumping. Applying the Wendland kernel to our forced turbulence simulations had a similar effect. It entirely eliminated the particle clumping at  $r = h$  and resulted in a highly regular distribution of particles. Figure 7.6 shows a typical distribution of particles in the forced turbulence simulation using the Wendland kernel and the corresponding radial particle density function  $R_\rho$ . The particles are evenly spaced and are distributed in a similar fashion to the previous figure showing the particle positions using the Tuned Cubic Spline (Figure 7.4). The plot of  $R_\rho$  is also similar, showing peaks corresponding to  $r = \Delta p$  and  $r = 2\Delta p$ , consistent with a regular distribution of particles.

Figure 7.7(a) compares the evolution of the total kinetic energy from the forced turbulence simulation using the Cubic Spline, the Tuned Cubic Spline and the Wendland kernels.

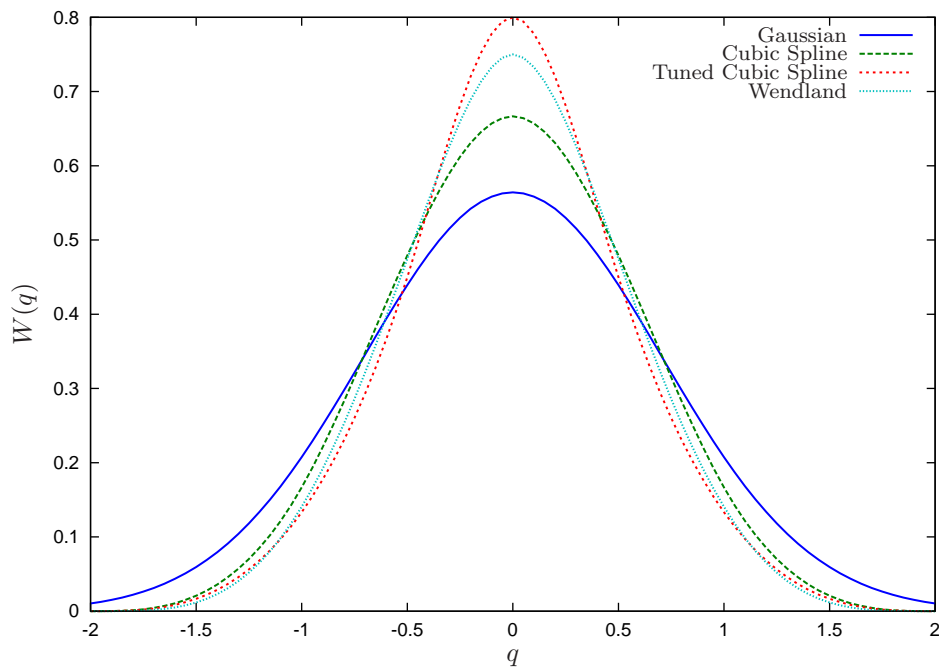


**Figure 7.5:** Comparison of four different kernels in one dimension. The traditional Cubic Spline (Equation 2.4.5), the Tuned Cubic Spline (Equation 7.2.2 with  $q_0 = 0.5$ ), the Gaussian (Equation 2.4.4) and the Wendland kernel (Equation 7.3.2)

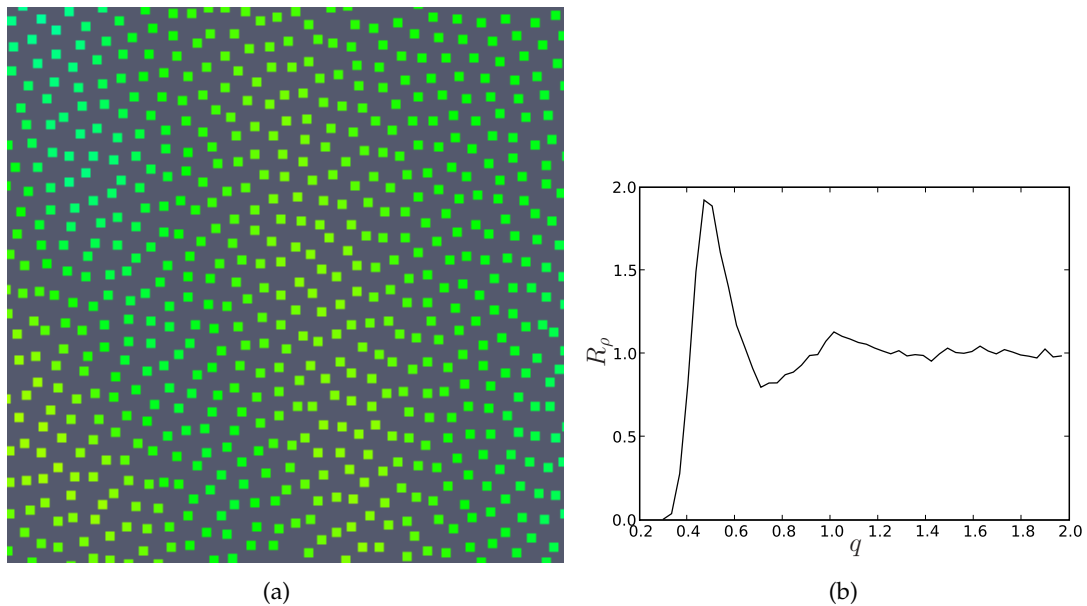


**Figure 7.6:** (a) A typical particle distribution using the Wendland kernel with  $h/\Delta p = 1.95$ . (b) Radial Particle Density.

The forcing term parameters are  $A = 6$  and  $\tau = 0.01683$ . The ratio of smoothing length to particle spacing is  $h/\Delta p = 1.95$  and  $\rho_0 = 995$ . The sound speed is  $c_s = 20$  and the box has dimensions of  $2 \times 2$ . The viscosity is  $\nu = 5 \times 10^{-4}$ . These parameters are identical to those given for the original forced turbulence simulation described in Chapter 6.

The strength of the inverse energy cascade, indicated by the rate of increase of the total kinetic energy, is clearly greatest for the Wendland kernel. Even the Tuned Cubic Spline, which has excellent anti-clumping properties, performs poorly compared with the Wendland kernel. The dissipation produced in the Cubic Spline simulation is enough to halt the inverse energy cascade entirely and prevent the formation of any turbulent flow.

Looking at the kinetic energy spectra in Figure 7.7(b), the results indicate that the use of the Wendland kernel helps to reduce the range of the small-scale velocity noise and gives the expected kinetic energy scaling down to a smaller length scale. While the Wendland kernel spectrum deviates from the expected  $k^{-3}$  scaling for  $\tilde{k} > 4.5$ , both the Cubic Spline spectra deviate for  $\tilde{k} > 3$ .

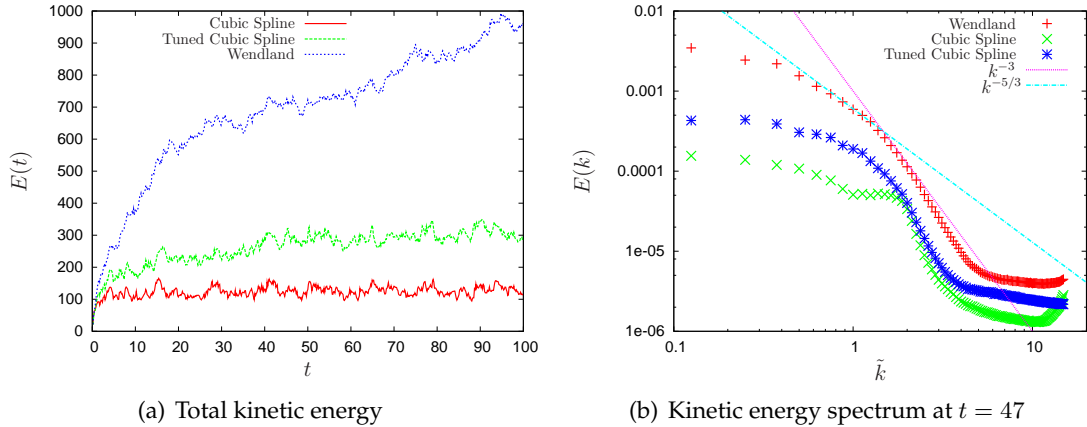


**Figure 7.7:** Comparison of three different kernels applied to the forced turbulence simulation

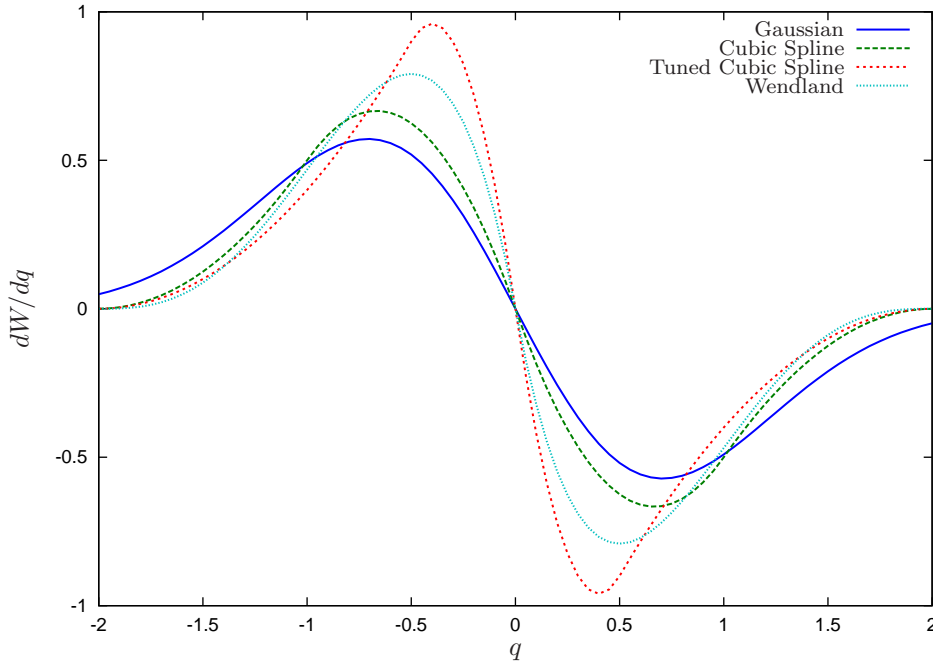
## 7.4 The First Derivative of the Kernel

The first derivative of four different kernels  $dW/dq$  can be seen in Figure 7.8. The kernels shown are the Wendland kernel, the Gaussian kernel, the traditional Cubic Spline and the Tuned Cubic Spline.

It is the first derivative of the kernel, rather than the kernel itself, that is used in the SPH equations for calculating derivatives. Therefore it is useful to consider the effect of  $dW/dq$  on the particle dynamics. Consider the SPH momentum equation (neglecting viscosity)

$$\frac{d\mathbf{v}_a}{dt} = - \sum_b m_b \left( \frac{P_b}{\rho_b^2} + \frac{P_a}{\rho_a^2} \right) \frac{\mathbf{r}_{ab}}{|\mathbf{r}_{ab}|} \frac{dW}{dq}. \quad (7.4.1)$$

As two SPH particles with constant density move closer together from an initial separation of  $2h$ , the pressure force between them grows along with the first derivative of the

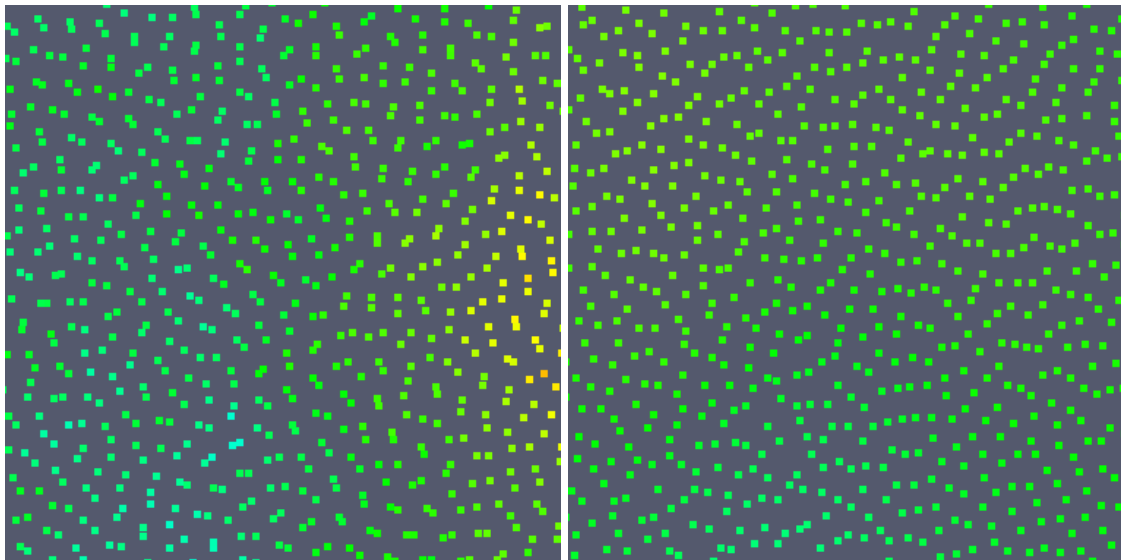
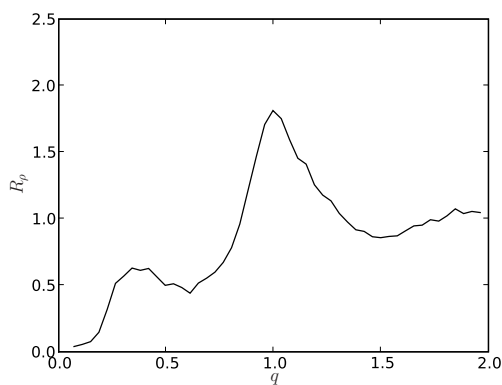
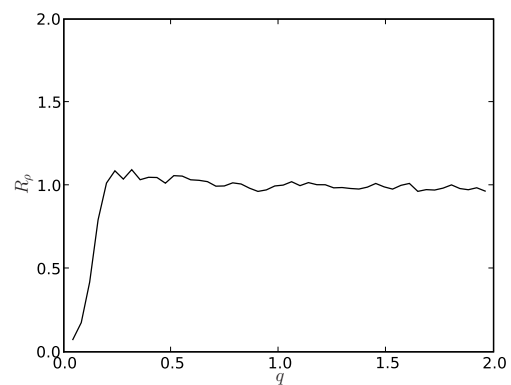


**Figure 7.8:** The first derivative of the four kernels shown in Figure 7.5

kernel. Once this function reaches its minimum at  $q = q_m$ , the pressure force begins to soften and drop down to zero as  $q \rightarrow 0$ . On first consideration, this is a possible explanation for particle clumping, as particles separated by  $0 \leq q < q_m$  will feel less pressure force to keep them apart. However, this does not take into account the increase in density as these particles come together nor the interactions with other neighbouring particles.

The results in Figure 7.9 clearly refute this explanation for the particle clumping. Figure 7.9(c) shows a plot of  $R_\rho$  taken from a forced turbulence simulation using the Cubic Spline kernel with  $\Delta p/h = 0.76$ . This is greater than the maxima of the Cubic Spline kernel ( $q_m = 0.67$ ) yet there is still significant particle clumping as indicated by the maxima in  $R_\rho$  at  $q = 1$ . Figure 7.9(d) shows the same results using the Wendland kernel with  $\Delta p/h = 0.25$ . This is much less than the maxima of the first derivative for the Wendland kernel ( $q_m = 0.5$ ), yet there is no significant particle clumping. Similar results have been obtained by repeating these simulations over the range  $0.5 < \Delta p/h < 0.76$ . Irrespective of the value of  $\Delta p/h$ , the Cubic Spline kernel results in particle clumping with a length scale of  $h$ , whereas the Wendland kernel eliminates all particle clumping.

Another commonly cited source of particle clumping is the SPH Tensile Instability. Sweigle et al. (1995) stated that the SPH method was unstable for particle  $a$  if  $\sum_b W''(r_{ab})T_a > 0$ , where  $W''(r_{ab})$  is the second derivative of the kernel evaluated at each neighbour particle  $b$ , and  $T_a$  is the total stress on  $a$ . Assuming a similar distribution of  $T_a$  for all particles, the criteria for the Tensile Instability is solely dependant on the location of  $W''(r) = 0$  (i.e. The minima of the first derivative at  $q = q_m$ ) in relation to the average scaled particle spacing  $\Delta p/h$ . In other words, if  $q_m h/\Delta p$  is identical for two different simulations with similar distributions of  $T_a$ , then  $\sum_b W''(r_{ab})T_a$  will also be similar and the effects of the Tensile Instability should be identical for both simulations. However, for two otherwise identical simulations using the Wendland and Cubic spline kernels, the parameter

(a) Sample particle distribution,  $h/\Delta p = 1.3$ (b) Sample particle distribution,  $h/\Delta p = 4.5$ (c) Radial particle density,  $h/\Delta p = 1.3$ (d) Radial particle density,  $h/\Delta p = 4.0$ 

**Figure 7.9:** *Left Column: Results using Cubic Spline kernel,  $\Delta p/h = 0.76$ . This is slightly greater than the maxima of the first derivative of the kernel, however there is still significant particle clumping. Right Column: Wendland kernel with  $\Delta p/h = 0.25$ . This is much less than the maxima of the first derivative, yet there is little particle clumping*

$q_m h / \Delta p$  can be made identical by choosing a suitable value of  $h / \Delta p$  for each kernel. We have already shown that the particle clumping in the forced turbulence simulations is independent of  $h / \Delta p$ , and therefore the Tensile Instability cannot be the source of this clumping.

## 7.5 The Fourier Transform of the Kernel

The results shown in this Chapter have consistently shown that the Cubic Spline results in significant particle clumping on a length scale equal to  $q_0$ , which is the location of the spline point. In contrast, the Wendland kernel does not show any significant clumping. The shape of  $W$  and  $dW/dq$  have not shown any differences between the two kernels that might account for this. However, their Fourier Transforms do reveal some interesting properties that offers a possible cause for the particle clumping.

The Fourier Transform of the kernel is known to be important in determining the stability properties of an SPH simulation. Morris (1996) performed a stability analysis of SPH and derived the dispersion relation for sound waves propagating along a regular one-dimensional row of particles in terms of the Fourier transform of the kernel

$$\omega^2 = \frac{2mc^2 R}{\rho_0 \Delta p} \sum_{l=-\infty}^{+\infty} \left[ \left( k + \frac{2\pi l}{\Delta p} \right) U \left( k + \frac{2\pi l}{\Delta p}, h \right) - \left( \frac{2\pi l}{\Delta p} \right)^2 U \left( \frac{2\pi l}{\Delta p}, h \right) \right] + \left( \frac{mc}{\rho_0 \Delta p} \right)^2 (1 - 2R) \left[ \left( k + \frac{2\pi l}{\Delta p} \right) U \left( k + \frac{2\pi l}{\Delta p}, h \right) \right]^2, \quad (7.5.1)$$

where  $U(k, h)$  is the Fourier transform of the kernel and  $R$  is a constant governing the global pressure, positive or negative, applied to the system. The stability study by Morris (1996) did not find any source of instability for the Cubic Spline kernel that might result in particle clumping at a lengthscale of  $h$ . However, this study only considered the stability of particles on a regular 1D or 2D grid (rectangular and hexagonal grids in 2D), and did not allow the particles to be significantly disordered. Nevertheless, there is certainly a link between the Fourier Transform of the kernel and the stability of the SPH method, and there is little doubt that this link remains when the particles become increasingly disordered.

Figure 7.10 shows the Fourier Transform  $\widehat{W}$  of these four kernels versus the normalised wavenumber  $\bar{k}$ , which is scaled so that  $\bar{k} = 1$  for a wavelength of  $\lambda = h$ . This plot is clipped for readability so that only  $\widehat{W} > 0.001$  is shown, but the Cubic Spline spectra has zeros occurring at  $\bar{k} = n$  where  $n = 1, 2, 3, \dots$  and the Tuned Cubic Spline has zeros at  $\bar{k} = 2n$ . Both the Gaussian and the Wendland kernels have no zeros and are strictly positive.

It is worth noting how quickly the Fourier Transforms fall off for  $\bar{k} < 1$ . Morris (1996) found that the stability properties are improved for kernels with Transforms that fall off rapidly. Furthermore, if the SPH kernel is thought of as a low-pass filter, the rate at which the Transform falls off around  $\bar{k} = 1$  governs how effectively “noise” (perturbations smaller than the smoothing length) is filtered out and how well the “signal” (flow

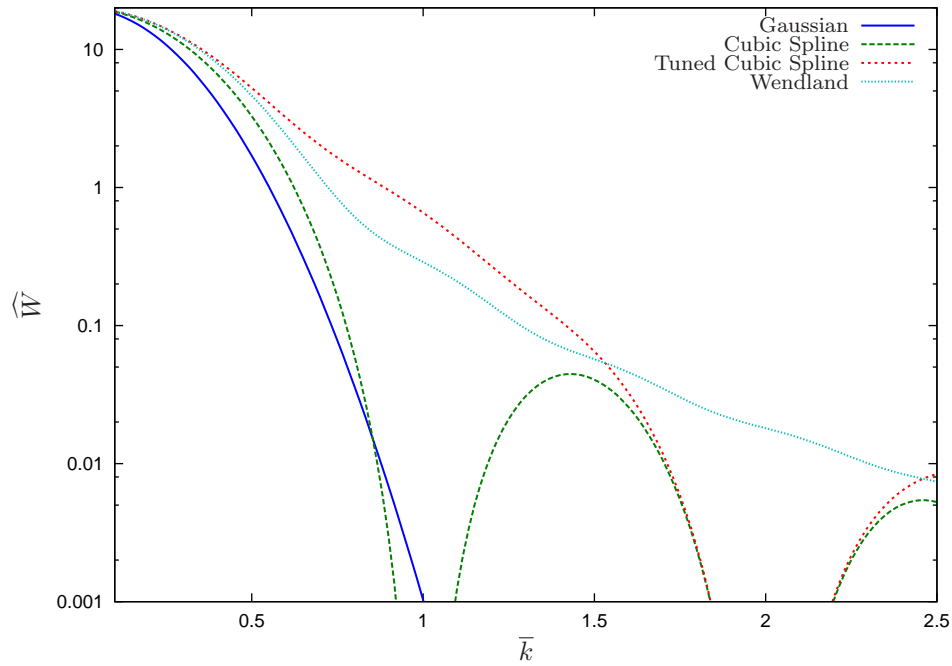


**Figure 7.10:** The Fourier Transform of the four kernels shown in Figure 7.5. The normalised wavenumber  $\tilde{k}$  is scaled so that  $\tilde{k} = 1$  for the mode with wavelength  $\lambda = h$ .

structures larger than the smoothing length) is preserved.

Looking at the Fourier Transforms for the given kernels, it can be seen that the Transform of the Wendland kernel falls off relatively slowly. In fact, only the Tuned Cubic Spline has a gradient less than the Wendland kernel. However, both these kernels eliminate the particle clumping and give more accurate results for the forced turbulence simulations. This indicates that the benefits of an orderly particle distribution are much more significant than any additional errors introduced by a Fourier Transform with a slow falloff.

It is interesting to note that the Cubic Spline has a zero occurring at  $\bar{k} = 1$ , which has a wavelength equal to the clumping length scale seen with this kernel. To see if this pattern continues for different spline point locations, the Fourier Transform of the Generalised Cubic Spline  $\widehat{W}_g(k, q_0)$  was calculated. Solving for  $\widehat{W}_g(k, q_0) = 0$ , it can be found that  $\widehat{W}_g$  is less than or equal to zero when

$$\cos(kq_0) \leq \frac{1}{4}q_0^2 \cos(2k) - \frac{1}{4}q_0^2 + 1. \quad (7.5.2)$$

Figure 7.11(a) plots this condition for  $q_0$  varying between  $0 < q_0 < 2$  and a normalised wavenumber  $\bar{k}$  between  $0 < \bar{k} < 4$ . The black areas indicate regions where  $\widehat{W}_g(k, q_0) < 0$ . The dashed line at  $q_0 = 1$  in this Figure corresponds to the Cubic Spline kernel, and tracing this line in Figure 7.11(a) one can see the zeros occurring at  $\bar{k} = 1, 2, 3, \dots$ . Similarly,  $q_0 = 0.5$  corresponds to the Tuned Cubic Spline, which results in zeros at  $\bar{k} = 2, 4, 6, \dots$ .

Figure 7.11(b) substitutes  $k = 2\pi/\bar{\lambda}$  in Equation 7.5.2, and re-plots this condition for  $\bar{\lambda}$  versus  $q_0$ , where  $\bar{\lambda} = \lambda/h$  is the normalised wavelength of each mode  $k$ . This plot shows

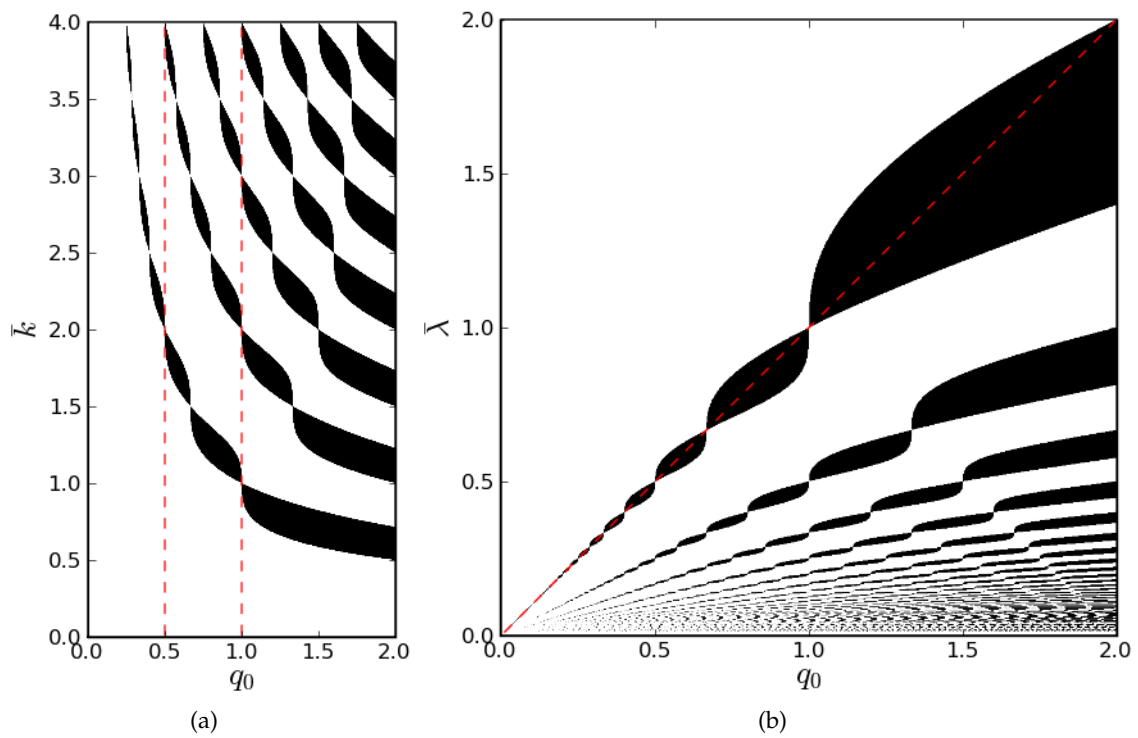


**Figure 7.11:** Areas in black indicate regions where the Fourier Transform of the Generalised Cubic Spline is negative (i.e.  $\widehat{W}_g < 0$ ). (a) Normalised Wavenumber  $\bar{k}$  versus Spline Location  $q_0$ . (b) Normalised Wavelength  $\lambda$  versus Spline Location  $q_0$ .

a linear relationship between the location of the spline point  $q_0$  and the negative region of  $\widehat{W}_g$ . The most important feature of this plot is highlighted by the dashed line at  $\bar{\lambda} = q_0$ . Moving from longer to smaller wavelengths, the first negative region of  $\widehat{W}_g$  occurs near this line for all values of  $q_0$ . Recall that the particle clumping was shown to occur at a length scale equal to  $q_0$ , so this dashed line also represents the clumping length scale for each value of  $q_0$ .

These results show, for the Generalised Cubic Spline kernel, that the length scale of the particle clumping always occurs at the longest wavelength where the Fourier Transform of the kernel  $\widehat{W}_g$  is less than or equal to zero. Furthermore, as  $q_0$  becomes larger, the span of wavelengths where  $\widehat{W}_g < 0$  becomes wider, and this corresponds to an identical widening of the peak in  $R_\rho$  (consult the sequence of  $R_\rho$  for  $q_0 = 0.5, 0.75, 1.0, 1.5$  in Figure 7.3). In contrast, the Fourier Transform of the Wendland kernel never becomes negative, and the use of this kernel results in a very regular particle distribution with no clumping.

## 7.6 Conclusion

The choice of kernel used has a dramatic effect on the nature of the forced turbulence simulations and the distribution of the SPH particles. For a given set of forcing term parameters, the difference between the Cubic Spline and the Wendland kernels may be the difference between the formation of a turbulent flow and none at all. The use of the Spline family of kernels has a long history in SPH and it is rare that any other kernel is considered. However, given the significant improvements that can be made with no increase in computational effort, it is perhaps useful to consider further the effect that the shape of the kernel has on the motion and distribution of the particles.

The forced turbulence simulations described in the previous chapter have the advantage that they produce homogeneous turbulent flows away from the boundaries. This allows for a statistical analysis of the particle distribution, which shows that the Cubic Spline kernel tends to separate particles by the location of the spline point  $q_0$ , which is traditionally set to the smoothing length  $q_0 = h$ . The use of the Wendland kernel eliminates this clumping entirely and results in very even particle distributions and significantly less numerical dissipation than the Cubic Spline.

The reason that the Cubic Spline kernel causes particle clumping at a length scale of  $q_0$  is unclear. However, it seems likely that the criteria for particle clumping is heavily influenced by the negative regions of the Fourier Transform of the kernel  $\widehat{W}(k)$ . For the Cubic Spline kernel,  $\widehat{W}(k) < 0$  for a range of wavenumber around  $k = 2\pi/q_0$ . The range of wavenumbers where  $\widehat{W}(k) < 0$  corresponds to the range of length scales where particle clumping can be seen, indicating that the distribution of particles tend to favour modes that result in a negative value of the kernel's Fourier Transform. This conclusion is strengthened by the Fourier Transform of the Wendland kernel, which is greater than zero for all  $k$ .

## Chapter 8

# Conclusion

---

This thesis explored the application of SPH to mixing flows at either end of the spectrum of Reynolds numbers.

For low Reynolds number flows, Smoothed Particle Hydrodynamics is a promising numerical method for the study of mixing in a typical industrial mixer. Complex, moving geometries can easily be incorporated into the method, and its Lagrangian nature provides a natural framework to model and analyse the transport of fluid. This thesis presented results from an SPH simulation of mixing within a 2D Twin Cam mixer, and showed that the fluid transport was modelled accurately in comparison to published experimental and numerical results.

For industrial mixers operating at a low Reynolds number, the correct simulation of the flow is only half of the problem. It is important to be able to analyse and understand the mixing in order to optimise the operation of the mixer. To this end, this thesis also presented a method to calculate the Finite Time Lyapunov Exponents from the SPH particle data. Ridges in the spatial distribution of the FLTE show the chaotic manifolds of the flow. These manifolds describe the short-term mixing processes and highlight areas that are isolated and slow to mix with the rest of the domain. Also presented is a novel measure of mixing that quantifies how well an initial dyed region of fluid is mixed into the rest of the domain. This provides a practical measure that is directly related to the primary aim of any industrial mixer, the homogenisation of fluid areas.

While SPH performs well for laminar problems, this thesis showed that it has significant problems with reproducing the important characteristics of a turbulent flow. While this is a problem for any SPH simulation of turbulent flow, it is particularly relevant for mixing simulations as turbulence is often a desirable quality in order to promote mixing.

SPH simulations of both decaying and forced 2D turbulence in a wall-bounded domain were presented. For decaying turbulence, the SPH method produced results that compared well with published results from a highly accurate pseudo-spectral simulation (Clercx et al. 1999). All the ensemble statistics of the flow given by Clercx et al. (1999) matched those calculated from the SPH results.

However, the SPH formulation used in this thesis is inadequate for the simulation of

---

continually forced turbulence. The fundamental problem of the method involves the production of small and medium scale fluctuations in the velocity of the particles, which results in excessive viscous dissipation. The dominant characteristic of 2D turbulence is the inverse energy cascade, which creates a flux of kinetic energy to longer length scales. The excess dissipation seen in the SPH simulations severely weakens this cascade, preventing the formation of the expected large scale vortex structures. The fluctuations in the velocity also affect the mixing properties of the flow, acting as an artificial forcing term and increasing the rate of mixing at small length scales.

SPH parameter studies indicate that the erroneous velocity fluctuations and the excess dissipation are very sensitive to the numerical sound speed, but are insensitive to increases in resolution. For the particular Reynolds number investigated ( $Re = 1581$ ), it is estimated that a resolution of  $3500 \times 3500$  particles is needed to reduce the scale of the velocity fluctuations below the dissipation length scale. Given that this would result in an average particle separation 44 times longer than the dissipation length scale, this resolution requirement is clearly excessive.

On a more positive note, the formation of vorticity filaments and subsequent roll-up of these filaments near the no-slip boundaries are reproduced well by the SPH method. In addition, the kinetic energy spectra for the forced turbulence simulations show that the direct enstrophy cascade is accurately modelled for length scales longer than 8 particle spacings.

The results from this thesis also identified the significant improvements (at no extra computational cost) that result from the use of the Wendland kernel. The more commonly used Cubic Spline kernel was found to induce particle clumping at a length scale equal to the smoothing length  $h$ . The Wendland kernel entirely eliminated this clumping, and resulted in a significant reduction in the excess numerical dissipation, allowing the formation of a stronger inverse energy cascade.

The focus of this thesis was on the simulation of two-dimensional turbulence. However, the velocity fluctuations and excess numerical dissipation seen in these results are perhaps more significant for 2D turbulence rather than 3D. Due to the inverse energy cascade, the small length scales must be correctly modelled in order to obtain the (more obvious) large scale flow. For three-dimensional turbulence, the flux of energy is reversed and any excess dissipation would only be expected to affect smaller length scales. In addition, 2D turbulence is expected to have a vanishing energy dissipation in the limit of infinite Reynolds number, whereas the dissipation in 3D turbulence is always finite. Therefore the addition of an excess numerical dissipation due to the SPH method would have a greater impact on the 2D results.

This is not to say that SPH would be an effective method for the simulation of 3D turbulence, as an accurate estimation of turbulent dissipation is important for many problems. However, this highlights the usefulness of 2D turbulence as a benchmark problem for SPH. It poses a particularly difficult problem that can be calculated at a significantly reduced computational cost. Furthermore, the homogeneous nature of the turbulence allows the use of Fourier analysis and statistical tools in order to analyse the results.

## 8.1 Recommendations for Future Research

It would be valuable to extend the work of this thesis in the following areas.

### 8.1.1 Three-dimensional Chaotic Manifolds

Chapter 3 describes a method for extracting the chaotic manifolds from 2D SPH data by the visual inspection of the FTLE spatial map. For the analysis of many industrial mixers, the extraction of manifolds from 3D SPH data is essential. Calculating the FTLE field in three dimensions is a trivial extension. However, it is not practical to assume that the user can visually extract the manifold from the FTLE field, as was done in this thesis. Therefore, the main challenges here would be in the development of ridge detection algorithms to extract the chaotic manifolds reliably from the FTLE field. Once the manifolds are extracted, the next problem would be how to display a complex manifold structure to the user. The most meaningful information provided by the manifolds is the intersection points of the unstable and stable manifolds, as well as the co-incident regions of these manifolds. Therefore, it would be useful to calculate and display the intersection of the two types of chaotic manifold.

### 8.1.2 Turbulent Boundary Condition and Boundary Layers

This thesis has described the effect of the no-slip boundary condition on the evolution of decaying and forced turbulence in 2D. In general terms, the net result is the spontaneous spin-up of the flow and the injection of high intensity vorticity gradients into the flow. For the SPH results, the effect of the walls was described using some vorticity plots, and Section 6.6 compared the strength of the vorticity filament generation and roll-up to the experimental data provided by Wells et al. (2007).

However, there is still many further questions that need to be answered about the SPH turbulent boundary layer. For instance, the representation of the no-slip boundary is still an active area of SPH research. This thesis has only used one particular method, by modelling the boundary using multiple layers of stationary SPH particles. This provides a first-order boundary condition. This can be extended to higher-order conditions (see, for example, Morris et al. (1997)). It would also be useful to use other boundary approximations such as boundary or ghost particles (see Section 2.6 for more details)

In addition, a more comprehensive analysis of the SPH boundary layer (a challenging topic in turbulence modelling) is needed. It would be useful to calculate the spectral decomposition of the turbulence close to the boundary. This can be compared against published results such as Clercx & van Heijst (2000), which presents the time evolution of the velocity spectrum near the boundary in a pseudo-spectral decaying turbulence simulation. While this would provide information on the statistical quantities of the SPH boundary layer, it is also useful to consider the specific interaction of vortices with the non-slip boundary. van Heijst et al. (2006) contains spatial and time-varying vorticity plots for the oblique collision of a dipole vortex and a no-slip boundary, which can be compared with a similar SPH simulation.

### 8.1.3 The Velocity Structure Function

The decomposition of a turbulent flow into its separate length scales is an important aspect of most turbulence studies, and this is often achieved through the use of the Fourier transform. This was the approach taken in this thesis. However, the estimation of the SPH Fourier transform introduces additional numerical errors, particularly at the important small length scales.

The velocity structure function (Section 4.1.3) also provides a method for decomposing the velocity field into different length scales. This function can be calculated directly from the SPH velocity data, with no additional numerical error. However, in three dimensions this function is dominated by the small scale velocity field and in two dimensions it is dominated by the large scale vorticity field. Davidson (2004) presents a few candidate functions, based on the velocity structure function, that aim to provide a real-space equivalent to the Fourier transform. These functions should be evaluated, extended if necessary, and applied to the SPH results.

### 8.1.4 Three-dimensional SPH Turbulence

The DNS simulation of 3D turbulence provides significant challenges in terms of raw computational resources. But, as 2D turbulence is primarily a theoretical construct and of limited use in a real-world flow, an understanding of how SPH reproduces 3D turbulence is essential. As already described in this Chapter, it is expected that in three dimensions, the effects of the small scale dissipation will have less effect on the large scale structures of the flow. However, it is likely that the small scale velocity fluctuations will remain and that the viscous dissipation will continue to be over-estimated by the SPH method.

### 8.1.5 Particle Clumping and Kernel Fourier Transform

Chapter 7 showed that a clear relationship exists between the particle clumping length scale and the Fourier transform of the SPH kernel. However, this is shown via the statistical analysis of a particular 2D forced turbulence simulation, and in order to provide generality it is necessary to derive this relationship directly from the SPH equations. This would also provide additional information on the effects of the kernel spectrum and suggest strategies for the improvement of the SPH method.

### 8.1.6 Small Scale Velocity Fluctuations

The most significant source of error in the SPH results is the small wavelength velocity fluctuations. These fluctuations lead to a large excess in the viscous dissipation and weaken the inverse energy cascade in 2D turbulence. They also have implications in the development of future turbulence models, which usually rely on the small scale velocity field to accurately estimate the local turbulence properties.

For these reasons and others detailed in Chapter 6, the most important avenue of research that has been identified by this thesis is the identification and elimination of the source of these fluctuations.

Different SPH formulations could be investigated and their effect on the fluctuations compared. For example, there has been much effort in the SPH community to provide SPH gradient estimations that have a higher order completeness than the base formulation used in this thesis (see Section 2.3). However, if the source of the fluctuations is viewed as an instability in the SPH equations, it seems likely that an increasingly accurate gradient estimation will only serve to slow the development of such an instability, rather than stop it altogether. Another option is to use a fully incompressible SPH formulation, of which a number of different options exist (Cummins & Rudman 1999, Shao & Lo 2003, Hu & Adams 2007).

A comprehensive stability analysis of SPH could reveal the source of the velocity fluctuations. While there have been SPH stability studies performed previously, most notably by Morris (1996), they have all assumed a regular particle distribution. The results of Chapter 7 have shown that the particle distribution is highly dependent on subtle changes in the kernel shape. This highlights the importance of understanding the properties of the feedback loop that exists between the SPH equations and the particle distribution.

Stability studies of SPH have assumed a regular particle distribution because it is unclear how to incorporate an irregular distribution and what form this distribution should take. The relative particle positions are not completely random, but are instead dependant on the particular form of the inter-particle forces and the local velocity field. A mathematical framework that could be of use in this instance is statistical mechanics, which deals with ensembles of molecules with a given inter-molecular force and small scale (thermal) fluctuations. Monaghan (2005) paraphrases a relevant quote by Von Neumann (1944) that argues the particle method is advantageous since it “gives the rigorous equations for a particle system which approximates the molecular system underlying, and more fundamental than the continuum equations”. Given the parallels that exist between the SPH method and a molecular system, perhaps it would be advantageous to treat the SPH equations as inter-molecular forces and perform the analysis accordingly. It is the opinion of this author that this would be a very interesting (and challenging) avenue of research.

# Bibliography

---

Aldridge, B., Haller, G., Sorger, P. & Lauffenburger, D. (2006), 'Direct Lyapunov exponent analysis enables parametric study of transient signalling governing cell behaviour', *Systems Biology, IEE Proceedings* **153**(6), 425–432.

Antoci, C., Gallati, M. & Sibilla, S. (2007), 'Numerical simulation of fluid-structure interaction by sph', *Comput. Struct.* **85**(11-14), 879–890.

Aref, H. (1984), 'Stirring by chaotic advection', *Journal of Fluid Mechanics Digital Archive* **143**(-1), 1–21.

Aref, H. (2002), 'The development of chaotic advection', *Physics of Fluids* **14**(4), 1315–1325.

URL: <http://link.aip.org/link/?PHF/14/1315/1>

Artale, V., Boffetta, G., Celani, A., Cencini, M. & Vulpiani, A. (1997), 'Dispersion of passive tracers in closed basins: Beyond the diffusion coefficient', *Physics of Fluids* **9**, 3162–3171.

Avalosse, T. & Crochet, M. (1997), 'Finite-element simulations of mixing: 1. Two-dimensional flow in periodic geometry', *AIChE Journal* **43**(3), 577–587.

Ayrton, H. (1919), 'On a New Method of Driving off Poisonous Gases', *Royal Society of London Proceedings Series A* **96**, 249–256.

Batchelor, G. K. (1953), *The theory of homogenous turbulence*, Cambridge University Press.

Batchelor, G. K. (1969), 'Computation of the Energy Spectrum in Homogeneous Two-Dimensional Turbulence', *Physics of Fluids* **12**, 233–+.

Batchelor, G. K. (1970), *An introduction in fluid dynamics / by G. K. Batchelor*, U.P., Cambridge :.

Belytschko, T., Krongauz, Y., Dolbow, J. & Gerlach, C. (1998), 'On the completeness of meshfree particle methods', *International Journal of Numerical Methods in Engineering* **43**, 785–819.

Benz, W. & Asphaug, E. (1995), 'Simulations of brittle solids using smooth particle hydrodynamics', *Computer Physics Communications* **87**(1-2), 253 – 265. Particle Simulation Methods.

**URL:** <http://www.sciencedirect.com/science/article/B6TJ5-40324WV-1G/2/e833e02894d0d5c688ebde24c3b99d67>

Bertrand, F., Thibault, F., Delamare, L. & Tanguy, P. A. (2003), 'Adaptive finite element simulations of fluid flow in twin-screw extruders', *Computers & Chemical Engineering* **27**(4), 491–500.

Boffetta, G. & Sokolov, I. M. (2002), 'Statistics of two-particle dispersion in two-dimensional turbulence', *Physics of Fluids* **14**, 3224–3232.

Bonet, J. & Lok, T. S. L. (1999), 'Variational and momentum preservation aspects of smooth particle hydrodynamic formulations', *Computer Methods in applied mechanics and engineering* **180**, 97–115.

Cameron, A. G. W. & Benz, W. (1991), 'The origin of the moon and the single impact hypothesis iv', *Icarus* **92**(2), 204 – 216.

**URL:** <http://www.sciencedirect.com/science/article/B6WGF-47317V0-20G/2/c78818c7d9faab429d2ea143d835f182>

Capone, T., Panizzo, A., Cecioni, C. & Darlymple, R. A. (2007), Accuracy and stability of numerical schemes in SPH, in '2nd SPHERIC Workshop', pp. 156–160.

Cleary, P. W. (1998), 'Modelling confined multi-material heat and mass flows using sph', *Applied Mathematical Modelling* **22**, 981–993.

Cleary, P. W. & Monaghan, J. J. (1993), Boundary interactions and transition to turbulence for standard cfd problems using sph, in 'Proc. 6th International Computational Techniques and Applications Conference', Canberra, pp. 157–165.

Cleary, P. W., Prakash, M., Ha, J., Stokes, N. & Scott, C. (2007), 'Smooth particle hydrodynamics: Status and future potential', *Progress in Computational Fluid Dynamics* **7**, 70–90.

Clercx, H. J. H., Maassen, S. R. & van Heijst, G. J. F. (1999), 'Decaying two-dimensional turbulence in square containers with no-slip or stress-free boundaries', *Physics of Fluids* **11**, 611–626.

Clercx, H. J. H. & van Heijst, G. J. F. (2000), 'Energy spectra for decaying 2d turbulence in a bounded domain', *Phys. Rev. Lett.* **85**(2), 306–309.

Clercx, H., van Heijst, G., Molenaar, D. & Wells, M. (2005), 'No-slip walls as vorticity sources in two-dimensional bounded turbulence', *Dynamics of Atmospheres and Oceans* **40**(1-2), 3–21.

Colagrossi, A. & Landrini, M. (2003), 'Numerical simulation of interfacial flows by Smoothed Particle Hydrodynamics', *Journal of Computational Physics* **191**, 448–475.

Cole, R. (1948), *Underwater Explosions*, Princeton University Press, Princeton, NJ.

Cummins, S. J. & Rudman, M. (1999), 'An SPH projection method', *Journal of Computational Physics* **152**(2), 584–607.

Dalrymple, R. & Rogers, B. (2006), 'Numerical modeling of water waves with the SPH method', *Coastal Engineering* **53**(2-3), 141–147.

- Davidson, P. (2004), *Turbulence: An introduction for scientists and engineers*, Oxford University Press.
- de Avillez, M. A. & Mac Low, M.-M. (2002), 'Mixing time scales in a supernova-driven interstellar medium', *The Astrophysical Journal* **581**, 1047.  
**URL:** <http://www.citebase.org/abstract?id=oai:arXiv.org:astro-ph/0208441>
- Delorme, L., Souto Iglesias, A. & Abril Perez, S. (2005), Sloshing loads simulation in lng tankers with sph, in 'Proceedings of the International Conference on Computational Methods in Marine Engineering, MARINE 2005'.
- Ecke, R. (2005), 'The turbulence problem: An experimentalist's perspective', *Los Alamos Science* **29**, 124–141.
- Fujiwhara, S. (1921), 'The natural tendency towards symmetry of motion and its application as a principle in meteorology', *The Quarterly Journal of the Royal Meteorological Society* **47**, 287–292.
- Geurts, B. J. & Holm, D. D. (2006), 'Leray and LANS- $\alpha$  modelling of turbulent mixing', *Journal of Turbulence* **7**, 10–+.
- Gingold, R. A. & Monaghan, J. J. (1977), 'Smoothed particle hydrodynamic: theory and application to non-spherical stars', *Monthly Notices of the Royal Astronomical Society* **181**, 375–389.
- Gingold, R. A. & Monaghan, J. J. (1978), 'Binary fission in damped rotating polytropes', *MNRAS* **184**, 481–499.
- Gray, J. P., Monaghan, J. J. & Swift, R. P. (2001), 'Sph elastic dynamics', *Computer Methods in Applied Mechanics and Engineering* **190**(49-50), 6641 – 6662.  
**URL:** <http://www.sciencedirect.com/science/article/B6V29-444P71C-8/2/425b46ac5f0edd9965ac569f19d6f839>
- Hairer, E., Lubich, C. & Wanner, G. (2003), 'Geometric numerical integration illustrated by the stormer/verlet method', *Acta Numerica* pp. 1–51.
- Hernquist, L. & Katz, N. (1989), 'TREESPH - A unification of SPH with the hierarchical tree method', *Astrophysical Journal* **70**, 419–446.
- Hobson, D. (1993), 'An Efficient Method for Computing Invariant Manifolds of Planar Maps', *Journal of Computational Physics* **104**, 14–22.
- Holmes, P. (1990), 'Poincaré, celestial mechanics, dynamical-systems theory and "chaos"', *Phys. Rep.* **193**, 137–163.
- Hu, X. Y. & Adams, N. A. (2007), 'An incompressible multi-phase sph method', *J. Comput. Phys.* **227**(1), 264–278.
- Issa, R., Violeau, D. & Laurence, D. (2005), A first attempt to adapt 3d large eddy simulation to the smoothed particle hydrodynamics gridless method, in 'Proceedings of the Int. Conf. Comput. and Experimental Eng. and Sciences, 1st Symposium on Meshless Methods'.

- Jana, S. C., Metcalfe, G. & Ottino, J. M. (1994), 'Experimental and computational studies of mixing in complex stokes flows: the vortex mixing flow and multicellular cavity flows', *Journal of Fluid Mechanics Digital Archive* **269**(-1), 199–246.
- Joseph, B. & Legras, B. (2002), 'Relation between Kinematic Boundaries, Stirring, and Barriers for the Antarctic Polar Vortex.', *Journal of Atmospheric Sciences* **59**, 1198–1212.
- Jun, Y. (2006), Statistical fluctuations of two dimensional turbulence, PhD thesis, University of Pittsburgh.
- Kaneda, Y., Ishihara, T., Yokokawa, M., Itakura, K. & Uno, A. (2003), 'Energy dissipation rate and energy spectrum in high resolution direct numerical simulations of turbulence in a periodic box', *Physics of Fluids* **15**(2), L21–L24.  
**URL:** <http://link.aip.org/link/?PHF/15/L21/1>
- Kolmogorov, A. N. (1941a), 'Decay of isotropic turbulence in an incompressible viscous fluid', *Dok. Akad. Nauk. SSSR* **31**, 538.
- Kolmogorov, A. N. (1941b), 'Energy dissipation in locally isotropic turbulence', *Dok. Akad. Nauk. SSSR* **32**, 19.
- Kolmogorov, A. N. (1941c), 'The local structure of turbulence in incompressible viscous fluid for very large reynolds numbers', *Dok. Akad. Nauk. SSSR* **30**, 9.
- Kraichnan, R. H. (1967), 'Inertial Ranges in Two-Dimensional Turbulence', *Physics of Fluids* **10**, 1417–1423.
- Krongauz, Y. & Belytschko, T. (1997), 'Consistent pseudo-derivatives in meshless methods', *Computer Methods in Applied Mechanics and Engineering* **146**, 371–386.
- Kundu, P. K. (1990), *Fluid Mechanics*, Academic.
- Lapeyre, G. (2002), 'Characterization of finite-time Lyapunov exponents and vectors in two-dimensional turbulence', *Chaos* **12**, 688–698.
- Lattanzio, J. C., Monaghan, J. J., Pongracic, H. & Schwarz, M. P. (1985), 'Interstellar Cloud Collisions', *MNRAS* **215**, 125–+.
- Lee, E. S., Moulinec, C., Xu, R., Violeau, D., Laurence, D. & Stansby, P. (2008), 'Comparisons of weakly compressible and truly incompressible algorithms for the sph mesh free particle method', *J. Comput. Phys.* **227**(18), 8417–8436.
- Li, S. & Montgomery, D. (1996), 'Decaying two-dimensional turbulence with rigid walls', *Physics Letters A* **218**, 281–291.
- Li, S., Montgomery, D. & Jones, W. B. (1997), 'Two-Dimensional Turbulence with Rigid Circular Walls', *Theoretical and Computational Fluid Dynamics* **9**, 167–181.
- Li, X.-X., Liu, C.-H. & Leung, D. Y. (2009), 'Numerical investigation of pollutant transport characteristics inside deep urban street canyons', *Atmospheric Environment* **43**(15), 2410 – 2418.  
**URL:** <http://www.sciencedirect.com/science/article/B6VH3-4VNH481-1/2/06ef751881bf5a4ee5398659425acea8>

- Lilly, D. K. (1969), 'Numerical simulation of two-dimensional turbulence', *Physics of Fluids* **12**(12), II-240–II-249.  
**URL:** <http://link.aip.org/link/?PFL/12/II-240/1>
- Lin, J.-T. (1972), 'Relative Dispersion in the Enstrophy-Cascading Inertial Range of Homogeneous Two-Dimensional Turbulence.', *Journal of Atmospheric Sciences* **29**, 394–395.
- Lindborg, E. & Alvelius, K. (2000), 'The kinetic energy spectrum of the two-dimensional enstrophy turbulence cascade', *Physics of Fluids* **12**, 945–947.
- Lowe, A. (2001), The direct numerical simulation of isotropic two-dimensional turbulence in a periodic square, PhD thesis, University of Cambridge.
- Lucy, L. B. (1977), 'A numerical approach to testing the fission hypothesis', *The Astrophysical Journal* **82**(12), 1013–1924.
- Maassen, S. R., Clercx, H. J. H. & van Heijst, G. J. F. (2002), 'Self-organization of quasi-two-dimensional turbulence in stratified fluids in square and circular containers', *Physics of Fluids* **14**, 2150–2169.
- Mansour, J. A. (2007), SPH and  $\alpha$ -SPH: Applications and Analysis, PhD thesis, Monash University.
- McWilliams, J. C. (1990), 'The vortices of two-dimensional turbulence', *Journal of Fluid Mechanics* **219**, 361–385.
- Meleán, Y., Sigalotti, L. D. G. & Hasmy, A. (2004), 'On the SPH tensile instability in forming viscous liquid drops', *Computer Physics Communications* **157**, 191–200.
- Metcalfe, G., Rudman, M., Brydon, A., Graham, L. J. W. & Hamilton, R. (2006), 'Composing chaos: An experimental and numerical study of an open duct mixing flow', *AIChE Journal* **52**(1), 9–28.
- Molenaar, D. (2004), Forced Navier-Stokes Flows on Bounded Two-Dimensional Domain, PhD thesis, Eindhoven University of Technology.
- Molenaar, D., Clercx, H. J. H. & van Heijst, G. J. F. (2004), 'Angular momentum of forced 2D turbulence in a square no-slip domain', *Physica D Nonlinear Phenomena* **196**, 329–340.
- Monaghan, J. J. (1992), 'Smoothed particle hydrodynamics', *Annual Review of Astronomy and Astrophysics* **30**, 543–574.
- Monaghan, J. J. (1994), 'Simulating free surface flows with SPH', *Journal of Computational Physics* **110**, 399–406.
- Monaghan, J. J. (1997), 'SPH and Riemann Solvers', *Journal of Computational Physics* **136**, 298–307.
- Monaghan, J. J. (2000), 'Sph without a tensile instability', *Journal of Computational Physics* **159**, 290–311.  
**URL:** <http://dx.doi.org/10.1006/jcph.2000.6439>
- Monaghan, J. J. (2002), 'SPH compressible turbulence', *MNRAS* **335**, 843–852.

- Monaghan, J. J. (2004), 'Energy transfer in a particle  $\alpha$  model', *Journal of Turbulence* **5**, 1–21.
- Monaghan, J. J. (2005), 'Smoothed particle hydrodynamics', *Reports of Progress in Physics* **68**, 1703–1759.
- Monaghan, J. J., Cas, R. A. F., Kos, A. M. & Hallworth, M. (1999), 'Gravity currents descending a ramp in a stratified tank', *Journal of Fluid Mechanics* **379**(-1), 39–69.
- Monaghan, J. J. & Gingold, R. A. (1983), 'Shock simulation by the particle method sph', *Journal of Computational Physics* **52**, 374–389.
- Monaghan, J. J., Kos, A. & Issa, N. (2003), 'Fluid motion generated by impact', *Journal of waterway, port, coastal and ocean engineering* **129**, 250–259.
- Morris, J. P. (1996), Analysis of Smoothed Particle Hydrodynamics with Applications, PhD thesis, Monash University.
- Morris, J. P., Fox, P. J. & Zhu, Y. (1997), 'Modeling low reynolds number incompressible flows using sph', *Journal of Computational Physics* **136**, 214–226.
- Oger, G., Doring, M., Alessandrini, B. & Ferrant, P. (2007), 'An improved sph method: Towards higher order convergence', *Journal of Computational Physics* **225**(2), 1472–1492.  
**URL:** <http://dx.doi.org/10.1016/j.jcp.2007.01.039>
- Ottino, J. M. (1989), *The kinematics of mixing: Stretching, chaos, and transport*, Cambridge and New York, Cambridge University Press, 1989, 375 p.
- Pierrehumbert, R. T. & Yang, H. (1993), 'Global Chaotic Mixing on Isentropic Surfaces.', *Journal of Atmospheric Sciences* **50**, 2462–2480.
- Poux, M., Fayolle, P., Bertrand, J., Bridoux, D. & Bousquet, J. (1991), 'Powder mixing: some practical rules applied to agitated systems', *Powder Technology* **68**, 213–234.
- Price, D. J. (2004), Magnetic fields in Astrophysics, Ph.D. thesis, Institute of Astronomy, University of Cambridge, Cambridge, UK.
- Randles, P. W. & Libersky, L. D. (1996), 'Smoothed particle hydrodynamics: Some recent improvements and applications', *Computer Methods in Applied Mechanics and Engineering* **139**(1-4), 375 – 408.  
**URL:** <http://www.sciencedirect.com/science/article/B6V29-41FDG4T-F/2/8220aeb1a97726e157007f98e4215d5a>
- Reynolds, O. (1883), 'An Experimental Investigation of the Circumstances Which Determine Whether the Motion of Water Shall Be Direct or Sinuous, and of the Law of Resistance in Parallel Channels. [Abstract]', *Royal Society of London Proceedings Series I* **35**, 84–99.
- Richardson, L. F. (1926), 'Atmospheric Diffusion Shown on a Distance-Neighbour Graph', *Royal Society of London Proceedings Series A* **110**, 709–737.
- Rivera, M. K. & Ecke, R. E. (2005), 'Pair Dispersion and Doubling Time Statistics in Two-Dimensional Turbulence', *Physical Review Letters* **95**(19), 194503–+.

- Robinson, M., Cleary, P. & Monaghan, J. (2008), 'Analysis of mixing in a twin cam mixer using smoothed particle hydrodynamics', *AIChE Journal* **54**(8), 1987–1998.  
**URL:** <http://dx.doi.org/10.1002/aic.11530>
- Rom-Kedar, V., Leonard, A. & Wiggins, S. (1990), 'An analytical study of transport, mixing and chaos in an unsteady vortical flow', *Journal of Fluid Mechanics* **214**, 347–394.
- Schoenberg, I. J. (1946), 'Contributions to the problem of approximation of equidistant data by analytic functions, part a: On the problem of smoothing or graduation, a first class of analytic approximation formulas', *Quart. Appl. Math.* **4**(45).
- Schussler, M. & Schmitt, D. (1981), 'Comments on smoothed particle hydrodynamics', *Astronomy and Astrophysics* **97**, 373–379.
- Shadden, S. C., Lekien, F. & Marsden, J. E. (2005), 'Definition and properties of Lagrangian coherent structures from finite-time Lyapunov exponents in two-dimensional aperiodic flows', *Physica D Nonlinear Phenomena* **212**, 271–304.
- Shao, S., Changming, J., Graham, D., Reeve, D., James, P. & Chadwick, A. (2006), 'Simulation of wave overtopping by an incompressible SPH model', *Coastal Engineering* **53**, 723–735.
- Shao, S. & Gotah, H. (2004), 'Simulating coupled motion of progressive wave and floating curtain wall by SPH-LES model', *Coastal Engineering* **46**, 171–202.
- Shao, S. & Lo, E. Y. M. (2003), 'Incompressible sph method for simulating newtonian and non-newtonian flows with a free surface', *Advances in Water Resources* **26**(7), 787 – 800.  
**URL:** <http://www.sciencedirect.com/science/article/B6VCF-48HXX4F-1/2/380162b8c29394cdf101a2dc3672598c>
- Shepard, D. (1968), A two dimensional function for irregularly spaced data., in 'ACM National Conference'.
- Smith, L. M. & Yakhot, V. (1993), 'Bose condensation and small-scale structure generation in a random force driven 2D turbulence', *Physical Review Letters* **71**, 352–355.
- Sommeria, J. (1986), 'Experimental study of the two-dimensional inverse energy cascade in a square box', *Journal of Fluid Mechanics* **170**, 139–168.
- Springel, V. & Hernquist, L. (2002), 'Cosmological smoothed particle hydrodynamics simulations: the entropy equation', *MNRAS* **333**, 649–664.
- Swegle, J. W., Hicks, D. L. & Attaway, S. W. (1995), 'Smoothed particle hydrodynamics stability analysis', *Journal of Computational Physics* **116**, 123–134.
- Ting, T. S., Prakash, M., Cleary, P. W. & Thompson, M. C. (2006), Simulation of high reynolds number flow over a backward facing step using sph, in A. Stacey, B. Blyth, J. Shepherd & A. J. Roberts, eds, 'Proceedings of the 7th Biennial Engineering Mathematics and Applications Conference, EMAC-2005', Vol. 47 of *ANZIAM J.*, pp. C292–C309.
- Tran, C. V. & Bowman, J. C. (2003), 'On the dual cascade in two-dimensional turbulence', *Physica D: Nonlinear Phenomena* **176**(3-4), 242 – 255.

---

**URL:** <http://www.sciencedirect.com/science/article/B6TVK-47FDMHW-3/2/9a679ed3b1114fe4de7582f08a0d1ef3>

Tran, C. V. & Bowman, J. C. (2004), 'Robustness of the inverse cascade in two-dimensional turbulence', *Physical Review E* **69**(3), 036303–+.

van der Hilst, R. (2004), 'Changing views on earth's deep mantle', *Science* **306**, 817–818.

van Heijst, G. J. F., Clercx, H. J. H. & Molenaar, D. (2006), 'The effects of solid boundaries on confined two-dimensional turbulence', *Journal of Fluid Mechanics* **554**, 411–431.

Violeau, D. & Issa, R. (2007), 'Numerical modelling of complex turbulent free-surface flows with the SPH method: an overview', *Int. J. Numer. Meth. Fluids* **53**, 277–304.

Violeau, D., Piccon, S. & Chabard, J. (2002), Two attempts of turbulence modelling in smoothed particle hydrodynamics, in 'Proceedings of the 8th Symposium on Flow Modelling and Turbulence Measurements', *Advances in Fluid Modelling and Turbulence Measurements*, World Scientific, Singapore, pp. 339–346.

Von Neumann, J. (1944), Proposal and analysis of a new numerical method for the treatment of hydrodynamical shock problem, in A. Taub, ed., 'Von Neumann Collected Works', Reader's Digest Young Families.

Warren, M. S. & Salmon, J. K. (1993), A parallel hashed oct-tree n-body algorithm, in 'Proceedings of Supercomputing'.

Warren, M. S. & Salmon, J. K. (1995), 'A portable parallel particle program', *Computer Physics Communications* **87**, 266–290.

Wells, M. G., Clercx, H. J. H. & van Heijst, G. J. F. (2007), 'Vortices in oscillating spin-up', *Journal of Fluid Mechanics* **573**, 339–369.

Welton, W. (1998), 'Two-Dimensional PDF/SPH Simulations of Compressible Turbulent Flows', *Journal of Computational Physics* **139**, 410–443.

Wendland, H. (1995), 'Piecewise polynomial, positive definite and compactly supported radial functions of minimal degree', *Advances in Computational Mathematics* **4**(1), 389–396.

Wiggins, S. (1992), *Chaotic transport in dynamical systems*, Springer-Verlag, New York.